

---

UNIVERSITÀ DEGLI STUDI DI FIRENZE  
DIPARTIMENTO DI FISICA  
Facoltà di Scienze Matematiche, Fisiche e Naturali

---

DOTTORATO DI RICERCA IN FISICA - XIX CICLO



## DISSERTATION IN PHYSICS

TO OBTAIN THE DEGREE OF

**DOTTORE DI RICERCA**  
IN FISICA

TITLE:

### **A NEW APPARATUS FOR ULTRACOLD K-RB BOSE-BOSE ATOMIC MIXTURES**

PRESENTED BY

**JACOPO CATANI**

SUPERVISOR..... PROF. MASSIMO INGUSCIO

COORDINATOR ..... PROF. ALESSANDRO CUCCOLI

REFEREES ..... PROF. JOOK T .M. WALRAVEN  
PROF. FABRIZIO BAROCCHI

EXAMINING COMMITTEE ..... PROF. MARK KASEVICH  
PROF. ENNIO ARIMONDO  
PROF. VALERIO TOGNETTI

Firenze, December 2006



*Alla mamma*



# Contents

<b>Introduction</b>	<b>1</b>
<b>1 Some Elements of Theory</b>	<b>7</b>
1.1 The Bose-Einstein Condensation . . . . .	7
1.2 The ideal trapped Bose gas . . . . .	9
1.2.1 $T=0$ . . . . .	9
1.2.2 $T>0$ . . . . .	10
1.3 The Interacting Bose Gas at $T=0$ : the Gross-Pitaevskii equation . . . . .	12
1.3.1 The ground state for $a>0$ : <i>repulsive is easy!</i> . . . . .	14
1.3.2 Free expansion of a repulsive condensate . . . . .	15
1.3.3 The ground state for $a<0$ : <i>the tricky attraction</i> . . . . .	15
1.4 Bose-Bose mixtures . . . . .	17
1.4.1 A model for the ground state . . . . .	18
1.4.2 Overlapping region . . . . .	20
1.4.3 Non-overlapping region . . . . .	21
<b>2 Ultracold Atoms in Optical Lattices</b>	<b>31</b>
2.1 Optical Dipole Forces . . . . .	32
2.1.1 The atom-light interaction . . . . .	32
2.2 Optical Lattices: <i>a beam against the other</i> . . . . .	36
2.2.1 Moving lattices and the band structure . . . . .	38
2.2.2 Dynamics of a Bloch wavepacket . . . . .	42
2.3 Multidimensional optical lattices . . . . .	43
2.4 A BEC in an optical lattice: role of interactions . . . . .	46
2.4.1 The Bose-Hubbard model and the Mott insulator phase . . . . .	48

2.4.2	Atomic mixtures in optical lattices . . . . .	55
<b>3</b>	<b>The New Machine</b>	<b>57</b>
3.1	The Laser System . . . . .	59
3.1.1	Potassium and Rubidium: <i>where's the real difference?</i> . . . . .	59
3.1.2	Laser sources: <i>lights on!</i> . . . . .	61
3.1.3	Main Beams Processing and Fibers Launching . . . . .	64
3.2	Magneto-Optical Traps . . . . .	67
3.2.1	The 2-Dimensional MOTs (2D-MOTs) . . . . .	68
3.2.2	Principle of operation: <i>only the coolest!</i> . . . . .	69
3.2.3	Our 2D-MOTs . . . . .	70
3.2.4	The 3D-MOT and the UHV chamber . . . . .	73
3.3	Purely Magnetic Trapping: <i>lights off!</i> . . . . .	75
3.3.1	The quadrupole field . . . . .	76
3.4	The Milli-Trap . . . . .	78
3.4.1	Measuring the trap frequencies . . . . .	84
3.4.2	Parametric heating . . . . .	84
3.4.3	Collective excitations . . . . .	87
3.5	Controlling the Magnetic Field . . . . .	89
3.5.1	The quadrupole current controller . . . . .	89
3.5.2	The milli-trap current controller . . . . .	91
3.5.3	Magnetic transport: <i>atoms and motors</i> . . . . .	92
3.6	Evaporative Cooling . . . . .	96
3.7	The Imaging System . . . . .	101
3.8	Experimental procedure to a BEC . . . . .	105
<b>4</b>	<b>Intense Slow Beams of Bosonic Potassium Isotopes</b>	<b>109</b>
4.1	Characterization of $^{39}\text{K}$ and $^{41}\text{K}$ Bright Sources . . . . .	109
4.1.1	Detection technique . . . . .	110
4.1.2	Trapping beam parameters . . . . .	112
4.1.3	Vapor pressure . . . . .	113
4.1.4	Push beam . . . . .	116
4.1.5	Summary . . . . .	119
4.2	A Simplified Multilevel Theoretical Model . . . . .	120
4.2.1	Numerical Simulations . . . . .	121

<b>5 Collisional Properties of Sympathetically cooled <math>^{39}\text{K}</math></b>	<b>125</b>
5.1 Sympathetic Cooling of $^{39}\text{K}$	126
5.1.1 Effects on the evaporation ramp	127
5.1.2 Experimental evidence for sympathetic cooling in the $^{87}\text{Rb}$ - $^{39}\text{K}$ mixture	129
5.2 Cross Thermalization in Ultracold $^{39}\text{K}$	137
5.2.1 Experimental procedure	139
5.2.2 Determination of the triplet scattering length of $^{39}\text{K}$	143
<b>Conclusions and Perspectives</b>	<b>149</b>
<b>Ringraziamenti</b>	<b>153</b>
<b>List of Figures</b>	<b>158</b>
<b>List of Tables</b>	<b>159</b>
<b>Bibliography</b>	<b>161</b>



# Introduction

During the last ten years, an intense and exciting research work concerning the investigation on ultracold and quantum degenerate matter has been performed by several groups all over the world. The possibility to mold and control pure quantum systems has been actually offered on a silver tray by the experimental observation of Bose-Einstein condensation (BEC), claimed in 1995 and awarding three Nobel Prizes in 2001 [1, 2]. This achievement has represented one of the most remarkable breakthroughs in the field of atomic physics all over the last century, since the capability to handle BECs opened the door to the observation of fundamental quantum phenomena on a *macroscopic* scale.

The investigation on BEC systems brought to study a wealth of processes that represent the intersection between many different research fields [3], ranging from quantum optics to solid state physics. This unique property arises from the nature of a Bose-Einstein condensate, where atoms occupy the same ground state and, when interactions are sufficiently small, are described by a global single particle wave function, whose extension is larger than the particles spacing. This confers to these ultracold atomic systems an undulatory character, where a moving condensate can be treated as a traveling *coherent matter wave*. By exploiting the forces arising amongst light and atoms, these matter waves can be managed and studied through interferometric techniques, proper of *atom optics*. In particular, the introduction of *optical lattices* provided unique tools devoted to this purpose, such as mirrors and beam splitters [4], or diffraction gratings [5] for atomic matter waves. The capability to load cold atoms in a periodic light structures such as those represented by optical lattices, traced the main route connecting the *atomic* and *solid state physics* frameworks. Indeed, the motion of an electron propagating through a material crystal

---

can be interpreted in terms of the motion of a single particle into a periodic array of microscopic potentials, following the ordinary solid state physics rules relying on the periodicity of the system. On the other hand, an ultracold degenerate sample moving into a periodic structure made of light shows an analogous behavior, with the relevant difference that an optical lattice can be reasonably considered as *perfect* even on a microscopic scale, since typical defects embedded in a material crystal (such as vacancies, dislocations or phonons) are absent. Moreover, the investigation scenario is enormously enriched by the presence of a well quantifiable interaction between atoms, giving rise to intriguing effects proper of the atom optics realm such as focusing and defocusing of the matter wave [6, 7], to novel quantum phase transitions such as the superfluid-Mott insulator one [8] or paving the way towards the experimental investigation of the Bose-glass regime [9] once a controlled disorder is added to the system. The first implementations of single and multi-dimensional periodic optical potential showed the capability to diffract the atomic matter wave [10, 11] mimicking the Bragg diffraction of electrons by a the material crystal. Further experiments employed these periodic light structures to confine and trap the cold sample and analyze the resulting quantized motion [12, 13]. Periodical light structures have been exploited to achieve remarkable sub-Doppler and Raman cooling of the sample [14, 15], while an ultracold sample has been shown to undergo Bloch oscillations in an accelerated frame [16] due to its reduced momentum spread compared to the lattice momentum  $\hbar k_{\text{lat}}$ , opening the door to ultra-high precision measurements of inertial forces, recently proposed for a degenerate fermionic sample [17] considered the reduced decoherence of this system. The ability to degenerate bosonic samples below the BEC temperature transition gave a unique tool to observe and investigate effects that were strictly related to the population of the lattice ground state, such as tunneling and Josephson dynamics [18, 19], Bloch oscillations [20] and dispersion inhomogeneity of the matter wave [6, 7]. Recent works reported insightful investigations of various dissipative mechanisms, such as Landau damping or dynamical instability, representing the main limit on the coherence of the system [21, 22, 23, 24, 25].

Even if ultracold single specie systems already show an extremely rich set of phenomena to be investigated, the research scenario has been further broadened by the recent development of sympathetic cooling techniques [26], allowing for the multiple cooling of different atomic species. This gave the possibility to enter the appealing world of *ultracold atomic mixtures*. Exciting research guidelines have been covered in this direction, and experiments and theoretical studies on degenerate mixtures of

---

cold gases have been acquiring a growing interest. The vast majority of works have featured Fermi-Bose mixtures, that have now been realized with several combinations of atoms:  ${}^6\text{Li}$ - ${}^7\text{Li}$  [27],  ${}^6\text{Li}$ - ${}^{23}\text{Na}$  [28],  ${}^{40}\text{K}$ - ${}^{87}\text{Rb}$  [29],  ${}^6\text{Li}$ - ${}^{87}\text{Rb}$  [30]. Many experiments focused on the degenerate Fermi gas, while the bosonic component has only been a tool to reach Fermi degeneracy via sympathetic cooling. Remarkable achievements include BCS-BEC crossover [31, 32, 33, 34, 35, 36], fermionic Bloch oscillations [37], observation of the 3D Fermi surface [38]. Besides, Fermi-Bose systems display a wealth of interesting phenomena genuinely related to the presence of two species. A few, like interspecies Fano-Feshbach resonances [39, 40, 41] and boson-induced collapse of the Fermi gas [42, 43], have already been observed but many more have been proposed and still await experimental confirmation, as e.g. boson-induced superfluidity [44] and mixed phases in optical lattices [45].

On the other hand, *Bose-Bose* mixtures have remained relatively unexplored: after the pioneering work on  ${}^{41}\text{K}$ - ${}^{87}\text{Rb}$  [46], only one other double-specie condensate has been recently produced, namely  ${}^{174}\text{Yb}$ - ${}^{176}\text{Yb}$  [47]. As for the K-Rb mixture, the recent precise determination of the interspecies scattering length by Feshbach spectroscopy [48] promises a rich phase-diagram for the two species loaded in an optical lattice, as recent theoretical works seem to proof [49, 50, 51, 52, 53]. Optical lattices have also been recently employed in combination with the intriguing capability to magnetically tune interspecies interactions to produce long-lived homonuclear molecules from a Bose gas [54, 55] or from a Fermi gas [56, 57], to produce heteronuclear cold molecules from [58], and to obtain a homonuclear molecular Mott-insulator state [59]. Contrarily to multi-component atomic mixtures, obtained from a single atomic specie in which a mix of internal states has been prepared, Bose-Bose mixtures compound by species of different mass such as  ${}^{87}\text{Rb}$ - ${}^{39}\text{K}$  or  ${}^{87}\text{Rb}$ - ${}^{41}\text{K}$  are, show the insightful perspective to realize a material grating fully immersed into a superfluid with tunable interactions, exploiting the capability to selectively obtain a Mott-insulator state onsetting for different values of the lattice depth for the two species. This intriguing system would not have any preceding analogous.

The broadness of evolution possibilities within this research panorama encouraged the realization of a new kind of experimental set-up to employ in the investigation of Bose-Bose ultracold mixtures, whose main features were at the same time a consistent versatility and robust stability. The decision to employ a Rb-K mixtures relies on two main facts: the first is that  ${}^{87}\text{Rb}$  is the most widespread atom in the laboratories devoted to laser cooling, and has good collisional properties with all the three potassium isotopes, necessary to an efficient sympathetic cooling process. The

---

second relies on the property of potassium to be the only alkali atom which has both fermionic ( $^{40}\text{K}$ ) and bosonic stable isotopes ( $^{39}\text{K}$  and  $^{41}\text{K}$ ), one of which is provided by attractive interaction ( $^{39}\text{K}$ ). Moreover, bosonic potassium isotopes are predicted to feature wide Feshbach resonances at moderate fields ( $< 1$  kG). As a consequence, optically trapped bosonic potassium appears a suitable candidate to realize a condensate with a scattering length tunable around zero. Such a condensate would be interesting for interferometric purposes, as the interaction energy limits the accuracy of interferometers employing Bose-Einstein condensates. In addition, wide Feshbach resonances make potassium condensates particularly appealing to realize double condensates in optical lattices, for quantum simulation purposes.

The experimental apparatus that has taken life during the three years of my Ph.D. has been devised to allow for a fast switch between the two bosonic isotopes  $^{39}\text{K}$  and  $^{41}\text{K}$  (and at the occurrence the fermionic isotope  $^{40}\text{K}$ ), to provide the opportunity to tune interactions amongst atoms by an external magnetic field (and hence to perform an accurate Feshbach spectroscopy on the Rb-K mixture), and to have a sufficient optical access to let a 3D optical lattice to be shone on the ultracold sample, generated exploiting the sympathetic cooling process between rubidium and potassium. The magnetic trapping of the mixture takes place in a novel kind of tightly confining magnetic trap, the *milli-trap*. The particular feature of this device is to provide a very strong confinement of the atomic sample without requiring a high power dissipation, that represent a net improvement respect to ordinary ex-vacuo magnetic trapping devices. Such features represent the most favorable starting point for an insightful and prolific research activity on ultracold Bose-Bose atomic mixtures, that can be eventually tailored on a wide range of investigation guidelines.

This thesis is structured as follows: Chapter 1 is focused on the fundamentals of theory concerning the BEC phenomenon and on the basic concepts concerning Bose-Bose mixture. A discussion on the topological state in the case of a K-Rb mixture is reported. Chapter 2 is devoted to the a theoretical overview on ultracold atoms in optical lattices, starting from the Bloch picture in the non-interacting regime and discussing the role of interactions, leading to the insurgence of the superfluid-Mott insulator transition, described in the Bose-Hubbard approach. Chapter 3 contains a detailed description of the new apparatus built during the thesis work, with particular attention to the characterization of the new magnetic trapping device, the *milli-trap*, that allows for a fast evaporation cycle leading to the Bose-Einstein condensation of the  $^{87}\text{Rb}$  sample. In Chapter 4 technical details on a new typology of 2D

---

cold atomic sources of  $^{39}\text{K}$  and  $^{41}\text{K}$ , developed and tested during the thesis work, are given together with an accurate characterization. Chapter 5 collects the results of an experimental investigation performed on both the  $^{87}\text{Rb}$ - $^{39}\text{K}$  mixture and on the collisional properties of  $^{39}\text{K}$  alone. In particular, in this Chapter an unprecedented experimental demonstration of the efficiency of sympathetic cooling in the  $^{87}\text{Rb}$ - $^{39}\text{K}$  mixture is reported. This method allowed to attain temperatures of the mixture as low as  $1\ \mu\text{K}$ , and to obtain a direct determination of the triplet s-wave scattering length  $a_T$  for ultracold  $^{39}\text{K}$  by means of a method that is completely different respect to the one that has been previously employed to determine  $a_T$  [60]. Finally, in the Conclusions and Perspective section, an overview on the research activity performed during the last three years by our experimental group is given.

---

# Chapter 1

## Some Elements of Theory

In this first Chapter I will point out the basic fundamentals of theory on ultracold gases. The dissertation will firstly focus on ultracold bosonic gases, whose quantum-mechanical behavior culminates at very low temperatures into the phenomenon of Bose-Einstein Condensation (BEC). This particular state of matter gives unique opportunities to study and observe exciting quantum effects on a macroscopic scale. The main difference between a BEC and other quantum systems such as standard superfluids or superconductors is the easier handling and ductility of the atomic system, allowing a full control of the intrinsic system properties as well as the atomic interactions, that can be controlled through an external magnetic field.

The second part of the Chapter will focus on double species bosonic mixtures, whose interaction can reveal intriguing properties strongly related to the presence of different co-existing atomic ensembles.

### 1.1 The Bose-Einstein Condensation

The Bose-Einstein condensation (BEC) is a phase transition relying on the indistinguishability of particles composing the atomic ensemble, and has to be treated using a pure quantum mechanical approach. The first prediction of this phenomenon was claimed for photons by Sathyendranath Bose in 1924 [61] and generalized to bosons by Albert Einstein between 1924 and 1925 [62] starting from studies on the black body radiation. The behavior of a classical Bose gas is completely determined by the Maxwell-Boltzmann distribution since for ordinary gases, independently on their fermionic or bosonic nature, the thermal energy  $k_B T$  is much higher than the in-

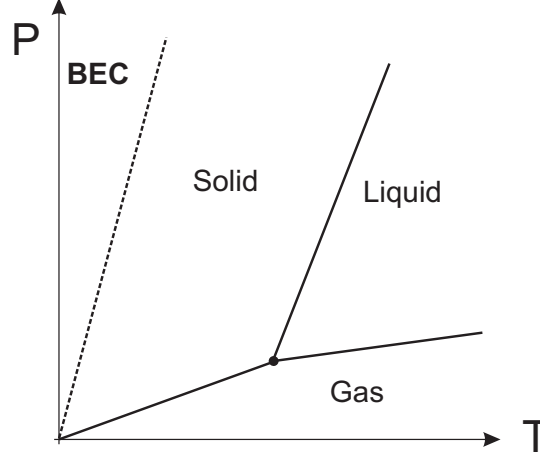


Figure 1.1: Schematic Pressure-Temperature phase diagram for a bosonic element. Dashed line marks the BEC transition for an ideal Bose gas.

intrinsic level spacing of the system. A continuum of states is statistically occupied and no quantum exchange phenomena have to be taken in account. Where the Maxwell-Boltzmann theory fails is near the relevant temperature  $T_{dB}$  below which the extension of the single atomic wavefunction become of the same order of magnitude than the interatomic separation. From a quantum mechanical point of view, the mean wavepacket extension at a certain temperature  $T$  is represented by the DeBroglie wavelength:

$$\lambda_{dB} = \frac{h}{\sqrt{2\pi k_B m T}}, \quad (1.1)$$

where  $m$  is the atomic mass, while the mean free path is inversely proportional to the density  $n$  of the sample. These considerations show as a first approximation that significant deviations the Maxwell-Boltzmann behavior should occur for  $\lambda_{dB} \simeq n^{-1/3}$ . In this situation, a coherence amongst the atomic wavepacket grows, and a macroscopic occupation of the ground state of the system appears. A more detailed grand-canonical analysis predicts the BEC phase transition for

$$\lambda_{dB}^3 = \frac{2.612}{n}, \quad (1.2)$$

where the quantity  $\lambda_{dB}^3 n$  has to be interpreted as the phase-space density (PSD) of the sample. As we will see in the following Sections, while a free ideal Bose gas undergoes only a momentum phase transition, a trapped Bose gas shows the transition

both in momentum and position spaces. Ordinary gases in the standard conditions have a PSD that is  $12 \div 14$  orders of magnitude smaller than the critical density. The PSD can be increased either increasing the density of the sample or decreasing the temperature. Anyway, as can be seen observing the schematic phase diagram sketched in Fig. 1.1, the way to BEC is narrowed by the presence of interatomic interactions, that in ordinary thermodynamic transformations lead to a stable solid phase. The choice of ultra-dilute weakly interacting gases helps to go around this obstacle, unavoidably preventing the observation of a full BEC in other standard superfluid systems such as  $^4\text{He}$ , where only a 10% fraction undergoes this phase transition.

## 1.2 The ideal trapped Bose gas

### 1.2.1 $T=0$

The vast majority of experiments on BECs exploits harmonic trapping potentials where the last part of the cooling process takes part. The description of the static degenerate system can be obtained in the  $T = 0$  limit considering a non-interacting atomic ensemble. The trapping potential is

$$V_{trap} = \frac{m}{2}(\omega_x^2 x^2 + \omega_y^2 y^2 + \omega_z^2 z^2). \quad (1.3)$$

If no interaction between the  $N$  particles composing the system occurs, the total Hamiltonian can be written as a sum of the  $N$  single-particle Hamiltonians. The eigenvalues of these single-particle Hamiltonians are

$$\varepsilon_{n_x n_y n_z} = (n_x + 1/2)\hbar\omega_x + (n_y + 1/2)\hbar\omega_y + (n_z + 1/2)\hbar\omega_z, \quad (1.4)$$

where  $n_i$ , are the quantum numbers associated to the specific direction, and  $\omega_i$  are the trapping frequencies. For  $T = 0$  the entire set of atoms occupies the ground state, and the system wavefunction is the product of the  $N$  eigenfunctions obtained setting  $n_x=n_y=n_z=0$ :

$$\Psi_0 = \prod_{i=1}^N \psi_0(\mathbf{r}_i), \quad (1.5)$$

with

$$\psi_0(\mathbf{r}) = \left(\frac{m\omega_{ho}}{\pi\hbar}\right)^{3/4} \exp\left(-\frac{m}{2\hbar}(\omega_x x^2 + \omega_y y^2 + \omega_z z^2)\right), \quad (1.6)$$

where  $\omega_{ho} = (\omega_x \omega_y \omega_z)^{1/3}$  gives the geometric mean oscillation frequency in the trap.

From Eq. (1.6) we can argue that, being  $n(\mathbf{r}) = N|\psi_0(\mathbf{r})|^2$  the particle density, the atomic distribution has a mean width equal to:

$$\sigma = a_{ho} = \left( \frac{\hbar}{m\omega_{ho}} \right)^{1/2}, \quad (1.7)$$

corresponding to the usual three-dimensional oscillator length. This is the first relevant length scale of our system, and in actual experiments is of the order of 1  $\mu\text{m}$ . The spatial extension of condensed particles remains finite even in the case  $T = 0$ , while the classical Maxwell-Boltzmann distribution width  $\sigma_T = a_{ho}(k_B T / \hbar\omega_{ho})^{1/2}$  tends to zero.

In our experimental apparatus, the milli-trap potential (Sec. 3.4) has a cylindrical symmetry along the  $z$  axis. The single-particle wavefunction takes the form:

$$\psi_0(\mathbf{r}) \propto \exp\left(-\frac{1}{2}\left(\frac{z^2}{\sigma_z^2} + \frac{\rho^2}{\sigma_\perp^2}\right)\right), \quad (1.8)$$

where  $\rho = \sqrt{x^2 + y^2}$  is the distance from the  $z$  axis and  $\sigma_i = (\hbar/m\omega_i)^{1/2}$  are the oscillator lengths along radial and longitudinal directions. The *aspect ratio* of the system is given by  $\xi = \sqrt{\omega_z/\omega_\perp}$ .

## 1.2.2 $T > 0$

An useful approach to describe the  $T > 0$  case is the grand-canonical theory. In this context, the total number of undistinguishable particles is given by

$$N = \sum_{n_x, n_y, n_z} \left\{ \frac{1}{\exp\left[\frac{1}{k_B T}(\varepsilon_{n_x n_y n_z} - \mu)\right] - 1} \right\}, \quad (1.9)$$

while the energy is

$$E(T) = \sum_{n_x, n_y, n_z} \varepsilon_{n_x n_y n_z} \left\{ \frac{1}{\exp\left[\frac{1}{k_B T}(\varepsilon_{n_x n_y n_z} - \mu)\right] - 1} \right\}, \quad (1.10)$$

where  $\mu = \partial E / \partial N$  represents the chemical potential and  $\varepsilon_{n_x n_y n_z}$  is the energy of the state labeled by the quantum numbers  $n_x, n_y$  e  $n_z$ .

The first equation shows that at low temperature the lowest energy level is the only to be relevantly populated. If the total number is fixed, this population become macroscopic, and the BEC phase transition onsets.

To determine the critical temperature  $T_C$ , it is convenient to separate the lowest level from the total sum:

$$N - N_0 = \sum_{n_x, n_y, n_z \neq 0} \left\{ \frac{1}{\exp\left[\frac{1}{k_B T}(\varepsilon_{n_x n_y n_z} - \mu)\right] - 1} \right\}. \quad (1.11)$$

## 1.2. The ideal trapped Bose gas

---

This quantity become small when  $\mu \rightarrow \mu_c = \frac{\hbar}{2}(\omega_x + \omega_y + \omega_z) = \frac{3\hbar}{2}\bar{\omega}$ . For a certain number of particles  $N$  the energy levels spacing  $\hbar\omega_{ho}$  becomes smaller than the typical excitation energy of the system  $k_B T$ , and Eq. (1.11) can be written as:

$$N - N_0 = \iiint \frac{dn}{\exp\left[\frac{\hbar}{k_B T}\boldsymbol{\omega} \cdot \mathbf{n}\right] - 1}, \quad (1.12)$$

where  $\boldsymbol{\omega}$  and  $\mathbf{n}$  collects the trapping frequencies and the quantum numbers along each direction. The integral can be analytically solved using the *Riemann Zeta function*  $\zeta(n)$ <sup>1</sup>:

$$N - N_0 = \zeta(3) \left(\frac{k_B T}{\hbar\omega_{ho}}\right)^{1/3}. \quad (1.13)$$

Imposing a null population of the ground state for  $T = T_C$  we obtain the BEC critical temperature:

$$T_c = \left(\frac{N}{\zeta(3)}\right)^{1/3} \frac{\hbar\omega_{ho}}{k_B} = 0.94 \frac{\hbar\omega_{ho}}{k_B} N^{1/3}. \quad (1.14)$$

Below this temperature the ground state is macroscopically populated and the condensate fraction grows. Inserting Eq. (1.14) into Eq. (1.13) we have:

$$\frac{N_0}{N} = 1 - \left(\frac{T}{T_c}\right)^3, \quad (1.15)$$

expressing the condensed atom fraction as a function of the temperature for  $T < T_C$ .

The two relevant energy scales of such a system are, as pointed out before, the thermal excitation energy and the mean levels separation. For our experimental apparatus, the typical trap frequencies for <sup>87</sup>Rb (Sec. 3.4) are  $\omega_z = 2\pi \cdot 19.6$  Hz,  $\omega_x = \omega_y = 2\pi \cdot 467$  Hz. Hence  $\omega_{ho} \simeq 2\pi \cdot 198$  Hz, corresponding to a mean levels spacing of 8 nK. From (1.14), setting  $N = 2 \times 10^5$ , we obtain  $T_c \simeq 530$  nK; since  $k_B T_c \gg \hbar\omega_{ho}$ , the semiclassical hypothesis exploited in Eq. (1.12) is fully confirmed.

It should nevertheless noticed that the critical temperature  $T_C$  is properly defined only in the thermodynamic limit, where  $N \rightarrow \infty$ ,  $N\omega_{ho}^3$  constant. It can be shown [63], that finite size effects have the main consequence to reduce the condensed atomic fraction at a certain temperature, or on the other hand to lower the ideal critical temperature by a factor proportional to  $N^{-1/3}$ .

---

<sup>1</sup>This function defined as  $\zeta(n) = \sum_{k=1}^{\infty} k^{-n}$

### 1.3 The Interacting Bose Gas at $T=0$ : the Gross-Pitaevskii equation

The presence of interactions between atoms confers a wealth of intriguing features to the ultracold atomic system, even in the case of one specie alone is studied. Effects such the creation of non-spreading traveling matter waves, labeled as *bright solitons*, have been predicted [64, 65, 66, 67, 68] in case of attractive interactions, and observed in recent experiments [69, 70]; the four-wave mixing, analogous to the standard non-linear optics observed in the laser light propagating in strongly non-linear materials, has been observed for sodium condensates with different momentum components [71] after it was predicted in presence of non-linear interaction between the particles [72, 73] (see below, Eq. (1.20)); again, self-focusing mechanisms have been theorized [74] and investigated in presence of an external periodic potential [6].

Let's consider the case of  $N$  interacting atoms, confined in an external potential of the form 1.3. Using the second quantization formalism the global Hamiltonian can be written as:

$$\begin{aligned} \tilde{H} = & \int d\mathbf{r} \tilde{\Psi}^\dagger(\mathbf{r}) \left[ -\frac{\hbar^2}{2m} \nabla^2 + V_{trap} \right] \tilde{\Psi}(\mathbf{r}) + \\ & + \frac{1}{2} \int d\mathbf{r} d\mathbf{r}' \tilde{\Psi}^\dagger(\mathbf{r}) \tilde{\Psi}^\dagger(\mathbf{r}') \left[ V_{int}(\mathbf{r} - \mathbf{r}') \right] \tilde{\Psi}(\mathbf{r}) \tilde{\Psi}(\mathbf{r}'). \end{aligned} \quad (1.16)$$

In this expression the last term represents the atom-atom interaction, and the form of interaction, as we will see in the following, determines the main behavior of the system.  $\tilde{\Psi}^\dagger(\mathbf{r})$  and  $\tilde{\Psi}(\mathbf{r})$  are bosonic field operators, creating or removing a particle in a certain position  $\mathbf{r}$ . Their expression can be reconstructed from ordinary creation and destruction operators as a function of the single-particle states  $\psi_j(\mathbf{r})$ :  $\tilde{\Psi}(\mathbf{r}) = \sum_j \alpha_j \psi_j(\mathbf{r})$ . The Bogoljubov theory exploits the macroscopic occupation of one of these states when BEC onsets. In the thermodynamic limit, hence,  $N_0/N$  has a finite value for every  $T < T_C$ . Since  $|N_0, \dots\rangle$  practically corresponds to  $|N_0 \pm 1, \dots\rangle$ , the  $\alpha$  operators can be treated as ordinary complex numbers where  $\alpha_0 = \alpha_0^* = \sqrt{N_0}$ . In the free case, the condensation process brings hence to the occupation of the single-particle state  $\tilde{\Psi}(\mathbf{r}) = \sqrt{N_0/V}$ , where  $V$  is the volume occupied by the gas. It should be noticed that this state is fully determined by a simple multiplication operator independent from  $\mathbf{r}$  or  $N$ . The Bogoljubov theory [75] takes life from this assumption to generalize it to the inhomogeneous time-dependent case,

and decomposes the field operator in the Heisenberg representation as:

$$\tilde{\Psi}(\mathbf{r}, t) = \Upsilon_0(\mathbf{r}, t) + \tilde{\Psi}'(\mathbf{r}, t), \quad (1.17)$$

where  $\Upsilon_0$  is the expectation value of the  $\tilde{\Psi}(\mathbf{r})$  operator and defines the condensate density, while the second term is a perturbation term.  $\Upsilon_0(\mathbf{r}, t)$  is a classical field, named as *order parameter*, and represents the condensate wavefunction. Assuming small perturbations on the system, corresponding to the position  $|\tilde{\Psi}'| \ll |\Upsilon_0|$ , the temporal evolution of the order parameter can be derived. The theory starts from the time dependent Schrödinger equation in the Heisenberg formalism for the Hamiltonian 1.16:

$$i\hbar \frac{\partial}{\partial t} \tilde{\Psi}(\mathbf{r}, t) = [\tilde{\Psi}(\mathbf{r}, t), \tilde{H}]. \quad (1.18)$$

Taking then the "point-like" interaction potential

$$V_{int}(\mathbf{r} - \mathbf{r}') = g \delta(\mathbf{r} - \mathbf{r}'), \quad (1.19)$$

where  $g$  is the interaction constant, and substituting  $\tilde{\Psi}$  by  $\Upsilon_0$  in Eq. (1.18) one obtains the noticeable Gross-Pitaevskii equation (GPE)(1961):

$$i\hbar \frac{\partial}{\partial t} \Upsilon_0(\mathbf{r}, t) = \left[ -\frac{\hbar^2 \nabla^2}{2m} + V_{trap}(\mathbf{r}) + g|\Upsilon_0(\mathbf{r}, t)|^2 \right] \Upsilon_0(\mathbf{r}, t). \quad (1.20)$$

The substitution of the field operator with the order parameter corresponds to the implicit assumption that the interaction range of the potential (1.19) is much smaller than the mean interatomic distance. Taking

$$g = \frac{4\pi\hbar^2 a}{m}, \quad (1.21)$$

with  $a$  scattering length for the atomic system, this corresponds to the condition  $\langle N/V \rangle a^3 \ll 1$ . In the  $^{87}\text{Rb}$  case,  $a \simeq 6$  nm. The dilution condition sets hence  $N/V \ll 5 \cdot 10^{18} \text{ cm}^{-3}$ , widely fulfilled in all the present experiments on BEC. The ground state of the system can be evaluated choosing a particular expression for the order parameter, normalized to the total number  $N$ :

$$\Upsilon_0(\mathbf{r}, t) = \phi(\mathbf{r}) e^{-i\mu t/\hbar}, \quad (1.22)$$

where  $\mu$  is the chemical potential, and  $\phi(\mathbf{r})$  is assumed as real. The GPE reduces then to:

$$\left( -\frac{\hbar^2 \nabla^2}{2m} + V_{trap}(\mathbf{r}) + g|\phi(\mathbf{r})|^2 \right) \phi(\mathbf{r}) = \mu \phi(\mathbf{r}). \quad (1.23)$$

As seen in this Section, the presence of interactions conspicuously alters the shape and the properties of the ground state. The Bogoljubov theory, anyway, leads in the perturbative regime to a relatively simple expression of the Schrödinger equation, i.e. the Gross-Pitaevskii equation, that can be employed at low temperatures to calculate variations of the order parameter over distances that should be larger than the inter-atomic distance. Its simple form is proved to be of crucial importance to obtain reliable numerical results on time-dependent problems concerning the BEC state. Moreover, in the repulsive case ( $a > 0$ , see next Section), if  $N$  is sufficiently large, a particular assumption can be done (the Thomas-Fermi approximation), and the GPE can be analytically solved. The procedure, on the contrary, is much more complicated in the case of attractive condensates ( $a < 0$ ), where only numerical and variational analysis can be developed.

### 1.3.1 The ground state for $a > 0$ : *repulsive is easy!*

In the previous section we pointed out that the dilution condition  $\langle N/V \rangle a^3 \ll 1$ , necessary to the derivation of the GPE, is commonly experimentally achieved. A further assumption, useful to derive a particular expression for the ground state of the system, can be taken in the so called *Thomas-Fermi* (TF) regime.

Comparing the interaction and the kinetic energies associated to  $N$  harmonic oscillators one obtains [63]:

$$\frac{E_{int}}{E_{cin}} \propto \frac{N|a|}{a_{ho}}. \quad (1.24)$$

In the case  $\frac{N|a|}{a_{ho}} \gg 1$ , the kinetic term  $-\frac{\hbar^2 \nabla^2}{2m}$  is much smaller than the external and interaction terms, and can be neglected. The GPE then becomes:

$$\left[ V_{trap}(\mathbf{r}) + g|\phi(\mathbf{r})|^2 \right] \phi(\mathbf{r}) = \mu \phi(\mathbf{r}), \quad (1.25)$$

allowing the non-trivial solution

$$|\phi(\mathbf{r})|^2 \doteq n(\mathbf{r}) = (\mu - V_{trap}(\mathbf{r}))g^{-1} \quad (1.26)$$

in the region defined by  $\mu > V_{trap}$ , while is  $|\phi(\mathbf{r})|^2 = 0$  otherwise. Formally, the density profile has the same shape of the confining potential (*Thomas-Fermi distribution*): for a harmonic trap, the density distribution is a inverted parabola whose maximum coincides with the potential minimum. The distribution has no tails extending to infinity, since  $n(\mathbf{r}) = 0$  for  $V_{trap}(\mathbf{r}) = \mu$ . The situation is really different from the non-interacting case (Eq. (1.6)), where the ground state is given by a

gaussian eigenfunction. From the normalization of Eq. (1.26) we can determine the chemical potential:

$$\mu = \frac{1}{2} \hbar \omega_{ho} \left( \frac{15Na}{a_{ho}} \right)^{2/5}. \quad (1.27)$$

Considering then the annihilation point of the density distribution defined by  $\mu = V_{trap}(\sigma_{TF})$ , with  $V_{trap}(\sigma_{TF}) = 1/2 m \omega_{ho}^2 \sigma_{TF}^2$  in the harmonic case, we can rewrite Eq. (1.27) to obtain the spatial extension of a condensate in the Thomas-Fermi regime for a spherical trap:

$$\sigma_{TF} = a_{ho} \left( \frac{15Na}{a_{ho}} \right)^{1/5}, \quad (1.28)$$

having trivial generalization to the anisotropic case. The dependency of the extension on the atom number  $N$  is a peculiar feature introduced by the presence of interactions in the TF regime.

### 1.3.2 Free expansion of a repulsive condensate

The small size and high densities proper of a BEC usually don't allow for a direct in-trap quantitative observation of the condensate. The sample can be observed after a certain release time from the trap, in such a way the sample is expanded and the density reduced. In this initial release phase, the residual energy of the sample, given by the presence of interactions, confers an initial spread velocity, proportional to the direction-specific trapping frequency. The result is that, for a repulsive condensate, the expansion is enhanced along the direction the sample was more confined, and less pronounced along the weak confinement axis. The quantitative dynamical analysis of the expansion can be performed introducing particular scaling parameters [76]. If  $\xi = \omega_z/\omega_\perp \ll 1$  is the aspect ratio of the system, given by the initial trapping frequencies  $\omega_\perp$  and  $\omega_z$ , the size of the condensate after a certain expansion time  $t$  along the  $\perp$  and  $z$  directions are:

$$R_\perp(t) \simeq R_\perp(0) \left[ \sqrt{1 + (\omega_\perp t)^2} \right] \quad (1.29)$$

$$R_x(t) \simeq R_x(0) \left[ 1 + \xi^2 \left( (\omega_\perp t) \arctan(\omega_\perp t) - \ln \sqrt{1 + (\omega_\perp t)^2} \right) \right]. \quad (1.30)$$

### 1.3.3 The ground state for $a < 0$ : the tricky attraction

The presence of attractive interaction, corresponding to a negative scattering length value, sources a completely different behavior of the atomic system. Early studies [77, 78, 79, 80] accomplished in the first years after the BEC was observed in

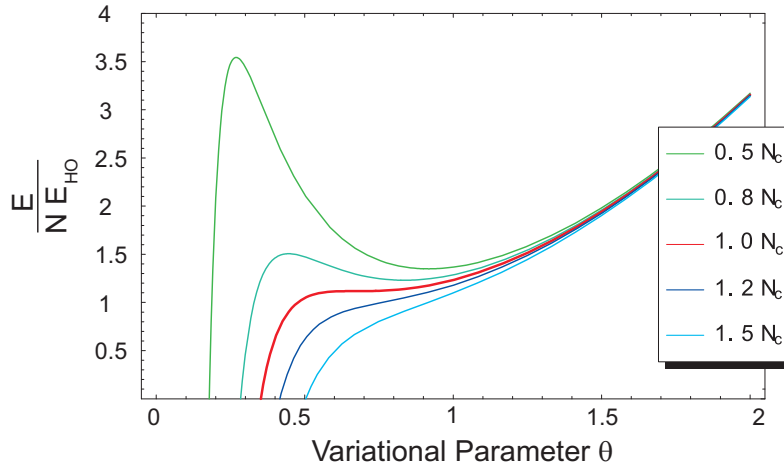


Figure 1.2: Numerical estimation of the unitary energy 1.32 for an attractive interaction between atoms. Different curves correspond to different total number of atoms. For  $N > N_C$  (red curve) no minimum exists and the condensate system is unstable.

repulsive samples, showed the presence of a critical atom number  $N_C$ , over which an unstable regime onsets. An attractive sample, indeed, tends to increase its inner density and to reduce its extension until the kinetic pressure term balances the interaction-driven contraction term. If the number of atoms is too high, the kinetic energy is always smaller than the interaction term, and a collapse of the system is predicted, induced by two main mechanisms individuated in multi-body recombination [81] and particle-ejection from the trap [78]. If the number of atoms is below the critical number, a metastable state is predicted and a condensate can be formed. The collapse dynamics have been investigated by several experimental [82, 83] and theoretical [84, 85] works.

The estimation of the critical number and the calculation of the ground state of the system as well can be done integrating the standard GP equation. The high central densities of an attractive sample, anyway, don't allow to exploit the TF approximation to obtain the ground state, since the kinetic term tends to grow as the compression of the sample increases. The integration of the GPE equation can hence be obtained through a variational analysis of the energy functional. The spherical trap case is investigated in Ref. [86] using a gaussian ansatz for the condensate wavefunction. To have an idea of the critical number of atoms in the case of  $^{39}\text{K}$  for our experimental conditions, we found convenient to introduce the mean harmonic os-

oscillator frequency  $\omega_{ho} = \sqrt[3]{\omega_{\perp}^2 \omega_z}$ , where  $\omega_{\perp}$  and  $\omega_z$  are the radial and axial trapping frequencies, in such a way to reduce the cylindrical symmetry of the trap to an effective spherical symmetry. The trial function we use is:

$$\phi(r) = \left( \frac{N}{\theta^3 a_{ho}^3 \pi^{3/2}} \right)^{1/2} \exp\left(-\frac{r^2}{2\theta^2 a_{ho}^2}\right), \quad (1.31)$$

where  $\theta$  is the variational parameter. The minimization of the energy functional leads to

$$\frac{E(\theta)}{N\hbar\omega_{ho}} = \frac{3}{4}(\theta^{-2} + \theta^2) - \frac{1}{(2\pi)^{1/2}} \frac{N|a_s|}{a_{ho}} \theta^{-3}, \quad (1.32)$$

giving the energy per particle in units of the oscillator energy. The annihilation of first derivative of above expression gives  $\theta \simeq 0.671$ , while through the annihilation of the second derivative we can fix the critical number of atoms  $N_C$ . For the typical frequency values reported in Sec 3.4, in the case of  $^{39}\text{K}$ , this method gives a critical number  $N_C \simeq 400$ . Fig. 1.2 shows numerical evaluations of Eq. (1.32), as a function of the variational parameter  $\theta$ . Each curve corresponds to a specific number of atoms. The red curve gives the limit case of  $N = N_C$ . As we can see, for  $N > N_C$  no minimum appears in the rescaled energy, and a stable condensate cannot exist.

The critical number of atoms obtained through this simple effective spherical model is in good agreement with the results given by a more detailed 3D-analysis reported in [87] despite of the strong anisotropy typical our magnetic trap (Sec. 3.4). Moreover, the model shows the capability to predict the right critical values corresponding to other experimental systems, such as  $^7\text{Li}$  or  $^{85}\text{Rb}$  reported in Ref.[82] and Ref.[83] respectively.

## 1.4 Bose-Bose mixtures

If the presence of interaction between atoms, as seen in Sec. 1.3, enriches the contents of the single specie research framework, in the case of a mixture, being either a Bose-Bose or a Fermi-Bose mixture, the interactions between atoms of different nature, and in particular the possibility to tune the interspecie scattering length  $a_{12}$ , opens a novel and relatively unexplored branch of investigation. In this paragraph we will consider two coexisting atomic species trapped in a harmonic potential such as the one described by Eq. (1.3) for a specific specie. We will focus on a Bose-Bose mixture, since a vast literature exist on the topic of Fermi-Bose mixtures, while a relatively small set of papers describes the properties of interacting Bose-Bose heteronuclear mixtures [88, 89, 90].

### 1.4.1 A model for the ground state

Adapting the theoretical model devised and discussed in Ref. [89], in this Section we will try to give some operating guidelines to deal with interacting binary Bose-Bose mixtures, focusing the numerical analysis on the case of a degenerate  $^{87}\text{Rb}$ - $^{41}\text{K}$ , already obtained at LENS in Florence via the sympathetic cooling technique [88] but still lacking a detailed phenomenological analysis. The strategy of the model [89] tries to reconstruct the ground state wavefunction of both species slicing each of the two atomic clouds in a non-overlapping portion (and hence without interspecies interaction) and an overlapping (and interacting) part. From a general point of view, the topological ground state of the mixture whose components are labeled by the index  $i$  is described by a coupled set of Gross-Pitaevskii equations for the condensates wavefunction  $\psi_i$  in which the mutual interaction term has been included:

$$\left[ -\frac{\hbar^2}{2m_1} \nabla^2 + U_1(\mathbf{x}) + u_{11}|\psi_1|^2 + u_{12}|\psi_2|^2 \right] \psi_1 = \mu_1 \psi_1 \quad (1.33)$$

$$\left[ -\frac{\hbar^2}{2m_2} \nabla^2 + U_2(\mathbf{x}) + u_{21}|\psi_1|^2 + u_{22}|\psi_2|^2 \right] \psi_2 = \mu_2 \psi_2, \quad (1.34)$$

with the normalization condition

$$\int d^3x |\psi_i|^2 = N_i. \quad (1.35)$$

The coupling constant matrix  $u_{ij}$  is given in terms of the scattering lengths  $a_{ij}$  [91] by

$$u_{ij} = \begin{pmatrix} u_{11} = \frac{4\pi\hbar^2}{m_1} a_{11} & u_{12} = \frac{2\pi\hbar^2(m_1+m_2)}{m_1m_2} a_{12} \\ u_{21} = \frac{2\pi\hbar^2(m_1+m_2)}{m_1m_2} a_{12} & u_{22} = \frac{4\pi\hbar^2}{m_2} a_{22} \end{pmatrix}$$

where we used the fact that  $a_{12} = a_{21}$ . Hereinafter we will label the rubidium by the index 1 and the potassium by the index 2. Since the intraspecies background triplet scattering lengths (the only ones playing a role in binary collision for stretched  $|F = 2, m_F = 2\rangle$  states, see Sec. 3.4) are  $99 a_0$  for  $^{87}\text{Rb}$  and  $60 a_0$  for  $^{41}\text{K}$  respectively [48], we will furthermore restrict the analysis to the case  $a_{11}, a_{22} > 0$ .

The total force acting on the atomic sample is the sum of the magnetic trapping force given by the potential 1.3 and of the gravitational force  $m_i g$ , that acts along the vertical  $z$  direction. The total potential can hence be put in the form:

$$U^{(i)}(\mathbf{x}) = \left[ \frac{1}{2} m_i \sum_{k=x,y,z} (\omega_k^{(i)} k)^2 + U_{0i} \right] + m_i g z \quad i = 1, 2, \quad (1.36)$$

with  $U_{0i} = \mu_B g_{Fi} m_{Fi} |B_0|$ , being  $g_{Fi}$  and  $B_0$  the specific Landé factor and the residual magnetic bias field in the center of the trap respectively (see Sec: 3.4). Note that the vertical equilibrium position is different for the two species, since the trap frequencies depend on mass as  $\sqrt{\frac{m_1}{m_2}}$ . This gives the so called *gravitational sag* between the two species. Through an appropriate unitary coordinate scaling  $x_k \rightarrow x'_k \equiv \lambda_k x_k$  the trap geometry can be reduced to spherical for *both* species, since the shape of both potentials is affected in the same way by the scaling. The parameter  $\lambda_k$  is determined by the ratio of the trap frequency along the  $k$  direction to the mean trap frequency  $\bar{\omega}^{(i)} = \left( \prod_{k=x,y,z} \omega_k^{(i)} \right)^{1/3}$ :

$$\lambda_k = \frac{\omega_k^{(i)}}{\bar{\omega}^{(i)}}. \quad (1.37)$$

The scaling factor, as anticipated some lines before, is independent on the atomic specie. Omitting the apices to simplify the notation, the simplified potential reads:

$$U_i(\mathbf{x}) = \frac{1}{2} m_i (\bar{\omega}^{(i)})^2 (r^2 + (z - z_{0i})^2) + U_{0i}, \quad (1.38)$$

where we have defined  $r^2 = x^2 + y^2$ , and

$$U_{0i} = \mu_B g_{Fi} m_{Fi} B_0 - \frac{1}{2} m_i \frac{g^2}{\lambda_z^2 (\bar{\omega}^{(i)})^2} \quad (1.39)$$

$$z_{0i} = -\frac{g}{\lambda_z (\bar{\omega}^{(i)})^2}. \quad (1.40)$$

Setting  $a_{ho}^{(i)} = \sqrt{\hbar/(m_i \omega^{(i)})}$  and  $dz = z_{02} - z_{01}$ , the system is then translated along the  $z$  axis by a quantity  $z_{01}$ . In this way the center of the reduced spherical profile corresponding to the specie 1 coincides with the center of the new reference frame. After this transformation, the rescaled potentials can be written as:

$$V_1(\mathbf{x}) \equiv U_1(\mathbf{x}) - U_{01} = \frac{1}{2} (r^2 + z^2) \quad (1.41)$$

$$V_2(\mathbf{x}) \equiv U_2(\mathbf{x}) - U_{02} = \frac{1}{2} \eta (r^2 + (z - dz)^2), \quad (1.42)$$

with

$$\eta = \frac{m_2 (\bar{\omega}^{(2)})^2}{m_1 (\bar{\omega}^{(1)})^2} = \frac{g_{F2} m_{F2}}{g_{F1} m_{F1}} \quad (1.43)$$

$$dz = \frac{g}{\lambda_z a_{ho}^{(1)}} \left( \frac{1}{(\bar{\omega}^{(2)})^2} - \frac{1}{(\bar{\omega}^{(1)})^2} \right) = \frac{g}{\lambda_z a_{ho}^{(1)} (\bar{\omega}^{(1)})^2} \left( \frac{m_2}{\eta m_1} - 1 \right). \quad (1.44)$$

Note that if both  $^{87}\text{Rb}$  and  $^{41}\text{K}$  (or equivalently  $^{39}\text{K}$ ) are prepared in the same hyperfine state we have  $\eta = 1$ , since the Landé factors are the same for both species.

If the number of atoms is not too small, we can rely on the Thomas-Fermi approximation (Sec. 1.3.1) and neglect the kinetic term appearing in the coupled GP equations, which become:

$$V_1(\mathbf{x}) + u_{11}|\psi_1|^2 + u_{12}|\psi_2|^2 = \mu_1 \quad (1.45)$$

$$V_2(\mathbf{x}) + u_{21}|\psi_1|^2 + u_{22}|\psi_2|^2 = \mu_2, \quad (1.46)$$

where the substitution  $\mu_i - U_{0i} \rightarrow \mu_i$  is done. The reduced coupling constant matrix  $u_{ij}$  is written as:

$$u_{ij} = \begin{pmatrix} u_{11} = 4\pi \frac{a_{11}}{a_{ho}^{(1)}} & u_{12} = 2\pi \frac{a_{12}}{a_{ho}^{(1)}} \left(1 + \frac{m_1}{m_2}\right) \\ u_{21} = 2\pi \frac{a_{21}}{a_{ho}^{(1)}} \left(1 + \frac{m_1}{m_2}\right) & u_{22} = 4\pi \frac{a_{22}}{a_{ho}^{(1)}} \frac{m_1}{m_2} \end{pmatrix}.$$

These coupled equations can be solved to obtain the ground state in the overlapping region, where the interaction is actually present between the different species. On the other hand, the solution in the non-overlapping region has to be found using the standard set of decoupled GP equation, obtained setting  $u_{12} = u_{21} = 0$ .

## 1.4.2 Overlapping region

By defining the quantities

$$\gamma_1 \equiv u_{21}/u_{11} \quad (1.47)$$

$$\gamma_2 \equiv u_{12}/u_{22} \quad (1.48)$$

$$\Delta = u_{11}u_{22} - u_{12}^2, \quad (1.49)$$

the solution of Eq. (1.45) and Eq. (1.46) is given by:

$$|\psi_1|^2 = \alpha_1 (R_1^2 - r^2 - (z - z_{c1})^2) \quad (1.50)$$

$$|\psi_2|^2 = \alpha_2 (R_2^2 - r^2 - (z - z_{c2})^2) \quad (1.51)$$

where we have defined the radii  $R_i$

$$R_1^2(\mu_1, \mu_2) = \frac{2(\mu_1 - \gamma_2\mu_2)}{1 - \eta\gamma_2} + \frac{\eta\gamma_2}{(1 - \eta\gamma_2)^2} dz^2 \quad (1.52)$$

$$R_2^2(\mu_1, \mu_2) = \frac{2(\mu_2 - \gamma_1\mu_1)}{\eta - \gamma_1} + \frac{\eta\gamma_1}{(\eta - \gamma_1)^2} dz^2 \quad (1.53)$$

the position of the centers along  $z$

$$z_{c1} = \frac{-\eta\gamma_2}{1 - \eta\gamma_2} dz \quad (1.54)$$

$$z_{c2} = \frac{\eta}{\eta - \gamma_1} dz \quad (1.55)$$

and the normalization factors  $\alpha_i$

$$\alpha_1 = u_{22} \frac{1 - \eta\gamma_2}{2\Delta} \quad (1.56)$$

$$\alpha_2 = u_{11} \frac{\eta - \gamma_1}{2\Delta}. \quad (1.57)$$

The qualitative behavior of the system in the overlap region can be constructed noticing that both right-handside members of Eq. (1.50) and Eq. (1.51) must be positive, since they have to equate a modulus squared. Each one of these members is given by the product of a factor  $\alpha_i$ , plotted in Fig. 1.3(a) as a function of  $a_{12}$ , times the value of an expression directly related to the equation of a sphere, namely  $R_i^2 = r^2 + (z - z_{ci})^2$ . If  $\alpha_i$  is negative, the interaction region occupied by the element  $i$  is given by  $R_i^2 > r^2 + (z - z_{ci})^2$ , and hence lies inside the spherical region  $\Sigma_i$  of radius  $R_i$ . In the case  $\alpha_i > 0$ , the interacting part of the cloud lies outside the surface  $\Sigma_i$ . The intersection of surfaces defined by the sign of  $\alpha_1$  and  $\alpha_2$  delimits the actual overlapping region between the two clouds. In this portion of space, the interaction between the two species is ruled by the off-diagonal elements of the coupling matrix.

### 1.4.3 Non-overlapping region

The wavefunctions, in this region, have the ordinary Thomas-Fermi profile, since no interaction between atoms of different species is present:

$$|\psi_{01}|^2 = \frac{1}{2u_{11}} (2\mu_1 - r^2 - z^2) \quad (1.58)$$

$$|\psi_{02}|^2 = \frac{\eta}{2u_{22}} \left( \frac{\mu_2}{\eta} - r^2 - (z - dz)^2 \right). \quad (1.59)$$

Differently from the overlapping case, these solutions are defined inside a region of space whose boundary is delimited by the surfaces  $\Sigma_{0i}$  of equation  $R_{0i}^2 = r^2 + (z - z_{ci}^0)^2$ , with  $R_{01}^2 = 2\mu_1$ ,  $R_{02}^2 = 2\mu_2/\eta$ ,  $z_{c1}^0 = 0$  and  $z_{c2}^0 = dz$ , with no dependence on the sign of external parameters. In this region, the shape of the wavefunctions is determined uniquely by the external potential. The presence of the interaction between atoms in the overlapping region influences the non-interacting portion of the cloud

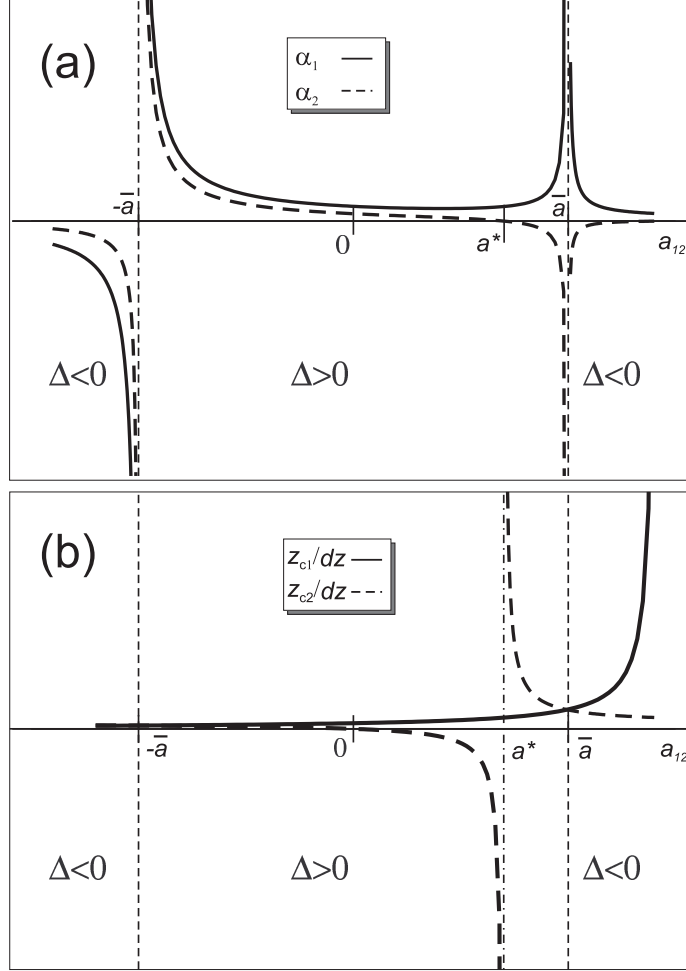


Figure 1.3: Normalization factors  $\alpha_i$  (Fig. (a)) and rescaled position  $z_{ci}/dz$  (Fig. (b)) plotted as a function of the interspecies scattering length  $a_{12}$  for the interacting surfaces  $\Sigma_i$ . Solid (dashed) lines correspond to  $^{87}\text{Rb}$  ( $^{41}\text{K}$ ).

only through a re-normalization in the atomic density, without changing the shape of the non-interacting wavefunction.

The continuity condition imposed on each of the  $\psi_i$  at the interface between the overlapping and non-overlapping regions requires  $\psi_1 = \psi_{01}$  on  $\Sigma_2$  (where  $|\psi_2|^2 = 0$ ), and vice-versa [89]. This is relevant to discern between self-consistent and not-self-consistent analytic solutions of Eqs. (1.52-1.53) once imposed the normalization

condition 1.35. We will discuss this statement in the last part of the Section. To qualitatively understand the behavior of the system, it is useful to notice that the sign of the factors  $\alpha_i$  depends on the interplay between the sign of  $\Delta$  (changing sign when  $u_{12} = \bar{u} \equiv \sqrt{u_{11}u_{22}}$ , independently on  $i$ , where  $\alpha_i$  has poles) and the sign of the numerators appearing in Eqs.(1.56)-(1.57). The latters change sign when  $u_{12}$  approaches the critical values  $u^* = \eta u_{11}, u_{22}/\eta$ , representing moreover a pole for the vertical position of the interacting profiles centers  $z_{ci}$ . The choice to attribute the index  $i = 1$  to  $^{87}\text{Rb}$  fulfills the condition  $\eta^2 \leq u_{11}/u_{22}$ , and selects the value  $u^* \equiv \eta u_{11}$  in the region where  $\Delta > 0$ . In terms of scattering lengths, the corresponding critical values are:

$$\bar{a} \equiv 2 \left( \frac{\sqrt{m_1 m_2}}{m_1 + m_2} \right) \sqrt{a_{11} a_{22}}, \quad (1.60)$$

$$a^* \equiv 2 \left( \frac{m_2}{m_1 + m_2} \right) a_{11}. \quad (1.61)$$

Note that, differently from the adimensional quantities  $\bar{u}, u^*$  the critical values for the scattering length do not depend on the trap frequencies. In the case the background intraspecies scattering lengths  $a_{11}$  and  $a_{22}$  are not influenced by the external tuning of the interspecies scattering length  $a_{12}$ , as usually happens in a Rb-K system when a Feshbach resonance is crossed to change the sign of  $a_{12}$ , the values of  $\bar{a}$  and  $a^*$  can be assumed as constant. For a  $^{87}\text{Rb}$ - $^{41}\text{K}$  mixture generated in the experimental conditions described in Sec. 3.4, the critical values are  $\bar{a} \simeq 72 a_0$  and  $a^* \simeq 63 a_0$ . Fig. 1.3 shows the plots for the normalization factors  $\alpha_i$  and of rescaled vertical positions of the interacting surfaces centers  $z_{ci}/dz$ . This figure summarizes the role of the critical values discussed before.

It can be show that an analytic overlap between the two condensates is admitted only in the case  $\Delta > 0$ , corresponding to the range  $a_{12} \in (-\bar{a}, \bar{a})$ . In the case the system approaches  $a_{12} = -\bar{a}^+$  a collapse of the system is predicted, while the strong repulsion between the two atomic species leads to a phase separation for  $a_{12} \rightarrow \bar{a}^-$ . Notice that if no external tuning of the mutual interaction  $a_{12}$  is imposed, the background interspecies scattering length of the mixture  $^{87}\text{Rb}$ - $^{41}\text{K}$  ( $164 a_0$ ) is bigger then the critical value  $\bar{a} = 72 a_0$ . In this case, right after both species cross the BEC phase transition temperature, a complete phase separation between rubidium and potassium is predicted by the model.

The spatial topology of the overlap between the two condensates can result in two main configurations, schematically sketched in left and right columns of Fig. 1.4.

- *External Overlap*: this case takes place when the two condensates are not

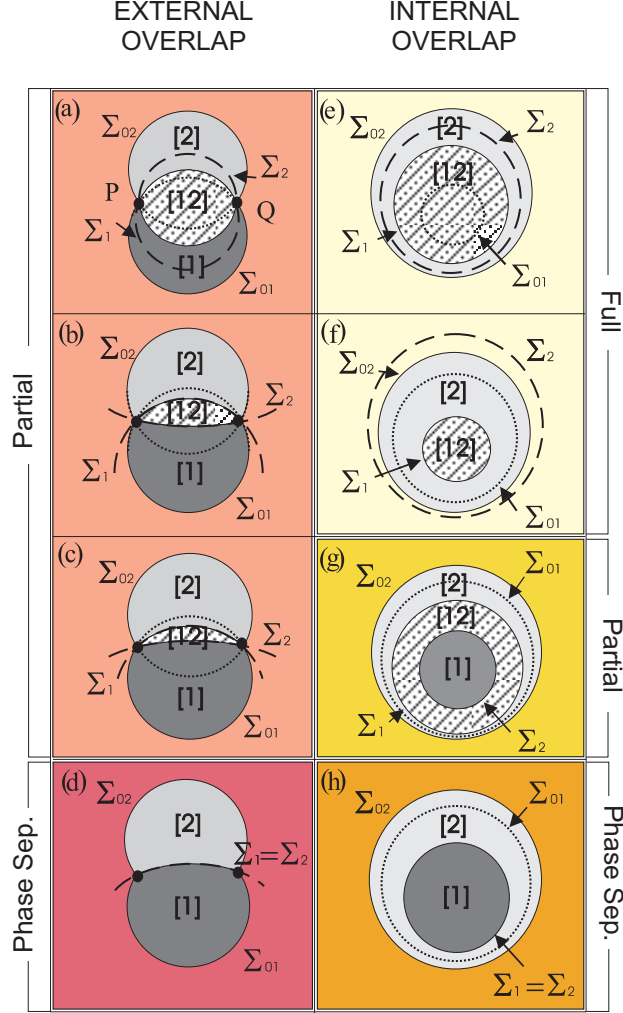


Figure 1.4: Possible topologies for a binary mixture of two BECs. The left column pictures the case of *external overlap*:  $a_{12} < 0$  (a),  $0 < a_{12} < a^*$  (b),  $a^* < a_{12} < \bar{a}$  (c), and phase separation  $a_{12} = \bar{u}$  (d). The right column schematizes the case of *internal overlap*: “full overlap” for  $a_{12} < 0$  (e) and  $0 < a_{12} < a^*$  (f); “partial overlap” for  $a^* < a_{12} < \bar{a}$  (g) and phase separation  $a_{12} = \bar{u}$  (h). Dark and light grey represent the regions occupied by the non-interacting condensates 1 and 2 respectively. The shaded area indicates the overlapping region. The boundary of these regions are delimited by the surfaces  $\Sigma_{0i}$  (non-interacting, continuous and dotted lines) and  $\Sigma_i$  (overlapping, dashed lines)[Adapted from [89]].

fully compenetrated into each other. This situation happens for  $|R_{01} - R_{02}| < |dz| < R_{01} + R_{02}$ , that is when the separation between the centers of the non-interacting profiles is grater than the difference between their radii (Figs. 1.4(a)-1.4(c)). The shape of the overlapping region, contained between the surfaces  $\Sigma_1$  and  $\Sigma_2$  (dashed lines in figure) is ruled by the interspecies scattering length  $a_{12}$ . The three possible sub-configurations are shown in figure:  $-\bar{a} < a_{12} < 0$  (a),  $0 < a_{12} < a^*$  (b),  $a^* < a_{12} < \bar{a}$  (c), and  $a_{12} = \bar{a}$  which is a case of phase separation (d). For  $a_{12} > \bar{a}$  the two condensates are no more interacting, and the profiles become independent on the interspecies scattering length.

- *Internal Overlap*: When one of the two condensates is fully surrounded by the other, namely for  $|dz| < |R_{01} - R_{02}|$ , the system can display two more sub-configurations, depending on the strength of mutual interactions: the first corresponds to a *full overlap*, occurring when one specie (let's say the specie 1) is fully immersed into the other and no regions containing only this specie appear. Fig. 1.4(e) and 1.4(f) show this case for  $a_{12} < 0$  and  $0 < a_{12} < a^*$  respectively. The second configuration (Fig. 1.4(g),  $a^* < a_{12} < \bar{a}$ ) represents a *partial overlap*, occurring when the overlap region is a shell separating two region of single specie condensates. The actual parameters set the inner and outer element [92]. Fig. 1.4 shows the limit case of phase separation.

The resolution procedure of the topological problem has to be performed in a self-consistent way, since in principle it is not possible to know *a priori* which of the configurations depicted in Fig. 1.4 will be the more adequate to describe the system. One has hence to write the normalization integrals for each of these configurations and solve Eq. (1.35) to obtain the chemical potentials  $\mu_i$ . This allows to construct the interacting surfaces  $\Sigma_i$  and hence the overlap region, given by the *intersection* of  $\Sigma_1$  and  $\Sigma_2$ . The noninteracting surfaces  $\Sigma_{0i}$  are obtained solving separately Eq. (1.58) and (1.59), without the intersection condition proper of the interacting surfaces. It should be noticed that the external global surface delimiting the binary system is represented by the *union* of the  $\Sigma_{01}$  surfaces, independently on the kind of overlap. Once reconstructed the four surfaces, the continuity condition on the wavefunction has to be written at the boundary of each region. Nevertheless, the number of initial trials can be reduced noticing that the value of the interspecies scattering length fixes the case along the vertical scale of Fig. 1.4. Given a certain value for the trapping frequencies, the number of atoms of both species discriminates between the external and internal overlap, i.e. between the left and right column of Fig. 1.4. An useful

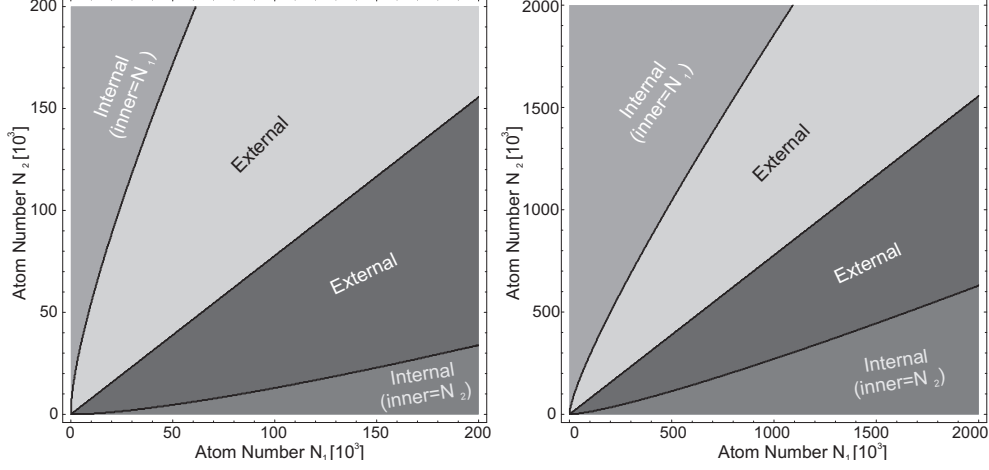


Figure 1.5: Different regions of validity for Eqs. (1.66) and (1.67) for two different atom number regimes in the case  $a_{12} = 0$ . In the inner dark (light) gray region both members of inequality 1.66 (1.67) are satisfied, and the system follows the external overlap configuration. The outer regions corresponds to the internal overlap situation, and only the first members of the above inequalities are satisfied. The relative abundance of the two species selects one of the two external regions.

hint about the best choice between external and internal normalization integrals can be obtained considering the equilibrium condition of the two non-interacting condensates, distributed on two independent Thomas-Fermi profiles. The extension of each distribution along the vertical direction equals the non-spherical Thomas-Fermi radius:

$$R_{\perp} = \sigma_{TF} \frac{\omega_{ho}}{\omega_{\perp}} = (15Na)^{1/5} a_{ho}^{4/5} \left( \frac{\omega_{ho}}{\omega_{\perp}} \right), \quad (1.62)$$

to be evaluated for both species. Notice that we employed the radial trap frequency  $\omega_{\perp}$  since we assumed the system to have a cylindrical symmetry along an axis that is orthogonal to the  $z$  direction. The vertical displacement between the two centers is induced by the gravitational potential is:

$$\Delta z = z_{01} - z_{02} = -\frac{g}{(\omega_{\perp}^{(1)})^2} \left( 1 - \frac{m_2}{m_1} \right), \quad (1.63)$$

and is equal to  $-0.53 \mu\text{m}$  for the  $^{87}\text{Rb} - ^{41}\text{K}$  mixture in our experimental conditions (see Sec. 3.4,  $\omega_{\perp}^{(1)} = 2\pi \times 497 \text{ Hz}$ ). The condition of external overlap  $|dz| > |R_{01} -$

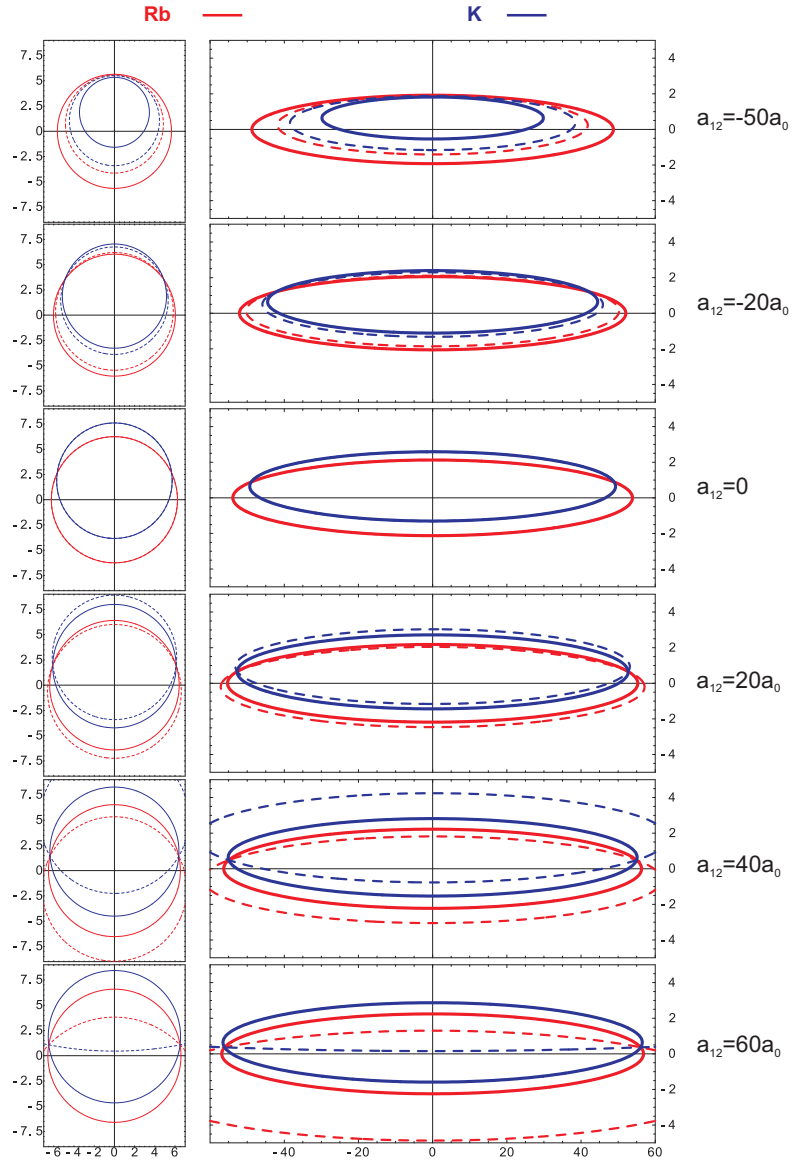


Figure 1.6: Overlap diagrams for the  $^{87}\text{Rb}$ - $^{41}\text{K}$  mixture for  $N_1 = 10^5$  and  $N_2 = 5 \times 10^4$ . The Thomas-Fermi profiles are calculated for 6 different interaction strength values, reported along the right side. The left insets (distances shown in arbitrary units) show the normalized profiles (compare to Fig. 1.4 for clarity), while the right insets show the actual ground state of the mixture. Distances are expressed in  $\mu\text{m}$ .

$R_{02}| = |R_{\perp 1} - R_{\perp 2}|$  corresponds to:

$$|\Delta z| > \sigma_{TF}^{(1)} \sqrt[3]{\frac{\omega_z}{\omega_{\perp}}} \left| N_1^{1/5} - \left( \frac{a_{22} m_1}{a_{11} m_2} \right)^{1/5} N_2^{1/5} \right|, \quad (1.64)$$

that in our case becomes:

$$3.013 > \left| N_1^{1/5} - 1.052 N_2^{1/5} \right|. \quad (1.65)$$

The two atomic clouds will hence have an external overlap (left column of Fig. 1.4) in the following different cases, depending on the relative abundance of the two species:

$$N_1 > 1.298 N_2 \quad \wedge \quad N_1^{1/5} < 1.052 N_2^{1/5} + 3.013; \quad (1.66)$$

$$N_1 \leq 1.298 N_2 \quad \wedge \quad N_1^{1/5} > 1.052 N_2^{1/5} - 3.103. \quad (1.67)$$

If the  $^{87}\text{Rb}$  sample is the most abundant, only the inequalities (1.66) are satisfied, while the inequalities (1.67) describe the case where the potassium sample is the most abundant. Consider for now only the former case, where the  $^{87}\text{Rb}$  sample is bigger than the  $^{41}\text{K}$  sample, if the second part of inequalities (1.66) is not satisfied, the potassium sample will fully penetrate into the rubidium cloud, and the system will enter the condition of "internal overlap", depicted in the right column of Fig. 1.4. The whole situation is summarized in Fig. 1.5, where the validity regions of different inequalities are represented with different colors. In the central diagonal region both members of inequality (1.66) (dark gray) or (1.67) (light gray) are satisfied, and the normalization integrals to be chosen are those corresponding to the external overlap. On the contrary where the unbalance between the atom number of the two species is more pronounced, i.e. in the outer regions of Fig. 1.5, the self-consistent normalization integrals are those corresponding to the internal overlap. In these regions, the less abundant element fills the inner core of the compound profile, while the other constitutes the outer shell (Fig. 1.4(e-g)). This choice of the specific normalization integrals set represents an *exact* method to obtain self-consistent solutions of the coupled GP equations (1.33) and (1.34) only in the  $a_{12} = 0$  case, since the phase diagram reported in Fig. 1.5 is obtained treating the initial Thomas-Fermi profiles as mutually non-interacting and only sensitive to the external gravitational potential, fixing their unperturbed vertical position. The gradual increase of the mutual interactions draws on the diagram represented in Fig. 1.5 a path that can bring the system in a different overlap region. This is evident in Fig. 1.6, where the ground state of the mixture is plotted for six different values of mutual interaction. The atom numbers

are  $N_1 = 10^5$ ,  $N_2 = 5 \times 10^4$ . As can be seen, the particular kind of overlap changes for  $-50 a_0 < a_{12} < -20 a_0$ , and the normalization integrals set has to be changed from "external" to "internal" when this range is crossed. The non-interacting choice method can nevertheless be reasonably employed in the case the interaction variation  $\Delta a_{12}$  is much smaller than the lowest critical value  $a^*$ , where a crossing of the overlap transition lines is very unlikely.

The relative number of atoms between the two species discriminates the evolution of the system when the interspecies scattering length is varied. For simplicity, consider an initially non-interacting mixture, and suppose to increase the value of  $a_{12}$ . If the initial atom number imbalance is weak, the system will evolve towards an external overlap configuration, even if the initial overlap configuration is internal. If, on the other hand, the population are strongly unbalanced, let's say  $N_1 \gg N_2$ , the system can follow an evolution in which the internal core is more and more compressed without being expelled, and the effect of repulsion can culminate in an internal phase separation between the two species, represented in Fig. 1.4(h). Anyway, a heuristic analysis performed varying both atom numbers and interspecies scattering length coupled GP equations, shows that the latter kind of overlap evolution is very unlikely and persists only in a very narrow range of experimental conditions, whose exact determination is beyond the scope of this thesis work.

A last thing to be noticed is the fact that the  $^{87}\text{Rb}$ - $^{41}\text{K}$  mixture is a strongly repulsive binary system. Since the background value of the interspecies scattering length  $a_{12} = 164 a_0$  definitely exceed the critical value  $\bar{a} = 72 a_0$ , in the Thomas-Fermi regime the two condensates are produced in a complete phase separation (insets (d) and (h) of Fig. 1.4) and the model is not adequate to describe the ground state of the system. If  $a_{12}$  is not tuned by an external potential, the two BECs can only interact via surface effects, while bulk interaction effects between the two species can be observed only for smaller values of the interaction strength.

*1. SOME ELEMENTS OF THEORY*

---

# Chapter 2

## Ultracold Atoms in Optical Lattices

This Chapter is devoted to the description of the basilar features characterizing the behavior of an ultracold atomic sample loaded in a periodic optical potential. Optical lattices represents the connection between the atomic and solid state physics realms, since the center-of-mass motion of a Bose-Einstein condensate inside a periodic arrangement of microscopic potential wells can be described, in the case of a shallow optical potential, by the standard solid state physics laws, governing the dynamics of a an electronic wavepacket inside a material crystal. Moreover, optical potentials have the unique property to be free from the vast majority of defects usually embedded in a material crystal, such as dislocations, vacancies and phonons. The ability to degenerate bosonic samples below the BEC temperature transition gave a unique tool to observe and investigate effects that were strictly related to the population of the lattice ground state, such as tunneling and Josephson dynamics [18, 19], Bloch oscillations [20] and dispersion inhomogeneity of the matter wave [6, 7]. Recent works reported insightful investigations of various dissipative mechanisms, such as Landau damping or dynamical instability, representing the main limit on the coherence of the system [21, 22, 23, 24, 25]. Optical lattices have also been recently employed in combination with the magnetic tuning of interactions to produce long-lived homonuclear molecules from a Bose gas [54, 55] or from a Fermi gas [56, 57], to produce heteronuclear cold molecules from [58], and to obtain a homonuclear molecular Mott-insulator state [59].

On the other hand, the realm of binary Bose-Bose mixtures loaded in an optical

lattice has remained relatively unexplored, since only theoretical works [49, 50, 51, 52, 53] have investigated these kind of systems. This typology of systems seems to be very promising as gives the possibility to explore the interplay between superfluids of different mass, and between a superfluid and a Mott-insulator state. The richness of the phase diagram is remarkably increased, since the critical point becomes dependent on the interspecie interactions, that are magnetically controllable.

In the first part of the Chapter the basic concepts related to the interaction between atoms and light are given in terms of dipole forces, and some fundamentals of the optical lattices theory are given. The motion of a condensate in a periodic structure is then analyzed through the concept of Bloch and Wannier states. A brief overview on the superfluid-Mott insulator transition is reported. Finally, some hints for further studies on Bose-Bose heteronuclear mixtures in optical lattices are given.

## 2.1 Optical Dipole Forces

The dynamics of an atom in an optical field is governed by a force that is proportional to the intrinsic complex polarizability of the atom. This force is the sum of two main terms:

- *Radiation Pressure*: this term represent the dissipative part of the force, and is related to the absorption and spontaneous re-emission of photons belonging to the light field by the atom. In this case the force acts an energy transfer between atoms and light field. The randomness of these processes puts the basis for the vast majority of the common laser cooling techniques.
- *Dipole Force*: the off-resonant dispersive behavior of the atom-light interaction generates a force that is proportional to the intensity of the laser field but is not capable to transfer energy amongst atoms and photons. This kind of force is relevant to generate an optical potential able to confine and trap atoms without changing the energy of the sample.

### 2.1.1 The atom-light interaction

An useful and comprehensive approach to the atom-light interaction is the semi-classical one, described in detail in [93]. If

$$\mathbf{E}(\mathbf{r}, t) = \hat{\mathbf{e}}E(\mathbf{r})e^{-i\omega t} + h.c. \quad (2.1)$$

## 2.1. Optical Dipole Forces

---

is the classical laser field oscillating at frequency  $\omega$  and propagating along the  $z$  direction, the electrical dipole moment induced by light on atom can be written as:

$$\mathbf{p}(\mathbf{r}, t) = \alpha \mathbf{E}(\mathbf{r}), \quad (2.2)$$

where  $\alpha$  is the complex polarizability of the atom, strongly depending on the laser frequency. The linear dependence of the induced dipole on the driving electrical field holds only far from the saturation regime, where non-linear effects introduce higher order terms in the above relation. The imaginary part of  $\alpha$  governs the absorptive phenomena and appears in the standard Lambert-Beer law, while the real part of the polarizability is responsible for the elastic light scattering properties of the medium and hence for the dispersion of light into it, and generates an out-of-phase oscillating term. The optical dipole potential produced by the interaction between  $\mathbf{E}$  and  $\mathbf{p}$  is:

$$U_{\text{dip}}(\mathbf{r}) = -\frac{1}{2} \langle \mathbf{p} \cdot \mathbf{E} \rangle = -\frac{1}{2\epsilon_0 c} \text{Re}(\alpha) I(\mathbf{r}), \quad (2.3)$$

where the brackets indicate the temporal mean over the optical oscillation period, much shorter than the typical atomic motion scale, and  $I(\mathbf{r})$  is the mean field intensity. Differentiating the previous expression one obtains the dipolar force acting on atoms by the light field:

$$F_{\text{dip}}(\mathbf{r}) = -\nabla U_{\text{dip}}(\mathbf{r}) = \frac{1}{2\epsilon_0 c} \text{Re}(\alpha) \nabla I(\mathbf{r}). \quad (2.4)$$

As happens for atoms moving in a magnetic induction field, the force vanishes when the field is uniform, and is stronger where the inhomogeneity of the field is more intense. This is relevant to engineer particular potentials starting from ordinary gaussian beams, intrinsically producing an attractive or repulsive potential (depending on the sign of  $\alpha$ , see below) due to their non-uniform spatial intensity profile. The number of absorption and re-emission cycles per unit time  $\Gamma_{sc}$  gives the intensity of the heating of the sample due to the presence of the light field. This quantity can be estimated by evaluating the ratio of the average absorbed energy by the atom in the unit time to the photon energy  $\hbar\omega$ :

$$\Gamma_{sc}(\mathbf{r}) = \frac{\left\langle \frac{d\mathbf{p}}{dt} \cdot \mathbf{E} \right\rangle}{\hbar\omega} = \frac{1}{\hbar\epsilon_0 c} \text{Im}(\alpha) I(\mathbf{r}). \quad (2.5)$$

In the semiclassical approach, again neglecting nonlinear terms in the polarizability expression, one can derive an expression for the complex polarizability that is the

same as the classical expression:

$$\alpha = 6\pi\epsilon_0 c^3 \frac{\Gamma/\omega_0^2}{\omega_0^2 - \omega^2 - i(\omega^3/\omega_0^2)\Gamma}, \quad (2.6)$$

provided the natural linewidth  $\Gamma$  is calculated evaluating the dipole matrix element  $\langle e|\mu|g\rangle$  in the semiclassical approximation:

$$\Gamma = \frac{\omega_0^3}{3\pi\epsilon_0\hbar c^3} |\langle e|\mu|g\rangle|^2. \quad (2.7)$$

In most experiments the laser frequency  $\omega$  is tuned sufficiently away from the resonance  $\omega_0$  to neglect nonlinear interaction terms, but still close to resonance in such a way the laser frequency detuning  $\Delta \doteq \omega - \omega_0$  is much smaller than the resonant frequency, i.e.  $|\Delta| \ll \omega_0$ . In this situation, the *rotating wave approximation* holds in a natural way, and Eq. (2.6) can be simplified to obtain the following useful expressions for the dipolar potential and dissipative scattering rate:

$$U_{\text{dip}}(\mathbf{r}) = \frac{3\pi c^2}{2\omega_0^3} \frac{\Gamma}{\Delta} I(\mathbf{r}), \quad (2.8)$$

$$\Gamma_{\text{sc}}(\mathbf{r}) = \frac{3\pi c^2}{2\hbar\omega_0^3} \left(\frac{\Gamma}{\Delta}\right)^2 I(\mathbf{r}). \quad (2.9)$$

From these expressions we can easily understand how the sign of the detuning determines the attractive or repulsive character of the interaction: in the case of *red* detuning ( $\Delta < 0$ ) the intensity maximum represents the *minimum* of the potential, and atoms will be attracted towards the center of the light intensity profile; on the contrary, when the detuning is *blue* ( $\Delta > 0$ ), atoms will be repelled from the light intensity maximum. The above expressions are valid for a generic light field interacting with a two-level atom, and constitute the basis for the light trapping mechanism. As can be seen, the trapping strength depends on  $I/\Delta$ , while the scattering rate has a  $I/\Delta^2$  behavior. The ratio of these two quantities suggests the optimal *red* trap configuration to be the one having detuning and intensity as large as possible in order to maintain the trapping strength  $I/\Delta$  constant, suppressing at the same time the ratio  $\Gamma_{\text{sc}}/U_{\text{dip}}$  by a factor proportional to  $\Delta$ .

In the case of a multilevel alkali atom, such as Rb and K are, the degeneracy of ground and upper levels is removed by the hyperfine interaction. Moreover, if the laser field wavelength is in the  $\mu\text{m}$  scale, the detunings  $\Delta_{1,F}$  and  $\Delta_{2,F}$  respect the two fine  $D_1$  and  $D_2$  transitions are appreciably different, and a common detuning can no more be assumed. In this situation, a more accurate treatment of the system

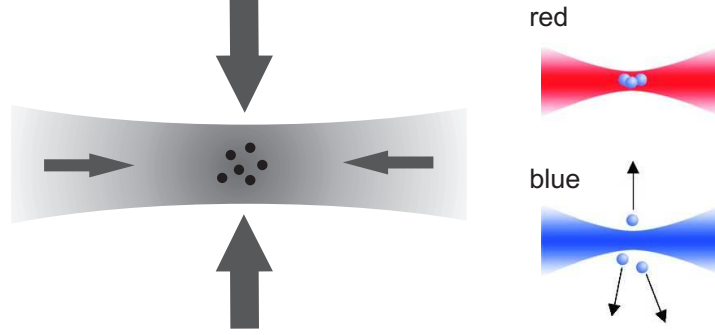


Figure 2.1: Schematic representation of a single gaussian beam optical trap. If the detuning is *red*, i.e.  $\Delta < 0$ , atoms are attracted towards the intensity maximum. The confining strength is pictorially represented by the size of arrows.

is required and it can be shown [93] that a slightly more complex formula for the potential should be employed:

$$U_{\text{dip}}(\mathbf{r}) = \frac{\pi c^2 \Gamma}{2\omega_0^3} \left( \frac{2 + \mathcal{P}g_F m_F}{\Delta_{2,F}} + \frac{1 - \mathcal{P}g_F m_F}{\Delta_{1,F}} \right) I(\mathbf{r}), \quad (2.10)$$

where  $g_F$  and  $m_F$  are the ground state Landé factor and Zeeman hyperfine state respectively, while  $\mathcal{P}$  is a polarization-dependent factor, equal to 0,  $\pm 1$  for linear and  $\sigma^\pm$  polarization respectively.

In a standard gaussian beam whose wavelength is  $\lambda$ , propagating along the  $z$  axis, the intensity profile is given by:

$$I(r, z) = \frac{2P}{\pi w(z)^2} \exp\left(-\frac{2r^2}{w^2(z)}\right) \quad (2.11)$$

where  $P$  is the beam power. The radial distance  $w(z)$  over which the intensity is reduced to  $1/e^2$  times its peak value is:

$$w(z) = w_0 \sqrt{1 + (z/z_R)^2}, \quad (2.12)$$

with  $w_0$  defined as the beam *waist* and  $z_R$  as the Rayleigh distance, defined by  $z_R = \pi w_0^2 / \lambda$ . If the beam frequency is red detuned, atoms will be attracted towards the center of the beam where the intensity is maximum, as Fig. 2.1 shows. The trapping strength will be much more pronounced along the radial direction, since along this line the light intensity variation is much steeper than in the axial direction. The recent development of commercial  $\mu\text{m}$ -range high power lasers ( $10 \div 100$  W) allowed

the realization of pure optical dipole traps exploiting focused gaussian beams, excellently suitable to trap the vast majority of alkali atoms with trapping frequencies that are comparable to those proper of standard high-confining magnetic traps. If two or more focused gaussian beams are crossed, a wealth of trap configurations can be engineered (for a review see. [93]), and a conspicuous control of the trapping strength along different directions can be obtained.

## 2.2 Optical Lattices: *a beam against the other*

The interference of two counterpropagating laser beams can be exploited to build a stationary light pattern once the relative phase is locked. The stationary light profile obtained in this way represents for an atom a periodic potential structure described by Eq. (2.3). To obtain the explicit expression of the stationary intensity profile, let's consider two plane waves propagating along the  $z$  axis with a constant relative phase  $\varphi$  and with frequencies  $\omega_1$  and  $\omega_2$  such as  $\Delta\omega \doteq \omega_2 - \omega_1 \ll \omega_1, \omega_2$ :

$$\begin{aligned}\mathbf{E}_{\rightarrow} &= \hat{\mathbf{e}}E_1\cos(kz - \omega_1 t) \\ \mathbf{E}_{\leftarrow} &= \hat{\mathbf{e}}E_2\cos(kz + \omega_2 t + \varphi),\end{aligned}\quad (2.13)$$

where  $\hat{\mathbf{e}}$  is the polarization vector. The total instantaneous intensity is:

$$I(z, \varphi) = \epsilon_0 c |\mathbf{E}_{\rightarrow} + \mathbf{E}_{\leftarrow}|^2. \quad (2.14)$$

The intensity profile is defined positive, and the deepest modulation is obtained for  $E_1 = E_2 = E$ . Supposing then the initial phase  $\varphi$  equal to zero, the total intensity is in this case written as:

$$I_{tot}(\Delta\omega, \Delta k) = 8\epsilon_0 c E^2 \cos^2\left(kz - \frac{\Delta\omega}{2}t\right) \cos^2\left(\frac{\Delta k}{2}z + \omega t\right), \quad (2.15)$$

where  $k \simeq (k_1 + k_2)/2$  and  $\omega \simeq (\omega_1 + \omega_2)/2$ . The potential effectively acting on atoms is obtained integrating the fast oscillation term over the oscillation period  $2\pi/\omega$ . This leads to an mean intensity profile equal to:

$$\bar{I}(\Delta\omega) = 4\epsilon_0 c E \cos^2\left(kz - \frac{\Delta\omega}{2}t\right) = 4I_0 \cos^2\left(kz - \frac{\Delta\omega}{2}t\right), \quad (2.16)$$

providing through Eq. (2.10) the optical potential that acts on atoms:

$$U_{lat} = sE_{rec} \cos^2\left(kz - \frac{\Delta\omega}{2}t\right), \quad (2.17)$$

## 2.2. Optical Lattices: a beam against the other

---

where we defined the height of the potential as measured in units of the atom-specific recoil energy  $E_{\text{rec}} = \hbar^2 k^2 / 2m$ <sup>1</sup>. Using Eqs. (2.8) and (2.11), in the realistic case of gaussian beams the potential height reads:

$$s = \frac{2P}{\pi w^2} \frac{4}{E_{\text{rec}}} \frac{\pi c^2 \Gamma}{2\omega_0^3} \left( \frac{2 + \mathcal{P}g_F m_F}{\Delta_{2,F}} + \frac{1 - \mathcal{P}g_F m_F}{\Delta_{1,F}} \right). \quad (2.18)$$

Introducing the atomic mass number  $Z$ , the lattice wavelength  $\lambda_{\text{lat}}$ , and the mean transition wavelength  $\lambda_0$  weighted on the  $D_1$  and  $D_2$  transitions, in the case of linear polarization the above expression becomes:

$$s = 2.19 \times 10^{20} \frac{P}{w^2} Z \Gamma \lambda_0^3 \lambda_{\text{lat}}^3 \left( \frac{2\lambda_2}{\lambda_{\text{lat}} - \lambda_2} + \frac{\lambda_1}{\lambda_{\text{lat}} - \lambda_1} \right) \quad (2.19)$$

where  $\lambda_1$  and  $\lambda_2$  represent the  $D_1$  and  $D_2$  transitions wavelength respectively, and all the quantities are expressed in SI units. In our setup (see Chap. 3)  $\lambda_{\text{lat}} = 1064$  nm, while the bosonic mixture to be loaded into the periodic lattice potential is the binary  $^{87}\text{Rb}$ - $^{41}\text{K}$  mixture. For  $^{87}\text{Rb}$  the in-air transition wavelength are  $\lambda_2^{\text{Rb}} \sim 780.0$  nm and  $\lambda_1^{\text{Rb}} \sim 795.0$  nm [94] respectively, while for K is  $\lambda_2^K \sim 767.0$  and  $\lambda_1^K \sim 770.4$  nm [95]. Assuming  $\lambda_0 = (\lambda_1 + \lambda_2)/2$ , the specific potential depths result:

$$s^{\text{Rb}} = 3.5 \times 10^6 \times \frac{P[\text{W}]}{(w[\mu\text{m}])^2} \quad (2.20)$$

$$s^K = 1.5 \times 10^6 \times \frac{P[\text{W}]}{(w[\mu\text{m}])^2}. \quad (2.21)$$

As we can see, the difference between the mass and level structure of Rb and K causes the total potential to be much shallower for potassium than for Rb.

A very common way to build a 1D optical lattice is to retroreflect a gaussian beam. If  $w_0$  is the minimum beam waist, the global potential acting on atoms is given by the sum of the periodic potential plus a radial confinement arising from the optical dipole force (2.8):

$$U_{\text{lat}}(r, z) = sE_{\text{rec}} e^{-\frac{2r^2}{w_0^2}} \sin^2(kz) \simeq sE_{\text{rec}} \left( 1 - 2\frac{r^2}{w_0^2} \right) \sin^2(kz), \quad (2.22)$$

where we assumed the radial extension of the atomic cloud to be much smaller than the beam waist.

---

<sup>1</sup>In our experimental setup,  $\lambda_{\text{lat}} = 1064$  nm. In this situation,  $E_{\text{rec}}^{\text{Rb}} = 1.34 \times 10^{-30}$  J, and  $E_{\text{rec}}^{\text{K}} = 2.84 \times 10^{-30}$  J

### 2.2.1 Moving lattices and the band structure

The total optical potential (2.17) generated by the laser intensity profile, as we have seen, is a periodic structure whose spatial period is  $\lambda_{\text{lat}}/2$ . The nodes and antinodes of the intensity profile are stationary only if the difference between the frequencies of the beam is zero and hence  $\Delta\omega t/2 = 0$  in time. If  $\Delta\omega \neq 0$ , the intensity profile is stationary in a reference frame that moves along the beam axis with a velocity  $-v_{\text{lat}}$ , where  $v_{\text{lat}}$  is given by:

$$v_{\text{lat}} = \frac{\Delta\omega}{2k} = \frac{\lambda_{\text{lat}}}{2} \Delta\nu. \quad (2.23)$$

This means that the lattice velocity in the laboratory frame  $v_{\text{lat}}$  can be easily managed through varying one or both the beam frequencies. Obviously, the occurrence of phase fluctuations between the two beams in time leads to a stochastic variation of the lattice velocity. For this motivation, the two lattice beams have to be split and generated using the same coherent laser source, and their frequencies have to be locked in such a way phase fluctuations between the two beams are suppressed. The residual phase modulation, in the case the rate of the photon-atom scattering (2.5) can be neglected, represents the main limit to the lifetime of the cold sample loaded into the lattice, since it corresponds to an effective shaking of the periodical potential along the beams axis.

The center-of-mass motion of a condensate through the moving lattice, as anticipated before, can be described using the single particle approach proper of the solid state physics, describing the motion of an electron through the ions lattice in terms of energy bands  $E_n$  and quasimomentum  $q$ . In such a situation, the wavefunction  $\Psi_{n,q}(x)$  of the particle obeys the standard Bloch-Floquet theorem,

$$\Psi_{n,q}(x) = e^{iqx} u_{n,q}(x) \quad (2.24)$$

$$u_{n,q}(x) = u_{n,q}(x + a) \quad (2.25)$$

with  $a = \lambda/2$ , and can be found solving the Schrödinger equation:

$$\hat{H}\Psi_{n,q}(x) = \left[ -\frac{\hbar^2}{2m} \frac{\partial^2}{\partial x^2} + sE_{\text{rec}} \cos^2(kx) \right] \Psi(x) = E_n(q)\Psi_{n,q}(x). \quad (2.26)$$

This equation, provided the bisection relation  $\cos^2(\alpha) \rightarrow \frac{1 + \cos(2\alpha)}{2}$  is applied, belongs to the class of *Mathieu equations* [97], whose solution is not analytic but can be numerically evaluated. The eigenfunctions  $\Psi_{n,q}(x)$  are called *Bloch states*. The discrete spatial translation invariance of the system stated by the Bloch-Floquet theorem

## 2.2. Optical Lattices: a beam against the other

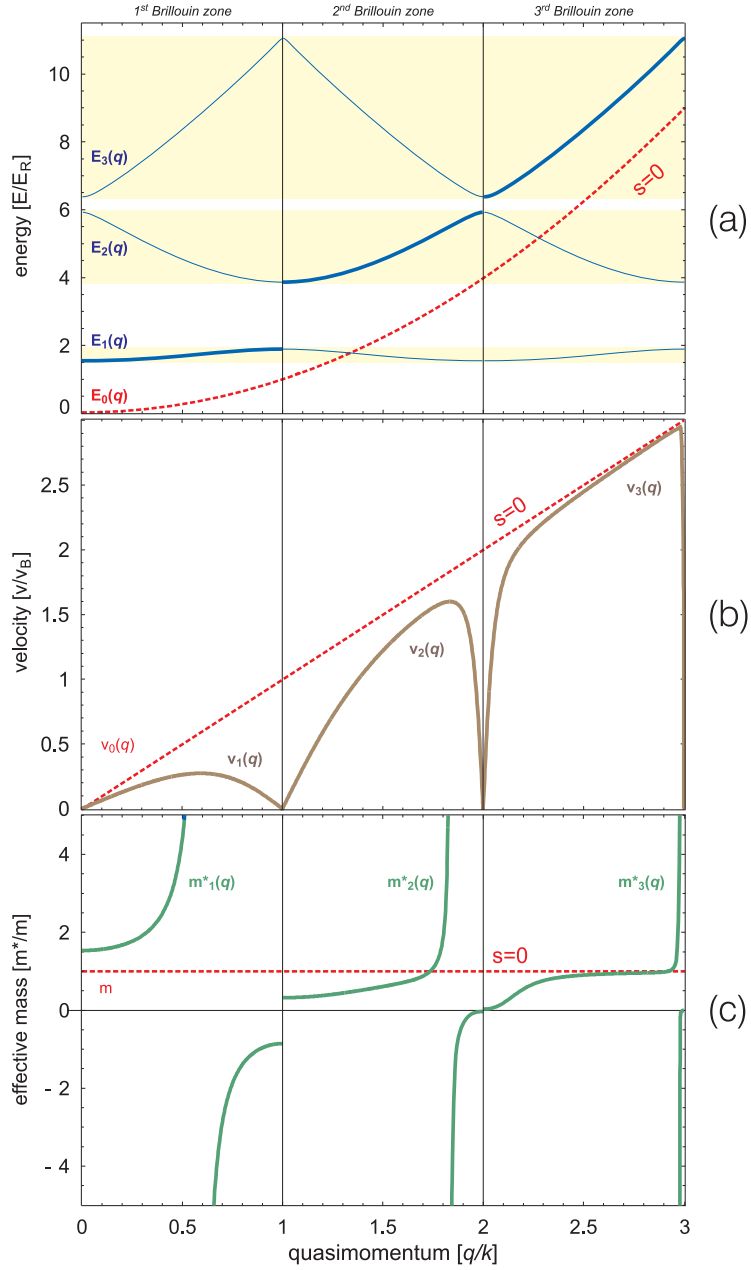


Figure 2.2: Solid lines: plot of the first three energy bands (a), their correspondent Bloch velocity (b), and effective mass (c). Dashed lines correspond to the free case ( $s = 0$ ). The potential height is set to  $s = 4$ . Adapted from [96].

does not allow to take the wavefunctions (2.24) as eigenfunctions of the momentum operator as well, that ceases to be a good quantum number once the periodic potential is switched on. On the other side, the Fourier transform of these eigenfunctions shows a correspondent periodicity in the momentum space as well. The minimal periodicity cells, whose width is  $2\pi/a = 4\pi/\lambda$  are the *Brillouin zones*, and the quantum number  $q$  appearing in the eigenfunctions (2.24), the *quasimomentum*, can assume the discrete values  $q = \frac{4\pi}{N\lambda}$ , where  $N$  is the number of lattice sites. If  $N$  is sufficiently large, as in actual experiments, the quasimomentum discretization dissolves and  $q$  acquires a physical meaning that, inside each of the Brillouin zones, is practically coincident with the ordinary momentum. For a given  $q$ , many Bloch eigenstates for the problem (2.26) do exist, each one labeled by the index  $n$  corresponding to a specific energy band  $E_n(q)$ . A numerical estimation of the energy bands obtained from Eq. (2.26) is reported in Fig. 2.2(a) for  $s = 4$ . The first three Brillouin zones are shown, together with the parabolic free particle energy spectrum (solid line). This periodic representation of the energy spectrum takes the name of *repeated zone* scheme. As we can see, three main features arise from this picture:

- Near the zone boundaries an energy gap appears, and its width is related to the potential height. In correspondence of the zone boundaries the bands have null derivative. Moreover, each band has a value of  $q$  corresponding to a flex point in the energy spectrum. This has relevant effects on the dynamics of a Bloch wavepacket, as we will show in the following.
- At low energies ( $E_n(q) \ll sE_{\text{rec}}$ ) the bands are almost flat. For increasing height of the periodic potential the flatness increases, and the energy asymptotically tends to the eigenenergies of the harmonic oscillator obtained with a parabolic approximation of the single lattice site potential.
- At high energies ( $E_n \gg sE_{\text{rec}}$ ) the energy spectrum is pretty similar to the free particle spectrum (except for a zero-point energy shift,  $E_1(q = 0)$ ) and differs from the latter only near the boundaries of the Brillouin zones. The difference increases with the potential height.

The specific shape of the Bloch states can be extracted in two main cases, corresponding to the *weak* and *tight* binding regimes. In the first case, the potential height is much smaller than the recoil energy ( $s \ll 1$ ), corresponding to the free energy at the first zone boundary. The Bloch function is almost completely delocalized all over the lattice and is well-fit by a plane wave whose momentum is  $q$ , since the peri-

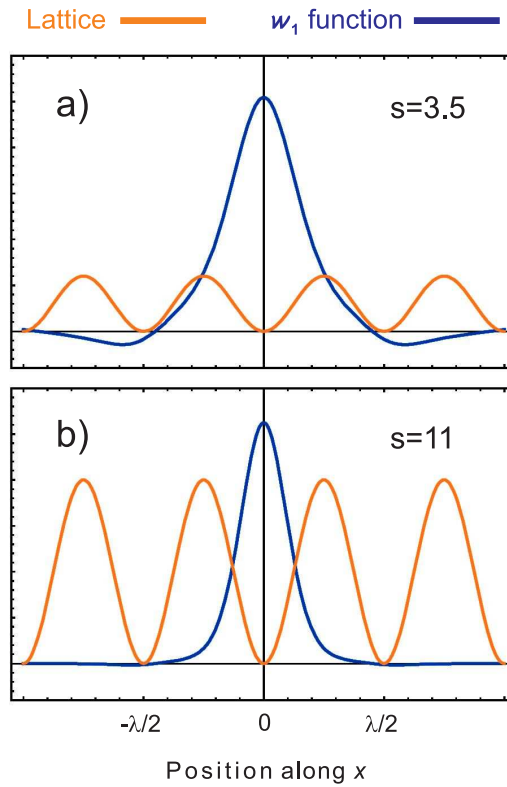


Figure 2.3: Plot of the first band Wannier function  $w_1(x)$  localized into the  $0^{th}$  lattice site for a lattice height  $s = 3.5$  (a) and  $s = 11$  (b). The periodic potential is represented in both cases as well. Both vertical and horizontal scales are in arbitrary units.

odic modulation term  $u_{n,q}(x)$  gives a small contribution. If the potential height is increased, the wavefunction becomes more and more localized at each lattice sites, and ceases to be delocalized over the entire lattice. In this case, the contribution of the  $u_{n,q}(x)$  factor becomes fundamental for the behavior of the global wavefunction of the particle. A convenient way to write the Bloch state can be obtained exploiting an orthonormal set of eigenfunctions located at each lattice sites, called *Wannier* functions  $w_n(x - ja)$ :

$$\Psi_{n,q}(x) = \sum_j e^{ijqa} w_n(x - ja), \quad (2.27)$$

where  $e^{ijqa}$  is a quasimomentum dependent phase factor. When the lattice depth is increased, each of the Wannier function acquires a stronger localization to the spe-

cific lattice site  $j$ , and their sidelobes exponentially vanish (see Fig. 2.3). In the limit of infinite lattice height and extension, the wavefunction is constituted by an equal distribution of Wannier functions whose tails do not overlap since the tunneling between adjacent sites is suppressed. It can be shown that in the tight binding regime a good approximation of the global wavefunction is provided by a sum of slightly overlapping narrow gaussian functions centered on each lattice site. The tunneling matrix element  $J$  describing the tunneling probability between two adjacent lattice sites is related to the width of the lowest energy band, and is given by [98]:

$$J = \frac{\max(E_0(q)) - \min(E_0(q))}{4}. \quad (2.28)$$

### 2.2.2 Dynamics of a Bloch wavepacket

If a condensate is loaded into an optical lattice, its wavefunction can be decomposed over a superposition of Bloch states, eigenstates of the Mathieu equation (2.26). If the wavepacket momentum spread  $\Delta q$  is much smaller than the extension of the Brillouin zone, i.e.  $\Delta q \ll 4\pi/\lambda$ , the mean momentum  $q$  can be identified with a well defined quasimomentum value, and the band theory can be applied to understand the center-of-mass dynamics. Actually, for a BEC this is not a hard task to be accomplished, since for a typical axial extension of  $\sim 100 \mu\text{m}$  the Heisenberg limit on the momentum gives  $\Delta q \sim 10^{-3}k$ . The physical consequence of this feature is that the motion of a condensate into an optical potential can be reasonably described using a single particle approach, motivating the employ of the standard energy bands theory, originally developed for electrons moving along a material crystal. Following this approach, the wavepacket moves along the lattice with a velocity equal to:

$$v_n(q) = \frac{1}{\hbar} \frac{\partial E_n(q)}{\partial q}, \quad (2.29)$$

which takes the name of *Bloch velocity* of the wavepacket. This quantity is analogous to the standard *group velocity*  $v_g$  describing the propagation of a free wavepacket, defined by  $v_g = \frac{\partial \omega}{\partial k}$ . In a semiclassical approach, the external forces  $F_{\text{ext}}$  acting on the wavepacket, that we assume as slowly varying on the timescale of the lattice potential and sufficiently small not to induce interband transitions, will modify its quasimomentum following the fundamental equation of dynamics

$$F_{\text{ext}} = \dot{p} = \hbar \dot{q}. \quad (2.30)$$

The above expression can be inserted in the temporal derivative of Eq. (2.29) to obtain:

$$\dot{v}_n = \hbar^{-2} \frac{\partial^2 E_n(q)}{\partial q^2} F_{ext}, \quad (2.31)$$

which suggests a particular viewpoint to interpret the wavepacket dynamics: the motion of the single particle center-of-mass along a periodic potential can be reconstructed through the standard second Newton's law once an *effective mass*  $m_n^*(q)$  is introduced. The value of this effective mass (see Fig. 2.2(c)) is varying throughout the Brillouin zone and depends on the band index  $n$ , and is obtained once the energy spectrum is known:

$$m_n^*(q) = \hbar^2 \left[ \frac{\partial^2 E_n(q)}{\partial q^2} \right]^{-1}. \quad (2.32)$$

Note that  $m_n^*(q)$  assumes negative values where the Bloch velocity (Fig. 2.2(b)) has a negative first derivative, diverging where the Bloch velocity reaches a local stationary point. In these points an external force tends to have a vanishing effect on the wavepacket, while it produces a *negative* acceleration in the zones where  $m_n^*(q) < 0$ .

When the approximation of weak forces ceases to be valid and the quasimomentum variations are fast, interband transitions (the so called *Landau-Zener tunneling*) may take place. The probability for this process to happen is [99]:

$$\Gamma \propto e^{-a_c/a}, \quad (2.33)$$

where  $a_c = d(\Delta E)^2/4\hbar^2$  is a critical acceleration dependent on the lattice spacing  $d$  and the energy gap  $\Delta E$  between the lower and the higher band.

## 2.3 Multidimensional optical lattices

If more than one couple of retroreflected beams cross orthogonally in a certain point of space, multidimensional and exotic periodic potentials can be obtained, whose peculiar features depend on the polarization and relative phase of the beams.

### 2D optical lattices

This configuration can be obtained crossing two orthogonal standing waves. At the trap center, the global potential acting on atoms will be:

$$U_{\text{lat}}(x, y) = sE_{\text{rec}} (\cos^2(kx) + \cos^2(ky) + 2\hat{\mathbf{e}}_1 \cdot \hat{\mathbf{e}}_2 \cos \varphi \cos(kx) \cos(ky)), \quad (2.34)$$

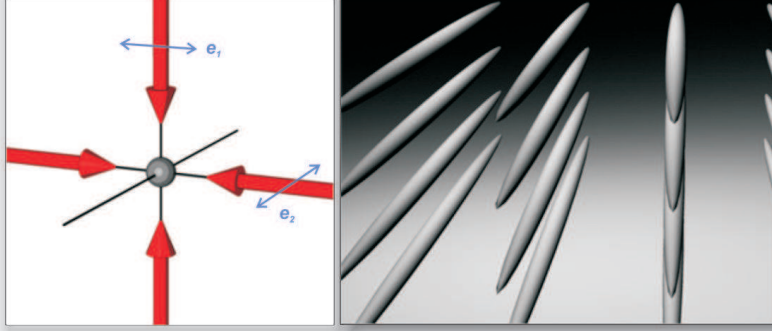


Figure 2.4: Schematic representation of a 2D optical lattice, constructed superimposing two orthogonal laser beam pairs. If the beam polarizations are those shown in figure, a bi-dimensional array of 1D wells is realized. Adapted from [100].

where  $\varphi$  represents a time phase between the orthogonal standing waves. As we can see, a fully separable potential can be obtained only if the third term vanishes. This happens in two cases:

- The two polarizations are mutually orthogonal, and hence  $\hat{e}_1 \cdot \hat{e}_2 = 0$ .
- A certain frequency difference is introduced between the two standing waves in such a way the time phase rapidly rotates, and the third term mediates to zero.

In order to avoid heating of the sample coming from residual phase fluctuations, anyway, the best thing to do is to employ both orthogonal polarizations and to introduce a frequency detuning (10 ÷ 100 MHz) between the beam pairs. If this is the situation, a 2D array of 1D atomic tubes is obtained (see Fig. 2.4), and once the radial confinements are included, the potential reads:

$$U_{\text{lat}}(x, y, z) = E_{\text{rec}} \left[ s_x e^{-2\frac{y^2+z^2}{w_x^2}} \sin^2(kx) + s_y e^{-2\frac{x^2+z^2}{w_y^2}} \sin^2(ky) \right]. \quad (2.35)$$

Here  $s_x$  and  $s_y$  are the lattice depths along the two beams directions  $x$  and  $y$ . Restricting to a small zone around the center, the trapping potential can be approximated as the sum of a homogeneous lattice plus an additional external harmonic confinement:

$$U_{\text{lat}}(x, y, z) \simeq E_{\text{rec}} [s_x \sin^2(kx) + s_y \sin^2(ky)] + \frac{m}{2} [\omega_x^2 x^2 + \omega_y^2 y^2 + \omega_z^2 z^2], \quad (2.36)$$

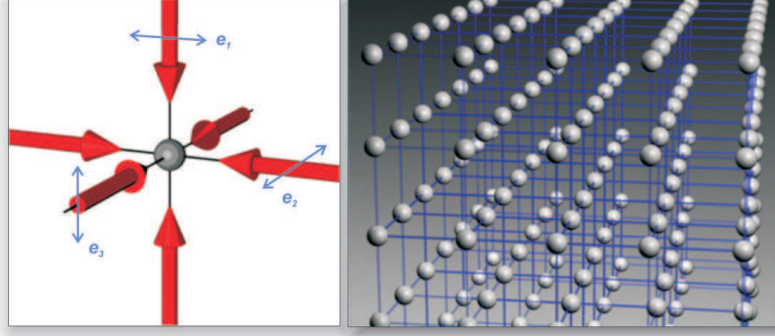


Figure 2.5: Schematic representation of a 3D optical lattice, constructed superimposing three orthogonal laser beam pairs. If the beam polarizations are those shown in figure, a simple cubic structure is realized. Adapted from [100].

where the frequencies result from the radial contributions of both standing waves and are given by:

$$\omega_x^2 = \frac{2s_y}{w_y^2} \left( \frac{h}{m\lambda} \right)^2, \quad \omega_y^2 = \frac{2s_x}{w_x^2} \left( \frac{h}{m\lambda} \right)^2, \quad \omega_z^2 = \omega_x^2 + \omega_y^2. \quad (2.37)$$

### 3D optical lattices

If three pairs of retroreflected beams are orthogonally superimposed, a 3D periodic arrangement of lattice sites can be constructed. The simple cubic lattice structure is obtained fixing a zero time phase between the three pairs of beams and inserting a detuning between their frequencies, analogously to what is done in the 2D case, in such a way to eliminate the inter-beams interference patterns (see Fig. 2.5). The trapping potential can be written as:

$$U_{\text{lat}}(x, y, z) \simeq E_{\text{rec}} [s_x \sin^2(kx) + s_y \sin^2(ky) + s_z \sin^2(kz)] + \frac{m}{2} [\omega_x^2 x^2 + \omega_y^2 y^2 + \omega_z^2 z^2], \quad (2.38)$$

where the frequencies have a general expression and can be calculated through a cyclical permutation on the parameters corresponding to the three directions:

$$\begin{aligned}\omega_x^2 &= 2 \left( \frac{s_y}{w_y^2} + \frac{s_z}{w_z^2} \right) \left( \frac{h}{m\lambda} \right)^2, \\ \omega_y^2 &= 2 \left( \frac{s_x}{w_x^2} + \frac{s_z}{w_z^2} \right) \left( \frac{h}{m\lambda} \right)^2, \\ \omega_z^2 &= 2 \left( \frac{s_x}{w_x^2} + \frac{s_y}{w_y^2} \right) \left( \frac{h}{m\lambda} \right)^2.\end{aligned}\tag{2.39}$$

If the lattice depth is sufficiently high, the external potential terms appearing in Eq. (2.38) are practically constant on a sufficiently small portion of space, where the single well potential can reasonably be assumed as harmonic. Restricting to the central trapping region, the single-well frequencies along each direction are hence given by:

$$\omega_{\text{lat},i}^2 = s_i \left( \frac{2\pi h}{m\lambda^2} \right)^2, \quad i = x, y, z.\tag{2.40}$$

In the case a mixture is inserted into the lattice, the relation between the lattice frequencies is  $\omega_{\text{lat}}^{(2)} = \omega_{\text{lat}}^{(1)} \frac{m_1}{m_2} \sqrt{\frac{s_2}{s_1}}$ . A detailed discussion on the single-well frequencies reduction, induced by the Gaussian beam shape when the analysis is not restricted to the trap center, can be found in Ref. [100]. Here we only notice that in ordinary experiments the typical frequency variation along the symmetry axis of the condensate does not exceed 5% and can usually be neglected when performing an energetic analysis of the system.

## 2.4 A BEC in an optical lattice: role of interactions

Up to now the discussion on ultracold atoms loaded in an optical lattice has been limited to a single particle approach, motivated by the reduced momentum spread of a BEC and by the peculiar property of condensed atoms to occupy *exactly* the same quantum level. This viewpoint is indeed adequate to the description of the center-of-mass motion of the atomic ensemble, especially in the low-density regime where the atom-atom interaction can be neglected. However, several recent works, starting from the ordinary Bloch theory, demonstrated the insurgence of exotic effects strictly related to the presence of interactions between particles. It has been demonstrated that in a regime where inter-atomic interactions are non negligible with respect to the tunneling energy, the energy spectrum of the BEC into the optical potential can

undergo noticeable deviations from the single particle case, in such a way loops ("swallow tails") appear in proximity of the band edges [101, 102, 103]. Moreover, strong cross-dimensional effects have been observed during the expansion of the condensate in a moving lattice [6, 7]. The recent observation of the superfluid to Mott insulator transition in a  $^{87}\text{Rb}$  condensate [8] and the generation of cold molecular samples through the management of the intra-specie scattering in optical lattices [59] represented only the first milestones in the investigation of interaction effects in optical lattices.

From a quantitative point of view, the single particle Schrödinger equation (2.26) has to be modified through the insertion of the non-linear Gross-Pitaevskii term, accounting for the presence of short-range interactions between atoms:

$$\hat{H}\Psi(x) = \left[ -\frac{\hbar^2}{2m} \frac{\partial^2}{\partial x^2} + U_{\text{lat}}(x) + g|\Psi(x)|^2 \right] \Psi(x) = E\Psi(x). \quad (2.41)$$

The effective shape of the localized wavefunctions  $\varphi_j(x, y, z)$  on which is convenient to decompose the global condensate wavefunction (see Eq. (2.27) valid for a 1D case) depends on the dimensionality of the system. Indeed, the presence of repulsive interactions tends to increase the size of the density profiles along the weak confinement directions. Qualitatively, in a 1D lattice configuration the localized wavefunctions will approximately look like 2D prolate disk profiles strongly confined along the lattice direction, while in a 2D lattice the confinement will localize the wavefunction along the two beam directions, while the density profiles will be broadened along the shallow-confining transverse direction. Along the lattice directions, the wavefunction profile corresponding to the  $j$ -th site is hence reasonably given by a localized Wannier-like function  $w$ , while along the axes of shallow confinement a broad gaussian function  $\Theta$  will provide a better fit to the actual profile:

$$\begin{aligned} \varphi_{\mathbf{j}}(\mathbf{x}) &= w_x(x - j_x d) \Theta_y(j_y d, y - j_y d) \Theta_z(j_z d, z - j_z d) & \text{1D lattice} \\ \varphi_{\mathbf{j}}(\mathbf{x}) &= w_x(x - j_x d) w_y(y - j_y d) \Theta_z(j_z d, z - j_z d) & \text{2D lattice} \\ \varphi_{\mathbf{j}}(\mathbf{x}) &= w_x(x - j_x d) w_y(y - j_y d) w_z(z - j_z d) & \text{3D lattice} \end{aligned} \quad (2.42)$$

where the vector  $\mathbf{j} = (j_x, j_y, j_z)$  identifies the specific lattice site. The global wavefunction is hence reconstructed by:

$$\Psi(\mathbf{x}) = \sum_{\mathbf{j}} \sqrt{\bar{n}_{\mathbf{j}}} e^{i\phi_{\mathbf{j}}} \varphi_{\mathbf{j}}(\mathbf{x}), \quad (2.43)$$

where  $\bar{n}_{\mathbf{j}}$  is the average occupation number of the  $\mathbf{j}$ -th lattice site. Notice that this number is usually much less than one in the case of thermal cold gases, and reaches

values comparable or bigger than unity only for condensate clouds. When the lattice depth is increased and the tunneling amplitude drops to zero, the average occupation becomes an exact quantum number and Fock states are adequate to provide the localized wavefunction, leading to the Gutzwiller approximation (see below). Notice again that the dependence of the wavefunction on the specific lattice site along the lattice directions is due to the inhomogeneity introduced by the external confinement potential. The energy shift  $\epsilon_j$  of the  $j$ -th site due to the external potential is given by  $\epsilon_j = m\omega_{\text{ext}}^2(a_j)^2/2$ , while the on-site interaction energy  $U$  is calculated as:

$$U = g \int |\varphi_j(\mathbf{x})|^4 d\mathbf{x}. \quad (2.44)$$

It can be shown that in the Thomas-Fermi regime the total energy corresponding to the  $j$ -th lattice site is approximately:

$$E_j \simeq \epsilon_j \bar{n}_j + \frac{U}{2} \bar{n}_j^2, \quad (2.45)$$

leading to the following expression for the inhomogeneous chemical potential:

$$\mu_j = \frac{\partial E_j}{\partial n_j} = \epsilon_j + U \bar{n}_j. \quad (2.46)$$

### 2.4.1 The Bose-Hubbard model and the Mott insulator phase

The dynamics of an interacting gas of bosons at zero temperature in an optical lattice has been shown to be accurately described in the second quantization formalism by the Bose-Hubbard model [104]. Beyond this purely ideal system, anyway, an ultracold bosonic sample represents an optimal tool to investigate the existence of nontrivial mean field effects arising from the presence of interaction in a periodic structure [105].

The mean field approach is conveniently obtained constructing the second quantization Hamiltonian operator:

$$\begin{aligned} \hat{H} = & \int d\mathbf{x} \hat{\Psi}^\dagger(\mathbf{x}) \left[ -\frac{\hbar^2}{2m} \nabla^2 + U_{\text{lat}}(\mathbf{x}) \right] \hat{\Psi}(\mathbf{x}) + \\ & + \frac{1}{2} \frac{4\pi\hbar^2}{m} a \int d\mathbf{x} \hat{\Psi}^\dagger(\mathbf{x}) \hat{\Psi}^\dagger(\mathbf{x}) \hat{\Psi}(\mathbf{x}) \hat{\Psi}(\mathbf{x}), \end{aligned} \quad (2.47)$$

where  $\hat{\Psi}(\mathbf{x})$  is a bosonic field operator for atoms in a given internal atomic state,  $U_{\text{lat}}(\mathbf{x})$  is the optical lattice potential, and  $a$  is the interatomic atomic scattering length. The lattice potential is given by Eq. (2.38) and potentially it includes the

confinement effects due to the gaussian beams profile or to an external magnetic potential. It is convenient to collect these contributions in an additional potential term  $U_{\text{ext}}$ , and to consider  $U_{\text{lat}}$  as a pure periodic potential. In the end of the Section we will discuss about how the inhomogeneity of the system affects the ground state and in particular how it eases the experimental observation of the Mott insulator phase. If  $a \ll \bar{a}_{ho} \ll d = \frac{\lambda_{\text{lat}}}{2}$  we can neglect the inter-band tunneling process, since the energies in play are much smaller than the mean oscillator energy gap  $\hbar\bar{\omega}_{ho} = \hbar^2/m\bar{a}_{ho}^2$  associated to the potential of each lattice site  $\mathbf{j}$ . Under this condition, we can expand the field operators in the Wannier basis (2.27), keeping only the first band contribution:

$$\hat{\Psi}(\mathbf{x}) = \sum_{\mathbf{j}} b_{\mathbf{j}} w(\mathbf{x} - \mathbf{j}d), \quad (2.48)$$

where the operators  $b_{\mathbf{j}}$  and  $b_{\mathbf{j}}^\dagger$  are respectively the annihilation and creation operator for a boson at the site  $\mathbf{j}$ , obeying the commutation relation  $[b_{\mathbf{i}}, b_{\mathbf{j}}^\dagger] = \delta_{\mathbf{i}\mathbf{j}}$  and  $d$  is the isotropic lattice periodicity. With this expression for the ground state wavefunction the Hamiltonian (2.47) reduces the usual *Bose-Hubbard* form:

$$\hat{H} = -J \sum_{\langle \mathbf{i}, \mathbf{j} \rangle} b_{\mathbf{i}}^\dagger b_{\mathbf{j}} + \sum_{\mathbf{i}} (\epsilon_{\mathbf{i}} - \mu) \hat{n}_{\mathbf{i}} + \frac{1}{2} U \sum_{\mathbf{i}} \hat{n}_{\mathbf{i}}(\hat{n}_{\mathbf{i}} - 1), \quad (2.49)$$

where the operator  $\hat{n} = b_{\mathbf{i}}^\dagger b_{\mathbf{i}}$  gives the number of particles occupying the  $\mathbf{i}$ -th site. The parameters  $U$  and  $J$  correspond to the on-site repulsion energy and to the tunneling energy respectively. The on-site interaction  $U$  (see also Eq. (2.44)) depends on the mean value of the single Wannier function corresponding to the  $\mathbf{j}$ -th site:

$$U = g \int |w(\mathbf{x} - \mathbf{j}d)|^4 d\mathbf{x}, \quad (2.50)$$

where  $g = \frac{4\pi\hbar^2}{m}a$ . This term describes the repulsive interaction of each atom populating the lattice site with the remaining  $\hat{n} - 1$ . A detailed analysis of the Bose-Hubbard model in presence of attractive interactions can be found in [106]. Since the expression of the coupling strength  $g$  requires a point-like interaction between particles the interaction range is very small compared to the lattice spacing, and considered the fact that the overlap between wavefunctions corresponding to different lattice sites is very small, all terms arising from nearest neighbor sites can be neglected. The tunneling of particles between adjacent sites gives a contribution  $J$  to the total energy of the system, proportional to the overlap of the Wannier wavefunc-

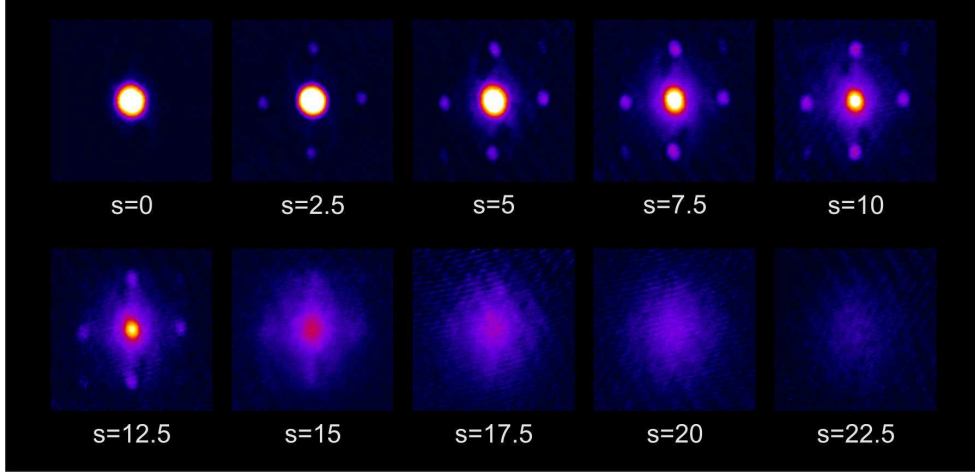


Figure 2.6: Momentum distribution of a BEC after expansion from an optical lattice, obtained at LENS in Florence (2005). Images are taken for different lattice height  $s$ . If the potential depth is above the critical value  $s_c \sim 12.5$  the system loses the long range coherence and the interference peaks broaden until they disappear in the deep insulator regime ( $s = 22.5$ ).

tion relative to two neighboring sites:

$$J = \int w(\mathbf{x} - \mathbf{j}d) \left[ -\frac{\hbar^2}{2m} \nabla + U_{\text{lat}}(\mathbf{x}) \right] w(\mathbf{x} - \mathbf{j}d) d\mathbf{x}. \quad (2.51)$$

The energy  $\epsilon_j$  represents the energy shift induced by the inhomogeneity of the potential, and can be hence evaluated as:

$$\epsilon_j = \int |w(\mathbf{x} - \mathbf{j}d)|^2 U_{\text{ext}} d\mathbf{x}. \quad (2.52)$$

The key point of the Bose-Hubbard model lays in the property of the Hamiltonian (2.47) to admit two distinct ground-states depending on ratio  $U/J$  and corresponding to two distinct phases of the system. When the interaction energy  $U$  has a value that is much smaller than the tunneling energy  $J$  the system behaves in superfluid way, well described by the Bloch picture reported in the previous Sections. The superfluid state of a  $N$ -particle superfluid spreading over  $M$  sites is given by:

$$|\Psi_{\text{SF}}\rangle = \left( \frac{1}{\sqrt{M}} \sum_{\mathbf{j}} \hat{b}_{\mathbf{j}}^\dagger \right)^N |0\rangle, \quad (2.53)$$

that represents a macroscopically coherent state. In this situation the phase is constant all over the lattice, and this leads to the insurgence of interference peaks in the expansion of the condensate through the lattice, acting as a grating for a matter wave. The conjugate variable of the lattice phase, the atom number, remains on the other hand undetermined under the effect of Poissonian fluctuations.

When the interaction is increased, or analogously the tunneling is decreased, the system enters a phase where atoms tend to be strongly localized into each lattice site, being the number fluctuations through tunneling processes very costly from an energetic point of view. The system starts to behave as an insulator, rather than a superfluid, and the phase transition obtained when  $U \simeq J$  takes the name of *Mott transition*. In this regime where  $U \gg J$  the number of atoms populating a single lattice site is perfectly determined, but the phase coherence is completely lost [8]. In the Mott insulator regime, indeed, the expansion of the condensate through the lattice does not lead to the insurgence of narrow peaks in the density profile. If the filling factor  $\bar{n} = N/M$  assumes an integer value and  $J \rightarrow 0$ , the insulator ground state is compound by  $M$  distinct condensates, each having a random phase:

$$|\Psi_{\text{MI}}(\bar{n})\rangle = \prod_{\mathbf{j}} (|\bar{n}\rangle_{\mathbf{j}}) \propto \prod_{\mathbf{j}} (a_{\mathbf{j}}^\dagger)^{\bar{n}} |0\rangle_{\mathbf{j}}, \quad (2.54)$$

representing the product of local Fock states with  $\bar{n}$  atoms per site. In this phase, the behavior of the system is driven by the strong coupling between atoms, whereas no macroscopic coherence proper of a superfluid survives along the lattice. In this situation the condensate is no more superfluid and the mean field GPE approach is no more valid, since no macroscopic wavefunction is present. The defining property of the gas in this phase is its incompressibility,  $\partial n / \partial \mu = 0$ . To understand the importance of optical lattices in reaching the strong coupling regime  $U \gg J$ , it is useful to extract an explicit (and approximate) form for the parameters  $J$  and  $U$ . This can be done in the deep lattice limit  $s = U_{\text{lat}}/E_{\text{rec}} \gg 1$ , where the localized wavefunction can be reasonably assumed as gaussian [107]. Solving the 1D Mathieu equation (2.26) we can calculate the tunneling amplitude:

$$J = \frac{4}{\sqrt{\pi}} E_{\text{rec}} s^{3/4} e^{-2\sqrt{s}}, \quad (2.55)$$

decreasing exponentially as the square root of lattice depth  $s$ . For the interaction strength, the dimensionality of the system plays a relevant role. In the 3D case one obtains:

$$U = 4 \frac{\sqrt{2\pi}}{\lambda_{\text{lat}}} a E_r s^{3/4}, \quad (2.56)$$

this time proportional to the height of the lattice potential. The ratio of the above quantities yields:

$$\frac{U}{J} \simeq \frac{\sqrt{2}\pi}{\lambda_{\text{lat}}} a e^{2\sqrt{s}}. \quad (2.57)$$

From this relation it is evident that an optical lattice represents a unique and easy tool to investigate the superfluid-insulator transition, since the relevant parameter  $U/J$  scales exponentially as the lattice depth  $s$ : the Mott insulator regime can be reached simply increasing the lattice beams intensity. Fig. 2.6 shows the expansion of a condensate after a certain hold time in an optical lattice for different lattice height. When the lattice depth is moderate the long range coherence yields to narrow Bragg peaks in the momentum space. When  $s$  approaches a critical value ( $s_c \sim 12.5$  in Figure) the long range coherence drops and the interference peaks start to broaden until they completely disappear for  $s = 22.5$ , where the deep insulator phase is reached.

The ratio (2.57) allows a rough estimate of the critical lattice depth  $s_c$  above which the insulating phase arises:

$$1 \simeq \left(\frac{U}{J}\right)_c = \frac{\sqrt{2}\pi}{\lambda_{\text{lat}}} a e^{2\sqrt{s_c}}. \quad (2.58)$$

The above calculation gives  $s_c \sim 3.6$  for  $^{87}\text{Rb}$  and  $s_c \sim 4.7$  for  $^{41}\text{K}$  if a laser with  $\lambda = 1064$  nm is employed to generate the 3D optical lattice. A more accurate 3D mean-field calculation of the ground state [105, 108, 109] gives  $(U/J)_c = z \cdot 5.8$  (with  $z = 2 \cdot D$  the number of nearest neighbors) in the case  $\bar{n} = 1$ , and  $(U/J)_c = z \cdot 4.2$  for  $\bar{n} \gg 1$ . In the 1D case, strong deviations from the mean field predictions are expected, and the critical value is seen to be  $(U/J)_c = 3.6$  [110]. In particular, Eqs. (2.55) and (2.56) are obtained assuming a gaussian ansatz for the localized wavefunction. If this assumption is released and Wannier function are rather employed, a significative deviation from the above behavior can be obtained [111].

The schematic phase diagram of the Bose-Hubbard Hamiltonian (2.47) is reported in Fig. 2.7, where the chemical potential, i.e. the density of the sample  $\mu/U$  is reported as a function of the interaction strength  $J/U$ . As we can see, different lobes appear, corresponding to different commensurate filling factor  $\bar{n}$ . If the mean atom number  $\langle \hat{n} \rangle$  is *exactly* integer and the potential height is raised up to the value  $s_c$ , the system moves along the dashed lines and enters the Mott phase from the extreme points of the lobes. In this case  $\bar{n}$  atoms are trapped at each lattice site the tunneling is heavily suppressed and the phase is no more defined on the entire sample. Nevertheless, in the realistic situation in which  $\langle \hat{n} \rangle$  is *not exactly* integer, e.g.

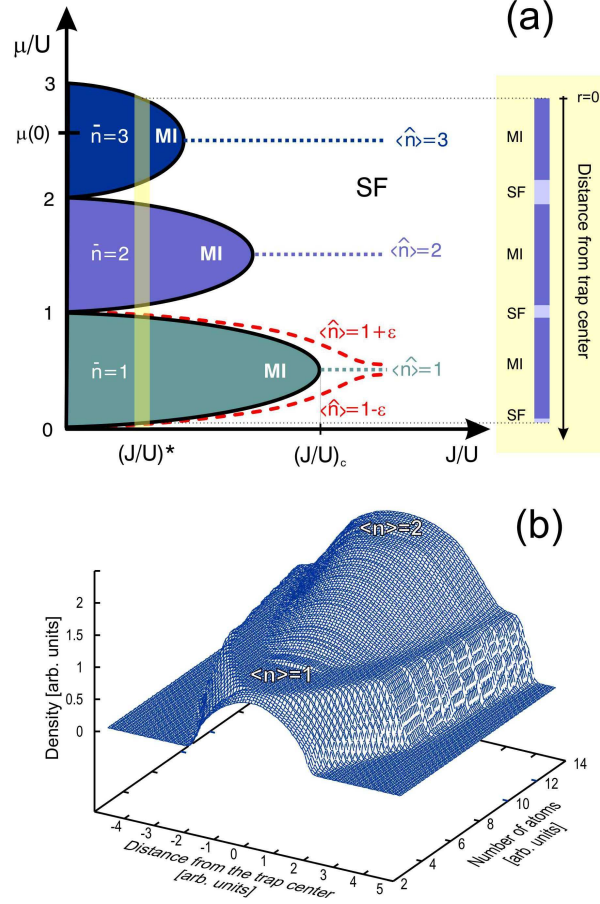


Figure 2.7: (a) Phase diagram of the Mott-Hubbard Hamiltonian. Under a critical value of  $(J/U)_c$ , and hence over a certain lattice depth  $s_{c,l}$ , Mott insulator lobes appear for different filling factors  $\bar{n}$ . The inhomogeneity of the system induces the formation of a shell structure with the mechanism reported in the right inset. (b) Density profile of the sample plotted as a function of the distance from the center of the trap and of the total atom number, leading to a different filling factor. Adapted from [112].

$\langle \hat{n} \rangle = 1 + \epsilon$ , even for  $(J/U) < (J/U)_c$  a superfluid component persists and a fraction  $\epsilon$  of atoms moves completely delocalized all over the lattice. If the potential barrier is increased, the system moves along the "grazing" dotted line, which never crosses the MI-SF transition lobe even for  $(J/U) \rightarrow 0$ . In this situation, the system would never enter the insulating phase, since the superfluid fraction would maintain a long

range phase coherence.

Consider now the real system in which a harmonic potential is added to the periodic lattice. In this situation, the density of atoms will no more be uniform all over the lattice, since atoms tend to accumulate in the center of the trap rather than in the external regions. The chemical potential  $\mu$  becomes hence dependent on position, and in particular it reaches the highest value  $\mu(0)$  in the center of the trap, while it rapidly decreases as the distance from the trap center is increased. Since the mean occupation number depend on the density, which is directly related to the chemical potential, the most populated sites will lay in the central region. With the assumption that the external potential is slowly varying on the lattice timescales, anyway, the local chemical potential  $\tilde{\mu} \rightarrow \mu(\mathbf{x}) - \epsilon_j$  is slowly varying and the system behaves locally as in the homogeneous case. The spatial configuration of a Mott insulator in this inhomogeneous case can thus qualitatively be understood with reference to the phase diagram reported in Fig. 2.7(a). Suppose the total atom number sufficient to reach the condition  $\bar{n} = 3$  in the center of the trap. If the potential depth is increased to a value  $s^* > s_c$ , only the portions of the cloud having an appropriate local density (and hence a proper value of the local chemical potential) will enter the Mott insulator phase, while the remaining shells will maintain a superfluid behavior. By increasing the distance from the trap center, the system shows several MI-SF shells with decreasing number of atoms per site, until the density is so low that  $\langle \hat{n} \rangle < 1$  and the last, outer SF shell is formed. Each insulating shell has a vanishing compressibility and as a consequence a constant density. This *wedding cake*-like structure of the density profile is schematically shown in Fig. 2.7(b), where the density of the atomic cloud is plotted as a function of the distance from the trap center and of the total atom number. It is evident that higher numbers of atoms corresponds to higher filling factors, and hence to a bigger number of shells constituting the Mott phase. The effect of increasing the potential is to reduce the extension of the SF shells: the step-like behavior of the density profile becomes sharper and sharper as the lattice height is increased and the tunneling probability reduced. In the limit  $s \rightarrow \infty$  the density is *exactly* constant over each insulating shell and the sample is perfectly incompressible, since no superfluid "pillows" are present.

A last remark on the Mott insulator phase properties. In the former part of this Section we saw how the loss of long range phase coherence represents a clear signature of the the insurgence of the phase transition. Actually, since in optical lattices many processes (see previous Sections of this Chapter) are responsible for a decoherence of the sample, an additional feature of the insulating phase can be exploited

as a textmark of the superfluid-insulator transition. Demanding to any solid state textbook for details on the argument, contrarily to what happens in a superfluid system, in a Mott insulator a gap is predicted to appear in the Bogoljubov excitation spectrum. The gap corresponds to energy of the simplest excitation allowed in the Mott phase, that occurs when a particle is removed from a site and tunneled in to the neighboring one. The energy cost is exactly the interaction energy  $U$ . This gap can be revealed applying a variable potential gradient [8, 100] along one of the lattice beams directions: if atoms are in the Mott insulator state, excitations are created only when the potential gradient equals the energy difference of two neighboring sites, that is  $U$ , giving chance to the pinned atoms in a certain site to tunnel to the next site and to create a particle-hole excitation. This corresponds to the insurgence of a sharp peak in the excitation spectrum, that is on the contrary very broad in the case the sample is in the superfluid regime.

### 2.4.2 Atomic mixtures in optical lattices

In the previous Section we have seen how a BEC trapped in an optical lattice exhibits novel and intriguing features such as the quantum phase transition from superfluid to Mott insulator. Moreover, in the previous Chapter we discovered how the presence of two bosonic interacting species, co-existing in an external confining potential, spans a rich set of configurations depending on the interspecies interaction strength, adjustable through an external magnetic field. It is worth to end this Chapter remarking the importance to have a *heteronuclear* binary system loaded into a periodic optical potential. For these systems, indeed, the richness of the phase diagram opens up a wealth of insightful research guidelines, up to now relatively unwalked, such as the study of the combined superfluidity of two different superfluids, or the determination of the topology of a double Mott insulator system. As an example, a binary system provides an unique tool to build a material lattice of particles and to immerse it into a superfluid sea, with the revolutionary breakthrough constituted by the ability to precisely control the interactions between the material lattice and the superfluid gas. However, since the literature concerning this topic is still debated or far away to give a simple and exhausting description of these systems in terms of experimentally accessible parameters we defer to existing theoretical works for a deeper insight on the double species phase diagram in optical lattices [49, 50, 51, 52, 53].

## *2. ULTRACOLD ATOMS IN OPTICAL LATTICES*

---

# Chapter 3

## The New Machine

In this Chapter I will focus on the experimental apparatus, born in a cold and empty room nearly three years ago, whose design and construction has represented the main work of my PhD thesis. The first year has been devoted to the development of the whole laser sources system, to their frequency stabilization and to the realization of the whole optical system requested to process and deliver the laser beams to the vacuum apparatus in which atoms are trapped and cooled. In this period the main part of the electronics necessary to control the experiment has been mounted and tested. The vacuum system, previously projected and designed with F. Minardi, has been assembled and completed during the second year, together with all the magnetic fields generation system, such as coils or low current drivers. The optical setup surrounding the science cells has been assembled in this period as well, while the magnetic translation scheme, as well as the PC interface to the experiment have been developed in a parallel effort. A novel kind of magnetic trap (called "milli-trap") has been designed and tested during these years.

The system can be schematically pictured as follows: two independent bright atomic sources (2D-MOT) generate atomic beams of  $^{87}\text{Rb}$  and  $^{39}\text{K}$ ,  $^{40}\text{K}$  or  $^{41}\text{K}$  selectively. The laser system is developed to allow a fast switch between the three potassium isotopes, in order to study both Bose-Bose and Fermi-Bose ultracold mixtures. The two cold beams converge in a ultra-high-vacuum (UHV) cell, with large 3D optical access, and feed a multi-specie 3D-MOT, that represents the starting point towards the degeneracy of the mixture. A snapshot of the vacuum system is reported in in Fig. 3.1. The evaporative and sympathetic cooling of the laser cooled atoms takes place in a novel kind of magnetic trap, previously named as *milli-trap* due to its

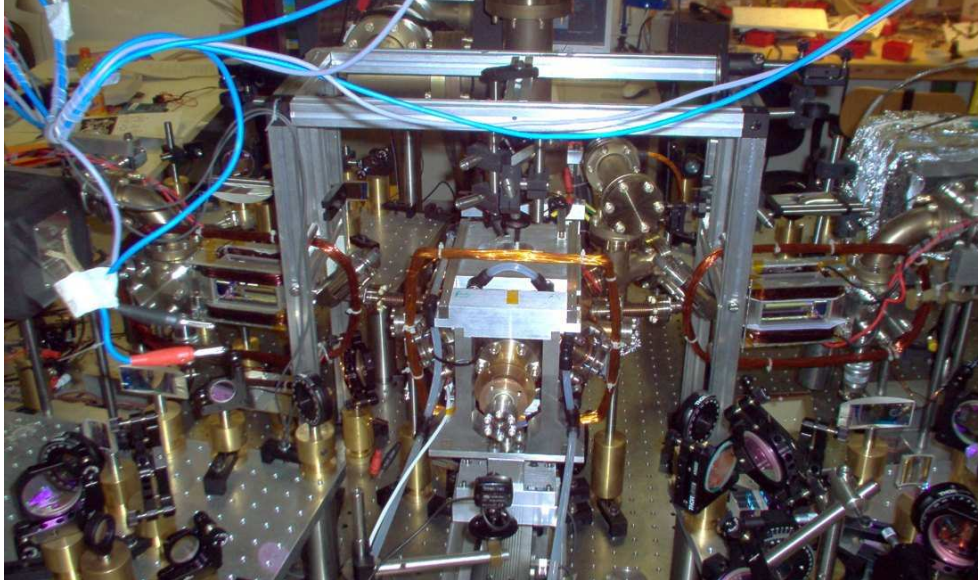


Figure 3.1: Snapshot of the vacuum apparatus and of the optical system surrounding the UHV cell (central zone) and 2D-MOT chambers (left and right sides). The translation stage is visible in front of the central cell. We defer to the text for a detailed description of the apparatus.

reduced extension (Sec. 3.4). The main feature of this trap is to be directly inserted in vacuo, hence requiring only few tenths of watts as current power to deliver the requested magnetic confinement, and to let a conspicuous 3D optical access to the science region. This trap shows the advantages of the tightest magnetic traps, i.e. the micro-chip traps, avoiding at the same time the disadvantages constituted by the non-3D optical access these traps provide. Test and simulations on the milli-trap can be found in Sec. 3.4. Since the 3D-MOT and milli-trap centers are not coincident, the quadrupolar magnetic field coils used to pre-load atoms in a purely magnetic environment after the MOT phase are mounted on a remotely controlled brushless translation stage, whose 3 cm travel connects the "milli-trapping" region to the MOT zone.

## 3.1 The Laser System

The development and experimental achievement of laser cooling and magneto-optical trapping (MOT) techniques, first studied in the '70s and then demonstrated in the late '80s [114, 115, 116, 117, 118] have represented the first feasible doorway to ultra-low energy physics, opening the way to cool dilute atomic samples to temperatures of the order of few recoil temperatures  $T_R = \hbar^2 k^2 / k_B m$  ( $\sim 350$  nK for Rb). The further milestone placed along the road of quantum manipulation of degenerate atomic ensembles is represented by the innovative evaporative cooling technique [119], taking place once atoms have been laser-cooled and held in a purely magnetic trap, thus avoiding all the heating mechanisms induced by the presence of the laser field. This evaporative stage allows a net increase in the density of the sample, whose diluteness would prevent any transition to Bose-Einstein condensate (BEC). The combination of these cooling techniques paved the way towards the reaching of quantum degeneracy in atomic dilute alkali gases, namely to BEC in dilute vapors, which brought to the assignment of the 2001 Nobel Prizes in Physics [1, 2].

### 3.1.1 Potassium and Rubidium: *where's the real difference?*

In Fig. 3.2 the levels diagrams for the bosonic isotopes of Rb and K are shown. As one can see from these diagrams, the level structure is similar for the two elements, since both have nuclear spin  $I=3/2$ . The  $D_2$  line links four hyperfine  $P$  states excited states to two low-lying  $S$  states, and the selection rules, since the angular quantum numbers are the same, are identical. This leads to identical allowed hyperfine transitions for both atoms. The natural linewidth is 6.0 MHz for  $^{87}\text{Rb}$  and 6.2 MHz for K.

The cooling transition used for both atoms is the  $|F = 2\rangle \rightarrow |F' = 3\rangle$ , being the only ideally closed transition present in the  $D_2$  structure. Nevertheless, the presence of a multiplet structure in the lower fine states unhinges the possibility to obtain a working MOT using only one transition: this is due to the fact that the presence of off-resonance contributions  $|F = 2\rangle \rightarrow |F' = 2\rangle$  and  $|F = 2\rangle \rightarrow |F' = 1\rangle$  would readily deplete the starting  $|F = 2\rangle$  level, filling the  $|F = 1\rangle$  ground state. This obstacle can be overwhelmed adding an extra beam tuned slightly below the  $|F = 1\rangle \rightarrow |F' = 2\rangle$  transition, whose purpose is to refill continuously the  $|F = 2\rangle$  level. For this reason this laser light is called *repumping*. Usually, for alkali atoms such as rubidium, the power needed for the repumping transition is much lower than the cooling power, since off-resonant terms give a transition probability some orders of magni-

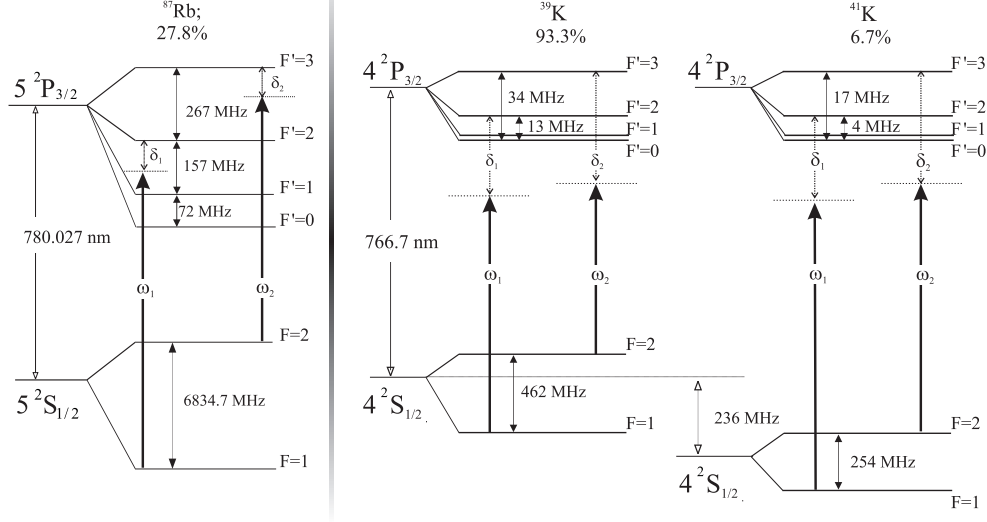


Figure 3.2: Atomic levels diagrams for  $^{87}\text{Rb}$  and K bosonic isotopes. In the upper part natural abundances are reported.  $\delta_1$  and  $\delta_2$  are the frequency detunings relative to repumping and cooling transitions respectively. Figure is not to scale.

tude smaller than the cooling term. The situation is completely different for bosonic potassium, where the tight hyperfine  $4^2\text{P}_{3/2}$  level spacings are comparable to the natural linewidth  $\Gamma$ . In this case, the cooling transition  $|F = 2\rangle \rightarrow |F' = 3\rangle$  is far to be closed since the  $|F' = 1, 2\rangle$  states are excited with similar rates. A fast depletion of the  $|F = 2\rangle$  ground state towards the  $|F = 1\rangle$  ensues, the repumping light needs to be fairly intense and the cooling force arises from both frequencies [120]. Hence, the distinction between cooling and repumping light makes no more sense. However, according to a widespread convention, we call *repumping* and *cooling* the transitions indicated respectively by  $\omega_1$  and  $\omega_2$  in Fig. 3.2. Moreover, while for  $^{87}\text{Rb}$  all the  $\text{D}_2$  hyperfine transitions are separated and clearly distinguishable by means of ordinary saturated absorption spectroscopy, for bosonic potassium the lines connecting one of the two possible starting levels, i.e. the  $4^2\text{S}_{1/2}$   $F = 1$  or  $F = 2$  level, with the tight  $4^2\text{P}_{3/2}$  excited level are melted in a unique broad transition profile, and excited  $F'$  states can be no more distinguished from each other.

This different quantitative structure of potassium makes its cooling really harder and more dependent on fine frequency tuning if compared to that of Rb. The difference, already evident in the study reported in in Ref. [120] for a 3D-MOT, becomes

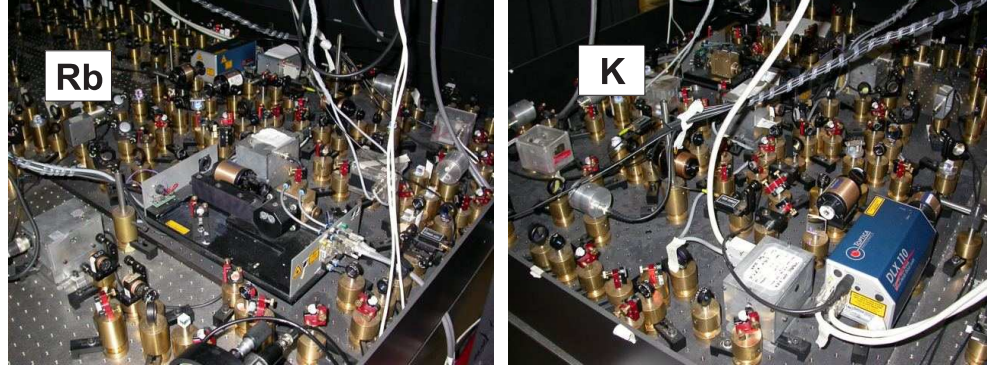


Figure 3.3: Snapshot of laser sources breadboard.

absolutely striking for a 2D-MOT system, realized and characterized for bosonic potassium isotopes for the first time in this thesis work (see Chap. 4).

#### 3.1.2 Laser sources: *lights on!*

The laser sources system has been projected and realized entirely during my first year of Ph.D. thesis. As seen before, we need four different frequencies, two for the rubidium and two for potassium.

##### Rubidium

Both repumping and cooling lights are generated by solid state diode lasers in hand-made external cavity. The radiation coming from a Sanyo DL7140-201 Diode Laser is collimated by a large aperture aspherical collimator (Thorlabs C330TM-B,  $f=3.1$  mm,  $NA=0.68$ ), then sent on a holographic diffraction grating (Edmund NT43-774, 1800 groves/mm) machined for UV radiation. In this Littrow configuration, the -1 order of diffraction is injected back into the diode laser facet with an efficiency below 10% to narrow the emission linewidth. An IR grating would inject too much power back into cavity, hence limiting the output power of the extended cavity and damaging the solid state junction even for current values well within the normal free-running operating range. The large number of groves per mm in the grating gives a high frequency selectivity to the diffracted order. In this way we obtain an output of  $\sim 20$  mW with an estimated linewidth of few hundreds kHz for both repumping and cooling cavities. The wavelength is coarse set by regulating

with a precision screw the angular position of the grating, while the fine tuning is obtained either by moving the current and the grating position by a piezoelectric actuator fixed besides the grating holder. The piezo gives thus the possibility to send a feedback to the cavity and hence to stabilize the laser frequency. While the output power, in the case of Rb, is fully sufficient for the repumping light, the cooling transition light needs to be amplified by means of a commercial Tapered Amplifier (Toptica TA-100), with 0.5 W nominal output power. This device exploits the particular funnel-like structure of a diode junction to enhance the injection light power with gain up to 30 dB, preserving its main spectral features as central emission and linewidth. The output power we obtain is  $\sim 600$  mW.

The frequency stabilization is obtained withdrawing a small fraction of output power directly from the extended cavities and sending it through a temperature controlled absorption cell filled with Rb vapors. For saturation spectroscopy we have chosen the modulation transfer scheme: in this scheme only the pump beam is processed by a double passage Acusto-Optical Modulation (AOM) stage. The frequency shift of the pump beam is  $2\delta$ ,  $\delta$  being the AOM induced frequency shift, while the effective locking point frequency shift is  $\delta$ . The saturated absorption signal is revealed by inversely polarized standard photodiodes, and the signal is processed by a custom lock-in amplifier to obtain a first derivative dispersive signal. A custom proportional-integral servo amplifier (PI controller) then processes the signal, and finally the feedback signal drives directly the piezo actuator to frequency stabilize the cavity.

The cavity output light is locked 168.8 MHz below the  $|F = 2\rangle \rightarrow |F' = 3\rangle$  transition for the cooling radiation, while is locked 77.7 MHz over the  $|F = 1\rangle \rightarrow |F' = 2\rangle$  line for the repumping light.

### Potassium

As shown in the previous Section, potassium bosonic isotopes require a much higher optical power to achieve an effective cooling process. This reason hinders to use, even for repumping light, a commercial diode laser alone to generate the required light. For this reason, in our setup, the repumping light is generated by a commercial Grating Stabilized Tapered Amplifier from Toptica (DLX-110). The first version of this device has been upgraded to the so called RockSolid version, since a high environmental acoustic noise dependence of output beam parameters was found in the former. This device exploits the spontaneous broadband back-emission of a tapered amplifier, diffracting it on a grating and reinjecting the -1 order, such as

### 3.1. The Laser System

	<sup>39</sup> K Reference locking line	Saturation Spectroscopy AOM frequency	Number of Multiple AOM Passages	Multiple Passage AOM frequency
<sup>39</sup> K	$F=2 \rightarrow F'$	- 85.3 MHz	2	161.1 MHz
<sup>41</sup> K	<i>crossover</i>	101.5 MHz	3	182.8 MHz

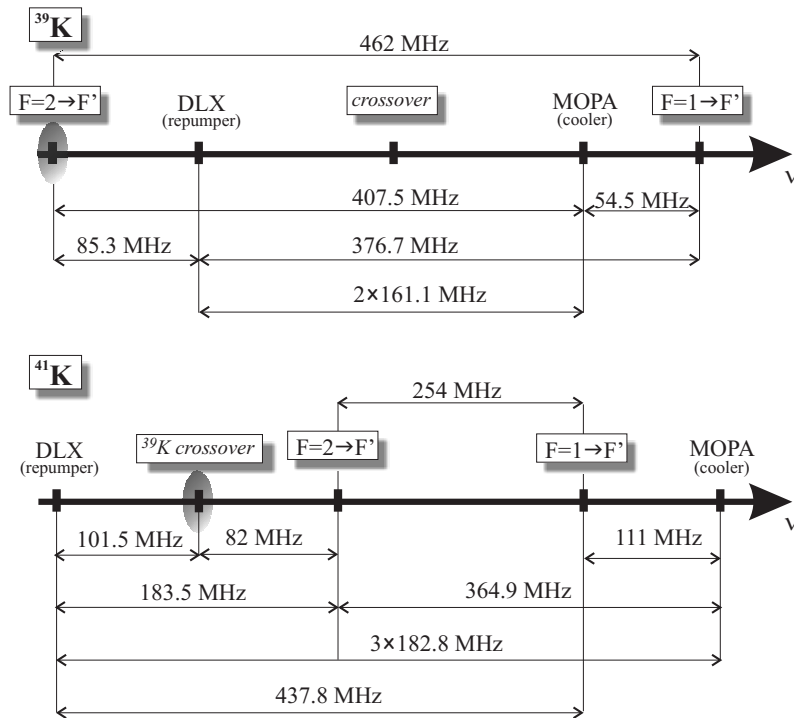


Figure 3.4: Laser frequency locking data and scheme for both <sup>39</sup>K and <sup>41</sup>K . The reference lines are chosen in the <sup>39</sup>K D<sub>2</sub> line spectrum. The gray circles in the figures represent the reference line in the <sup>39</sup>K spectrum.

the standard Littrow configuration does. The radiation is therefore frequency narrowed and is amplified by the chip itself. To reach the lasing region of the cavity, the output facets of these chips should be more reflective than those of common tapered amplifiers. These feature reduces the maximum output power of the chip if com-

pared to the simple tapered amplifier configuration. The DLX can deliver an output power to 550 mW and has 1 MHz linewidth. Part of the output power is withdrawn, processed by a multiple passage AOM stage and injected into a hand-made tapered amplifier. In this way the repumper laser source acts as master oscillator for cooling light as well. The tapered amplifier chip (EagleYard EYP-TPA-0765) is optimized for potassium wavelength of 767 nm, and is capable to deliver, working at a current of 2.5 A, an output power of 1.3 W with a mode-matched 12 mW input. Actually, since the multiple passage AOM stage deteriorates the DLX beam quality (that actually is very poor *ab-initio*,  $M^2 \sim 1.6$ ), the actual value for the TA output power is 900 mW. The copper base supporting the chip has a very good thermal conductivity to flow away the conspicuous dissipation coming from the chip. The input and output collimation stages are identical to those used in the external diode laser cavities, and are solidly glued to the base, without any regulation stage, to avoid any possible drift in time of the beam output characteristics.

The multiple passage AOM stage that shifts the repumping laser main frequency to the right value for the cooling light is suitable for both  $^{39}\text{K}$  and  $^{41}\text{K}$  isotopes, provided the frequency value and the number of passages are changed. The AOMs configuration has been devised with the requirement that no optical components or AOMs need to be replaced or moved to switch between the isotopes. Furthermore, in this novel scheme, only the repumping laser has to be frequency locked, and only one set of stabilization electronics is needed. In Tab. 3.4 frequency locking details for both isotopes are reported. The frequency stabilization is realized exactly as for rubidium, hence through modulation transfer saturated absorption spectroscopy. Both  $^{39}\text{K}$  and  $^{41}\text{K}$  are locked on a  $^{39}\text{K}$  transition, being the most abundant isotope in the natural composition of potassium (see. Fig. 3.2). The locking point, as anticipated before, can be chosen relying only on the  $4^2\text{S}_{1/2} |F = 1, 2\rangle \rightarrow 4^2\text{P}_{3/2}$  mean transitions, being the upper level structure spacing comparable to the linewidth  $\Gamma$ . In Fig. 3.4 details of the laser frequency locking are reported for both  $^{39}\text{K}$  and  $^{41}\text{K}$ .

### 3.1.3 Main Beams Processing and Fibers Launching

The six main beams obtained in this way have still to be split to create the sufficient number of beams for the science cells, and tuned in frequency to reach the right working values, lying between the resonance and some  $\Gamma$  of red detuning depending on the purpose of the single specific beam. This is obtained through a series of 12 double-passage AOM branches (see the picture in Fig. 3.5, 4 for rubidium and 8 for potassium. This system gives both frequency and amplitude remote control

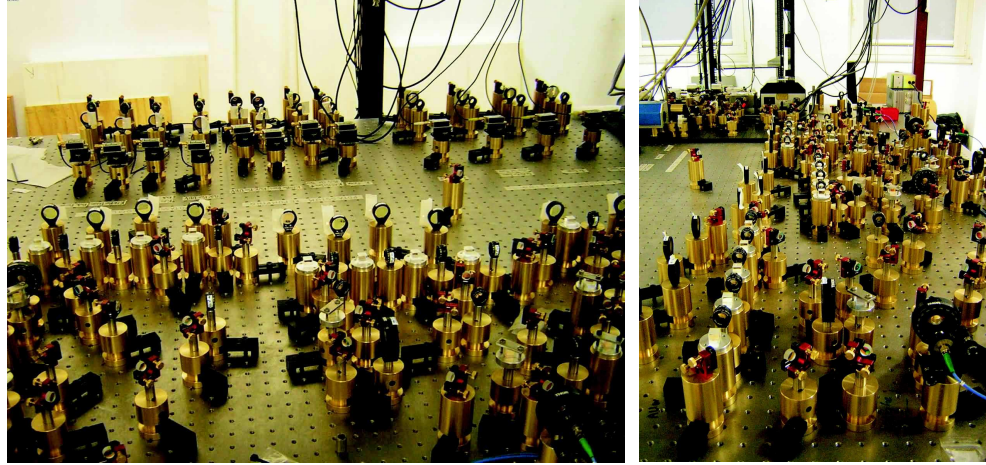


Figure 3.5: Snapshot of AOM branches processing and splitting the six main cooling and repumping beams.

possibility on every beam utilized in the experiment. For Rb we use 80 MHz AOMs (Crystal Technology 3080-122, 1 W RF power), while for K we employ 200 MHz AOMs (Crystal Technology 3200-124, 2 W RF power). All the AOM branches are set in the "cat's-eye" configuration, to reduce any possible deflection of the beam once their frequencies are changed.

Differently from the case of Rb, where the use of the same repumping frequency  $\omega_1$  for 3D and 2D MOTs (see Sec. 3.2.1 and Sec. 3.2.4) is not affecting the quality of the cooling process, the trapping and cooling of K requires a more specific control of the beams frequencies. In particular, the 2D and 3D cooling schemes require different detunings even for repumping light, hence increasing the necessary number of beams. For this reason, the AOMs employed for rubidium are 5, i.e. only one for the repumping beam, while for  $^{39}\text{K}$  and  $^{41}\text{K}$  we have a completely symmetrical situation (4+4) between cooling and repumping AOMs.

Once all beams have been prepared each exiting from an AOM branch, they need to be properly overlapped and mixed with the right polarization to be launched in a fiber system and transferred to the second table. This system is compound by 7 different fibers (OZ Optics PMJ series, core PANDA, 80  $\mu\text{m}$  cladding), and three of them have to bring 4 different frequency components (2 for Rb and 2 for K), maintaining anyway their incoming polarizations. Since every fiber has two specific polarization maintaining axes, i.e. the fast and slow one, this requires to employ particular

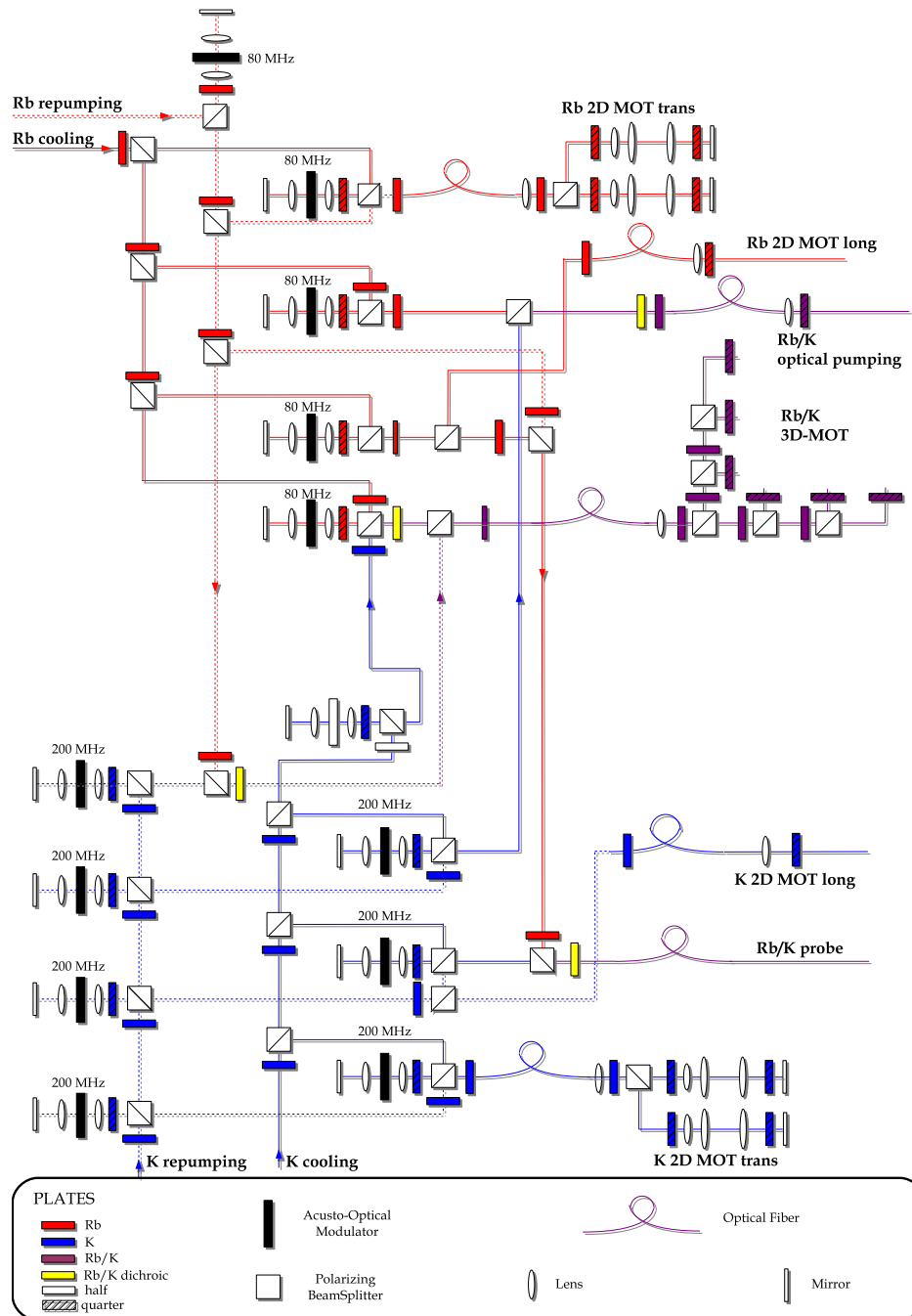


Figure 3.6: Schematics of the optical setup realized during the thesis work. Red lines represent the Rb system, blue lines the K system, while purple ones indicate the mixed frequency (Rb+K) parts.

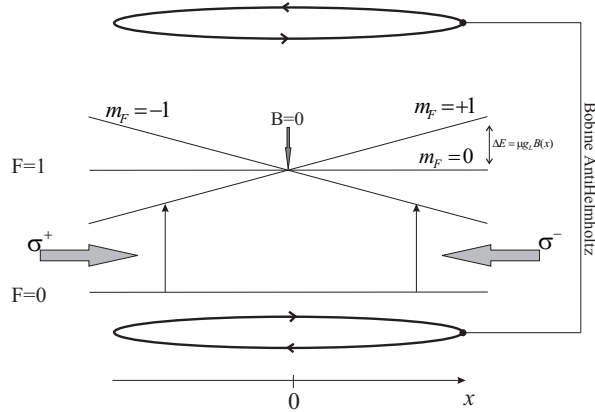


Figure 3.7: Sketch of a 1D-MOT. A two level atom is in the central region, where two anti-Helmholtz coils generate a linear field. Two laser beams with opposite polarization are shone along the horizontal direction.

dichroic polarizing  $\lambda/2$  plates, custom made by LENS-Optics GmbH, with the peculiarity to act only on the 767 component of the light, leaving untouched the Rb beams polarization. Their purpose is more clear with reference to Fig. 3.6, where the schematics of the whole beam splitting optical setup is sketched.

### 3.2 Magneto-Optical Traps

This kind of trap is based on both laser and magnetic fields, whose particular combination gives the net effect to transfer the kinetic energy of room temperature atoms to the electromagnetic field through spontaneous emission processes. The resulting global force acting on an atom moving with velocity  $\mathbf{v}$  at a distance  $|\mathbf{x}|$  from the zero magnetic field point has the form  $\mathbf{F} = -\gamma\mathbf{v} - k\mathbf{x}$ , that is the sum of a dissipative plus a conservative harmonic term. This force has the capability to cool and confine atoms entering the magnetic+laser field region. The working principle of a MOT can be understood considering a two level atom with  $|F = 0\rangle$  ground state and  $|F = 1, m_F = 0, \pm 1\rangle$  excited state, moving away from center of a quadrupolar magnetic field  $B = bx$ . This situation is depicted in Fig. 3.7 for the 1D case. The linear field is commonly obtained using two coils placed in a anti-Helmholtz configuration, so that we can consider with good approximation the field

as linear in the central region. Two counterpropagating red detuned<sup>1</sup> laser beams with opposite polarization are shone in this region along the flight direction. The Zeeman energy shift  $E_Z(x)$  of atomic levels corresponds to zero for the ground state, while is  $E_Z(x) = \mu_B g_F m_F B(x)$  for the excited state sublevels,  $\mu_B$  and  $g_F$  being the Bohr magneton and the upper level Landé factor respectively. In this configuration, an atom leaving the center of the MOT will preferably receive a momentum kick from the laser beam propagating in the opposite direction, since it is red detuned and the selection rules allow the transition towards the downward shifted excited level. This has the effect to reduce the velocity of the atom of an amount  $\hbar k_L/m$ , where  $k_L$  is the wavevector of the laser. If the transition as in our case is closed, many absorption cycles will take place, so that the stochastic photon re-emission processes will average to zero the velocity variations along all the three directions. The velocity of the atom along the  $x$  direction will progressively decrease until the particle will invert its motion. The atom will cross the center of the MOT, and again it will prefer to absorb photons coming from the counterpropagating beam, again slowing down the particle. Due to its dissipative term, the force will drive the atom closer and closer to the center of the MOT with a damped oscillating trajectory, with the net effect to cool and store atoms near the central region of the trap. We can generalize this reasoning to all the three directions, and obtain the stationary state balancing the MOT force with the scattering pressure coming from the re-emission processes involving the other atoms. The typical fluorescence coming from atoms stored in a MOT represents the energy the trap is subtracting to the atomic sample. Typical temperatures of a MOT are of the order of  $100 \mu\text{K}$ , or of the order of a few  $\mu\text{K}$  if the hyperfine structure of the atom allows a strong sub-Doppler cooling process.

The line structure of the atom will obviously influence the behavior and the efficiency of the MOT. In particular, the assumption to work with perfectly closed transitions is hardly adequate for the major part of the employed elements.

### 3.2.1 The 2-Dimensional MOTs (2D-MOTs)

Our set-up is designed to generate independently two bright cold atomic beams of  $^{87}\text{Rb}$  and  $^{39}\text{K}$  (or  $^{41}\text{K}$ ), both exploiting a 2-dimensional trapping and cooling scheme. In the last years, two-dimensional magneto-optical traps (2D-MOTs) of  $^{87}\text{Rb}$  have been investigated by several groups [121, 122]. While this technique is well established in the case of  $^{87}\text{Rb}$ , an extensive study of a 2D cooling scheme in

<sup>1</sup>Hereinafter we will use the convention to call *red* detuned a radiation if  $\omega_{rad} < \omega_0$ , the latter being the resonance frequency of the considered atom.

the case of K was not present before this thesis work was completed.

An intense and reliable source of cold atoms represents a favorable starting point for every degenerate mixture experiment, but since ultracold atomic samples lifetimes are really dependent on the background gas pressure, a single 3D-MOT system directly loaded from background vapor pressure does not represent an optimal environment to reach degeneration of atoms. A net improvement is obtained if an extra 3D-MOT is added in a ultra-high-vacuum (UHV) region of the apparatus, connected to the high pressure zone by a narrow pipe with limited conductance. If a beam, usually called *push beam*, is properly shone along the line connecting the high-pressure to the low-pressure 3D-MOT centers, a high flux of cold atoms can be extracted from the former and driven to feed the UHV 3D-MOT without increasing the low background pressure, provided the small pipe and the pumping system are able to maintain a good differential vacuum between the two regions. Ordinary BEC experiments are based on such double 3D-MOT system [123], where the first high pressure MOT has the only function to load a second UHV MOT. Anyway, this 3D-3D loading scheme generates typical atomic fluxes of  $10^7 \div 10^8$  atoms/s, and several tens of seconds are required to load the second MOT to a typical size of  $10^9$  atoms. On the other hand, 2D-MOTs represent one of the brightest sources of slow atoms, providing fluxes up to  $10^{10}$  atoms/s for  $^{87}\text{Rb}$ . Since the 2D-MOT scheme provides high atomic flux through a small aperture between the two chambers, it appears perfectly suited for loading an ordinary 3D-MOT in UHV environment. This motivation led us to choose 2D-MOTs as atomic sources for our apparatus.

#### 3.2.2 Principle of operation: *only the coolest!*

The 2-dimensional trapping and cooling mechanism follows the same guidelines of the 3-dimensional scheme. To understand qualitatively the behavior of a 2D-MOT (see Chap. 4 for a more quantitative description), let's consider a standard 3D-MOT, and suppose to remove one of the three counterpropagating beams pairs, say the one lying along the  $z$  direction. In this situation, no cooling mechanism is present along the free  $z$  direction. Thermal atoms will therefore maintain their initial velocity  $v_T$  along this direction (densities in an ordinary MOT are not sufficient to give reasonable cross-dimensional thermalization rates), and after a certain time  $t_c$  (strictly depending on the velocity class they belong to and hence on  $v_T$ ) they will escape from the volume, since the MOT magnetic gradient (usually  $\sim 10$  G/cm) is too shallow to confine room temperature particles. Atoms entering the beams region will be cooled along the  $xy$  plane exactly for a time  $t_c$ . Let's now imagine to stretch the

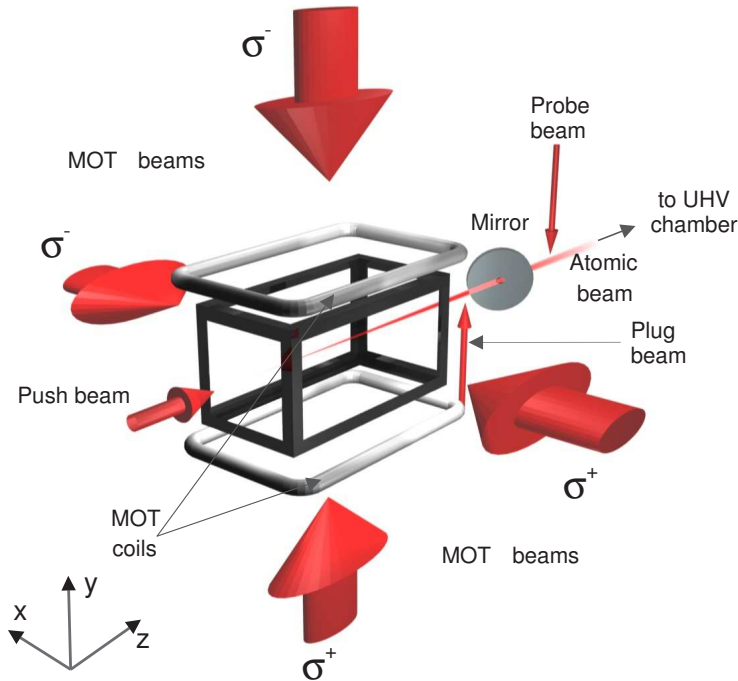


Figure 3.8: Schematics of the 2D-MOT system designed to provide bright atomic fluxes for both Rb and bosonic K in our experiment.

MOT beams and the quadrupole field along the  $z$  direction, and to place at a certain distance on the  $z$  axis a small diaphragm with diameter  $d$ . Atoms entering the MOT region will now be cooled along the  $xy$  plane for a time  $t'_c < t_c$ , and will fly towards the diaphragm with velocity  $v_T$  and residual transverse velocity spread  $\sigma_{xy}$ . The only atoms flying through the diaphragm will be the ones whose velocity  $v_T$  is so small to give them a sufficient cooling time  $t_c$  to reduce the transverse spread, in such a way their extension will be smaller than the hole diameter  $d$ . Strictly speaking, for this reason a 2D-MOT acts like a *temperature reducer* along the  $xy$  plane, and only as a *velocity selector* along the  $z$  direction, allowing only the coolest atoms to pass through the small aperture.

### 3.2.3 Our 2D-MOTs

In our system the 2D-MOT chambers for K and Rb are perfectly identical, and, if not specified otherwise, we will hereafter describe the common details of the two

2D systems. The 2D-MOT set-up is schematically reported in Fig. 3.8. Four rectangular  $80 \times 35$  mm BK7 antireflection coated windows, providing optical access to the four transverse trapping beams, are glued on a metallic rectangular frame, machined from a titanium block. The bi-component epoxy glue (Aremco 631C) is a commercial product, specially designed to be employed in UHV environment, whose thermal expansion coefficient is very similar to the coefficient of the BK7 glass. For the chamber structure, titanium was preferred over stainless steel for its lower thermal expansion coefficient, closer to the value of BK7 glass [124]. This is devised to avoid as far as possible any mechanical stress on the glass windows. If mechanical stresses are present, heavy vacuum losses would be induced even for small temperature variations. The rear part of the chamber is designed to hold five standard CF-35 flanges, to connect the ion pumps (Varian Diode Cell 20 l/s, one per chamber), the current feedthrough for dispensers (see below) and a glass window to give optical access along the longitudinal  $z$  direction. The atomic vapor is released in natural abundance for both Rb and K by dispensers (SAES Getters), whose regulated injection current controls the pressure in the 2D-MOT chambers from vapor pressure up to some  $10^{-7}$  mbar (see Sec. 4.1.3). In the actual working regime, dispensers operate in DC mode and, especially for Rb, the stabilization of the pressure is reached only after a quite long period ( $\sim 1$  h) from the initial ignition. This is due to a non negligible heating of the vacuum system part surrounding the dispensers current feedthrough, leading to a vapor outgassing from the chamber walls that increases with the dispensers temperature. Better stabilization would be obtained by stabilizing the chamber walls temperature as well. For this reason our 2D-MOT loading regime can be defined as *combined*, since atoms entering the cooling region are fed both by the dispensers and the outgassing from overheated chamber walls. The front part of the chamber is equipped via a CF-16 connection providing access to the UHV region.

Two pairs of retroreflected laser beams with  $\sigma$  polarization are shone orthogonally on atoms along the  $x$  and  $y$  directions, and intersect in the center of the cell. The shape of the beams is elliptic with a 3:1 aspect ratio. This is realized through a pair of confocal cylindrical lenses ( $f=-50$  mm and  $+150$  mm respectively), which stretches the beam waist along the horizontal direction of a factor 3, leaving untouched the vertical waist, starting from a standard 1" optics aperture limited beams set. The retroreflection is done after a  $\lambda/4$  waveplate to reverse the backpropagating beam polarization in order to fulfil the proper MOT cooling scheme (see Sec. 3.2.2).

The magnetic quadrupole field is obtained through a pair of anti-Helmholtz rectangular coils, surrounding the protruding edges of glass windows, wired by em-

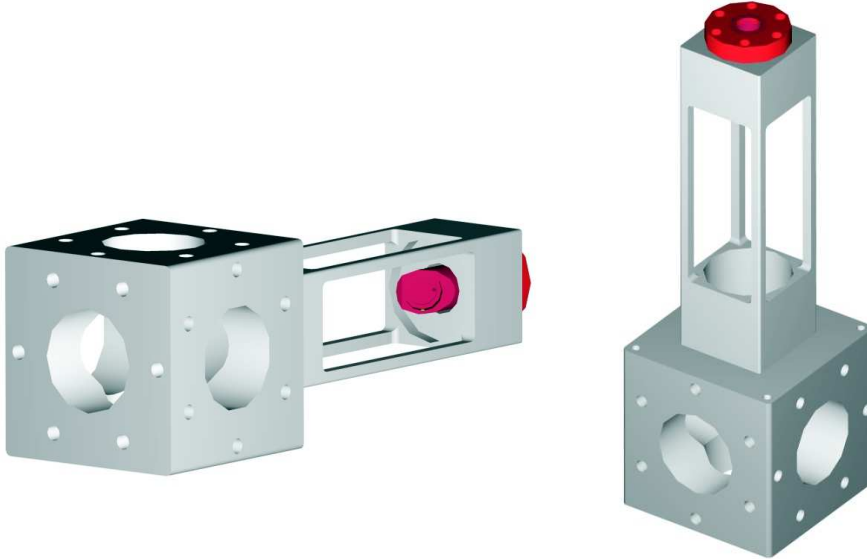


Figure 3.9: Sketch of the main titanium structure constituting the 2D-MOT chamber. The red part represents the hollow mirror housing and the CF-16 connection to the UHV chamber.

ploying a  $1\text{ mm} \times 3\text{ mm}$  copper wire and gluing the loops on an aluminum support directly fixed on the vacuum system. This shape gives a cylindrical symmetry along the  $z$  axis to the magnetic field, required by the 2D-MOT scheme. The currents on each coil are independently regulated by linear current generators (CEP 03LD15B), so that they can be unbalanced to match the vertical alignment of the quadrupole field with the laser field. This current balance is found to be very critical for the optimization of the flux: current drifts of the order of  $\sim 5\%$  can heavily deplete the atomic beam especially in the case of potassium. The typical transversal magnetic gradient is  $\sim 17\text{ G/cm}$  for a  $5\text{ A}$  current, while the longitudinal gradient is ten times smaller and will be neglected in the following. Coils are air cooled.

The atomic flux obtained using a 2D-MOT can be heavily enhanced if a proper laser beam is shone through the rear glass windows along the  $z$  direction towards the UHV region (see Sec. 4.1.4). This laser beam, whose waist is  $1.5\text{ mm}$ , is called *push beam*.

A metallic mirror, tilted  $45^\circ$  with respect to the longitudinal axis, is placed near the end of the 2D-MOT chamber and close to CF-16 exit tube. A  $1\text{ mm}$  hole is drilled

at the center of the mirror to let the atoms exit the 2D-MOT chamber. This mirror allows us to send a hollow beam along the  $z$  direction, counterpropagating with respect to the atoms and obtained simply inserting a horizontal beam from a side window, so that, if necessary, we can turn to a 2D<sup>+</sup>-MOT configuration [121]. Actually, as explained later, we found convenient not to shine this hollow beam, since no particular flux enhancement is observed when the beam is on. The mirror is machined polishing a simple stainless steel disk. The reflectivity of the mirror is  $\sim 0.5$  at  $\lambda=780$  nm. The small hole in the mirror, then, acts as a diaphragm for atoms, necessary to give thermal selectivity along the  $z$  direction to the 2D-MOT system. Again, the hollow mirror has the fundamental purpose to reduce the conductance of the connection between the 2D and UHV chambers, so that an efficient differential pumping scheme can be established (see Sec. 3.2.4). A vertical resonant laser beam (*plug beam*) is shone in front of the hole when the atomic flux has to be shuttered, e.g. when time-of-flight tests on the 2D-MOTs are performed (Sec. 4.1.1).

The 2D and UHV chambers are connected via a 10 cm long flexible stainless steel CF-16 bellow, whose main purpose is to absorb the mechanical stresses between the chambers. In order to increase the differential pumping ratio, inside the bellow are placed three graphite tubes of increasing inner diameter (6-8-10 mm respectively). Their diameters are chosen as the smallest still not limiting the solid angle defined by the center of the 2D-MOT and the hole in the metallic mirror. An in-line valve (Meca2000) is inserted to physically separate, in case of partial bake-out of the vacuum system, the 2D and UHV regions.

#### 3.2.4 The 3D-MOT and the UHV chamber

The 3D-MOT is realized in a steel chamber designed to give a large optical access all over the three directions for MOT, imaging and optical dipole traps beams. The height of the chamber is 90 mm, while its outer diameter is 180 mm. The schematic drawing is reported in Fig. 3.10. The main horizontal viewports are antireflection coated glass windows with a clear diameter of 130 mm, allowing for vertical MOT beams and vertical high resolution imaging beam. The vertical MOT windows are held by standard CF-35 flanges and have a clear aperture of more than 1". Two additional CF-35 flanges are placed along the symmetry axis of the cell. One of them connects the UHV region to a 55 l/s ion and to a Ti sublimation pump, leaving a longitudinal wide optical access. The other one is used to insert and hold the milli-trap system (see. Sec. 3.4), providing at the same time optical access along the longitudinal direction, which is used to shine horizontal imaging and dipole trap beams. The

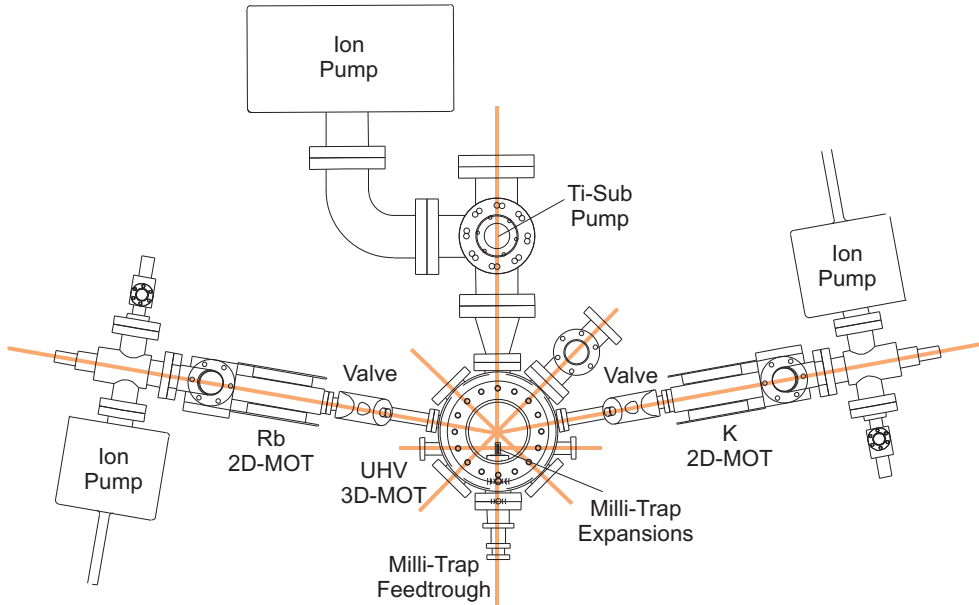


Figure 3.10: Schematics of the vacuum apparatus (top view). In the center there is the large optical access UHV cell in which the combined 3D-MOT is generated. The expansions of the milli-trap are visible in the lower part of the UHV cell. On opposite sides two independent 2D-MOT chambers for Rb (left) and K (right) are shown, together with their connections to the central chamber. The shaded areas represent the optical accesses through the UHV chamber. Vertical beams and the magnetic translation stage are not shown.

MOT and magnetic trap centers are displaced by 25 mm, in such a way the milli-trap expansions don't interfere with the horizontal MOT beams. For this reason, either the horizontal transverse lattice beams, shone through two additional CF-16 windows, and the vertical imaging beam are displaced from the center of the chamber to intersect the atom cloud in the center of the milli-trap. This is the reason for the very large diameter of the horizontal viewports.

The magnetic field for the MOT (see. Sec. 3.5) is generated by means of a pair of copper wired coils (wire section  $1 \text{ mm} \times 3 \text{ mm}$ ), fixed on an aluminium water-cooled plain heatsink, with a 65 mm radius and a 40 mm clear aperture to provide vertical optical access to the chamber (see Fig. 3.19). This structure can be smoothly moved towards the milli-trap and hence gives the capability to magnetically transport the atoms from the MOT to the magnetic trap. The vertical magnetic gradient is

### 3.3. Purely Magnetic Trapping: lights off!

	Cooling Beams		Repumping Beams		Number of Atoms
	Detuning $\delta_2$ [ $\Gamma$ ]	Power [mW]	Detuning $\delta_1$ [ $\Gamma$ ]	Power [mW]	
<sup>87</sup> Rb	- 2.8	40	- 0.5	6.0	$3 \times 10^9$
<sup>39</sup> K	- 3.0	45	- 7.5	23	$1 \times 10^7$
<sup>41</sup> K	- 1.0	43	- 4.0	22	$3 \times 10^6$

Table 3.1: Experimental parameters optimizing the 3D-MOT for <sup>87</sup>Rb and both bosonic isotopes of K

$\sim 15$  G/cm for a 4 A current.

The MOT beams, contrarily to the 2D-MOT case, are not retroreflected: to reach a finer optimization, in the 3D case we split the main cooling and repumping beams in six beams whose polarization can be independently controlled by  $\lambda/4$  waveplates. The four frequencies for Rb and K, as said before, are brought to the UHV chamber by the same fiber, and consequently split by the same optical elements. This method gives a practically perfect alignment between the Rb and K beams, hence simplifying the task of overlapping the cold atomic clouds in the MOT. The fine overlapping of the MOTs is obtained regulating the micrometric waveplate rotators acting on the UHV beam splitting system (see Fig. 3.6). In this way one can exactly overlap the two MOTs slightly unbalancing the relative intensity of the beams. Table 3.1 summarizes the optimal parameters found for <sup>87</sup>Rb, <sup>39</sup>K and <sup>41</sup>K 3D-MOT, and the typical number of atoms. Detunings  $\delta_1$  and  $\delta_2$  (see Fig. 3.2) are expressed in units of linewidth  $\Gamma$ .

The presence of external fields like the magnetic field of the earth is balanced by three set of remotely controlled Helmholtz-like coils, called *shim* coils, giving a uniform field near the center of the UHV cell.

### 3.3 Purely Magnetic Trapping: *lights off!*

After the pre-cooling MOT stage, where temperatures of the order of 100  $\mu$ K are reached, atoms have still to gain a factor  $10^8$  in their phase-space density to reach quantum degeneration. A way to avoid the heating of the atomic sample natu-

rally induced by multiple light scattering is to load atoms in a purely magnetic trap, where no atom-photon processes take place. Lifetimes of magnetic traps are generally very long, and this is a fundamental requirement for a final evaporative cooling phase. The magnetic trapping of an atomic sample was firstly demonstrated for a Zeeman-slowed sodium beam [125]. This trapping technique relies on the position-dependent Zeeman magnetic shift induced on atoms by an inhomogeneous magnetic  $\mathbf{B}(\mathbf{r})$  field. If the field variations felt by an atom are slower than the Larmor precession time, i.e. if

$$\frac{1}{B} \left| \frac{dB}{dt} \right| \ll \frac{\mu_B B}{\hbar} = \omega_L, \quad (3.1)$$

the magnetic dipole of the atom will adiabatically align to the field, and the magnetic interaction energy can be written as:

$$U(\mathbf{r}) = -\boldsymbol{\mu} \cdot \mathbf{B}(\mathbf{r}) = \mu_B m_F g_F |\mathbf{B}(\mathbf{r})|, \quad (3.2)$$

where  $\mu_B$  is the Bohr magneton,  $|F, m_F\rangle$  is the hyperfine atomic state and  $g_F$  is the hyperfine Landé factor. As a first consequence, atomic states for which the product  $m_F g_F$  is positive are "low-field seeking", and hence will be trapped in a minimum of the external magnetic field. Before loading a magnetic trap, atoms are optically pumped into the specific sublevel by a short light pulse with a specific  $\sigma$  polarization.

The simplest B field configuration having the capability to confine atoms is the quadrupole configuration, obtained, as explained in Sec. 3.2, using the two MOT coils. As we will see below, anyway, this field doesn't allow the degeneration of the sample, since it is completely inadequate to hold atoms at very low temperatures.

To circumvent this problem, a widely used magnetic trap configuration is the Ioffe-Pritchard one [126, 127], where a harmonic potential is generated near the center of the coils system. Beyond the quadratic dependence of the field on position, the IP configuration mainly differs from the quadrupolar one by the presence of an overall bias field  $B_0$  preventing Majorana spin-flip induced trap losses (see next Section). Lots of different conductors arrangements (QUIC [128], cloverleaf [129], baseball [130]) provide the same IP field near the center of the trap. In our system, this IP configuration is obtained by means of the novel milli-trap system described in Sec. 3.4.

### 3.3.1 The quadrupole field

For small distances  $x$  from the center of the system, where the field has zero value, this configuration gives a linear behavior of the B field along the three directions,

### 3.3. Purely Magnetic Trapping: lights off!

---

$\mathbf{B}(x, y, z) = b(\mathbf{x} + \mathbf{y} - 2\mathbf{z})$ . The trapping potential results:

$$U_Q(x, y, z) = \mu_B m_F g_F b \sqrt{x^2 + y^2 + 4z^2}. \quad (3.3)$$

The main disadvantage of this kind of trap is the presence of a zero in the field for  $x = 0$ , where the Larmor frequency  $\omega_L$  diverges and the adiabaticity condition (3.1) is not fulfilled. This leads to a high trap losses rate due to Majorana spin-flips [131], exponentially increasing as temperature decreases, and hinders the creation of ultracold samples directly in a quadrupole trap. On the other hand, an intense quadrupole field can be obtained simply using the MOT two-coils set, and gives a simple way to compress the atomic cloud cooled in the MOT to match the magnetic trap size where the evaporation will take place. Indeed, the extension of a MOT for a given temperature  $T$ , a given magnetic field gradient  $\nabla B$  and a certain number of atoms  $N$  can be really different from that of a magnetic trap. In our case, the typical size of the MOT is  $\sim 1$  mm, while in the same conditions the milli-trap potential has an extension of  $10 \times 100 \mu\text{m}$ . These different extensions can be matched by an appropriate quadrupole compression before inserting the atoms into the milli-trap (see below). The quadrupole current matching our 3D-MOT dimensions can be estimated equating the measured size of the MOT to the theoretical RMS width of the cloud trapped in a quadrupolar field:

$$\sigma_Q^2(T) = \frac{\int \mathbf{x}^2 \exp[-\beta(\frac{\mathbf{p}^2}{2m} + U_Q(\mathbf{x}))] d^3 \mathbf{p} d^3 \mathbf{x}}{\int \exp[-\beta(\frac{\mathbf{p}^2}{2m} + U_Q(\mathbf{x}))] d^3 \mathbf{p} d^3 \mathbf{x}}, \quad (3.4)$$

where we used the expression (3.3) for the magnetic energy. Factorizing the  $\mathbf{p}$  dependent terms we obtain:

$$\sigma_Q^2(T) = \frac{\int \mathbf{x}^2 \exp[-\beta(\mu_B m_F g_F b \sqrt{x^2 + y^2 + 4z^2})] d^3 \mathbf{x}}{\int \exp[-\beta(\mu_B m_F g_F b \sqrt{x^2 + y^2 + 4z^2})] d^3 \mathbf{x}}. \quad (3.5)$$

From an analytical evaluation of this expression we obtain

$$\sigma_Q^2(T) = \frac{4(kT)^2}{(\mu_B m_F g_F)^2 b^2}. \quad (3.6)$$

This expression gives the possibility to estimate the matching current, that in our experimental conditions is found to be 20 A. After the MOT phase, hence, a current *boost* (see next Section) raises the current from 4 (MOT value) to 20 A, in such a way the atomic cloud is transferred into the quadrupolar field without heating. A 500 ms adiabatic ramp, then, brings the quadrupole current to 65 A, compressing the

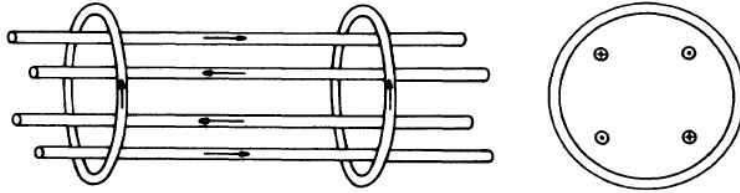


Figure 3.11: Schematic drawing of the Ioffe-Pritchard trap scheme. Four bars are generating the quadrupolar field, while the two coils give a bias field.

sample to reduce again its extension before transferring the sample into the milli-trap. The field has a cylindrical symmetry along coils axis, and the vertical gradient is 260 G/cm, while the horizontal is 130 G/cm.

Even though no BEC degeneration can take place in a purely quadrupolar magnetic trap, this kind of potential can be used to match the transfer of atoms from the MOT to the milli-trap and to obtain an efficient magnetic transport scheme (Sec. 3.5.3).

### 3.4 The Milli-Trap

This novel trapping geometry, that is a direct evolution of the one presented in [132], substantially mimics a Ioffe-Pritchard field configuration. Extensive tests on this trap are reported in this Section.

The core of this device (Fig. 3.12) is machined out of an oxygen-free copper cylinder (9.0 mm external diameter and 17.0 mm height). Along the  $z$  axis a 5 mm clear hole is drilled to provide longitudinal optical access, while four 45° radial slits give radial optical access to the center of the structure and create the characteristic four lateral quadrupole bars, typical of a Ioffe-type trap. Both ends of the trap have a semicircular shape to provide an overall bias field  $B_0$ , mimicking the function of the two Helmholtz coils of Fig. 3.11. The upper part of the milli-trap is bound by a particular brazing procedure to 300  $\mu\text{m}$  thick copper routes etched on a ceramic chip. A 4 mm diameter hole in the center of the chip provides longitudinal optical access to the trapping region. The negative pole of the chip is in electrical contact from the rear side with a copper tube. The positive pole of the trap is connected to the external power supply by a copper via inserted into the chip and brazed to

### 3.4. The Milli-Trap

---

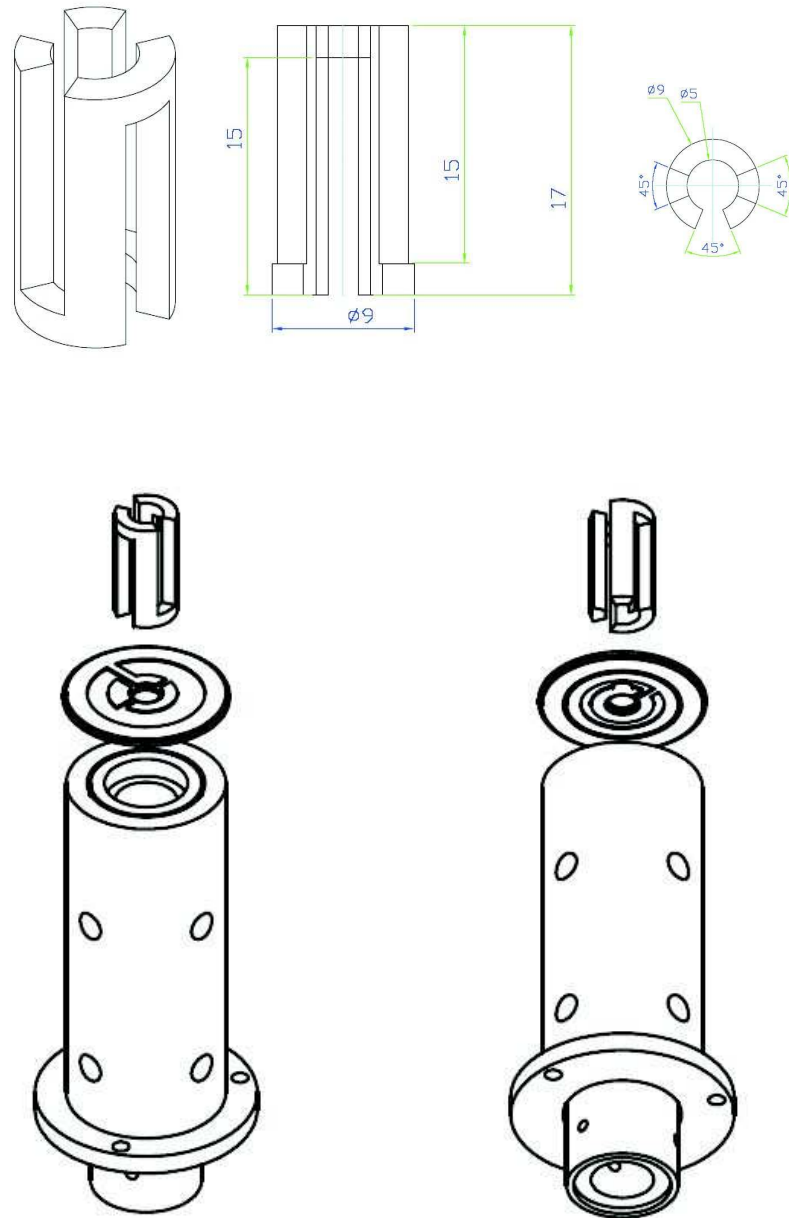


Figure 3.12: Schematic drawing of the milli-trap inserted in our system.

the base of another copper tube, coaxially inserted inside the first. Both tubes are welded to vacuum connections by a Kovar-ceramic soldering. The inner copper tube is holding a CF-16 glass viewport, while the outer is fixed to a CF-35 flange blocking the entire trapping system to the vacuum apparatus. Current is fed wiring the copper terminals exiting from the vacuum system. The impedance of the milli-trap expansions is 1.5 mΩ, while the impedance of the whole electrical circuit is 40 mΩ. For a 95 A working current, the required power is less than 400 W, mainly sinking on connection cables and MOSFETs, and not directly on the in-vacuo parts. This is a fundamental feature of the milli-trap system, since ordinary off-vacuum magnetic traps require 1÷5 kW as standard driving power to obtain the same confining strength (see below).

The intrinsic bias field  $B_0$  can be adjusted by controlling the current intensity flowing in an external *bias coil*, generating a longitudinal uniform field  $B'_0$ . This bias coil is a 90 loops square coil with a side length of 25 cm, and is orthogonal to the  $z$  axis, placed 4 cm away from the center of the trap.

The magnetic field generated in the central region of the milli-trap has the Ioffe form and can be expanded to the second order of multipoles in cylindrical coordinates:

$$|B(z, \rho)|^2 = \left( (B_0 + B'_0) + \frac{1}{2} B_2 z^2 \right)^2 + (B_1 \rho)^2, \quad (3.7)$$

where  $B'_0$  is the bias coil uniform field,  $B_1$  and  $B_2$  are the first and second order terms of multipoles expansion, and  $B_0$  is the intrinsic bias field of the trap for  $r=0$ .  $B_0$ ,  $B_1$  and  $B_2$  depend on the current  $I$ . For

$$z^2 \ll 2 \left( \frac{B_0 + B'_0}{B_2} \right) \quad \rho^2 \ll \left( \frac{B_0 + B'_0}{B_1} \right)^2 \quad (3.8)$$

the trap field is harmonic and has cylindrical symmetry:

$$|B(z, \rho)| = (B_0 + B'_0) + \left( \frac{B_2}{2} \right) z^2 + \left( \frac{B_1^2}{2(B_0 + B'_0)} \right) \rho^2. \quad (3.9)$$

Near the center, hence, atoms will follow oscillatory trajectories with the frequencies

$$\omega_z^2 = \mu_B m_F g_F \frac{B_2}{m}, \quad \omega_\perp^2 = \mu_B m_F g_F \frac{B_1^2}{(B_0 + B'_0)m}, \quad (3.10)$$

where  $\omega_z$  and  $\omega_\perp$  are the axial and radial frequencies respectively, and  $m$  is the mass of the atom. Since  $m_{\text{Rb}} = \frac{87}{39} m_{\text{K}}$ , the frequencies for  $^{39}\text{K}$  can be obtained directly rescaling the frequencies for Rb:

$$\omega_{\text{K}} = \sqrt{\frac{87}{39}} \omega_{\text{Rb}}, \quad (3.11)$$

### 3.4. The Milli-Trap

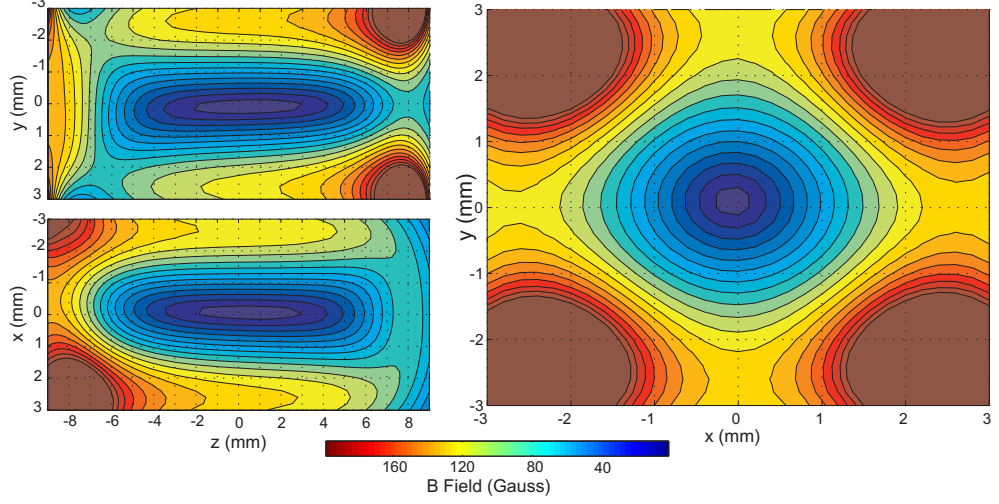


Figure 3.13: Milli-trap magnetic field simulations along the three axis for a current of 100 A. The field represents the intrinsic field, without the contribution of the additional bias coils.

and vice-versa. If not specified otherwise, we will hereinafter refer to Rb trapping frequencies.

As we can see from (3.10), the axial frequency depends only on the milli-trap design and current, while the radial frequency can be conspicuously increased varying  $B'_0$  via the the bias coil: virtually, in the situation  $B_0 = -B'_0$  the radial frequency diverges, while the axial frequency is not affected. Recently an additional 6 loops square coil was inserted in series to the milli-trap circuit to reduce the high intrinsic bias field  $B_0$  from 18 to 7.9 G for a 95 A working current, in such a way the bias field can be varied by the bias coil from few mG to 15 G. For a typical bias field of 2 G we have

$$\begin{aligned}\omega_z &\simeq 2\pi \times 19.6 \text{ Hz} \\ \omega_{\perp} &\simeq 2\pi \times 497 \text{ Hz}\end{aligned}\tag{3.12}$$

for Rb atoms in the  $|F = 2, m_F = 2\rangle$  state.

To find the extension of the harmonic trapping region, we can insert these frequency values in (3.10) and extract the corresponding values  $B_1 = 552 \text{ G/cm}$  and  $B_2 = 237 \text{ G/cm}^2$ . From these values, having as first approximation the physical meaning of *gradient* and *curvature* of the induction field, we rewrite the harmonic

limit (3.8) to obtain

$$z_{ho} \lesssim 1.5 \text{ mm} \quad \rho_{ho} \lesssim 40 \text{ } \mu\text{m}, \quad (3.13)$$

which gives a mean harmonic extension  $\sigma_{ho} = (z_{ho}\rho_{ho}^2)^{1/3} = 135 \text{ } \mu\text{m}$ . A fundamental parameter is the limit temperature above which atoms start to feel anharmonic contributions coming from higher order terms in the multipole expansion (3.7) [133]. Given a certain temperature  $T$  the Maxwell-Boltzmann distribution width for atoms trapped in a harmonic potential can be evaluated using the energetic equipartition theorem:

$$\sigma^2(T) = \frac{k_B T}{m (\omega_z \omega_{\perp}^2)^{2/3}}, \quad (3.14)$$

where we exploited the cylindrical symmetry to evaluate the mean 3D oscillator frequency  $\omega_{ho} = (\omega_x \omega_y \omega_z)^{1/3}$ . Now, only atoms having  $\sigma(T) \lesssim \sigma_{ho}$  will respect the harmonic approximation (3.10) and move in the harmonic region of the potential. In the case of  $^{87}\text{Rb}$ , this gives a related upper limit on the temperature of atoms of  $T \lesssim 150 \text{ } \mu\text{K}$ . Atoms trapped at higher temperature will feel a more complex potential that can be as first approximation taken as quadrupolar. Numerical simulations on the milli-trap field corresponding for a current  $I = 100 \text{ A}$  are displayed in Fig. 3.13. The graphs show orthogonal 2D sections along the three planes of the estimated intrinsic field generated by the milli-trap, when no contributions arising from the bias coils are present. The ceramic chip is on the left side of the  $xz$  and  $yz$  contour plots. The trap depth is defined as the difference between the magnetic field value at its lowest saddle point and the intrinsic bias  $B_0$ . From Fig. 3.13 we can extract a trap depth of 86 G, set by a the saddle point generated in the center of the two half-rings connecting the end of the four Ioffe bars. At the opposite end of the trap another saddle point arises, laying anyway at a higher field due to the closeness of the bias copper route etched on the ceramic chip. The cylindrical asymmetries in the magnetic field shape come mainly from the asymmetries in the rear side Ioffe half loops, that shifts the center of the trap from the  $z$  axis by  $\sim 0.1 \text{ mm}$ . The expected cylindrical symmetry, anyway, is not corrupted near the center of the trap.

The trap depth sets the maximum temperature allowed for atoms to be trapped by the device. Indeed, atoms are trapped until their thermal energy is lower than the maximum potential energy  $U_B$ . The critical temperature, obtained imposing  $k_B T_{\mu} \sim U_B$ , is:

$$T_{\mu} \sim 67 \times m_F g_F |B[\text{G}]| \text{ } \mu\text{K}, \quad (3.15)$$

and hence atoms in the  $|F = 2, m_F = 2\rangle$  state are trapped until their temperature is lower than  $\sim 6 \text{ mK}$ . This trap depth is 5 times higher than the temperature of atoms

### 3.4. The Milli-Trap

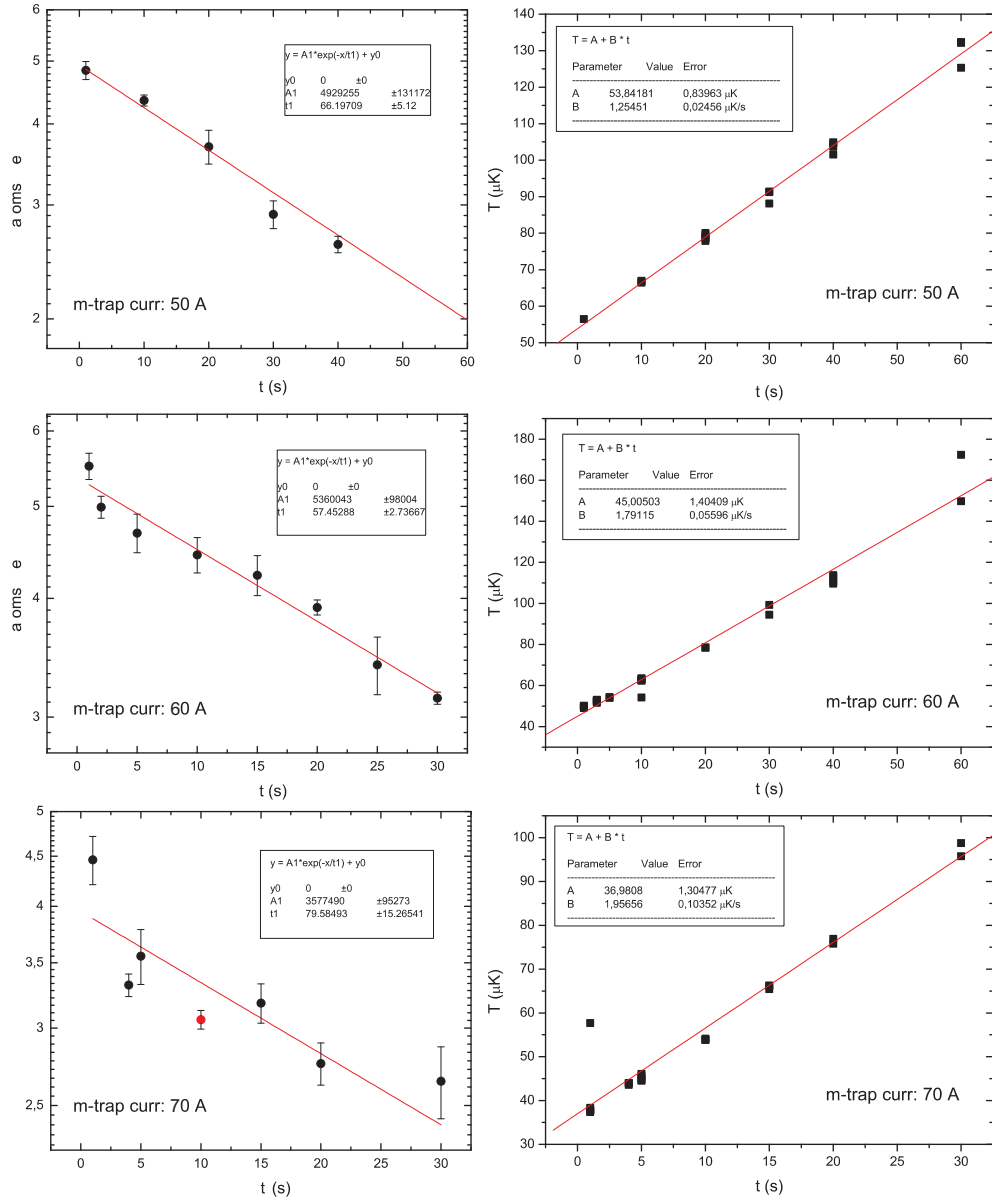


Figure 3.14: Measured milli-trap mean life (left column) and heating rate (right column) for different values of the current, shown in each panel.

trapped in the milli-trap right after the transfer phase, and hence is not limiting the atom number in the first phase of the evaporation.

Fig. 3.14 reports measured mean life (left column) and heating rate (right column) of our milli-trap. The solid lines represent exponential fits on lifetime datasets and linear fits on heating rate datasets. Measurements are performed for different values of the current, in order to determine if and how the milli-trap temperature influences the quality of the atomic sample. The observed lifetimes do not show a strong dependence on the trap current, attesting on a value that is around 60 s. On the contrary, the heating rate  $H$  is strongly dependent on the current value. This behavior is compatible with the presence of a ripple noise in the milli-trap circuit, that has however been measured to be less than  $5 \times 10^{-4}$ . This noise seems to be able to shake the sample held during the evaporation, but not to expel atoms from the trap through resonant coupling to untrapped Zeeman sublevels. For a current of 70 A (chosen as working value to obtain the  $^{87}\text{Rb}$  BEC) the heating rate is  $H=1.9 \mu\text{Ks}^{-1}$ . The value of this parameter is fundamental when working with sub- $\mu\text{K}$  samples, since it remains constant even at low temperatures, hence giving a fast depletion of the BEC state.

### 3.4.1 Measuring the trap frequencies

A fundamental test performed on the milli-trap is the measurement of the trap frequencies. There are substantially two ways to obtain their values:

- Parametric Heating
- Collective oscillations

### 3.4.2 Parametric heating

This method is based on the heating of the sample induced by a small modulation of the trapping potential:

$$U(t) = U_0[1 + \epsilon(t)]. \quad (3.16)$$

The transition rate from a stationary state  $n$  to another final stationary state  $m$  can be calculated following the first order perturbation theory [134]:

$$R_{m,n} = \frac{1}{T\hbar^2} \left| \int_0^t \langle m|U_0|n\rangle \epsilon(t) e^{i\omega_{mn}} dt \right|^2, \quad (3.17)$$

### 3.4. The Milli-Trap

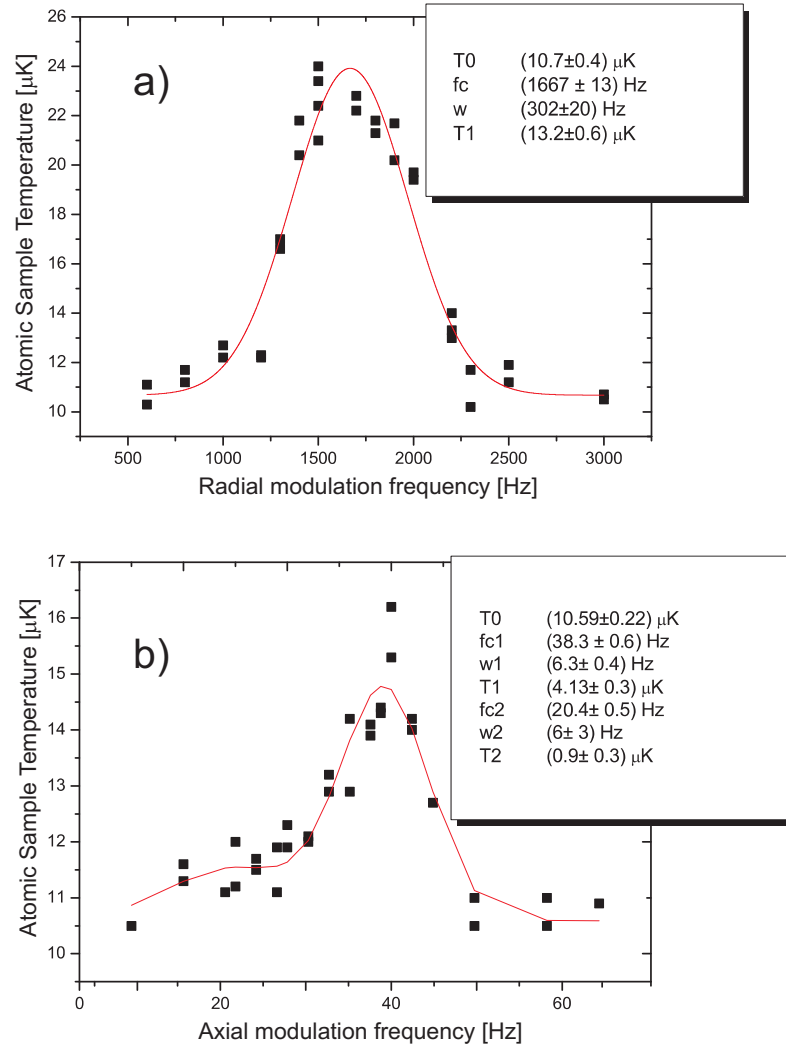


Figure 3.15: Measured temperature of the cold atomic sample after a 2s modulation as a function of the radial (a) and axial (b) modulation frequency  $\omega$ . The peaks correspond to  $\omega = 2\omega_{\perp}$  and  $\omega = 2\omega_{z}$ , where  $\omega_{\perp,z}$  are the radial and axial trap frequencies respectively. The solid lines are fits obtained using the function reported in the insets. A broad peak, coming from higher order terms in the perturbation theory, is visible in (a) for  $\omega = \omega_z$ .

where  $\omega_{mn} = (E_m - E_n)/\hbar$ . If the temperature of the atomic sample is below  $T_\mu$ , the potential can be taken as harmonic along both radial and axial directions, and the above integral gives:

$$R_{n,n} = \frac{\pi\omega_i^2}{16} S(0)(2n+1) \quad (3.18)$$

$$R_{n,n\pm 2} = \frac{\pi\omega_i^2}{16} S(2\omega_i)(n+1\pm 1)(n\pm 1), \quad i = z, \perp \quad (3.19)$$

where  $S(2\omega_i) = \frac{2}{\pi} \int_0^T \cos\omega_i \langle \epsilon(t)\epsilon(t+\tau) \rangle d\tau$ . Hence selection rules forbid  $n \pm 1$  transitions, and heating will be present only for  $\omega = 2\omega_z, 2\omega_\perp$  modulation of the trapping potential. The thermal heating of the cold sample can be evaluated from Eq. (3.19) [134]:

$$\frac{\langle \dot{E} \rangle}{\langle E \rangle} = \frac{\pi}{2} \omega_i^2 S(2\omega_i). \quad (3.20)$$

Integrating this equation, we obtain an exponential growth of the temperature in time after the onset of excitation.

The radial vibrational mode can be excited by a modulation of the bias field  $B'_0$ , that influences only the radial direction (Sec. 3.4), executed through the external bias coil. The axial modes, on the contrary, have to be excited modulating the whole potential through a modulation of the milli-trap current. The cold sample ( $T=10 \mu\text{K}$ ) is excited for 2 s, then 2 s are required to achieve cross-dimensional thermalization of the sample. After an expansion time  $t$  the sample is then imaged (Sec. 3.7), and the final temperature  $T$  is extracted from the gaussian widths  $\sigma_i$  of the cloud:

$$T = \frac{m}{k_B} \left( \frac{\omega_i^2}{1 + \omega_i^2 t^2} \right) \sigma_i^2. \quad (3.21)$$

Since the actual relevant measurement is not the absolute temperature  $T$  of the sample, but the temperature variation after the parametric heating, the dependence of  $T$  on  $\omega_i$  is not relevant, and one can use an estimated trap frequency to plot the estimated final temperature as a function of the modulation frequency. Fig. 3.15(a) and Fig. 3.15(b) report the data for radial and axial modulation respectively. The maximum variation in the sample temperature corresponds to a modulation frequency  $\omega = 2\omega_\perp, 2\omega_z$ . The above measurements are performed on a  $^{87}\text{Rb}$  sample with a total bias of 0.8 Gauss and a trap current of 95 A, and the obtained trap frequencies are  $\omega_\perp = (833 \pm 7) \text{ Hz}$  and  $\omega_z = (20.4 \pm 0.5) \text{ Hz}$ . The first lower peak slightly visible in the axial modulation profile comes from an excitation at  $\omega = \omega_z$  corresponding to higher order terms of the perturbation theory.

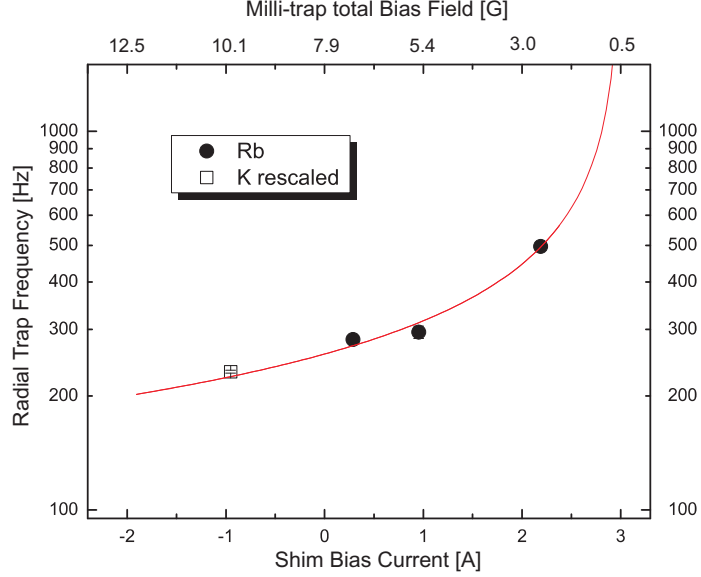


Figure 3.16: Calibration of the milli-trap radial frequency as a function of the external bias field  $B'_0$ , obtained through dipolar oscillations of the sample. The solid line is a fit obtained using the function (3.22). The black points are data obtained from  $^{87}\text{Rb}$  sample, while the empty point refers to a  $^{39}\text{K}$  sample. Measurements are performed at  $T = 10 \mu\text{K}$ .

### 3.4.3 Collective excitations

The other way to measure the milli-trap frequencies relies on the theory of collective excitations of an interacting atomic ensemble trapped in a magnetic potential. The motion of a bosonic atomic ensemble in a harmonic trap has been subject of insightful studies [135, 136, 137, 138, 139]. In this context, anyway, it will be sufficient to limit our discussion to the low density regime: observed densities for a temperature well above the critical temperature  $T_c$ , indeed, don't allow the system to enter in the hydrodynamic region, that is hardly attainable even for degenerate systems. Considering an atomic sample whose temperature is  $10 \mu\text{K}$  the regime is collisionless and substantially three different collective modes can be excited by a sudden variation in the trapping potential, i.e. the *dipole*, the *quadrupole* and the *breathing* modes. Each mode will preferentially be excited depending on the excitation frequency and way of excitation.

- *dipole mode*: this mode represents a collective center of mass oscillation into the harmonic trapping potential, and can be excited simply displacing the trap center along the axial or radial direction. The cloud starts to oscillate with frequencies  $\omega_d = \omega_{\perp, z}$  depending on the direction of displacement of the trap. Observing the periodic motion of the center of mass one obtains the direct measurement of the trap frequency along a certain direction.
- *quadrupole mode*: this mode represents an out-of-phase periodic variation of both radial and axial sizes and hence of aspect ratio of the system. After a sudden variation of the potential shape, the axial cloud starts to oscillate with frequency  $\omega_q = 2\omega_z$ . Observing the periodic variation of the axial or both radial and axial sizes of the cloud gives a direct measurement of the trap frequency.
- *breathing mode*: this mode represents a in-phase periodic variation of both axial and radial sizes. The mode of excitation is the same as the quadrupole mode. The cloud radial size starts to oscillate with frequency  $\omega_b = 2\omega_{\perp}$ . Observing the periodic variation of the radial size of the cloud gives a direct measurement of the trap frequency.

In order to obtain the radial trap frequency value, we performed an analysis of the simplest dipolar motion of a  $^{87}\text{Rb}$  cloud along the vertical radial direction. The temperature of the sample is  $10 \mu\text{K}$ . The displacement of the trap center is obtained adding a vertical uniform field to the trapping potential via a pair of horizontal Hemholtz coils. The oscillating sample is held in the trap for a time going from zero to several oscillation periods after the trap is displaced, and then is imaged after 10 ms of free expansion. In this way we reconstruct the sinusoidal motion of the center of mass as a function of the oscillation time and extract the trap frequency through a three parameters fit. The measurement is performed for various values of current flowing into the bias coil, in order to obtain an experimental calibration of the radial trap frequency as a function of the total bias field. The experimental data are reported in Fig. 3.16. The solid line is the fit obtained using the function

$$\omega_{\perp} = \frac{2\pi f_0}{\sqrt{B_0[\text{G}] - 2.45 I_B[\text{A}]}} \quad (3.22)$$

directly derived from Eq. (3.10). In the previous formula,  $f_0$  is the trap frequency when the total bias field equals 1 G,  $B_0$  is the intrinsic trap bias field,  $I_B$  is the bias coil current, and the factor 2.45 comes from the measured current-field characteristic of the bias coil. The best fitting values are found to be  $f_0 = 726 \text{ Hz}$  and  $B_0 = 7.9$

Gauss. A measurement performed on  $^{39}\text{K}$  is reported in Fig. 3.16 for  $I_B = -1$  A (empty squares), after the frequency has been rescaled by the mass-to-mass ratio  $\sqrt{m_{Rb}/m_K}$ .

## 3.5 Controlling the Magnetic Field

The control of the magnetic fields during the transfer phase from the quadrupole the milli-trap plays a fundamental role for the efficiency of the process. In particular, time constants of the control circuits have to be carefully set. To this scope, both the quadrupole and milli-trap controllers are designed and realized by our research group.

### 3.5.1 The quadrupole current controller

The quadrupole coils have an impedance of  $0.5 \Omega$  and an inductance of 2 mH. The power supply (Agilent 6692A, 6.6 kW) can deliver 110 A at a maximum voltage of 60 V. Even if the actual current needed for the MOT phase is only 4 A and 65 A for the quadrupole, we can use the same coils set to produce Fano-Feshbach uniform fields up to 1000 G at 110 A, once the current directions are switched to the Helmholtz configuration. The power supply is remotely controlled via the GPIB interface and an analog current control. The former is used to program the current and voltage working values of the power supply during a run when no particular temporal resolution is needed, since typical jitter of instructions on the GPIB bus is  $\sim 20$  ms. The latter is used to control the current in the circuit when higher temporal accuracies are required, e. g. during the short (5 ms) molasses phase.

A schematic drawing of the control circuit is shown in Fig. 3.17. The intrinsic time constant of the quadrupole coils+supply circuit is  $\tau_c=50$  ms. An IGBT transistor (Motorola n-channel MG200Q1US51,  $V_{\text{max}}=1.2$  kV) is inserted to break the current flow when the magnetic field has to be turned off in sub-ms time intervals, as before the molasses phase. When the base-emitter voltage is driven to zero via a TTL driver, the circuit is suddenly opened, and the potential drop between source and drain terminals can reach very high values (exceeding some kV). A 75 volts AC varistor is connected between collector and emitter terminals, and has the double feature to protect the IGBT from the aperture extra-voltage and to set the fall time of the magnetic field. With this value of breakdown voltage the current fall time is reduced to 1 ms. When a fast extinguishing of the field is not required the GPIB interface can be employed.

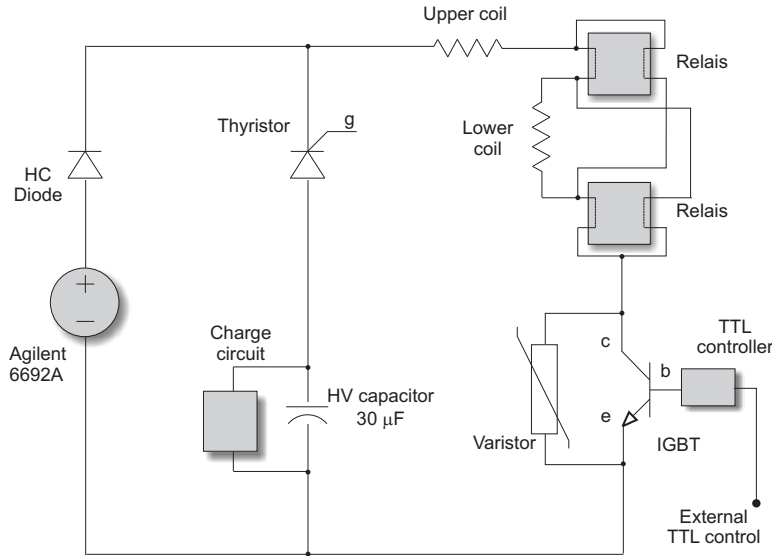


Figure 3.17: Schematics of the circuit employed to control the quadrupole coils current.

To reduce the field rise time as well, a *boost* circuit is inserted parallel to the power supply terminals. The  $30\ \mu\text{F}$ , 1000V capacitor is loaded during the stationary operation of the circuit. A thyristor (30TPS16 *nnpn* 300 A 1000V), in this phase, connects the positive terminal of the power supply to the upper coil, so that the power supply feeds the stationary required current. When a TTL signal is sent to the thyristor gate, the connection is extended to the positive terminal of the capacitor, that acts like a current reservoir for the circuit. Its loading voltage  $V_c$  sets the peak current  $I_B$  fed by the boost circuit, while its capacity sets the rise time  $\tau_B$ . The thyristor maintains the connection until the power supply reaches an operating value equal to the residual capacitor voltage, and then disconnects the capacitor from the current circuit. Beyond this point, the current grows again with the slow time constant  $\tau_c$  up to the programmed value. A high current diode (IOR 15DU120 150 A,  $V_{break}=1200\ \text{V}$ ) is placed in series to the power supply positive terminal to avoid any reverse current pumping into the supply when the capacitor is connected by the thyristor. This system provides a fast non-adiabatic deformation of the potential from the MOT value to the quadrupole value, allowing a matching of the MOT and quadrupole extension. The optimal value for the peak boost current is 20 A with a rise time  $\tau_B=0.5\ \text{ms}$ , while the slow time constant  $t_c$  does not substantially influence the quadrupole

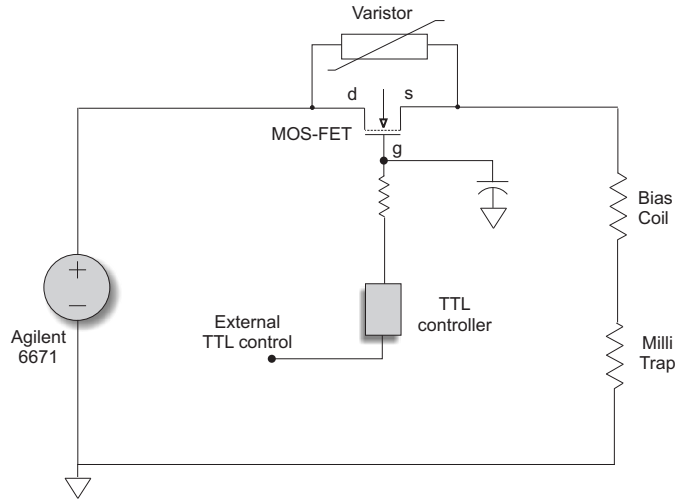


Figure 3.18: Schematics of the circuit employed to control the milli-trap and bias coil current.

loading efficiency. A set of two electromechanical normally-open relays can be used to revert the current flow in one of the two coils, so that a Fano-Feshbach uniform field can be established in the center of the coil system. This switching operation can only take place when no current is flowing in the coils, and the commutation time of the relays is  $\sim 200$  ms.

The current stability of the whole system is the nominal stability of the Agilent 6692A power supply.

### 3.5.2 The milli-trap current controller

As seen before, due to its particular design, the milli-trap system has small impedance and inductance if compared to the quadrupole coils system. The handling of currents, hence, is much easier than in the case of the quadrupole coils. In this case, indeed, both the switching on and off of the current are managed by a MOSFET transistor (IXFN230N10 n-channel, 230 A, 100 V), whose gate is controlled by a TTL signal. The schematic drawing of the circuit is shown in Fig. 3.18. The power supply (Agilent 6671) delivers a maximum current of 240 A at 8 V, and can in principle increase the current to the working value of 95 A with a rise time of 0.5 ms. As we will see in the following Section, anyway, the loading of the milli-trap should take place adiabatically respect to the radial trapping frequencies (Sec. 3.4). For this

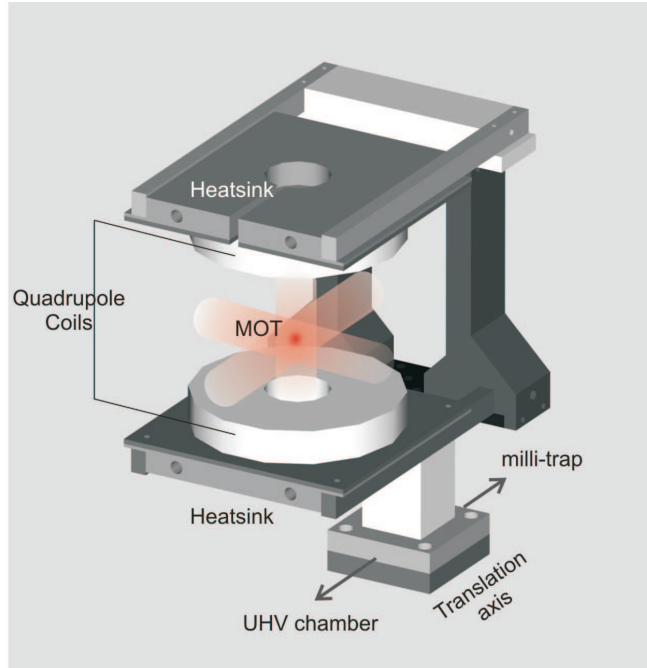


Figure 3.19: Schematics of the coils support directly fixed to the translation stage (not shown). The coils are employed to generate both the MOT and the high quadrupole field to transport the atoms from MOT to milli-trap region.

reason, the rise time has been increased adding a RC circuit directly acting on the MOSFET gate. The capacity is fixed to  $10 \mu\text{F}$ , while the variable resistor allows the variation of the rise time  $\tau_m$  from 1 to 2500 ms. The optimal loading time is set to  $\tau_m=300$  ms. The fall time of the current, as in the quadrupole case, is established by a varistor (07D180K) connected between the drain and the source terminals of the transistor. In these conditions, the fall time is  $600 \mu\text{s}$ . The bias coil, placed in series to the milli-trap, is driven by the same control circuit.

### 3.5.3 Magnetic transport: *atoms and motors*

Since the milli-trap center is 25 mm away from the center of the 3D-MOT, atoms has to be physically moved from their initial position, coinciding with the center of the UHV cell. This can be done translating the atoms while they are trapped in the quadrupole field after the molasses phase. To this scope, the MOT coils sup-

port is directly fixed to a linear endless screw translation stage, and can travel along the longitudinal axis of the cell until its center exactly matches the milli-trap center. This translation stage (THK KR series) is driven by a brushless DC motor (Parker SMH82), which is remotely controllable with a precision of 1/1024 turns. The complete motion takes 500 ms, and the velocity profile of the rail velocity is trapezoidal: 100 ms of acceleration ( $0.7 \text{ m/s}^2$ ), 300 ms of uniform velocity and 100 ms of deceleration ( $0.7 \text{ m/s}^2$ ). 200 ms after the rail is stopped the current in the milli-trap is raised to 95 A, and the quadrupole current is lowered to 10 A in 80 ms and then switched off by the MOSFET transistor.

The DC motor driver emulates a stepping-like behavior of the motor, that can be thus controlled by a sequence of TTL pulses, without introducing additional noise coming from the discretization of the motion as a common stepping motor does. This gives the system a mechanical position reproducibility of  $6 \mu\text{m}$ , substantially limited by the mechanical features of the linear translation stage. The particular design (see Fig. 3.19) avoids any limitation to the optical access of the cell, and the stainless steel bars holding the coils confer a high robustness to the system, since high forces are acting between the coils when the current is raised. The repulsive (quadrupole configuration) or attractive (Feshbach field configuration) force can be estimated as  $\sim 5 \text{ Kgf/kA}$ . This can lead to very strong attraction between the coils when a high Feshbach field is activated. To avoid as much as possible any field deviation or drift, the entire structure is built in amagnetic aluminium and steel. The efficiency of the transfer procedure is strictly related to the vertical and horizontal alignment of the system respect to the milli-trap longitudinal axis. The vertical set of shim coils, conventionally called *lambda*, is employed to compensate the vertical misalignment, while the horizontal position of the rail is mechanically optimized by means of two horizontal locking screws acting directly on the rail base.

To optimize the transfer process, the motion of the quadrupole field is stopped 1.8 mm after the center of the milli-trap. This could result at a first sight somewhat surprising, since one expects to find the best performance when the two trap centers are perfectly overlapped. To understand this behavior, we analyzed through simulation the shape of the total magnetic field resulting from the addition of the quadrupole and milli-trap potentials varying the distance between the two centers. Simulations show the growth of a local secondary minimum connecting the region in which atoms are trapped to a saddle point that can reduce the trap depth to  $\sim 10$  Gauss during the quadrupole switch off phase. The presence of a 1.8 mm distance between the two center maximizes the potential barrier between the two minima in

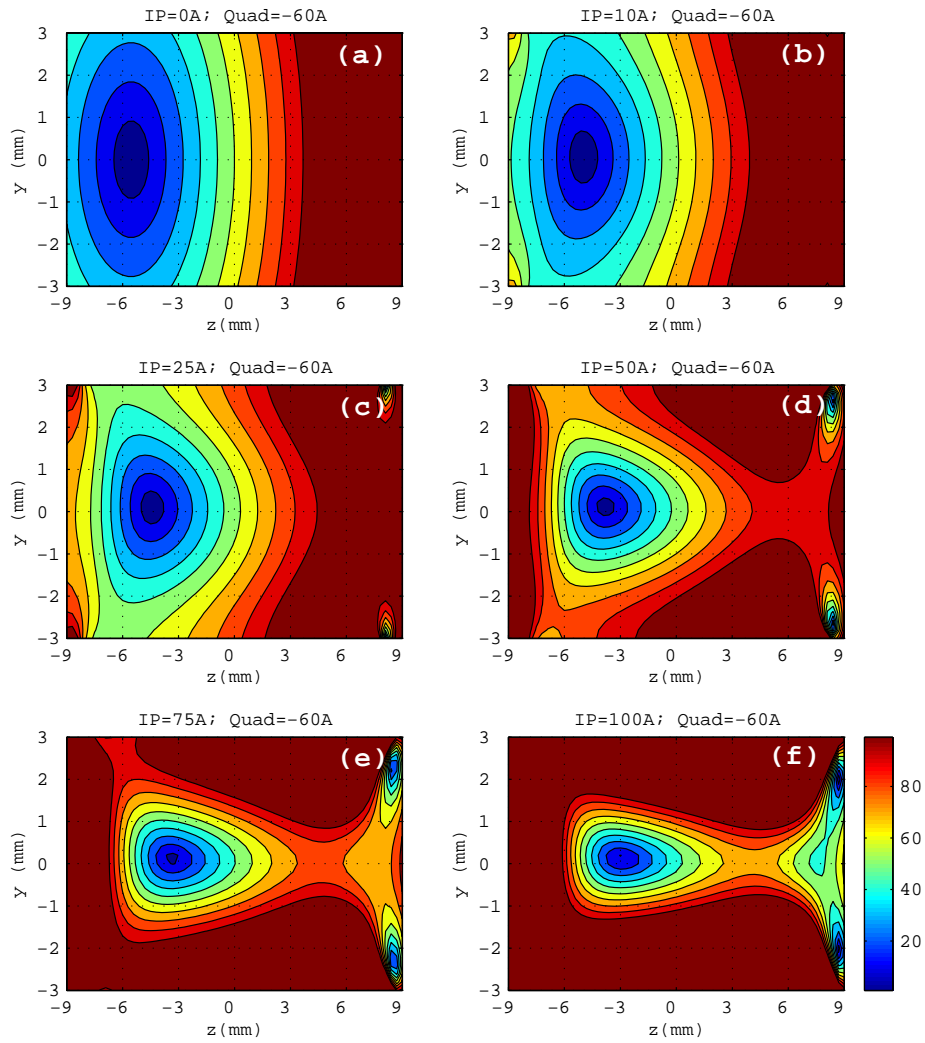


Figure 3.20: Magnetic field simulations during the milli-trap switch on process. The simulations are done along the vertical plane containing the longitudinal  $z$  axis of the milli-trap. The magnetic field intensity is expressed in Gauss.

### 3.5. Controlling the Magnetic Field

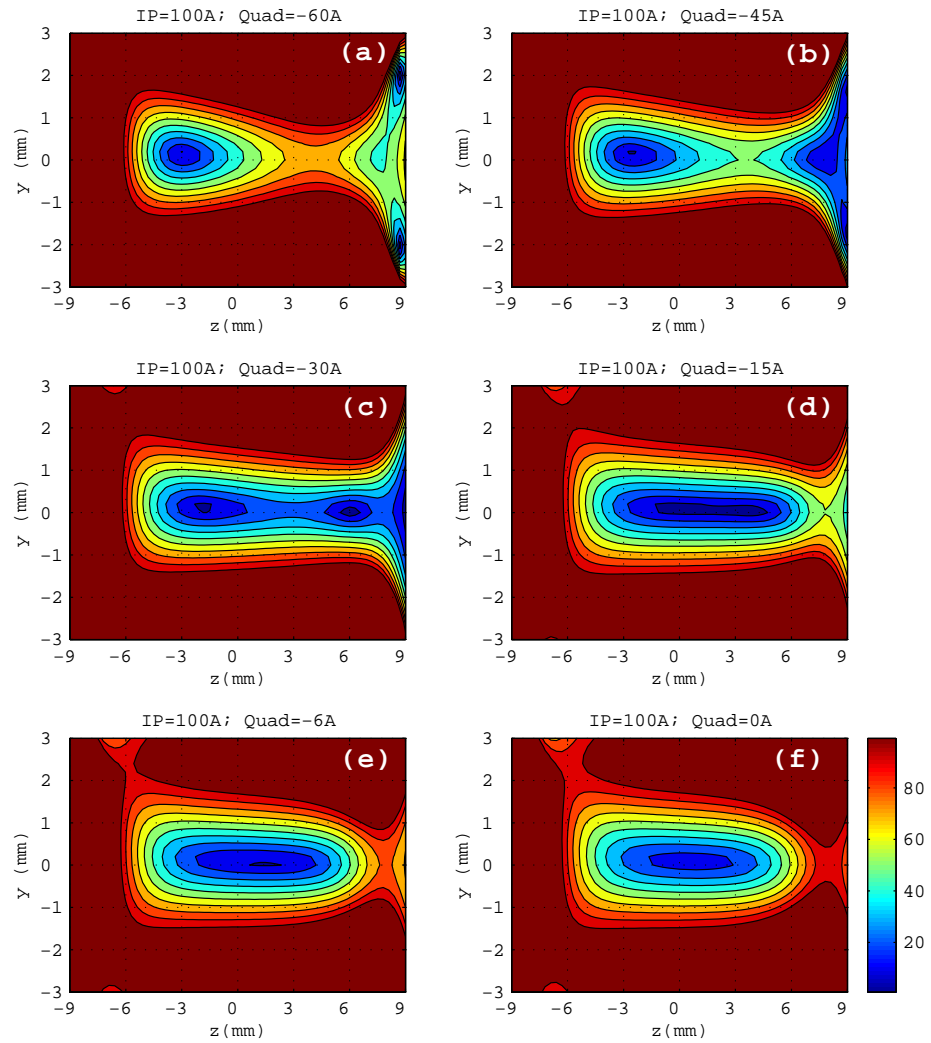


Figure 3.21: Magnetic field simulations during the quadrupole switch off process. The simulations are done along the vertical plane containing the longitudinal  $z$  axis of the milli-trap. The magnetic field intensity is expressed in Gauss.

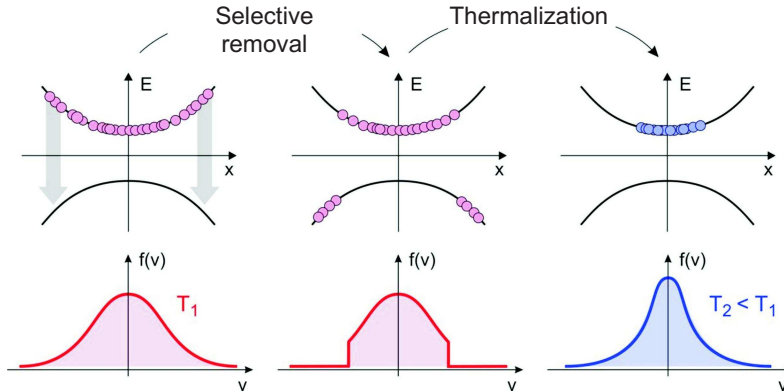


Figure 3.22: Schematic picture of evaporative cooling: trapped atoms in  $|2, 2\rangle$  state are selectively removed by a microwave radiation, which transfers atoms with higher temperature into the  $|1, 1\rangle$  state, and are hence expelled from the trap. After a certain rethermalization time, atoms redistribute following a new Maxwell-Boltzmann distribution with smaller width.

the intermediate phase, hence minimizing the reduction of trap depth during the last phase of the transfer. It could be easier to understand this peculiarity looking to the simulations describing this optimal configuration, reported in Figs. 3.20 and 3.21. Fig. 3.20 reports the simulations of the field when the milli-trap is progressively switched on while the quadrupole is still active and holds the atoms after the translation. Fig. 3.21 reports the next phase, when the quadrupole is progressively switched off and atoms are transferred in the milli-trap potential. Both figures show a vertical planar section containing the milli-trap longitudinal  $z$  axis. While during the first transfer phase the minimum trap depth is 70 Gauss (Fig. 3.20(f)), in the second phase, when the quadrupole current is decreased to 30 A, the trap depth is reduced by the presence of the second maximum and the saddle point to 25 Gauss (Fig. 3.21(c)) before increasing again to the final milli-trap value of 70 G. In this optimal configuration we obtain an overall transfer process efficiency near 30%.

### 3.6 Evaporative Cooling

Evaporative cooling technique [140], firstly demonstrated in the polarized hydrogen cooling [141], represented the decisive final step toward the Bose-Einstein degeneration of a dilute gas in a magnetic trap [142, 143]. This technique up to now has been applied to cool several neutral atomic species from mK to sub- $\mu$ K temper-

atures, and different schemes relying on purely optical trapping are demonstrated [144]. Finally, evaporative cooling showed to have fruitful employments in other fields of research, as the one reported in [145].

The idea of evaporative cooling relies on a continuous energy-selective removal of hottest atoms from the magnetic trapping volume, so that the temperature of the remaining sample is progressively reduced. Atoms trapped in a harmonic magnetic potential (Sec. 3.3) will feel a position-dependent Zeeman shift of their energy levels equal to:

$$\Delta E(F, m_F, x) = \mu_B m_F g_F |B(x) - B(0)| = \mu_B m_F g_F \left| \frac{B''}{2} x^2 - B_0 \right|, \quad (3.23)$$

where  $x$  is the distance from the center of the trap,  $B''$  is the field curvature and  $B_0$  is the bias field at the center of the trap. Since trapped atoms are described by a Maxwell-Boltzmann distribution, particles having a big velocity and hence a higher energy belong to the tails of the distribution function, and will preferentially move away from the trap center. A particular energy class is thus directly connected to a certain spatial position in the trap and, as a consequence of Eq. (3.23), has a precise magnetic energy.

Using a narrow microwave radiation, atoms trapped in the  $|2, 2\rangle$  level can be transferred into the untrapped state  $|1, 1\rangle$  and hence expelled from the trap. The frequency  $\nu_\mu$  determines the energy class to be expelled. Hence, as Fig. 3.22 sketches, by setting the right microwave frequency we can cut the distribution tails. A progressive reduction of the cutting frequency can thus lead to a cooling of the sample at the expense of the atom number. If the frequency sweep is too fast, anyway, the sample has not time to rethermalize between two consecutive steps of the evaporation, and atoms are expelled from the trap before they have time to be cooled down. The maximum sweep velocity is determined by the elastic collision rate  $\gamma_{el}$  which leads to the sample rethermalization without inducing trap losses:

$$\gamma_{el} \propto \bar{n} \sigma \bar{v}, \quad (3.24)$$

where  $\bar{n}$  is the numerical density,  $\sigma = 8\pi a^2$  is the elastic cross section (with  $a$  the s-wave scattering length) and  $\bar{v} = 4\sqrt{k_B T / (\pi m)}$  is the mean thermal velocity. During the evaporation,  $\bar{n}$  grows while  $\bar{v}$  reduces, but a good evaporation should maintain their product at least constant. If the initial atom number and phase space density (PSD) are sufficiently large, the sample can reach a temperature  $T$  lower than the critical temperature  $T_C$ , and a BEC is obtained. In elongated samples, if the frequency

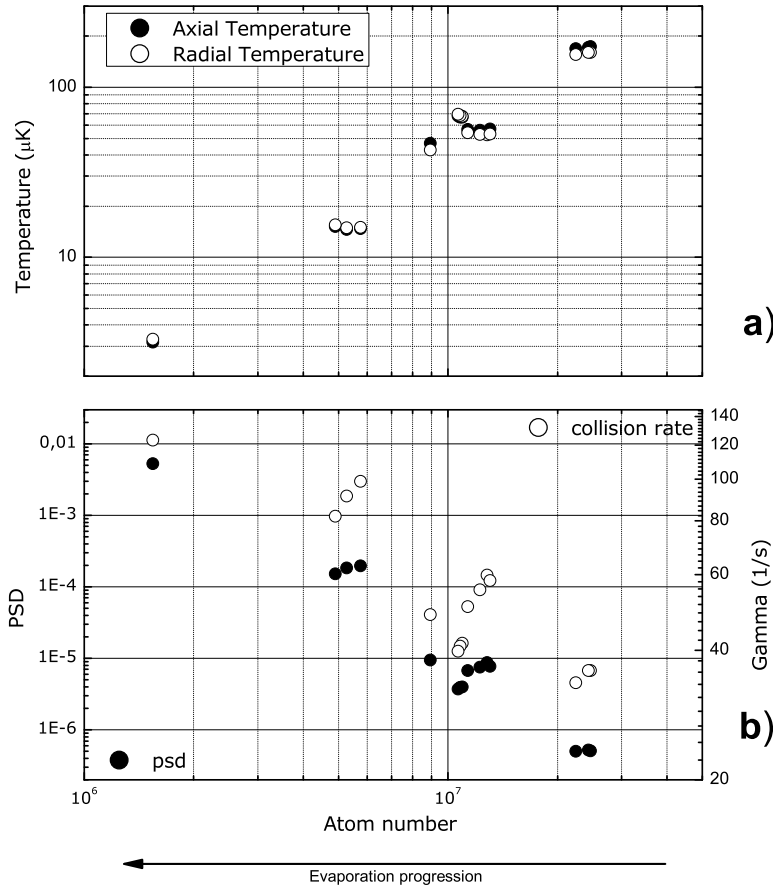


Figure 3.23: Evolution of the temperature (a) and of the phase space density (b) of a  $^{87}\text{Rb}$  sample during a typical evaporation ramp (see Fig. 3.24). The milli-trap current is set to 70 A.

sweep is too fast, an inhomogeneity between temperatures along radial and axial direction could appear, since the system is not able to follow a quasi-equilibrium path in the phase space. On the contrary, if a proper sweep is employed the system is step by step in a quasi-equilibrium state and both radial and axial temperatures take the same value. This optimal situation is shown in Fig. 3.23(a), where the measured temperatures are reported as a function of the evaporation process progression. As

can be seen, no inhomogeneity between radial and axial temperatures arises during the whole process. The efficiency of the entire process is connected to the scattering length amplitude  $a$ : the larger  $a$ , the faster the rethermalization time. This fact gives important constraints on the particular atomic species that can be cooled by an evaporation technique. For  $^{87}\text{Rb}$  the scattering length  $a$  corresponds to  $99 a_0$ , where  $a_0$  is the Bohr radius, while for  $^{39}\text{K}$  ( $^{41}\text{K}$ ) is  $a \sim -33 a_0$  ( $a \sim 60 a_0$ ). For this reason, while  $^{87}\text{Rb}$  can be nicely condensed by this technique, collisional rates for potassium bosonic isotopes are very weak and efficient evaporative cooling requires long evaporation times for this elements. Moreover, the direct evaporation process wastes a big amount of atoms, and since the number of K atoms that are collectable in a MOT is reduced, this would lead to a very poor potassium sample at the end of the evaporation process. Anyway, K-Rb interspecie collisional rates are sufficiently large to allow an efficient sympathetic cooling process, as shown in Sec. 5.1.

In our system the required microwave frequency is generated by a coaxial resonator oscillator (Miteq BCO-10-6830 series) locked on the  $683^{\text{th}}$  harmonic of a master signal of frequency  $\nu_M$  coming from a synthesized function generator (Stanford Research DS345). The frequency ramp is sent to the instrument and triggered via the GPIB bus. The frequency resolution is  $683 \times 0.001$  Hz, the latter being the nominal resolution of the 10 MHz reference signal. The output signal is amplified by 55 dB, and the 8 W output total power is coupled to the atomic system via a five loops antenna that induces magnetic dipole transitions on atoms.

In our  $^{87}\text{Rb}$  system, the sample is prepared and trapped in the  $5^2\text{S}_{1/2} |2, 2\rangle$  Zeeman sublevel, and transitions are induced towards the  $5^2\text{S}_{1/2} |1, 1\rangle$  state. The hyperfine splitting between  $F = 1$  and  $F = 2$  levels is  $\nu_0 = 6.8346826$  GHz, and the magnetic field dependence for these levels is  $0.7|m_F|$  MHz/Gauss. Therefore the frequency  $\nu_M$  corresponding to a cut in the atomic distribution at an energy  $E_T$  is:

$$\nu_M[\text{MHz}] = \frac{1}{683} \left[ \nu_0[\text{MHz}] + 0.7 \times (m_F^{\text{tr}} + m_F^{\text{untr}}) (B_0 + B'_0)[\text{G}] + 10^{-6} \frac{E_T}{h} \left( 1 + \frac{m_F^{\text{untr}}}{m_F^{\text{tr}}} \right) \right] \quad (3.25)$$

valid for every  $m_F^{\text{tr}}$ . In this expression,  $m_F^{\text{tr}}$  and  $m_F^{\text{untr}}$  are the trapped starting level and the untrapped target level respectively, connected by the selection rule  $m_F^{\text{untr}} = m_F^{\text{tr}} \pm 1, 0$ . Usually,  $E_T$  is expressed as a function of the actual temperature of the sample by  $E_T = \eta k_B T$ , where  $\eta$  is an experimental parameter that can be considered as constant throughout the whole evaporation. A reasonable value

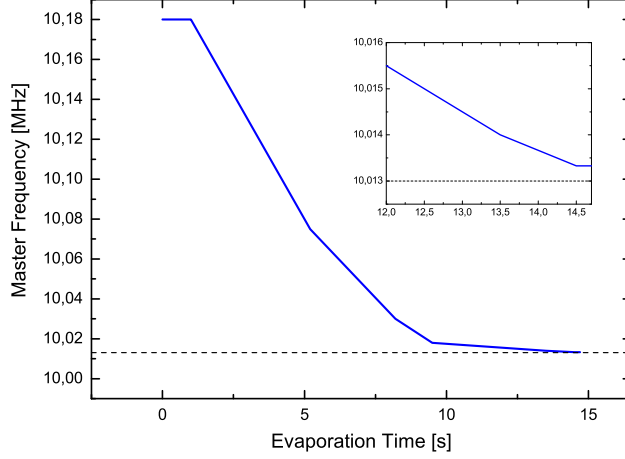


Figure 3.24: Typical evaporation ramp (solid line) for a total bias field of 2 Gauss. The dashed line represents the threshold frequency for atoms in the  $|2, 2\rangle$  state. The inset shows the last part of evaporation ramp.

for this parameter is  $\eta \sim 6$ . In the above expression, setting  $T = 0$ , one finds the threshold frequency  $\nu_{th}$  below which no atomic class is resonant with the radiation and no transitions are carried out. For atoms prepared in the  $|2, 2\rangle$  state we have:

$$\nu_{th} = \left( 10.006856 + \frac{2.1}{683} (B_0 + B'_0) [\text{G}] \right) \text{ MHz}, \quad (3.26)$$

that for a typical total bias field of 2 Gauss gives  $\nu_{th} = 10.013005$  MHz.

We observed a conspicuous dependence of the evaporation efficiency on the purity of the  $|2, 2\rangle$  sample. In the case a small fraction of  $|2, 1\rangle$  population is left in the trap by an imperfect hyperfine optical pumping after the molasses phase, or is generated by spurious spin-flipping events during the evaporation phase, we observed a critical collisions-induced heating of the sample for temperatures lower than  $5 \mu\text{K}$ , preventing the phase transition to BEC. To avoid this harmful heating, we mixed to the evaporation radiation an additional frequency, whose power is 3 W, to blow away atoms belonging to  $|1, 1\rangle$  level. This is done sweeping a signal whose master frequency is tuned on the  $|1, 1\rangle$  threshold frequency (10.008906 MHz @ 2 Gauss). The sweep amplitude is  $\pm 4$  kHz, while the sweep period is 2 s. In this way, atoms in the unwanted state are continuously removed, while atoms in the  $|2, 2\rangle$  state are not

influenced, since they are never resonant with the sweeping frequency.

The typical evaporation ramp profile is composed by 5 linear steps (Fig. 3.24), each optimized by maximizing the final collisional rate  $\gamma_{el}$  or, analogously, the final PSD. This can be done by measuring the evolution of the sample temperature as a function of the evaporation progression. Fig. 3.23(b) shows the behavior of the PSD (left) and  $\gamma_{el}$  (right) during the evaporation ramp. If the temperature is sufficiently low for atoms to be trapped in the harmonic region of the potential (see above), the PSD can be reconstructed by integrating the Maxwell-Boltzmann distribution to obtain the mean atomic density  $\bar{n}$ , and remembering that  $PSD = \bar{n} \lambda_{dB}^3$ :

$$PSD = N \left( \frac{\hbar \bar{\omega}_{ho}}{k_B T} \right)^3, \quad (3.27)$$

where  $\bar{\omega}_{ho}$  is the mean oscillator frequency of the trap. In a similar way, from Eq. (3.24) one obtains the expression for the collision rate:

$$\gamma_{el} = \frac{1}{2\pi^2} \left( \frac{m \bar{\omega}_{ho}^3}{k_B T} \right) N \sigma_{el}, \quad (3.28)$$

As can be seen in Fig. 3.23(b), the optimal evaporation ramp shown in Fig. 3.24 increases both PSD and  $\gamma_{el}$  as the number of atoms is decreased, and the efficiency of this process decreases only in the very last part of the evaporation. For this last fundamental step we found convenient to optimize the peak optical density (see Sec. 3.7) which is proportional to the collisional rate, amounting to a net decrease of the evaporation sweep rate. The total duration of the ramp depends on the density of the sample, hence on atomic number and on the trap frequencies. The lower the frequencies, the longer has to be the ramp duration. This argument privileges strong traps, like the milli-trap, since a short evaporation time reduces background collision losses from the trap and hence results in a higher number of condensed atoms. For typical bias field of 2 Gauss, the milli-trap allows evaporation ramps shorter than 15 s. This value has to be compared to typical ramp durations in QUIC or baseball traps, usually longer than 30 s.

### 3.7 The Imaging System

The imaging technique is based on the absorption of a resonant laser light by the ultracold atomic sample. Since atomic densities in the condensed state can achieve very high values ( $10^{13} \div 10^{14} \text{ cm}^{-3}$ ), this method can give a high signal-to-noise ratio even for relatively small atomic samples ( $10^4$  atoms). Since in our system both

$^{87}\text{Rb}$  and  $^{39}\text{K}$  samples are cooled in the  $|2, 2\rangle$  state, the imaging light is resonant with the  $|F = 2\rangle \rightarrow |F' = 3\rangle$  transition, and no repumping light is needed to observe the atomic clouds. The radiation has a  $\sigma^+$  polarization. The cloud can be imaged along the milli-trap axis, or in the vertical direction. The horizontal and vertical imaging beams cross the center of the milli-trap, and have a power of  $\sim 30 \mu\text{W}$ , corresponding to a maximum relative intensity of  $0.5I_{sat}$ . The resolution of the system is given by the diffraction limit  $l = 1.22(f/D)\lambda$ , where  $f$  and  $D$  are the focal length and diameter of the exit lens respectively, and  $\lambda$  is the radiation wavelength. The horizontal imaging system has an actual resolution of  $15 \mu\text{m}$  and the magnification factor is 2. The vertical beam has an actual resolution of  $8 \mu\text{m}$ , and the magnification factor is 2.5. The imaging procedure is the following: after the evaporative cooling the milli-trap and the bias coil are simultaneously switched off. The atomic sample falls under the effect of the gravity, and the cloud expands because of the residual internal energy. After a certain expansion time  $t_{exp}$  the laser beams are shone on the atomic sample, and the resulting planar intensity profile is collected on a CCD camera (Theta System SIS1-s285, CCD sensor: Sony ICX285AL  $1040 \times 1392$  pxl,  $6.45 \times 6.45 \mu\text{m}$ ). This imaging method is destructive, since the ultracold atomic sample is blown away directly by the resonant probe beam. To increase the S/N ratio of the planar intensity distribution, three images are consequentially snapped:

1. *Atoms+Probe*: for  $^{87}\text{Rb}$  a  $50 \mu\text{s}$  pulse ( $30 \mu\text{s}$  for K) is shone on atoms while the CCD is integrating. The absorption intensity profile  $I_{AT}$  is collected on the CCD.
2. *Probe*: an identical pulse is shone once atoms have been blown away, and the probe beam intensity profile  $I_{LAS}$  is captured.
3. *Obscure*: an empty image, registering only intensity profile  $I_O$  coming from the electronic noise and the environmental stray light, is captured by the CCD after an integration time equal to the previous two snapshots.

In the case of a homogeneous material, the residual intensity after absorption is given by the standard Beer law  $I = I_0 e^{-\alpha y}$ , where  $I$  and  $I_0$  are the incoming and outgoing beam intensities,  $y$  is the thickness of the absorber along the imaging direction, and  $\alpha = \sigma_0 n$  is the absorption coefficient, proportional to the absorption cross section  $\sigma_0$  and hence to the material density  $n$ . In the case of an inhomogeneous atomic cloud, the Beer law can be extended defining the optical density  $\tilde{n}$  directly

from the column density of the distribution along the imaging direction:

$$\tilde{n}(x, z) = \sigma_0 \int n(\mathbf{x}) dy, \quad (3.29)$$

being  $\sigma_0 = 3\lambda^2/2\pi$  the absorption scattering length for a two level atom and  $n(\mathbf{x})$  the spatial density of the sample. In this way, the Beer law for each pixel of coordinates  $(x, z)$  takes the form  $-\ln(I/I_0) = \tilde{n}(x, z) = \sigma_0 \int n(\mathbf{x}) dy$ . The optical density can hence be obtained through a numerical combination of the three intensity profiles:

$$\tilde{n}(x, z) = -\ln \left( \frac{I_{AT} - I_O}{I_{LAS} - I_O} \right). \quad (3.30)$$

This technique, if the initial distribution function of trapped atoms is known, gives the opportunity to reconstruct important information about the atomic cloud, such as the total atom number  $N$ , the temperature  $T$  or the spatial widths  $\sigma_i$ .

### Thermal atoms

In this case, the initial distribution of trapped atoms can be reasonably taken as gaussian [146], where the width are directly connected to the momentum distribution of the atoms and hence to their temperature. For an harmonic trap, symmetric along the  $z$  direction and centered in  $\mathbf{x}_0$ , we can write

$$n(x, y, z) = \frac{N}{(2\pi)^{3/2} \sigma_{\perp}^2 \sigma_z} \exp \left( -\frac{(x - x_0)^2 + (y - y_0)^2}{2\sigma_{\perp}^2} - \frac{(z - z_0)^2}{2\sigma_z^2} \right) \quad (3.31)$$

$$\tilde{n}(x, z) = \sigma_0 \frac{N}{(2\pi) \sigma_{\perp} \sigma_z} \exp \left( -\frac{(x - x_0)^2}{2\sigma_{\perp}^2} - \frac{(z - z_0)^2}{2\sigma_z^2} \right). \quad (3.32)$$

The function we use to fit the optical density is:

$$\tilde{n}^{\dagger}(x, z) = \frac{A}{10^3} \exp \left( -\frac{(x - x_0)^2}{2\sigma_{\perp}^2} - \frac{(z - z_0)^2}{2\sigma_z^2} \right) + \frac{B}{10^3}, \quad (3.33)$$

where  $A$ ,  $B$ ,  $\sigma_{\perp}$ ,  $\sigma_z$ ,  $x_0$ ,  $z_0$  are the fit parameters. From this choice we obtain:

$$\text{peak OD} = 10^{-3} A \quad (3.34)$$

$$N = \left( \frac{2\pi}{\lambda} \right)^2 \frac{A}{3 \times 10^3} \sigma_{\perp} \sigma_z \quad (3.35)$$

$$T_i = \frac{m}{k_B} \left( \frac{\omega_i^2}{1 + \omega_i^2 t^2} \right) \sigma_i^2, \quad (3.36)$$

where  $t$  is the expansion time from the trap and  $\lambda$  the specific resonance wavelenght.

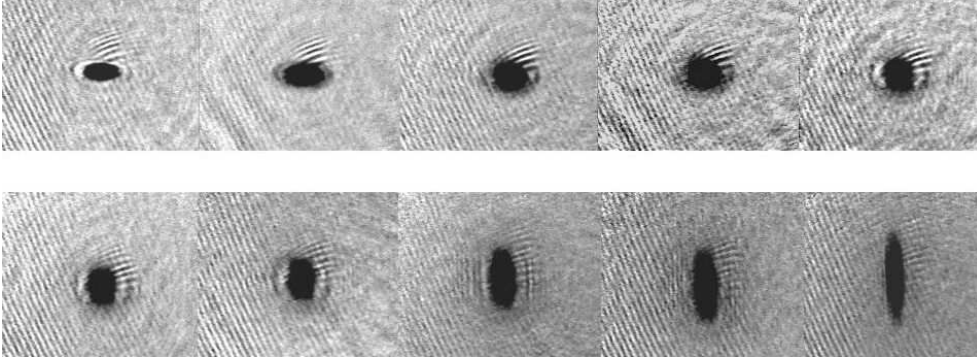


Figure 3.25: Typical expansion of a  $^{87}\text{Rb}$  BEC from the anisotropic axially symmetric milli-trap. The absorption images show different expansion times, going from 2 to 45 ms. The expansion is enhanced in the direction the trap is tighter (radial), while is strongly reduced in the shallow direction (axial).

### Bose-Einstein Condensates

When the temperature of the sample trapped in a harmonic potential is lowered down to  $\sim T_c$ , the system undergoes the Bose-Einstein phase transition, and as density increases a narrow peak in the phase space density distribution appears (see Fig. 3.26). In the limit of pure condensates, the momentum spread  $\Delta p_i$  and Thomas-Fermi radius  $\sigma_i$  are Heisenberg limited, giving  $\Delta p_i \sigma_i \sim \hbar$ . If the trap is strongly anisotropic, the uncertainty limit enhances the expansion of the sample in the direction the trap is tighter, i.e. in the radial direction  $\perp$ , as consecutive absorption images reported in Fig. 3.25 show. The BEC distribution is described by the Thomas-Fermi function (see Eq. (1.26)). Differently from the thermal case, anyway, in a BEC no details on the sample temperature can be extracted from the free expansion of the system. Again, for a symmetric trap along the  $z$  direction we have:

$$n(x, y, z) = \frac{15N}{8\pi R_{\perp}^2 R_z} \left( 1 - \frac{(x - x_0)^2 + (y - y_0)^2}{R_{\perp}^2} - \frac{(z - z_0)^2}{R_z^2} \right) \quad (3.37)$$

$$\tilde{n}(x, z) = \frac{5N}{2\pi R_{\perp} R_z} \left( 1 - \frac{(x - x_0)^2}{R_{\perp}^2} - \frac{(z - z_0)^2}{R_z^2} \right)^{3/2} \quad (3.38)$$

These expressions are valid for  $(x - x_0)^2, (y - y_0)^2 < R_{\perp}^2$ ;  $(z - z_0)^2 < R_z^2$ , where  $R_i$  are the Thomas-Fermi radius of the distribution. The fitting function for the optical

density is:

$$\tilde{n}^\dagger(x, z) = \frac{A}{10^3} \left( 1 - \frac{(x - x_0)^2}{R_\perp^2} - \frac{(z - z_0)^2}{R_z^2} \right)^{3/2} + \frac{B}{10^3}, \quad (3.39)$$

where  $A$ ,  $B$ ,  $R_\perp$ ,  $R_z$ ,  $x_0$ ,  $z_0$  are the fit parameters. From this choice we obtain:

$$\text{peak OD} = 10^{-3} A \quad (3.40)$$

$$N = \left( \frac{8\pi}{1.5 \times 10^4} \right) R_\perp^2 R_z A. \quad (3.41)$$

### 3.8 Experimental procedure to a BEC

In this Section we summarize the typical experimental sequence employed to generate a  $^{87}\text{Rb}$  BEC exploiting the new milli-trapping system features. For the moment we focus in the  $^{87}\text{Rb}$  sample alone, since the whole procedure is mainly symmetrical for  $^{87}\text{Rb}$  and  $^{39}\text{K}$  (or  $^{41}\text{K}$ ). Details on the sympathetic cooling process between  $^{87}\text{Rb}$  and  $^{39}\text{K}$  are given in Chap. 5.

1. *MOT phase*: 2D-MOT and 3D-MOT beams are turned on, together with the 2D and 3D quadrupole current coils. In this way two independent bright beams of cold  $^{87}\text{Rb}$  and  $^{41}\text{K}$  or  $^{39}\text{K}$  source from the 2D-MOTs and go to feed the 3D-MOT situated in the UHV region of the apparatus. The typical loading time for the  $^{87}\text{Rb}$  3D-MOT is around 5 seconds, while for potassium isotopes the optimal sympathetic cooling is reached for loading time of  $\sim 0.5$  s (see Chap. 5 for details). In this phase, typically  $2 \times 10^9$  atoms are pre-cooled to a temperature of  $100 \mu\text{K}$  (1 mK for K).
2. *C-MOT phase*: In order to increase the density of the sample without increasing its temperature before loading the quadrupole, after the 3D-MOT phase the current is raised from 4 A to 10 A, and after 85 ms the cooling beams are shifted further away from the resonance ( $-5\Gamma$  for both  $^{87}\text{Rb}$  and  $^{39}\text{K}$ ), while the frequency detuning of the  $^{39}\text{K}$  repumping beams is set to  $-8.5\Gamma$ . The latter phase has a duration of 10 ms.
3. *Molasses and Optical pumping phase*: The 2D beams are turned off, together with the currents in the 2D and 3D magnetic coils. In order to obtain a further decrease in the temperature of the sample, the  $^{87}\text{Rb}$  cooling beams are moved to the MOT frequency detuning value ( $-2.8\Gamma$ ), while for  $^{39}\text{K}$  they are shifted very close to resonance. The  $^{39}\text{K}$  repumping beams are moved to  $-4.5\Gamma$  from

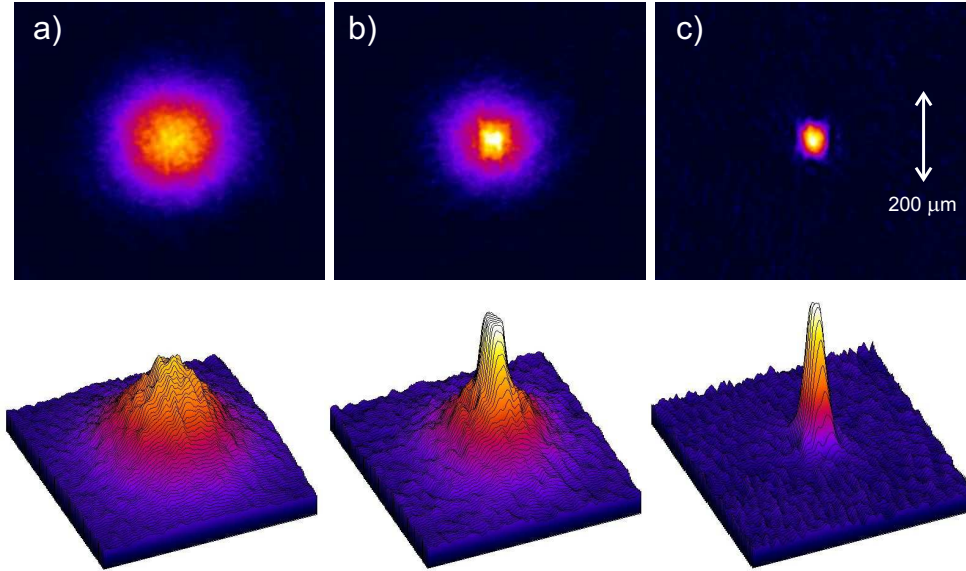


Figure 3.26: Typical absorption images of  $^{87}\text{Rb}$  taken for different values of the evaporation frequency cut. (a) Thermal atoms right above the transition: the density profile is fitted by a gaussian function. (b) Mixed cloud: a narrow peak arises from the thermal background during the phase transition to BEC. (c) Pure condensate: all atoms occupy the ground state and the density profiles is fitted by an inverted parabola (Thomas-Fermi function). Images are taken after 15 ms of expansion.

resonance. This *molasses* phase has a duration of 2.5 ms, after which the cooling beams for both species are turned off, while the repumping beams are left on 1 ms further, in order to populate the desired  $F = 2$  ground hyperfine level. The molasses has a duration of 3.5 ms. To achieve a full hyperfine transfer of atoms in the desired Zeeman sublevel, we generate a uniform 0.5 G bias field along a horizontal direction, and shine herein a resonant  $\sigma^+$  polarized beam with both repumping and cooling components (*optical pumping* beam). Again, the switching-off order enhances the efficiency of the specific optical pumping. Initially all the  $^{87}\text{Rb}$  and  $^{39}\text{K}$  optical pumping beams are shone simultaneously. After  $190 \mu\text{s}$  the potassium cooling beams are turned off;  $160 \mu\text{s}$  later the rubidium cooling beams are turned off as well, so that only the repumping beams are still on. At this point the quadrupole field is activated, and after 3 ms the repumping beams are switched off. The total length of the optical pumping pulse is hence 3.350 ms, divided in a different way for  $^{87}\text{Rb}$  and  $^{39}\text{K}$ . The light

power is  $200 \mu\text{W}$  for both the  $^{87}\text{Rb}$  beams, while in the case of  $^{39}\text{K}$  it is  $200 \mu\text{W}$  and  $600 \mu\text{W}$  for repumping and cooling beams respectively.

4. *Quadrupole loading and transfer to milli-trap:* After the optical pumping phase, the fast quadrupole current boost is activated, and then the current is raised to the stationary value of 65 A in 50 ms. Atoms are hence moved from the MOT zone to the milli-trap region by means of the brushless translation stage. During this phase all beams shutters are closed in order to avoid any heating due to spurious photons entering the UHV cell. The current in the milli-trap is adiabatically raised in 350 ms, and after it has reached its working value the quadrupole current is turned off.
5. *Evaporative cooling:* After 200 ms necessary to the stabilization of the system, typically  $2 \times 10^8$  rubidium atoms are ready to undergo the evaporative cooling process. The initial temperature ranges between 0.2 and 1 mK. The number of potassium atoms depends on the loading time and is critical for the efficiency of the eventual sympathetic cooling process. After the evaporation ramp (whose duration depends on the number of species to be cooled and on the milli-trap frequencies, and can vary between 10 and 30 s), the sample reaches the critical temperature necessary for the degeneration and enters the BEC phase. Fig. 3.26 shows three images corresponding to different values of the final  $\mu$ -wave frequency employed for the evaporation process.



# Chapter 4

## Intense Slow Beams of Bosonic Potassium Isotopes

One of the remarkable features of the new apparatus, as explained in Sec. 3.2.1, is the possibility to load the UHV 3D-MOT necessary to collect and pre-cool the atomic mixture by means of two independent bright sources of cold atoms, one for  $^{87}\text{Rb}$  and the other for  $^{39}\text{K}$  or  $^{41}\text{K}$ . Both sources exploit a 2D-MOT cooling scheme. Even though different schemes relying on the 2D-technique have been developed by several groups for  $^{87}\text{Rb}$  [121, 122, 147], to our knowledge no detailed characterization of such schemes was present for K isotopes at the time this thesis work started. The aim of this part of the work is to address the question of how efficiently the 2D-MOT scheme works for bosonic potassium isotopes, since the physical features of  $^{87}\text{Rb}$  and K are consistently different each other (Sec. 3.1.1).

In the first part of this Chapter we will report the results of extensive tests and calibration of the 2D-MOTs apparatus, whose structural features have already been described in the previous Chapter (Sec. 3.2.3). In the last part of the Chapter a simplified multilevel theoretical model, tailored to obtain a simulation of the atomic flux behavior, is reported.

### 4.1 Characterization of $^{39}\text{K}$ and $^{41}\text{K}$ Bright Sources

The characterization of the 2D-MOT system has been performed for both  $^{39}\text{K}$  and  $^{41}\text{K}$ , before the milli-trap was inserted into the vacuum system and the coils system for the 3D-MOT were placed. The investigation analyzed three main aspects of the

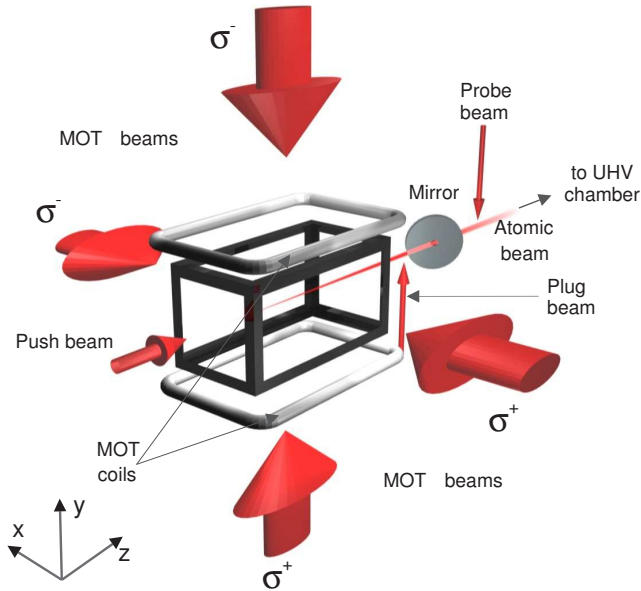


Figure 4.1: Schematics of the 2D-MOT system, reported again for clarity. In the time-of-flight imaging technique, a plug beam is placed near the hole in the mirror to shutter the atomic beam, and a probe beam is used to detect the atomic flux in the UHV chamber.

system: the trapping beams parameters, the vapor pressure influence on atomic flux, and the push beam effects. The analysis has been performed on the same guidelines as Ref. [121]. The characterization of  $^{41}\text{K}$  source was started only after optimization of frequencies and power for the  $^{39}\text{K}$ , the former having lower relative abundance (6.7%) than the latter (93.3%). The region of vapor pressure spanned in the analysis goes from  $2.9 \times 10^{-8}$  to  $3.9 \times 10^{-7}$  mbar, corresponding to the maximum allowed current in the dispenser. We estimate the background gas pressure to be around  $10^{-9}$  mbar. If not otherwise specified, in the experiment we set the K gas total pressure to  $7 \times 10^{-8}$  mbar.

#### 4.1.1 Detection technique

The whole optimization of the 2D-MOT system has been performed analyzing the atomic flux (Sec. 3.2.2) by means of time-of-flight (TOF) fluorescence detection. This is accomplished exposing the atomic flux to a vertical sheet of light (called, in

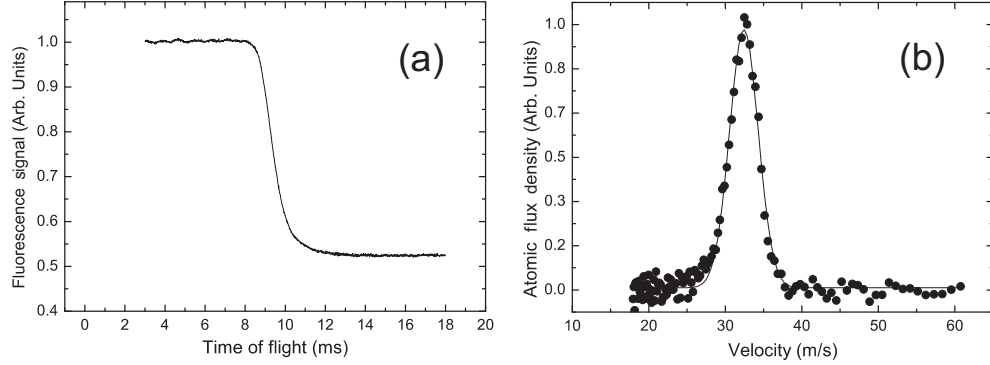


Figure 4.2: (a) Typical acquisition of the fluorescence signal. At  $t=0$  ms the plug beam is turned on, and after a delay of  $\sim 8$  ms the fluorescence starts decaying to zero. (b) Measured velocity distribution (dots) of atomic beam obtained by a discrete derivative of (a) and Gaussian fit to data (solid line). The fitted peak velocity is 32 m/s with a FWHM of 4.5 m/s.

this Chapter, *probe* beam, and not to be confused with the probe beam for the cold atomic cloud) near the center of the UHV chamber, 30 cm after the mirror hole, and collecting the emitted fluorescence into a broad area photodiode. The peak intensity of the probe beam exceeds  $0.5 \text{ W/cm}^2$ , divided between  $\omega_1$  and  $\omega_2$ , both resonant, in a ratio 1:2.

Switching on the plug beam (see Sec. 3.2.3) we interrupt the atomic flux; then, from the analysis of the decaying fluorescence signal  $S_F(t)$  as a function of time, we obtain the longitudinal velocity distribution  $\rho(v)$  of atoms. Denoting with  $\tau$  the time required for an atom with velocity  $v$  along  $z$  to travel the distance  $L$  between the plug beam and the probe light sheet, we can write the total flux  $\Phi$  as:

$$\Phi = \int \rho(v) dv, \quad \text{where} \quad \rho(v) = -\frac{\tau}{\eta} \frac{d}{d\tau} S_F(\tau), \quad (4.1)$$

with  $\tau = L/v$ . Here  $\eta$  is an experimental coefficient accounting for the calibration of the photodiode and for the collection solid angle. Fig. 4.2(a) shows a typical acquisition of the TOF signal, while the corresponding velocity distribution  $\rho(v)$ , as derived from Eq. (4.1), is displayed in Fig. 4.2(b). To obtain the total atomic flux  $\Phi$ , the peak velocity and the velocity spread, we fit the data with a gaussian function.

The divergence of the atomic beam is measured by imaging with a CCD camera the fluorescence emitted in the  $-x$  direction. The image profile along  $z$  corresponds to the gaussian profile of the short axis of probe light sheet, while the vertical ( $y$

direction) image profile extension is limited by the mirror hole. From the known width of the probe beam we calibrate the image magnification and therefore measure the size of the atomic beam in the  $y$  direction. Given the distance of the probe beam from the mirror hole, we calculate a divergence of  $(34 \pm 6)$  mrad.

### 4.1.2 Trapping beam parameters

To characterize the 2D-MOT, we first set the intensity of both repumping and cooling 2D-MOT beams to their maximum, respectively 50 and 80 mW per beam. We then make a scan of both frequencies  $\omega_1$  and  $\omega_2$ , searching for the values that maximize the fluorescence signal, hence the total flux of atoms.

We only present data on the total flux  $\Phi$  because the atomic velocities display no significant variations with the 2D-MOT parameters. The measured peak velocities span a range between 28 and 35 m/s, while the typical distribution spread is 4.5 m/s (FWHM). Experimental results for  $^{39}\text{K}$  detunings are plotted in arbitrary units normalized to the maximum value in Fig. 4.3(a). The detunings are defined throughout as follows:  $\delta_1 = \omega_1 - \omega_{12}$  and  $\delta_2 = \omega_2 - \omega_{23}$ , where we denote with  $\omega_{FF'}$  the atomic transition  $|4^2\text{S}_{1/2}, F\rangle \rightarrow |4^2\text{P}_{3/2}, F'\rangle$ . Note that for these measurements the push beam contains only the repumping component with a power of 6 mW and frequency  $\omega_p = \omega_{12} - 5.2\Gamma$ . A more detailed analysis of the push beam features is reported in Sec. 4.1.4. The detunings optimizing the atomic flux are  $\delta_1 = -3.9\Gamma$  and  $\delta_2 = -5.8\Gamma$ , which correspond to neither of the two configurations reported in [120]. In that work, a MOT is best loaded with both lasers detuned below all hyperfine components, in a Raman configuration such as  $|\delta_2 - \delta_1| = \Delta_{32}$  where  $\Delta_{32} = 2\pi \times 21$  MHz is the hyperfine separation between the  $|F' = 3\rangle$  and  $|F' = 2\rangle$  excited levels. Similar results were later confirmed in [148]. We speculate that, since our available laser beam intensities are a fifth to a tenth of those in [120], we are unable to reach such large values of detunings.

Then we fix the detunings and decrease both the cooling and repumping beams intensity. Fig. 4.3(b) shows the  $^{39}\text{K}$  atomic flux as a function of the beams intensity: as we see, there are no maxima in the explored range. Thus, an increase of the laser power should make the atomic beam more intense.

The analysis on  $^{41}\text{K}$  is performed along the same lines. Here, the push beam power is set to 6 mW and its frequency to  $\omega_p = \omega_{12} - 4.5\Gamma$ . Experimental results are plotted in Fig. 4.3(c, d). As before, while a peak is clearly visible in the frequency dependence of the signal, there is none in the intensity-dependent plot. Even for  $^{41}\text{K}$ , more laser power would enhance the number of atoms in the beam.

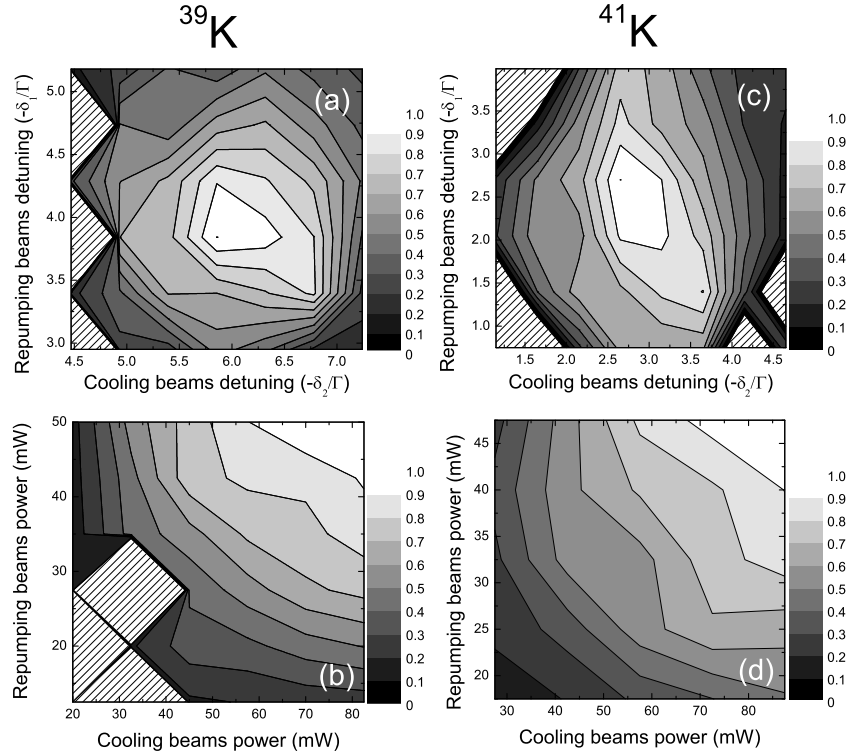


Figure 4.3: Measured  $^{39}\text{K}$  atomic flux normalized to unity as a function of transverse 2D-MOT beams detuning (a), and of their intensities (b). The detuning values that maximize the atomic flux are  $\delta_1 = -3.9\Gamma$  and  $\delta_2 = -5.8\Gamma$ . In (c) and (d) we report equivalent results obtained for  $^{41}\text{K}$  atomic beam, for which the optimal detunings are  $\delta_1 = -2.5\Gamma$  and  $\delta_2 = -3\Gamma$ . No data are taken in the patterned regions.

The largest contribution to the error on the measured total flux comes from the calibration parameter  $\eta$ , more precisely from the evaluation of the solid angle in which fluorescence is collected. We estimate this systematic uncertainty to be 20%, while the statistical error is 5%.

### 4.1.3 Vapor pressure

In order to investigate the dependence of the atomic flux upon the potassium gas pressure, we found it convenient to establish a calibration of the vapor pressure  $p$  against the dispenser supply current  $I$ . This is done by probing the atomic vapor

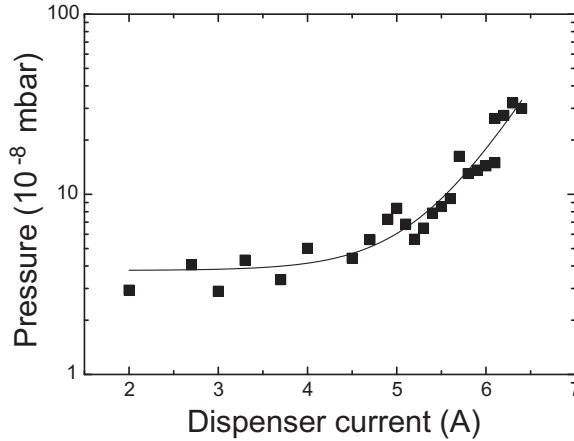


Figure 4.4: Measured  $^{39}\text{K}$  gas pressure  $p$  in the 2D-MOT chamber reported as a function of dispenser current  $I$ . The solid line is a fit obtained using Eq. (4.2).

using linear absorption spectroscopy. We simultaneously record the Doppler absorption profiles of the cooling transition in the 2D-MOT chamber and in the reference cell used for laser frequency locking. The pressure of the latter is inferred from its temperature:  $2.2 \times 10^{-7}$  mbar at  $43^\circ\text{C}$ . The calibration curve of  $p$  as a function of  $I$  is well-fit by an exponential function:

$$p = A + \exp(I/I_0 - B), \quad (4.2)$$

with  $A = (3.8 \pm 1) \cdot 10^{-8}$  mbar,  $I_0 = (0.54 \pm 0.07)$  A and  $B = (26.7 \pm 1.8)$ . Both the experimental data and the fit for  $^{39}\text{K}$  are reported in Fig. 4.4.

The maximum allowed current in the dispenser, 6.4 A, sets the highest pressure we reach, i.e.  $3.9 \times 10^{-7}$  mbar. Below the dispenser ignition point, a residual pressure of  $4 \times 10^{-8}$  mbar is likely due to potassium vapor slowly released by the chamber walls. This contribution is very dependent on the temperature of the vacuum chamber walls, and is conspicuous for long running times when chamber walls are warmed up by thermal contact with dispensers.

In Fig. 4.5(a) we report the measured atomic flux as a function of the pressure for  $^{39}\text{K}$ . As we can see, the flux increases with pressure until a critical point and then decreases. In the case of  $^{39}\text{K}$  this critical point occurs at  $p = 2.1 \times 10^{-7}$  mbar where a flux of  $1.0 \times 10^{11}$  atoms/s is reached. Such a critical point has been observed also for Rb [121, 122, 149] and ascribed to collisions with the background vapor. When the inverse collision rate becomes of the same order of the cooling time  $t_c$ , i.e. the time

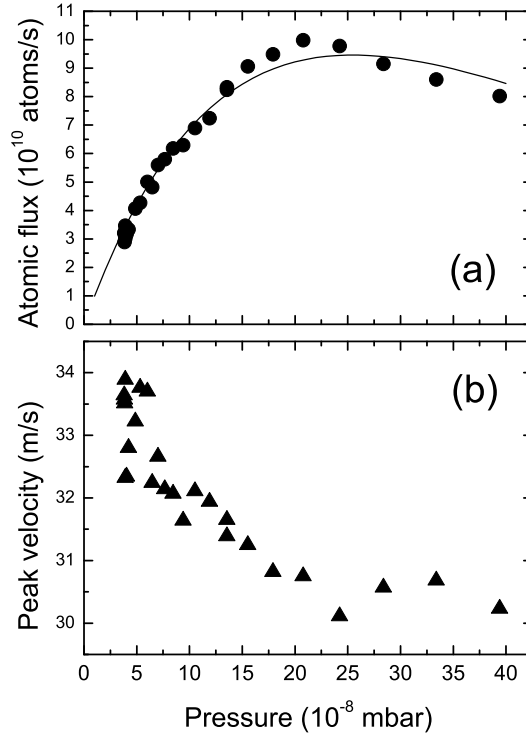


Figure 4.5: Measured  $^{39}\text{K}$  atomic flux (a) and peak velocity (b) reported as a function of gas pressure in the 2D-MOT chamber. Over the critical value  $p = 2.1 \times 10^{-7}$  mbar the atomic flux starts to be depleted by collisional effects. The solid line is a fit obtained using Eq. (4.4).

required to reach the mirror hole, the probability for an atom to reach the mirror hole drops. Assuming this is the case also for  $^{39}\text{K}$ , we fit our data to obtain the collision rate. The total flux is:

$$\Phi = \int_0^{\infty} \varphi(t_c) dt_c \quad (4.3)$$

where  $\varphi(t_c)$  is the cooling time distribution.

In the collisionless regime  $\varphi(t_c)$  is linearly proportional to the density, hence the pressure, in the 2D-MOT chamber. In presence of collisions with the background vapor,  $\varphi(t_c)$  is depleted for  $t_c > \gamma$ , where  $\gamma = \kappa p$  is the collision rate, proportional to the pressure  $p$ . Indeed, a single collision with an atom at room temperature ( $v_{th} =$

250 m/s) is sufficient to remove the cold atoms from the 2D-MOT velocity capture range. Then, if we assume that the cooling time distribution is a Gaussian

$$\varphi(t_c) = \frac{\Phi}{\sqrt{2\pi}\sigma} \exp\left(-\frac{(t_c - t_0)^2}{2\sigma^2}\right),$$

Eq. (4.3) is modified to

$$\begin{aligned} \Phi &= \int_0^\infty \varphi(t_c) e^{-\gamma t_c} dt_c \\ &= \frac{\Phi}{2} e^{-\gamma t_0 + \gamma^2 \sigma^2 / 2} \left(1 + \text{Erf}\left(\frac{t_0 - \gamma \sigma^2}{\sqrt{2}\sigma}\right)\right), \end{aligned} \quad (4.4)$$

where  $\text{Erf}(x) = \frac{2}{\sqrt{\pi}} \int_0^x \exp(-t^2) dt$  is the usual definition of the error function.

From the numerical simulations illustrated below, we obtain the first and second moment of the cooling time distribution:  $t_0 = 5.1$  ms and  $\sigma = 1.7$  ms. We then use Eq. (4.4) to fit the data, with two free parameters: an overall scaling factor and the collision rate to pressure ratio  $\kappa$ . The results of the fitting is shown by the solid line in Fig. 4.5(a). The collision rate given by the fit  $\gamma(\text{s}^{-1}) = (8.6 \pm 0.6) \times p$  ( $10^{-8}$  mbar) is approximately one order of magnitude larger than the value reported in [150]:  $0.3 \text{ s}^{-1}$  at  $p = 4 \times 10^{-9}$  mbar, i.e.  $0.75 \text{ s}^{-1} \times p$  ( $10^{-8}$  mbar). Our value is closer to the collision rates observed with rubidium. A meaningful comparison with Ref. [150] requires a more detailed investigation on the role of light-assisted collisions, assumed negligible for the 2D-MOT.

Another noticeable effect upon pressure increase is the slowing down of the atomic beam, as shown by the plot of the peak velocity in Fig. 4.5(b). This behavior is in contrast with the case of the simple rubidium 2D-MOT described in [122], where an increase of the gas pressure corresponds to the increase of the peak velocity. Therefore we attribute the observed effect to the progressive absorption of the push beam along its propagation path by the atomic gas since, as reported below, the peak velocity decreases as the push beam intensity is reduced.

As mentioned before, when not otherwise specified all data reported in this work have been taken at  $p = 7 \times 10^{-8}$  mbar.

#### 4.1.4 Push beam

We turn to the experimental investigation of the atomic beam behavior when the push beam parameters are changed. This is a crucial characterization since we observe no atomic flux in absence of the push beam, in accordance with the findings in experiments with rubidium [121, 122] where the 2D-MOT without push beam

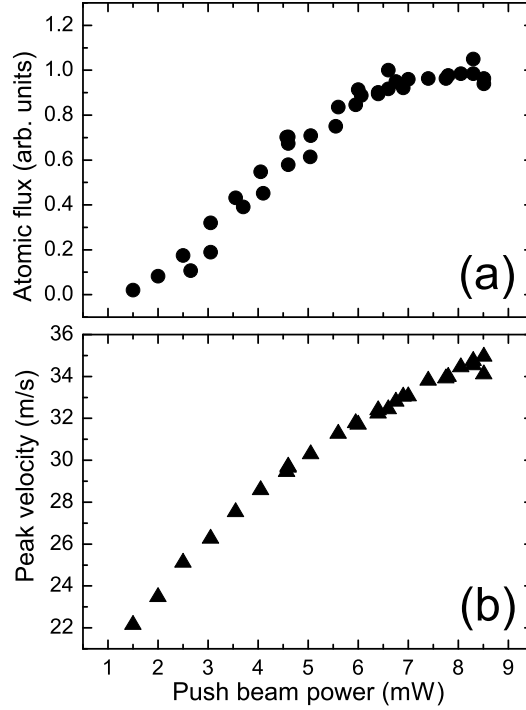


Figure 4.6: Atomic flux  $\Phi$  (a) and peak velocity (b) measured for  $^{39}\text{K}$  atomic beam as a function of the push beam power. In this analysis we set  $\delta_p = -5.2\Gamma$ .

is not efficient in our pressure range. Surprisingly, for potassium the push beam works best if one uses only repumping light, and therefore we define the push beam detuning  $\delta_p = \omega_p - \omega_{12}$ . We defer the discussion of this point to the end of the Section.

First we report the atom flux and peak velocity, Figs. 4.6(a) and 4.6(b) respectively, for  $^{39}\text{K}$  at fixed detuning  $\delta_p = -5.2\Gamma$  as a function of power. Above 6 mW, the atom number is approximately constant, while the peak velocity keeps increasing. Therefore, we use a power equal to 6 mW (peak intensity of  $170 \text{ mW}/\text{cm}^2$ ) in order to have the maximum flux with a velocity distribution still within the capture range of the 3D-MOT in which the atoms will be collected. Then, setting this value of power, we study the dependence of atomic flux and peak velocity on the push beam frequency for both  $^{39}\text{K}$  and  $^{41}\text{K}$ . Experimental results are reported in Fig. 4.7.

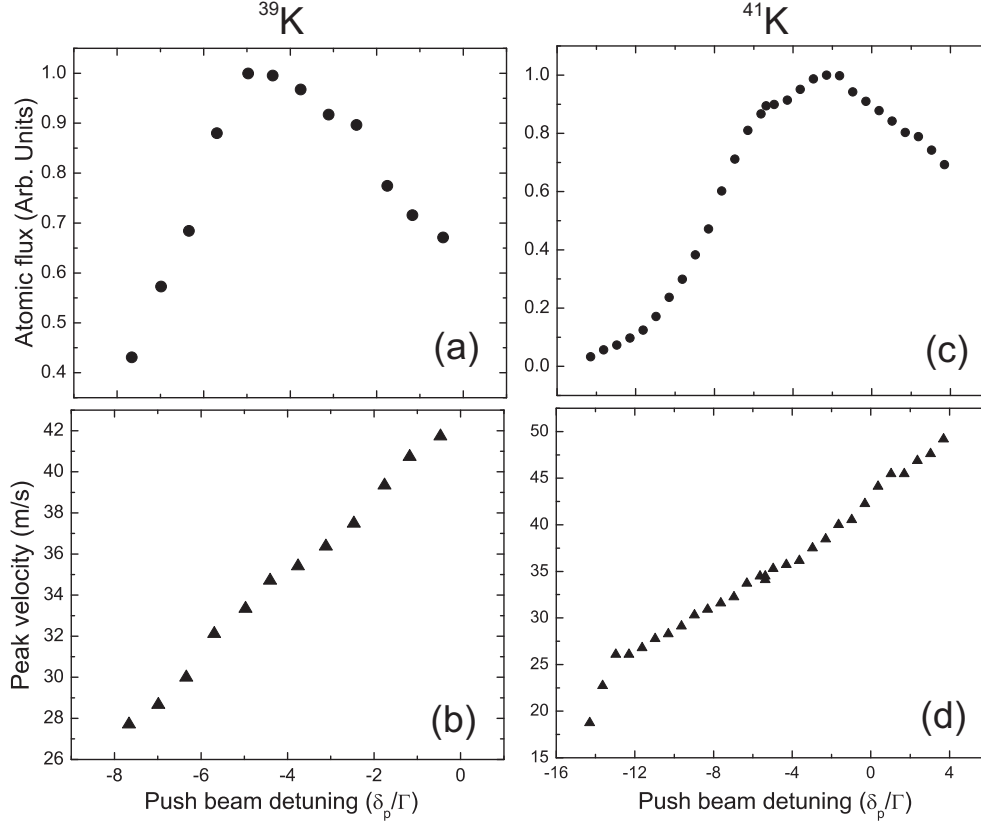


Figure 4.7: Measured atomic flux  $\Phi$  and peak velocity of  $^{39}\text{K}$  (a, b) and  $^{41}\text{K}$  (c, d) as a function of the push beam frequency detuning  $\delta_p$ . The push beam power is set to 6 mW.

No clear enhancements of the flux stem from the addition of a counterpropagating hollow beam along  $-z$  direction ( $2\text{D}^+$ -MOT configuration). Only a 20% reduction in mean velocity was found for a  $\sigma^-$  beam polarization.

Given the hyperfine structure of potassium, one would expect to increase the efficiency of the push force using both cooling and repumping beams, since this avoids the depletion of the ground state population. On the contrary, the atomic beam is deteriorated even by a small fraction of cooling light  $\omega_2$  and it is almost extinguished when the  $\omega_2$  intensity approaches that of  $\omega_1$ . We attribute this effect to an increase of both the longitudinal velocity and the radial temperature of the atoms, when pushed by both frequencies. Instead, with a single frequency the hyperfine

#### 4.1. Characterization of $^{39}\text{K}$ and $^{41}\text{K}$ Bright Sources

	Repumping beams		Cooling beams		Push beam		Atomic flux [atoms/s]	Peak velocity [m/s]
	$P$ [mW]	$\delta_1$ [ $\Gamma$ ]	$P$ [mW]	$\delta_2$ [ $\Gamma$ ]	$P$ [mW]	$\delta_p$ [ $\Gamma$ ]		
$^{87}\text{Rb}$	1.5	-0.3	55	-1.2	5	-1.5	$5 \times 10^9$	30
$^{39}\text{K}$	50	-3.9	80	-5.8	6	-5.2	$6.2 \times 10^{10}$	35
$^{41}\text{K}$	47	-2.5	85	-3.0	6	-4.5	$5.2 \times 10^9$	33

Table 4.1: Optimal experimental beams power values ( $P$ ) and detunings ( $\delta$ ) used to generate a cold beam of  $^{87}\text{Rb}$ , of  $^{39}\text{K}$  and  $^{41}\text{K}$ . In the right part of the table the total flux  $\Phi$  values and the corresponding peak velocities are reported. The pressure working point is set to  $7 \times 10^{-8}$  mbar. The magnetic field gradient is 17 Gauss/cm.

optical pumping confines the action of the push force within the 2D-MOT volume and the atoms drift freely after the mirror hole.

One may argue that the push beam should then work also with the frequency  $\omega_2$  alone. We experimentally find that, at equal power,  $\omega_2$  light is far less efficient than  $\omega_1$ . We speculate that this is due to  $\omega_2$  being more prone to hyperfine optical pumping for two reasons: (i) in the 2D-MOT there is more cooling than repumping light, (ii)  $\omega_2$  detuned a few linewidths to the red of the  $|F = 2\rangle \rightarrow |F' = 3\rangle$  transition is near to the  $|F = 2\rangle \rightarrow |F' = 1, 2\rangle$  resonances causing hyperfine optical pumping (the same effect is less important for the  $\omega_1$  light, since the transitions  $|F = 1\rangle \rightarrow |F' = 2, 1\rangle$  are closer and there is no hyperfine optical pumping for  $|F = 1\rangle \rightarrow |F' = 0\rangle$ ). Another possible way to avoid hyperfine optical pumping is to use a blue detuned cooling light [151], even if this would increase the pushing efficiency mainly on fast atomic classes and hence confer to the atomic flux a higher peak velocity.

As Fig. 4.6(a) shows, decreasing the intensity of the laser beam the atomic flux decreases as well. In the pure 2D-MOT configuration, when no push beam is shone on atoms, no flux is detected, independently of both power and frequency of transverse beams and quadrupole magnetic field gradients.

#### 4.1.5 Summary

In Tab. 4.1.5 are summarized all the experimental parameters which maximize the total atomic flux  $\Phi$  of  $^{87}\text{Rb}$  and of the two K isotopes, and the values of the corre-

sponding fluxes. For  $p = 7 \times 10^{-8}$  mbar high atomic fluxes are achieved, containing  $6.2 \times 10^{10}$  atoms/s and  $5.2 \times 10^9$  atoms/s for  $^{39}\text{K}$  and  $^{41}\text{K}$  respectively. The pressure value and their small peak velocities, respectively 35 and 33 m/s, are perfectly adequate to an efficient subsequent loading in a UHV environment 3D-MOT. By increasing  $p$  up to  $2.1 \times 10^{-7}$  mbar a flux of  $1.0 \times 10^{11}$  atoms/s of  $^{39}\text{K}$  is then observed. Nearly the same gain is expected for  $^{41}\text{K}$  flux as well at the same value of pressure  $p$ .

The high intensity of atomic fluxes is an essential point in order to reach a degenerate regime for K isotopes following a double MOT cooling and trapping scheme. At optimal detunings, with a 15 times lower light intensity, we achieve a 3D-MOT loading rate higher than the one reported in [120]. Thus, we conclude that, to generate a cold atomic beam, a 2D-MOT shows a much higher efficiency when compared to an ordinary 3D-MOT.

## 4.2 A Simplified Multilevel Theoretical Model

To have a quantitative description of our observations we use an extension of the theoretical model discussed in [149]. This model shortcuts the integration of the optical Bloch equation by assuming a heuristic expression of the total force exerted by the different beams, all having the same frequency, on a two-level atom:

$$\begin{aligned} \mathbf{f} &= \frac{\hbar\Gamma}{2} \sum_i \mathbf{k}_i \frac{s_i}{1 + \sum_j s_j}, \\ s_j &= \frac{I_j}{I_s} \frac{\Gamma^2}{\Gamma^2 + 4(\delta_j - \mathbf{k}_j \cdot \mathbf{v})^2} \end{aligned} \quad (4.5)$$

where  $i, j$  denote the beams and  $I_s = \pi\hbar c\Gamma/(3\lambda^3)$  is the two-level saturation intensity, equal to  $1.8 \text{ mW/cm}^2$  for potassium  $D_2$  line. Authors of Ref. [149] employ this model to analyze a 3D-MOT of Rb with the addition of a push beam. The extension of this treatment to bosonic potassium, because of the narrow upper level structure, requires to take into account all the allowed hyperfine transitions. For this purpose, we introduce the further assumption that forces arising from different transitions add independently. This consistently disregards coherences among the two  $4S_{1/2}$  hyperfine states, which however play no role in the Doppler cooling mechanism. In principle, we should consider even the Zeeman structure of the hyperfine levels; in practice, to reduce the number of transitions contributing to the total force, we calculate the detunings and the line strength in a manner to average out the Zeeman sublevels. For each laser beam  $i$  and each transition  $|F\rangle \rightarrow |F'\rangle$ , we define the average detuning  $\Delta_i^{FF'}$  as the center-of-mass of all the Zeeman components weighted

by the squared Clebsch-Gordan coefficients  $|c(F', m'; 1, \sigma_i, F, m)|^2$ , where  $\sigma_i$  denotes the beam polarization (all beams are circularly polarized with the MOT required helicity). This detuning depends linearly on the displacement from the 2D-MOT axis via the magnetic field gradient. We then define the strength of each hyperfine transition:

$$G_i^{FF'} = \frac{\sum_{m,m'} |c(F', m'; 1, \sigma_i, F, m)|^2}{\sum_{F',m,m'} |c(F', m'; 1, \sigma_i, F, m)|^2}.$$

We incorporate hyperfine optical pumping by breaking the force into two parts, due to the cooling and the repumping light, weighted by the relative populations in the  $F = 2$  and  $F = 1$  ground levels. Therefore, the expression (4.5) of the total force is generalized as follows:

$$\mathbf{f} = \frac{p_1}{p_1 + p_2} \mathbf{f}_1 + \frac{p_2}{p_1 + p_2} \mathbf{f}_2 \quad (4.6)$$

$$\mathbf{f}_F = \frac{\hbar\Gamma}{2} \sum_i \mathbf{k}_i \frac{s_{i,F}}{1 + s_F}, \quad F = 1, 2 \quad (4.7)$$

with

$$s_{i,F} = \frac{I_{i,F}}{2I_s} \sum_{F'} G_i^{FF'} \frac{\Gamma^2}{\Gamma^2 + 4(\delta_{i,F} - \mathbf{k}_i \cdot \mathbf{v} - \Delta_i^{FF'})^2},$$

where  $s_F = \sum_j s_j$ . Here,  $I_{i,1}, I_{i,2}$  are respectively the repumping and cooling intensity of the  $i$ -th beam, and  $\delta_1, \delta_2$  the corresponding detunings as defined earlier. The populations  $p_1, p_2$  are taken as the equilibrium values of the rate equations for the six hyperfine components.

### 4.2.1 Numerical Simulations

A numerical integration of the classical equations of motion yields the phase-space trajectories. We consider only the atoms that, at  $t = 0$ , lie on the boundary surface  $S$  of the 2D-MOT volume, approximated by a rectangular box with sizes equal to the beam diameters. In sampling the velocity-space, the Boltzmann factor is nearly unity for all velocities lying within the 2D-MOT capture range, well below the 250 m/s thermal velocity. From the integration we extract: (i) the fraction  $\wp$  of the atoms exiting the mirror hole to the atoms entering the 2D-MOT volume, (ii) the longitudinal velocity distribution of the atomic beam, and (iii) the distribution of the cooling time  $\varphi(t_c)$ , as defined earlier. To obtain the total flux, we only need to

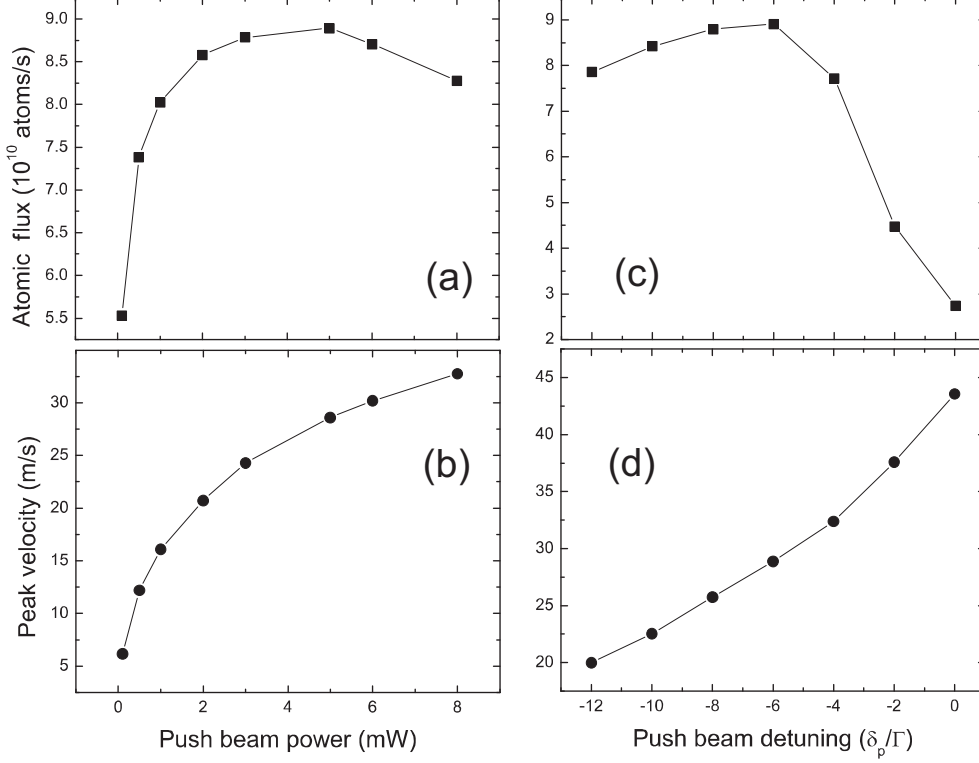


Figure 4.8: Results of simulations for  $^{39}\text{K}$ : total flux and peak velocity as a function of the push beam power (a,b) and detuning (c,d).

multiply  $\varphi$  by the total number of atoms entering the cooling volume per second, at pressure  $p$  and room temperature  $T$ :

$$\Phi = \varphi \times S \frac{p}{\sqrt{2\pi m k_B T}}. \quad (4.8)$$

In our simulation multiple scattering of light and intra-beam atomic collisions are neglected. The collisions with background gas, occurring at rate  $\gamma = 60 \text{ s}^{-1}$ , are accounted for by weighting each trajectory with a factor  $\exp(-\gamma t_c)$  to deplete the tail of atoms with long cooling times  $t_c$ . We also select only those atoms flying in a cone 34 mrad wide around the longitudinal axis  $z$ .

Setting the experimental parameters as in Table 4.1.5, with a quadrupole magnetic field gradient of 17 Gauss/cm, for  $^{39}\text{K}$  we obtain a total flux  $\Phi_{\text{sim}} = 8.7 \times 10^{10}$  atoms/s, with a peak velocity of 30.2 m/s, in good agreement with the experi-

mental values reported in Table 4.1.5. Repeating the simulation for different values of the push beam power and detuning we find the curves plotted in Fig. 4.8. The agreement with the experimental findings is satisfactory for the peak velocities. As for the total flux, the model shows saturation in push power at lower values than in the experiment and an optimum detuning of  $-6\Gamma$  close to the observed value of  $-5.2\Gamma$ . The calculated dependence of atomic flux on push beam power and detuning reproduces only qualitatively the experimental curves of Figs. 4.6(a) and 4.7(a). We believe that coherent effects ignored in our simulations are likely responsible for the discrepancies with data. A more exact analysis based on the integration of optical Bloch equations is needed to address these issues but is beyond the scope of our simplified model.

*4. INTENSE SLOW BEAMS OF BOSONIC POTASSIUM ISOTOPES*

---

# Chapter 5

## Collisional Properties of Sympathetically cooled $^{39}\text{K}$

In this Chapter I report the state of the art of our experimental investigation about the properties of a sympathetically cooled  $^{39}\text{K}$  sample. The experimental demonstration of the efficiency of sympathetic cooling process among  $^{87}\text{Rb}$  and  $^{39}\text{K}$  represented one of the main goals of this work, since it opens the way to the investigation of *true ultracold* collisional studies, previously restricted to a MOT environment via a photoassociation method [60]. This method allowed a determination of the intra-specie scattering length value of  $^{39}\text{K}$ , measured as  $-33 a_0$  [60], negative and one third in modulus the intra-specie scattering length of  $^{87}\text{Rb}$ . The attractive and weak character of the interactions, together with the limited number of  $^{39}\text{K}$  atoms that is collectable in a MOT, determines the importance of an efficient sympathetic process in the  $^{87}\text{Rb}$ - $^{39}\text{K}$  mixture. The presence of  $^{87}\text{Rb}$  as a "refrigerative" specie, indeed, eases the cooling of  $^{39}\text{K}$  to ultra low temperatures, since the relatively small initial number of  $^{39}\text{K}$  atoms coming out from the MOT phase is preserved during the sympathetic cooling process, and allows to obtain a reliable ultracold potassium sample in the  $\mu\text{K}$  regime. Moreover, in the case of attractive samples, the scattering theory predicts a sudden reduction of the cross section in proximity of a certain value of the temperature (Ramasauer minimum), corresponding to  $320 \mu\text{K}$  for  $^{39}\text{K}$ . This obstacle is overcome by the sympathetic cooling process, since the character of interspecies interaction in the  $^{87}\text{Rb}$ - $^{39}\text{K}$  mixture is repulsive ( $a_{12} = 36 a_0$ ) and no reduction of the cross section is predicted.

In the first part of the Chapter we will describe the optimization of the sympa-

thetic cooling process via the calibration of the evaporative ramp when both species have to be cooled, while the second part will be devoted to report the measured intraspecie collisional properties obtained through a cross thermalization procedure on the sympathetically cooled  $^{39}\text{K}$  sample.

## 5.1 Sympathetic Cooling of $^{39}\text{K}$

The technique of sympathetic cooling has been first proposed for two-component plasmas [152], and subsequently applied to cool neutral atoms and obtain double state BEC [26]. By means of this technique Fermi gases has recently been brought to fractional Fermi energy [153] and the degeneration has clearly been signed by the direct observation of Fermi pressure [154, 155], while double species condensates has been simultaneously obtained and characterized [88, 156]. The idea of sympathetic cooling relies on the efficiency of the rethermalization process occurring between two different atomic species, among which only one is provided by a high scattering length value and hence can undergo an effective cooling via an evaporation procedure. In this way the most interacting specie acts as a coolant for the other specie.

Obviously, this procedure is far away to work for every elements pair. In particular, if the interspecie triplet cross section  $\sigma_{12}$  does not reach a proper value the sympathetic cooling process, occurring on a timescale of the order of the thermalization time  $\tau_{th}$ , would require such long times to give to the background collision processes the time to ruin the binary sample. The zero energy cross section for the  $^{87}\text{Rb}$ - $^{39}\text{K}$  mixture is  $\sigma_{12}^0 = 4\pi a_{12}^2 = 4\pi (36 a_0)^2$ , corresponding approximately to  $\frac{1}{8}$  the  $^{87}\text{Rb}$  intraspecie value. This does not give the possibility to predict *a priori* the effectiveness of a sympathetic cooling for this mixture. Moreover, as we will briefly see in the following, the temperature dependence of the scattering amplitude can lead to a strong deviation of the collisional rate from its zero energy expression, which becomes a good approximation only in the last part of the evaporation procedure when  $\mu\text{K}$  temperatures are reached. On the other hand, this behavior would be much more accentuated in the case  $^{39}\text{K}$  is directly cooled by means of an evaporative procedure. Indeed, as shown in Ref. [26], the attractive character of the intraspecie interaction opens the possibility for a system (not necessarily binary) to undergo a drop in the interaction strength due to the Ramsauer-Townsend effect, predicting a zero in the cross section for a certain collision energy (and hence temperature). Last but not least, the reduced number of atoms in a potassium MOT (see Chap. 3) would not allow for a direct evaporation process due to its intrinsic atom-wasting nature,

which would lead to an eventual very poor ultracold sample. For this motivations the demonstration of the reliability of a sympathetic process in the  $^{87}\text{Rb}$ - $^{39}\text{K}$  mixture is far from being trivial and acquires a consistent relevance.

The temperature dependence of the interspecies  $s$ -wave cross section  $\sigma_{12}$  comes out from effective range theories and is embedded in the dependence on temperature of the relative wave vector  $k$ :

$$\sigma_{12} \simeq \frac{4\pi a_{12}^2}{\left(1 - \frac{1}{2}r_s k^2 a_{12}\right)^2 + a_{12}^2 k^2}, \quad (5.1)$$

where  $r_s$  is the effective range of the potential, depending on the van der Waals coefficients and more in general on the shape of the interaction potential. If the temperature is not exceeding values of the order of  $\sim 50 \mu\text{K}$ , the dependence on  $k^2$  (i.e. on energy) can be usually neglected, to recover the usual energy independent expression for the cross section:

$$\sigma_{12}^0 \simeq 4\pi a_{12}^2. \quad (5.2)$$

In our experimental apparatus a cold mixture of  $^{87}\text{Rb}$  and  $^{39}\text{K}$  is prepared after a MOT pre-cooling phase with the procedure described in Sec. 3.8. A total number of  $N_{Rb} = 2 \times 10^8$   $^{87}\text{Rb}$  atoms with a starting temperature of  $\sim 500 \mu\text{K}$  is prepared as a thermal bath for the  $^{39}\text{K}$  sample that comes out from the pre-cooling stage with a higher temperature ( $\sim 1 \text{ mK}$ ) due to the absence of sub-Doppler processes (see Sec. 3.1.1). As we will see in the following, the initial atom number  $N_K$  for  $^{39}\text{K}$  shows a deep influence on the sympathetic evaporation process, eventually leading to a full depletion of the  $^{87}\text{Rb}$  sample before the evaporation end is reached if  $N_K$  exceeds a critical value.

### 5.1.1 Effects on the evaporation ramp

As a first consideration, since the interspecies scattering length  $a_{12}$  is smaller than the  $^{87}\text{Rb}$  intraspecies scattering length  $a_1$ , we expect the interspecies rethermalization process to be the limiting factor in the evaporation ramp velocity. We would hence expect a longer duration of the whole evaporation process if compared to the  $^{87}\text{Rb}$  alone. To get an idea of the timescale over which the sympathetic evaporation should take place, we neglect the effective range correction to Eq. (5.1) and the eventual contribution of  $p$ -wave collisions to the thermalization process, usually negligible for temperatures below  $\sim 100 \mu\text{K}$  if particular shape resonances are absent.

We then note that the variation timescale  $\tau_{ev}$  of the  $\mu$ -wave cut in the <sup>87</sup>Rb velocity distribution should not exceed the interspecie thermalization rate  $\tau_{th}$  of the binary mixture, determined by the interspecie collision rate  $\gamma_{12} = 1/\tau_{12}$  and thermalization cross section  $\sigma_{th}$ , in such a way the potassium sample walks through a continuous series of quasi-equilibrium states and follows the <sup>87</sup>Rb temperature, decreasing throughout the evaporation. It can be shown, analogously to the single specie case [157, 158], that the evaporation rate for <sup>87</sup>Rb is given by the expression:

$$\tau_{ev} = \sqrt{8\bar{n}} \sigma_1 \bar{v} \eta e^{-\eta}, \quad (5.3)$$

where  $\bar{n}$  and  $\bar{v}$  represent the mean density and collisional velocities, given by Eq. (5.10). The parameter  $\eta$  is an experimental factor of proportionality between the energy corresponding to the frequency cut and the actual temperature of the sample during the evaporation in such a way  $E_T = \eta k_B T$ . A reasonable value of this parameter is usually much higher than 1, where the above expression for  $\tau_{ev}$  holds. For our evaporation, the typical initial value for  $\eta$  is 6, and is assumed constant throughout the whole evaporation process.

For a binary mixture compound by  $N_1 + N_2$  atoms the thermalization rate has recently shown to be [159]:

$$\frac{1}{\tau_{th}} = \frac{8}{3} \frac{N_1 + N_2}{N_1 N_2} \frac{m_1 m_2}{(m_1 + m_2)^2} \frac{\langle \sigma_{th} \rangle}{\langle \sigma_{12} \rangle} \Gamma_{12} \quad (5.4)$$

where the  $\langle \cdot \rangle$  quantities represent the thermal average of the collisional and thermal cross sections keeping into account for the energy distribution of the clouds. The total number of collision events per unit time is calculated as:

$$\Gamma_{12} = N_1 N_2 c \frac{\langle \sigma_{12} \rangle}{\pi^2 \sqrt{2}} \left( \frac{\mu \omega_1 \omega_2}{k_B T} \frac{(m_1 + m_2) \omega_1 \omega_2}{m_1 \omega_1^2 + m_2 \omega_2^2} \right)^{3/2}, \quad (5.5)$$

with  $\omega_{1,2}$  mean oscillator frequencies of the trap for both species and  $c = \sqrt{2k_B T/\mu}$ . For a cross section of the form  $\sigma_{12} = 4\pi a_{12}^2 / (1 + a_{12}^2 k^2)$ , one finds:

$$\begin{aligned} \langle \sigma_{12} \rangle &= 4\pi a_{12}^2 \xi [1 - \xi e^\xi \Gamma(0, \xi)], \\ \langle \sigma_{th} \rangle &= 2\pi a_{12}^2 \xi [1 - \xi + \xi^2 e^\xi \Gamma(0, \xi)], \end{aligned} \quad (5.6)$$

where  $\xi = \hbar^2 / (2\mu k_B T a_{12}^2)$  and  $\Gamma(a, z) = \int_z^\infty t^{a-1} e^{-t} dt$ , being  $\mu$  the reduced mass of the system. In the very low temperature limit  $\xi \gg 1$ , we have  $\langle \sigma_{12} \rangle = \langle \sigma_{th} \rangle = 4\pi a_{12}^2$ ; in the unitary limit  $\xi \ll 1$ , we obtain  $\langle \sigma_{12} \rangle = 2\langle \sigma_{th} \rangle = 2\pi \hbar^2 / (\mu k_B T)$ . As a consequence, in the case of distinguishable atoms having the same mass, the number

$\tau_{th}\Gamma_{12}/N_i$  of inter-species collisions per atom required to equilibrate the temperature of a two-component system made of atoms of the same mass varies from 1.5 in the very low temperature limit to 3 in the unitary limit. It is worth noticing that the validity of condition  $r_e \ll a_{12}$  has to be verified in each single case, and that where  $r_e \simeq a_{12}$  the  $a_{12}r_e k^2$  term appearing in the expression (5.1) is of the same order of the  $a_{12}^2 k^2$  term and can no more be neglected.

With the above expressions, we can calculate the collisional rate  $\gamma_{12}$  at a given temperature  $T$  and hence the expected ratio  $\tau_{th}/\tau_{ev}$  for each point of the ramp. A good sympathetic cooling efficiency is obtained if  $\tau_{th} < \tau_{ev}$ , that we call *runaway condition*. For  $N_1 = 2 \times 10^8$ ,  $N_2 = 4 \times 10^4$  and  $T = 200 \mu\text{K}$ , representing a point lying typically initial part of the ramp, we obtain  $\tau_{th}/\tau_{ev} \sim 2$ , meaning that the ramp velocity has to be nearly 2 times the value that is optimizing the ramp for the  $^{87}\text{Rb}$  alone. For a typical point representing the end of the evaporation process ( $N_1 = 1 \times 10^5$ ,  $N_2 = 2 \times 10^4$  and  $T = 1 \mu\text{K}$ ) we obtain  $\tau_{th}/\tau_{ev} \sim 1.3$ , that is closer to the runaway condition but still higher than 1. By doubling the ramp duration we obtain  $\tau_{th}/\tau_{ev} < 1$  both in the initial and final part of the evaporation, due to the fact that the  $\eta$  parameter value depends on the sweep rate of the ramp, increasing with the ramp duration. A typical value of  $\eta = 7$  is sufficient to achieve the runaway of the sympathetic cooling process, since in this case we get  $\tau_{th}/\tau_{ev} < 0.8$ .

### 5.1.2 Experimental evidence for sympathetic cooling in the $^{87}\text{Rb}$ - $^{39}\text{K}$ mixture

As done for the  $^{87}\text{Rb}$  alone, the procedure to optimize the evaporation ramp when a mixture has to be sympathetically cooled consists in the maximization of the phase space density (PSD) or elastic collisional rate  $\gamma_i$  for each specie after every linear step of the  $\mu$ -wave frequency sweep. This can be done both by varying the frequency sweep and by adjusting the relative number of atoms between the two species. The goal is to obtain a sub- $\mu\text{K}$  binary sample with a balanced atom number. Since the evaporative cooling procedure acts on  $^{87}\text{Rb}$  alone while the atom losses due to background gas collisions act on both species with the same rate, the  $^{87}\text{Rb}$  atom number  $N_{\text{Rb}}$  will be strongly depleted if compared to the  $N_{\text{K}}$ . On the other hand, if during the procedure the thermal bath reduces too much the  $^{39}\text{K}$  sample starts to overheat the  $^{87}\text{Rb}$  cloud, leading the latter towards a premature cut by the  $\mu$ -wave radiation. More quantitatively, the condition for  $^{87}\text{Rb}$  to represent a good thermal bath for the  $^{39}\text{K}$  sample corresponds to a condition on the thermal capacities  $C_i$  of the two species, namely  $C_{\text{Rb}} \geq C_{\text{K}}$ . For an ideal classical gas the thermal capacity is

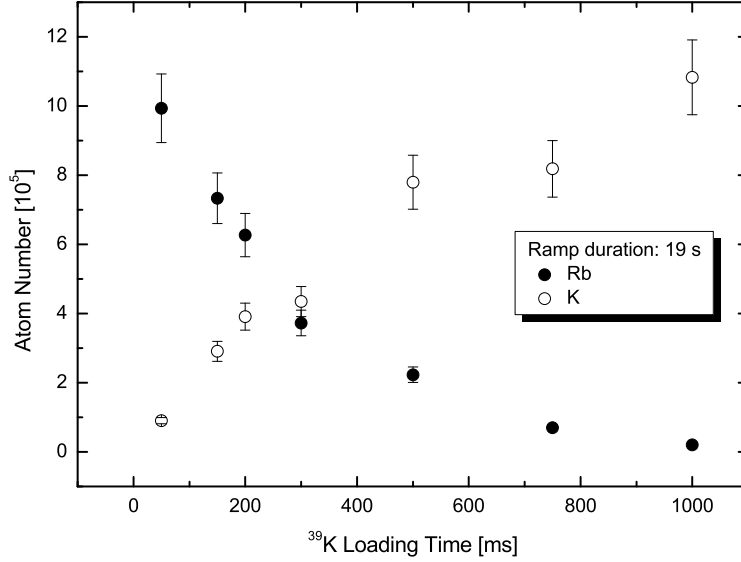


Figure 5.1: Atoms numbers of the two species for a fixed duration of the evaporation ramp (19 s). Full and empty circles represent  $^{87}\text{Rb}$  and  $^{39}\text{K}$  respectively. Data are reported as a function of the 3D-MOT loading time, varied through the duration of the push beam generating the  $^{39}\text{K}$  cold atomic beam. The initial  $^{87}\text{Rb}$  atom number is fixed to  $2 \times 10^8$ .

independent on the mass of the atoms, and is given by  $C_i = 3N_i k_B T$ , thus leading to:

$$N_{\text{Rb}} \geq N_{\text{K}}, \quad (5.7)$$

holding for two atomic clouds with the same temperature. This condition has to be fulfilled during the whole ramp.

The initial relative atom number can be varied simply by controlling the duration of the  $^{39}\text{K}$  atomic flux feeding the 3D-MOT (Sec. 3.2.1), that is nicely proportional to the total atom number loaded into the milli-trap before evaporation starts. The results of the measurement of  $N_{\text{Rb}}$  and  $N_{\text{K}}$  for both species after an evaporation ramp of 19 s are reported in Fig. 5.1. The initial atom number for  $^{87}\text{Rb}$  is set to  $2 \times 10^8$ , obtained for a fixed loading time of the  $^{87}\text{Rb}$  3D-MOT equal to 8 s. If the

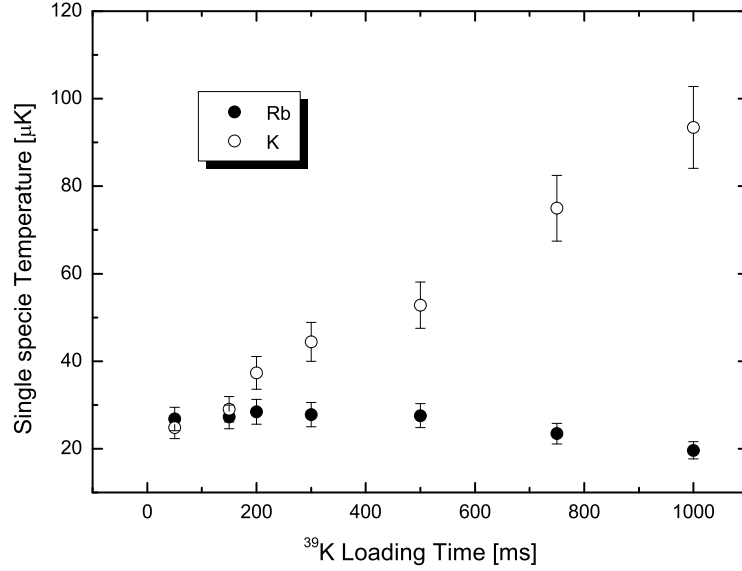


Figure 5.2: Absolute temperature of the two species for a fixed duration of the evaporation ramp (19 s). Full and empty circles represent  $^{87}\text{Rb}$  and  $^{39}\text{K}$  respectively. Data are reported as a function of the 3D-MOT loading time, varied through the duration of the push beam generating the  $^{39}\text{K}$  cold atomic beam. The initial  $^{87}\text{Rb}$  atom number is fixed to  $2 \times 10^8$ .

$^{39}\text{K}$  push beam duration is very short the initial  $^{39}\text{K}$  atom number remains much smaller than the  $^{87}\text{Rb}$  atom number during the whole evaporation, and the  $\mu$ -wave manages to cool down the  $^{87}\text{Rb}$  atomic cloud without particular losses respect to the single specie case, corresponding to  $t = 0$ . For increasing loading times the initial  $^{39}\text{K}$  atom number increases, and the cooling process becomes harder and harder for the  $^{87}\text{Rb}$  sample. The effect is a reduction of the final  $^{87}\text{Rb}$  atom number, due to the fact that a bigger fraction of  $^{87}\text{Rb}$  is overheated and undergoes an expulsion from the trap by the frequency cut. For this specific evaporation ramp, the critic condition (5.7) is reached for a loading time of  $\sim 300$  ms, where  $N_{\text{Rb}} = N_{\text{K}} = 4 \times 10^5$  is measured at the end of the ramp. A further increase of the loading time has as effect to shift the critical condition towards earlier steps of the ramp, and the final  $^{87}\text{Rb}$  atom number results conspicuously depleted, vanishing for loading times of

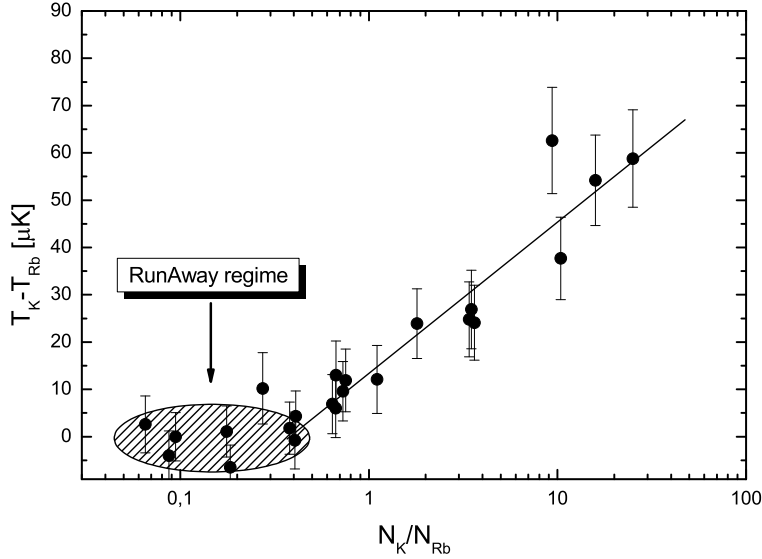


Figure 5.3: Temperature difference between the two species measured as a function of the relative atom number. The ramp length is 19 s, while the initial  $^{87}\text{Rb}$  atom number is set to  $2 \times 10^8$ .

the order of 1 s. Error bars are obtained for a statistical uncertainty of 10% over measured temperatures and atom numbers. Since the final temperature in the critical case is  $27 \mu\text{K}$  for the  $^{87}\text{Rb}$  sample, a further decrease of the final temperature requires a reduction of the initial  $^{39}\text{K}$  atom number, in such a way the critical condition is avoided for longer evaporation times as well.

If the temperatures of both species, rather than the atom numbers, are reported as a function of the loading time of this evaporation ramp (Fig. 5.2), the effect of the presence of  $^{39}\text{K}$  atoms on  $^{87}\text{Rb}$  sample is mapped onto the permanence of a temperature difference  $\Delta T$  among the two species at the end of evaporation. The amplitude of  $\Delta T$  is a direct hint on the goodness of the initial conditions and ramp details that have been chosen. As we can see, for long loading times the big  $^{39}\text{K}$  atom number unhinges the efficiency of the sympathetic cooling process since the thermal capacity of  $^{87}\text{Rb}$  drops as the  $^{87}\text{Rb}$  atom number. In this situation the residual  $\Delta T$  is of

the same order of the final temperature. The  $^{87}\text{Rb}$  temperature is practically fixed by the final frequency of the  $\mu$ -wave cut. In an optimized situation the ramp should lead to a runaway condition (see above), meaning that no lag between the two temperatures should appear. Fig. 5.2 shows how this ramp attains this condition for loading times  $t \lesssim 200$  ms, where the temperatures of both species are equal within the experimental uncertainty.

A deeper information on the runaway regime can be extracted from Fig. 5.3, where the measured difference between the temperatures of the two species is reported as a function of the final relative atom number  $N_{\text{K}}/N_{\text{Rb}}$ . Here an optimized ramp is employed to cool the mixture for a fixed time of 21 s. As we can see, the actual runaway condition for the sympathetic cooling process is reached for  $\frac{N_{\text{K}}}{N_{\text{Rb}}} \lesssim 0.3$ . Below this value the  $^{39}\text{K}$  sample maintains a thermal equilibrium with the  $^{87}\text{Rb}$  cloud throughout the whole evaporation, and no temperature difference is observed among the two species. Notice that this experimental value differs by a factor 3 from the value (5.7), that represents anyway a simple estimation obtained through intuitive considerations.

The evolution of the binary system during an optimized ramp is shown in Fig. 5.4, where the absolute temperatures (a) and atom number (b) of both samples are reported as a function of the ramp evolution time. The final temperature attained is  $T \simeq 2 \mu\text{K}$ , while the atom numbers are  $N_{\text{K}} = 2 \times 10^4$  and  $N_{\text{Rb}} = 8 \times 10^4$ . In this situation, the efficiency of the sympathetic cooling in the  $^{87}\text{Rb}$ - $^{39}\text{K}$  mixture is demonstrated by the absence of any lag among the temperature of  $^{87}\text{Rb}$  (full circles) and  $^{39}\text{K}$  (empty dots) along the whole evaporation of  $^{87}\text{Rb}$ . The  $^{87}\text{Rb}$  atoms number is exponentially decreasing following the  $\mu$ -wave frequency sweep, while the  $^{39}\text{K}$  atoms number decreases under the only effect of the background gas hot collisions on the milli-trap lifetime timescale ( $\sim 30$  s for a trap current of 95 A).

Up to now we have shown the efficiency of the sympathetic cooling to achieve ultra-low temperatures, anyway higher than  $1 \mu\text{K}$ . A further cooling of the binary system towards sub- $\mu\text{K}$  temperatures requires a small change in the strategy of the very last part of the sympathetic cooling process. Indeed, our experimental investigation pointed out that when one tries to cool the mixture below  $3 \mu\text{K}$  by slowly reducing the  $\mu$ -wave frequency cut, the net effect is a rapid depletion of the  $^{87}\text{Rb}$  sample, while the  $^{39}\text{K}$  temperature starts to lag above the  $^{87}\text{Rb}$  temperature. This process onsets for  $T \simeq 3 \mu\text{K}$ . We have found that a way to come around this obstacle is to avoid an excessive slowing down of the frequency sweep in the last part of the ramp ( $\lesssim 3 \mu\text{K}$ ), while is preferable to maintain the same slope of the ramp until the fre-

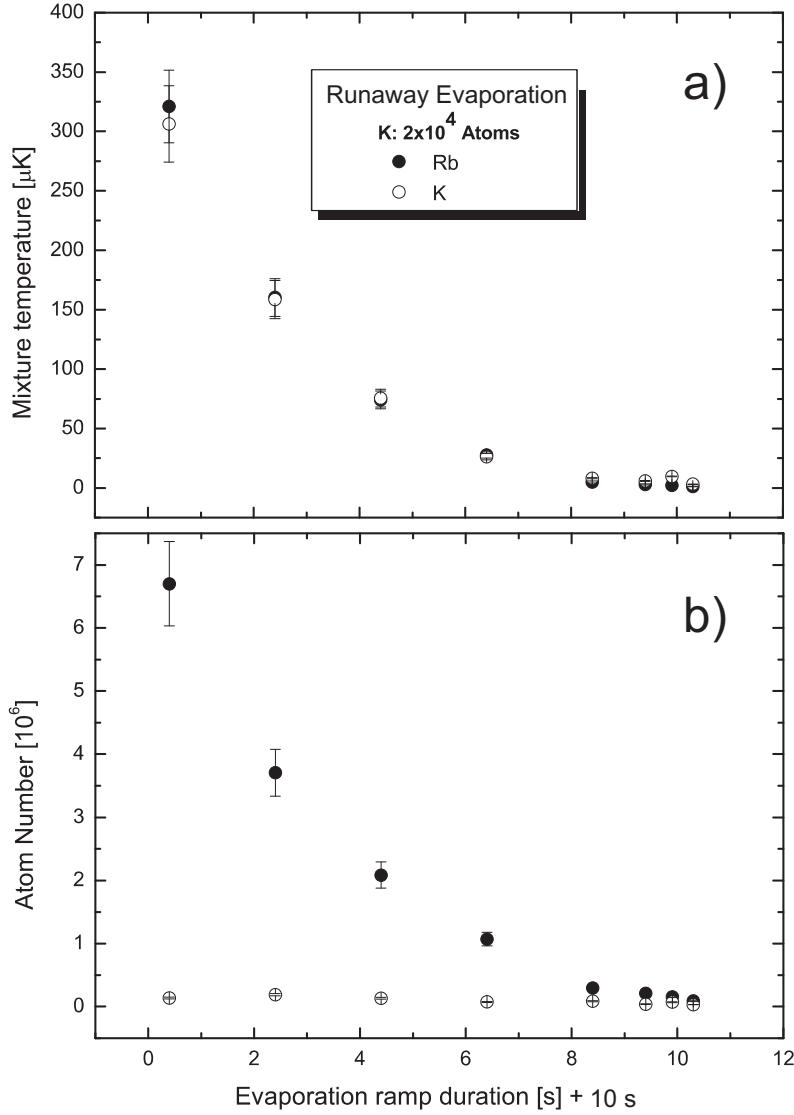


Figure 5.4: Typical evolution of the binary sample in an evaporation runaway. Measured temperatures (a) and atom numbers (b) for both species as a function of the evaporation time. The runaway of sympathetic cooling is demonstrated by the absence of any lag among the temperature of  $^{87}\text{Rb}$  (full circles) and  $^{39}\text{K}$  (empty dots). The final temperature is  $T \simeq 2 \mu\text{K}$ , while the atom numbers are  $N_{\text{K}} = 2 \times 10^4$  and  $N_{\text{Rb}} = 8 \times 10^4$  respectively.

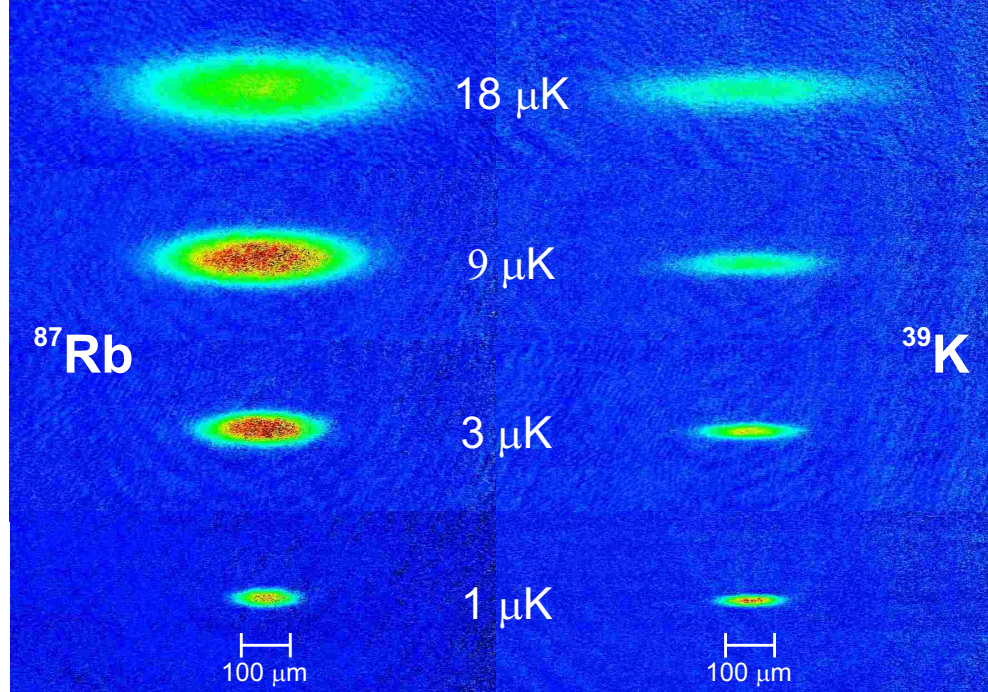


Figure 5.5: Snapshots of the  $^{87}\text{Rb}$  sample (left) and  $^{39}\text{K}$  sample (right) taken in the last part of the evaporation ramp after 1 ms of free expansion from the milli-trap. The corresponding atom numbers are  $N_{\text{K}} = 2 \times 10^4$  and  $N_{\text{Rb}} = 3 \times 10^4$ .

quency value corresponding to  $T_{\text{Rb}} \simeq 1 \mu\text{K}$  is reached. Then the  $\mu$ -wave is left on for a rethermalization time of  $\sim 1$  s required to complete the sympathetic cooling process. During this time the small lag in the  $^{39}\text{K}$  vanishes at the expense of the  $^{87}\text{Rb}$  atom number, that anyway does not undergo a fast depletion as in the previous case. In this phase the  $^{87}\text{Rb}$  sample acts as a *thermal buffer* for the  $^{39}\text{K}$  sample. The presence of the microwave frequency is crucial to achieve a  $\mu$ -wave shielding against a heating of the  $^{87}\text{Rb}$  cloud, whose population is in this phase comparable to the population of  $^{39}\text{K}$ . The result of this change in the sympathetic cooling strategy is evident in Fig. 5.5, where a final temperature of  $1 \mu\text{K}$  is obtained for both rubidium and potassium. The atoms numbers are  $N_{\text{K}} = 2 \times 10^4$  and  $N_{\text{Rb}} = 3 \times 10^4$  respectively. The thermal buffer depletion, testified by an enhanced decrease of the  $^{87}\text{Rb}$  optical density (Sec. 3.7) is evident for  $T < 1.2 \mu\text{K}$ . This depletion experimentally increases if the plateau in the ramp is held at lower frequencies, since the probability for a

$^{87}\text{Rb}$  atom to receive an energy kick beyond the cutting edge of the evaporation frequency from a hotter  $^{39}\text{K}$  atom gets higher.

Lower temperatures could probably be attained if the initial  $^{87}\text{Rb}$  atom number is increased and the duration of the plateau is slightly increased, in such a way the thermal buffer is more populated and the final buffer cooling process can be actuated at a lower frequency cut.

## 5.2 Cross Thermalization in Ultracold $^{39}\text{K}$

In this second part of the Chapter we report experimental results concerning cross thermalization measurements performed on an ultracold  $^{39}\text{K}$  sample, cooled by means of a sympathetic procedure described and characterized in the previous part of the Chapter. This technique allowed us to measure the low energy cross section for  $^{39}\text{K}$  and to obtain an estimation of the triplet s-wave scattering length  $a_T$  [160].

Cross thermalization refers to the relaxation process of an atomic sample after an energy imbalance has been introduced between two orthogonal directions. Since the temperature of an harmonically trapped gas is proportional to the squared RMS width of the gaussian atomic distribution (see Sec. 3.4), the evolution of this energy imbalance can be extracted by observing the size of the cloud along different directions. Notice that since the system is brought away from thermal equilibrium by an external excitation the temperatures along different directions are not necessarily coincident. We will hereinafter refer to these temperatures as *orthogonal* temperatures. In a cylindrical system where  $z$  is the symmetry axis we will label as  $T_z$  and  $T_r$  the axial and radial temperatures respectively. In the ideal case of a noninteracting gas, anyway, if an initial difference is induced between two orthogonal temperatures, shaking for instance the system in a specific direction for a certain time, this difference will not vary in time. This behavior comes directly from the independence of the orthogonal degrees of freedom of a harmonically trapped ideal gas, reflecting the separability of the trapping potential. On the other hand, if the gas is interacting the thermal equilibrium can no more be defined for both directions separately, and the collisions between atoms, whose rate is proportional to the squared intraspecie scattering length  $a^2$  drive the system towards a global thermal equilibrium through a *cross dimensional* rethermalization. The number of collisions  $\alpha$  necessary to an effective cross dimensional energy exchange is usually taken as a free parameter and can be obtained for our system through a numerical simulation of the collisional processes after the directional excitation is induced, yielding  $\alpha = 2.7$ . This number represents the ratio of the collisional rate  $\gamma_{\text{el}}$  to the thermalization rate  $1/\tau = \gamma_{\text{th}}$ :

$$\alpha = \gamma_{\text{el}} \tau . \quad (5.8)$$

The collisional scattering rate can be obtained once the mean density  $\bar{n}$  is introduced:

$$\gamma_{\text{el}} = \bar{n} \langle \sigma v \rangle , \quad (5.9)$$

where  $\sigma$  represents the collisional cross section,  $v$  the thermal velocity of two colliding atoms and  $\langle \cdot \rangle$  an average over the thermal distribution of the atoms. For low temperatures  $\sigma$  is barely dependent on temperature (Sec. 5.1) and results  $\sigma = 8\pi a_T^2$ , with  $a_T$  the triplet scattering length. In this way the average  $\langle \cdot \rangle$  appearing in the above equation can be factorized as  $\langle \sigma v \rangle = 8\pi a_T^2 \langle v \rangle$ . It is worth mentioning that for appreciable temperature variations the analogous of the formula (5.1) should rather be employed to obtain an average cross section weighted on the atomic momentum distribution. The last part of this Section contains a deeper analysis of this issue. For an harmonic trap whose radial and axial frequencies are  $\omega_r/(2\pi)$  and  $\omega_z/(2\pi)$  respectively we have:

$$\bar{n} = \left( \frac{m}{4\pi k_B \bar{T}} \right)^{3/2} N \bar{\omega}^3 \quad (5.10)$$

$$\langle v \rangle = 4 \left( \frac{k_B \bar{T}}{\pi m} \right)^{1/2}, \quad (5.11)$$

where  $\bar{T} = \sqrt[3]{T_r^2 T_z}$  and  $\bar{\omega} = \sqrt[3]{\omega_r^2 \omega_z}$  indicate the geometric average of the two orthogonal temperatures and frequencies respectively. Thus, assuming a constant average density during the relaxation process, and defining an average temperature-dependent cross section as:

$$\tilde{\sigma} = \frac{\langle \sigma v \rangle}{\langle v \rangle}, \quad (5.12)$$

the relaxation rate can be written as:

$$\frac{1}{\tau} = \frac{\tilde{\sigma}(\bar{T})}{\alpha} \frac{N}{2\pi^2 k_B} \frac{m \bar{\omega}^3}{\bar{T}}. \quad (5.13)$$

As we checked by means of numerical calculations, the average cross section defined by Eq. (5.12) represents, in our experimental conditions, a good approximation of the actual cross section  $\sigma$ . The assumption of constant density in time holds only if the relaxation time is much smaller than the typical trap lifetime, limited by the background gas collisions rate. In our experiment the atom losses during the relaxation process are not negligible. It can be numerically shown that these losses have as a consequence to shift the equilibrium value of the temperature aspect ratio  $T_z/T_r$  from 1, which is hence left as a free parameter in our data analysis. This obviously influences the equilibrium value of the physical aspect ratio of the cloud as well, deviating the system from the stationary value  $\Delta z/\Delta r = \sqrt{\omega_r/\omega_z}$ , where we used the RMS gaussian widths of the cloud.

Using Eq. (5.13) it is clear that by performing a measurement of the cross collisional thermalization time  $\tau$  one can trace back the value of the triplet scattering

length  $a_T$  at low energies, or more in general, the value of the collisional cross section  $\sigma$  and its dependence on temperature.

It is important to stress that the relaxation time  $\tau$  refers to the *energetic* relaxation of the system, that is directly related to the temperature relaxation along each direction. We will henceforth extract the relaxation time constant by looking at the *temperatures*, rather than by measuring directly the evolution of the *size* of the system as in other works is done [161, 162, 163]. This is equivalent to observe the evolution of the *squared size* of the cloud. An *a posteriori* analysis has nevertheless demonstrated that with our experimental timescale and within experimental uncertainties these two time constants are undistinguishable and, for all practical purposes, both the width of the cloud and its square relax exponentially. A typical evolution of the cloud RMS axial and radial sizes and of their ratio is reported in Fig. 5.6. This measure corresponds to a  $^{39}\text{K}$  sample compound by  $N = 3 \times 10^5$  atoms at a mean temperature of  $16 \mu\text{K}$ . As can be seen, the axial extension progressively grows under the effect of the cross dimensional rethermalization, while the initially excited axial extension slightly decreases. Notice that the total energy, i.e. the mean RMS size of the cloud has to remain constant during the evolution, and possible observed variations have to be attributed to the effect of the collisions with the background gas.

### 5.2.1 Experimental procedure

The cold  $^{39}\text{K}$  sample is prepared by means of the experimental procedure described in the previous Section and in Chap. 3, through a sympathetic cooling technique with  $^{87}\text{Rb}$ . The evaporation is stopped when the desired temperature is reached, and then the  $^{87}\text{Rb}$  sample is blown away from trap by means of a fast resonant light pulse ( $200 \mu\text{s}$ ) with 10 mW of power. The milli-trap current is set to 95 A with  $\sim 6$  G as bias field, producing frequencies  $\omega_r = 2\pi \times 447$  Hz and  $\omega_z = 2\pi \times 29.2$  Hz for  $^{39}\text{K}$ . This step avoids any further collisional relaxation between the two different species. The initial energetic imbalance between the two directions is introduced by modulating for a time  $t_{\text{mod}}$  the radial frequency of the magnetic trap at twice its stationary value  $\omega_r$  for  $^{39}\text{K}$ . This procedure introduces a parametric heating in the system (see Sec. 3.4.2), and if  $t_{\text{mod}}$  is sufficiently small compared to the relaxation time  $\tau$  only the radial direction will be affected by this excitation. In our procedure the modulation is performed on the bias field current, acting on the radial frequency alone, for a time  $t_{\text{mod}} = 100$  ms that is much longer than  $\omega_r^{-1}$ . The RMS current modulation depth is 15%. Starting from this point we follow two different procedure to measure the evolution of the system:

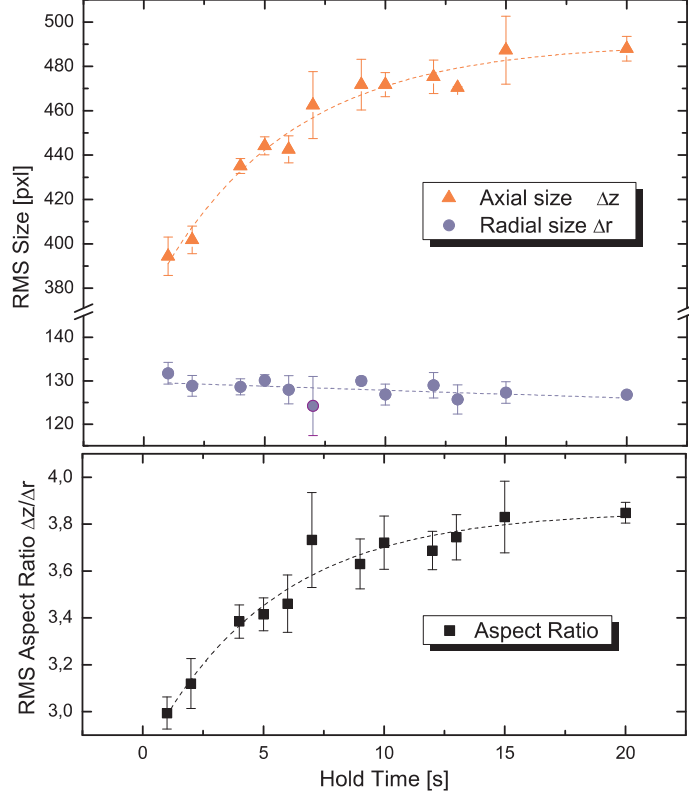


Figure 5.6: Axial and radial RMS widths (upper panel) and their ratio (lower panel) in a  $^{39}\text{K}$  sample with  $N = 3 \times 10^5$  and  $\bar{T} \simeq 16 \mu\text{K}$ , measured after a variable hold time following a radial excitation of the trap and a fixed expansion time of 2 ms. The trap current is set to 50 A with 3 G as bias field. Dashed lines represent exponential fits to data. During the relaxation the shape of system evolves towards the unperturbed configuration.

- we let evolve the cloud into the trap with the original frequencies  $\omega_r = 2\pi \times 447$  Hz and  $\omega_z = 2\pi \times 29.2$  Hz for an evolution time  $t$ , and then we perform an *in situ* imaging of the  $^{39}\text{K}$  cloud. The orthogonal temperatures are extracted from the cloud size by  $T_i = m\omega_i^2 \Delta x_i^2 / k_B$ ; the advantages of this scheme is to provide a good S/N ratio due to the high optical densities of the trapped cloud. On the other hand the radial size is very small, even if it remains bigger than the diffraction limit of the optical system, and suffers of a conspicuous uncertainty. We checked that the magnetic field inhomogeneity due to the presence

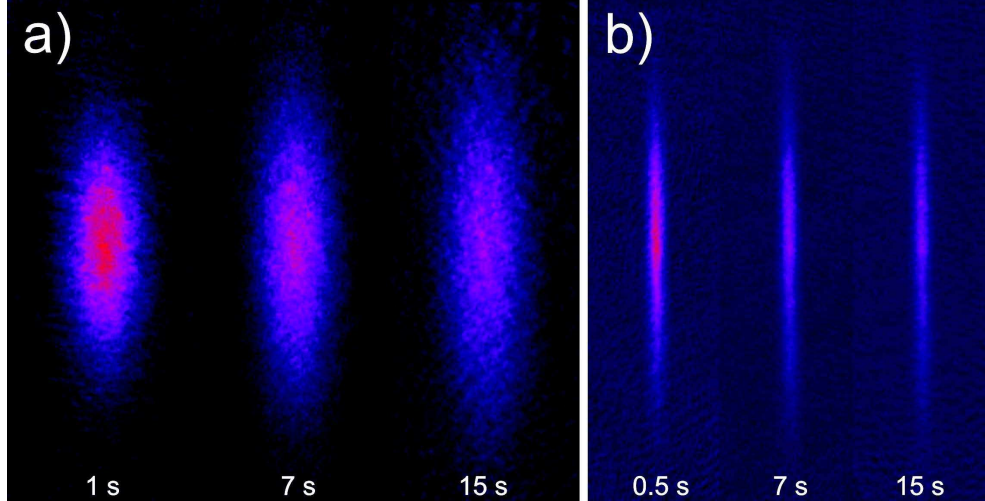


Figure 5.7: Absorption images of the  $^{39}\text{K}$  cloud for different evolution times after the parametric heating taken in the decompressed trap after 2 ms of expansion (a), and *in situ* (b). The axial direction is the vertical, and the two panels are not to scale. As can be seen, in both cases the system relaxes by increasing its axial width in time.

of the trap did not introduce uncontrolled effects in the imaging. The mean initial temperature of the sample is  $\bar{T} \simeq 29 \mu\text{K}$ .

- After the modulation phase we adiabatically decompress the magnetic trap, lowering the current to 50 A and increasing the bias field to 6 G. In this situation the evolution of the cloud sizes takes place with  $\omega_r = 2\pi \times 290 \text{ Hz}$  and  $\omega_z = 2\pi \times 21.2 \text{ Hz}$ . After a variable hold time  $t$  the trap is released and the cloud expands for  $T_{\text{exp}} = 2 \text{ ms}$ . This procedure allows a zero-field imaging of the sample, avoiding any possible spurious effects due to the inhomogeneity of the magnetic field. Moreover, each experimental cycle is consistently reduced, thus allowing for longer evolution times of the sample in the trap. On the other hand, optical densities are smaller if compared to the trapped case and the detection of the sample is harder. The mean initial temperature of the sample is  $\bar{T} \simeq 16 \mu\text{K}$ .

Fig. 5.7 reports a series of three images taken for different evolution times in the case of decompressed trap (a) and with an *in situ* observation (b). The axial direction is the vertical, and the two panels are not to scale. As can be seen, in both cases the

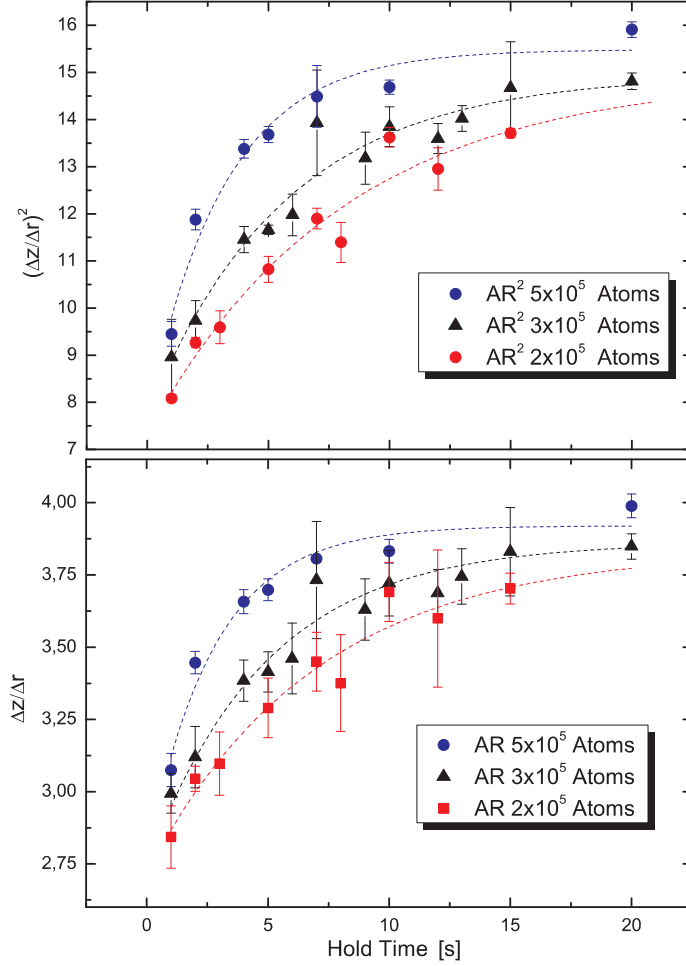


Figure 5.8: Evolution of the aspect ratio  $(\Delta z/\Delta r)$  (lower panel) and of  $(\Delta z/\Delta r)^2$  (upper panel), proportional to the orthogonal temperatures, in a  $^{39}\text{K}$  sample with  $N = 3 \times 10^5$  and  $\bar{T} \simeq 16 \mu\text{K}$ . The evolution is measured after a variable hold time following a radial excitation of the trap and a fixed expansion time of 2 ms. The trap current is set to 50 A with 6 G as bias field. Dashed lines represent exponential fits to data. For a given atom number the time constants for the evolution of  $(\Delta z/\Delta r)$  and  $(\Delta z/\Delta r)^2$  are consistent each other within the experimental uncertainties.

system relaxes by increasing its axial width in time. These measurements require a careful control on the atom number. The uncertainty on  $N$  is represented by the standard deviation on the measured initial atom number. If a binning is performed

on  $N$ , three different datasets for each of the procedures above mentioned can be extracted, reported as different symbols in Fig. 5.8 in the decompressed trap case. The atoms numbers are  $N_1 = 2 \times 10^5$  (red circles),  $N_2 = 3 \times 10^5$  (black squares), and  $N_3 = 5 \times 10^5$  (blue triangles). As comes out from Eq. (5.13), the thermalization rate  $1/\tau$  is observed to depend on the atom number  $N$ . The dashed lines represent exponential fits of the form  $y = y_0 - y_1 \exp(-t/\tau_N)$ , where  $\tau_N$  gives the relaxation time for a specific atom number  $N$ . Notice that the asymptotic value  $y_0$  is left as a free parameter and is slightly different for each  $N$ , reflecting the effect of atom losses from the trap during the evolution time. Error bars are obtained taking the standard deviation on both  $\Delta z$  and  $\Delta r$  and adding their relative uncertainties.

### 5.2.2 Determination of the triplet scattering length of <sup>39</sup>K

Our measurements provide two distinct sets of thermalization times  $\tau$ , each depending on the specific trap configuration employed during the evolution of the system after the parametric heating. In both expanded and *in situ* configurations the determination of the axial and radial temperatures does not represent a particular task, due to the relatively big size of the sample. The mean temperature  $\bar{T}$  appearing in Eq. (5.13) is hence tagged with sufficient accuracy by the 2D fits performed on the absorption images (see Sec. 3.7) and can be taken as a known value. On the contrary, for lower temperature values the determination of the temperature in the trapped system usually represents a hard task, since the radial extension of the cloud becomes comparable to the diffraction limit of our imaging system, hindering a precise determination of the temperature and atom number of the sample. The measured thermalization rates  $\gamma = 1/\tau_N$  are reported in Fig. 5.9 as a function of the atom number  $N$ . The two panels correspond to the decompressed trap case after 2 ms of free expansion (a), and to *in situ* configuration (b). As can be seen in figure, in both experimental cases the cross thermalization rate  $1/\tau$  shows a linear dependence on the atoms number  $N$ . To determine the collisional triplet cross section  $\sigma$  from the measured scattering rates it is worth noticing that Eq. (5.13) holds only in the case the trapping potential is fully separable. In a real trap, anyway, the presence of a residual anharmonicity (Sec. 3.4) and more in general of a non complete separability of the potential causes the system to cross-relax even in the ideal case of non interacting particles, the relaxation being mediated by the coupled degrees of freedom of the trapped atoms. We refer to this process as to *ergodic mixing* of the atomic ensemble. This mixing potentially can deviate the dependence of the scattering rate on the number of atoms, introducing a residual collisional rate  $\gamma_{\text{mix}}$  occurring for  $N = 0$ .

The ergodic mixing contribution can be taken into account by separating the component of the relaxation rate which is linear in  $N$ , from the extrapolation in the limit of zero density where relaxation can only occur through ergodic mixing. One can therefore assume that

$$\frac{1}{\tau} = \frac{1}{\alpha} \frac{d\gamma_{\text{el}}}{dN} N + \gamma_{\text{mix}} = AN + \gamma_{\text{mix}}. \quad (5.14)$$

By using Eq. (5.13) one hence has:

$$A = \frac{\tilde{\sigma}}{\alpha} \frac{m\omega_r^2\omega_z}{2\pi^2 k_B \bar{T}}, \quad (5.15)$$

The values of this parameter can be extracted, together with the residual mixing rate  $\gamma_{\text{el}}$ , from a two parameter linear fit of the form  $y = AN + \gamma_{\text{mix}}$  performed separately on the two datasets. The best fit functions are reported in Fig. 5.9 as dashed lines. We note here that one should expect the ergodic mixing effect to be less severe in the weak trap case than in the tight trap regime, since the harmonic trapping region has an extension that is decreasing as  $\bar{\omega}^{-1}$ . From the fit results, reported in the figure insets, we extract a residual ergodic mixing that is largely consistent with zero within the experimental uncertainties. From the value of the parameter  $A$  optimizing the fit to the data we obtain two different values for the triplet scattering length, corresponding to two distinct values of the temperature:

$$\tilde{\sigma} = (2.2 \pm 0.8) \times 10^{-16} \text{ m}^2; \quad \tilde{\sigma}' = (0.91 \pm 0.22) \times 10^{-16} \text{ m}^2, \quad (5.16)$$

for  $\bar{T} = (16.0 \pm 0.9) \mu\text{K}$  and  $\bar{T}' = (28.9 \pm 1.0) \mu\text{K}$  respectively. Even if these values are statistically different, the zero energy approximation does not include any dependence of the thermalization cross section on temperature, and the difference in the values we measured cannot be directly addressed to the temperature difference between the two datasets. Within the zero energy approximation we have  $\sigma = 8\pi a_T^2$ , and the measured values for the scattering length  $a_T$  are:

$$|a_T(16 \mu\text{K})| = (57 \pm 11)a_0; \quad |a_T'(29 \mu\text{K})| = (36 \pm 5)a_0, \quad (5.17)$$

where  $a_0$  is the Bohr radius. The presence of the absolute value is due to the temperature independence of the scattering length expression.

Actually, in order to account for the occurrence of a temperature dependence of the collisional rate the simple zero energy form  $\sigma = 8\pi a_T^2$  can no more be employed for the determination of the scattering length even in a low temperature regime. As explained above, in an effective potential picture one has to account for the effective

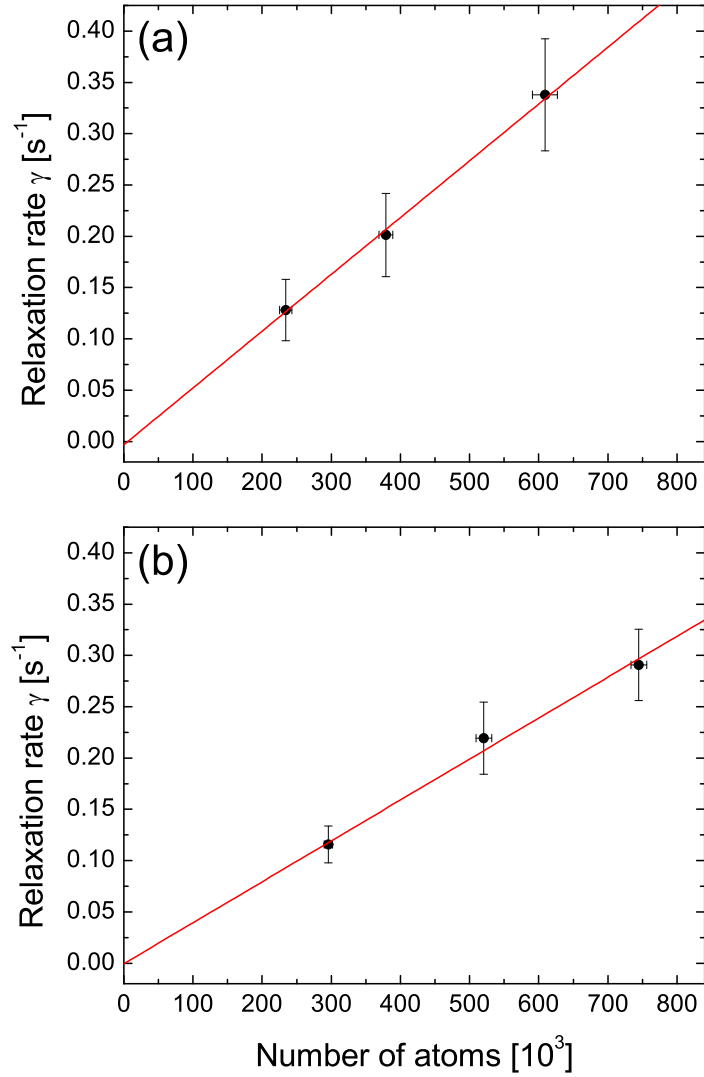


Figure 5.9: Cross thermalization rates  $\gamma = 1/\tau$ , reported as a function of the number of atoms, in the case of decompressed trap (a) and *in situ* (b) measurement. Each data-point is extracted from a fit performed on different set of measurements as the ones reported in Fig. 5.8. The two different methods correspond to two different temperatures,  $16 \mu\text{K}$  (a) and  $29 \mu\text{K}$  (b) respectively. The fit results are:  $\gamma_{\text{mix}} = -(0.003 \pm 0.065) \text{ s}^{-1}$  and  $A = (5.5 \pm 1.6) \times 10^{-7} \text{ s}^{-1}$  for figure (a) and  $\gamma_{\text{mix}} = (0.0005 \pm 0.034) \text{ s}^{-1}$  and  $A = (4.0 \pm 1.0) \times 10^{-7} \text{ s}^{-1}$  for figure (b).

range contribution to the expression of the cross section, given by Eq. (5.1) provided a factor 2 is introduced to account for the undistinguishability of the particles. We remark that this involves the calculation of the effective range for the specific collisional potential [164], that can be calculated once the  $C_6$  coefficient of the van der Waals potential is known [165]. This should confer a temperature dependence to the cross section, that remains anyway closely tied to the theoretical values of the collisional parameters mentioned above. If the values of the effective range obtained combining Refs. [164, 165] are employed, a significative modification of the scattering length values is obtained:

$$a_T(16 \mu\text{K}) = -(65 \pm 11) a_0; \quad a'_T(29 \mu\text{K}) = -(45 \pm 5) a_0. \quad (5.18)$$

These values are different by  $1.75 \Delta a$ , where  $\Delta a = \sqrt{(\Delta a_1)^2 + (\Delta a_2)^2}$  is the combined standard deviation calculated from the specific standard deviations  $\Delta a_1$  and  $\Delta a_2$ . The calculated effective range values are  $r_s = 2119 a_0$  and  $r_s = 995 a_0$  for  $a_T = -33 a_0$  and  $a_0 = -57 a_0$  respectively. For comparison, we notice that, if we neglect the effective range contribution, the absolute values of above scattering lengths would be  $(57 \pm 11) a_0$  and  $(36 \pm 5) a_0$  respectively. The quoted uncertainties derive mainly from the error on the time constant of the relaxation process obtained by fits on data as the ones reported in Fig. 5.8, and from the atom number calibration ( $\pm 20\%$ ), performed independently for each data set.

We carefully checked that the systematical contributions to this discrepancy have been, as far as possible, minimized. The main contributions can arise from: (a) the calibration factor that gives the number of atoms from the absorption images in the two different trap configurations; (b) an imperfect optical pumping procedure that leads to a residual population of the  $|F = 2, m_F = 1\rangle$  state, whose presence would alter the effective collisional properties of the sample. Since the whole discrepancy cannot be fully attributed to a temperature dependence of the collisional cross section, from the above values we extract the final value for the triplet s-wave scattering length  $a_T$  by calculating the weighted mean value, and by multiplying the associated uncertainty by a factor  $\sqrt{\chi^2} = 1,65$  in order to set the confidence level to 68% [166]:

$$a_T = -(51 \pm 7) a_0. \quad (5.19)$$

We remark that a detailed analysis of the collisional properties of an ultracold  $^{39}\text{K}$  sample requires a temperature dependent expression for the cross section even for temperatures as low as  $16 \mu\text{K}$ , since the deviations introduced by the effective potential approach are not negligible.

We notice again that, even if the measured triplet scattering length should in principle be sufficiently large to allow for a direct evaporative cooling of the  $^{39}\text{K}$  sample, the relatively low number of atoms that can be collected in a MOT for the potassium isotopes (Sec. 3.1) is expected to prevent the possibility to exploit the direct evaporation to cool a reliable number of atoms to the  $\mu\text{K}$  temperature regime.



# Conclusions and Perspectives

This thesis has been devoted to the description of a new generation apparatus devised to produce ultracold K-Rb atomic mixtures and to study their fundamental properties. The design, the realization and the characterization of this new machine have represented the main part of my Ph.D. work, which started three years ago.

The decision to develop a reliable and highly versatile experiment to employ in the investigation of heteronuclear Bose-Bose mixtures has been motivated by the relatively small amount of experimental and theoretical works available at that time [88, 89, 90]. This could appear somewhat surprising, since the coexistence of two *different* bosonic species in external potentials opens the way to the observation of intriguing and insightful phenomena. In particular, the possibility to reach a combined BEC and to tune the interspecies scattering length through an external magnetic field in proximity of a Fano-Feshbach resonance gives the opportunity to study the interplay between two superfluids whose interaction can be easily managed. The basilar features of the ground state of such a system have been theoretically revised in the end of the first chapter. Moreover, the recent development of high power infrared lasers eases the exploration of the quantum phase transition from superfluid to Mott insulator, recently observed in single specie systems [8]. The ability to create a multi-specie BEC with tunable interactions and to load it into a high power optical lattice paves the way towards the experimental investigation of an insightful physical system of unprecedented realization: since the phase transition to Mott insulator represents a localization of an integer number of atoms per lattice site, and its onset differs for the two species, one can in principle achieve the condition in which one of the two species is in the superfluid phase, while the other is in the insulating regime and is arranged in discrete and regularly spaced clusters, constituting an actual material

lattice for the superfluid. The intriguing dynamics of a superfluid immersed into a periodical material crystal whose interactions can be arbitrarily controlled could in principle be studied, as well as the phase diagram of the heteronuclear mixture in the optical lattice [49, 52, 53]. A whole chapter has been devoted to the extraction of the crucial theoretical aspects concerning ultracold atoms in optical lattices.

Having these guidelines in mind, a highly reliable cold atoms sources system has first of all been designed. The development of this 2D-MOT system for both  $^{87}\text{Rb}$  and bosonic potassium isotopes yielded a net improvement on the existing methods to generate cold atomic beams, the starting point for every experiment designed to achieve quantum degeneracy in dilute atomic gases with high efficiency. Bi-dimensional magneto-optical trapping methods in potassium isotopes were lacking of studies before this work has been started. Despite of the difficulties arising from the levels structure of bosonic potassium isotopes, a detailed experimental analysis performed on both  $^{39}\text{K}$  and  $^{41}\text{K}$  2D-MOTs has demonstrated an unprecedented efficiency in the production of cold atomic beams, leading to atomic fluxes as high as  $10^{11}$  atoms/s with a mean velocity not exceeding 35 m/s. This allowed to shorten the 3D-MOT loading time by a factor 3 respect to preceding ordinary double 3D-MOT schemes with heavy reflections on the experiment duty cycle.

A conspicuous part of the thesis work has then been devoted to the characterization of a novel kind of magnetic trap, that we named "milli-trap", whose introduction has improved the confining capabilities of standard magnetic confining systems for neutral atoms such as ordinary QUIC traps. This is due to the fact that this new device is directly inserted in-vacuo, and the distance to the trapped sample is on the mm scale. Hence, the current power to be employed is significantly reduced, as well as the power that sinks on the trapping system. To our knowledge, the milli-trap is the most tightly confining magnetic device still providing a full three-dimensional optical access to the atomic system. Radial trap frequencies can attain values as high as 800 Hz with a bias field of 1 G. This allows to compress the atomic sample during the evaporative cooling process and to increase its density up to values that allow for a very fast evaporation process, whose timescales are of the order of 10 s. This represented an improvement of a factor  $3 \div 5$  respect to ordinary ex-vacuo traps, where the evaporation process for  $^{87}\text{Rb}$  takes  $30 \div 50$  s. Exploiting these unique features and the intensity of atomic sources our apparatus is capable to degenerate  $\sim 2 \times 10^5$   $^{87}\text{Rb}$  atoms to the BEC regime in experimental cycles as short as 25 s.

During the last period of my Ph.D. work two main experimental results have been obtained concerning both the  $^{87}\text{Rb}$ - $^{39}\text{K}$  mixture and the  $^{39}\text{K}$  alone. It is worth

remembering that this element presents attractive intraspecie interactions due to the negative value of the triplet scattering length. This confers to the  $^{39}\text{K}$  system intriguing features, such as the presence of a critical atom number over which the degeneration is not allowed and the system is supposed to collapse [78, 84, 85], or the possibility to study the evolution of particular solutions of the non-linear Schrödinger equation that governs the system, namely the dynamics of solitons. On the other hand, the inefficiency of the 3D-MOT cooling scheme that is intrinsic in the level structure of this isotope does not allow to employ an atoms-wasting technique such as the direct evaporative cooling to bring to the sub- $\mu\text{K}$  regime a  $^{39}\text{K}$  sample. This motivates the relevance of an experimental demonstration of the feasibility of a sympathetic cooling process among  $^{87}\text{Rb}$  and  $^{39}\text{K}$ , that is one of the main results obtained during the last six months of the Ph.D. work. By loading the binary mixture in the milli-trap and optimizing the evaporation procedure on  $^{87}\text{Rb}$ , we have been able to sympathetically cool  $\sim 2 \times 10^4$  potassium atoms to the sub- $\mu\text{K}$  regime. This represents a waypoint for eventual investigations on attractive condensates, never obtained up to now by means of the sympathetic cooling technique [82, 83].

Having demonstrated the feasibility of the sympathetic cooling process in the  $^{87}\text{Rb}$ - $^{39}\text{K}$  mixture, we exploited this technique to investigate the intrinsic collisional properties of ultracold  $^{39}\text{K}$  for temperature below  $50 \mu\text{K}$ . In particular, through the observation of cross-dimensional rethermalization processes we measured the triplet collisional cross section of  $^{39}\text{K}$  [160], finding a value ( $\sigma = -(51 \pm 7) a_0$ ,  $a_0$  being the Bohr radius) that is only partially consistent with the previously direct measurements result of [60], obtained by means of a completely different approach.

It is worth mentioning that exploiting the high versatility of the experimental apparatus, we have recently observed the simultaneous BEC of a  $^{41}\text{K}$ - $^{87}\text{Rb}$  heteronuclear mixture, with temperatures as low as  $70 \text{ nK}$  and number of atoms around  $2 \times 10^4$  for each specie.

The nearest perspectives of the experiment aim to the investigation of the dynamics of  $^{87}\text{Rb}$ - $^{39}\text{K}$  and  $^{87}\text{Rb}$ - $^{41}\text{K}$  Bose-Bose mixtures, in particular to the modification of the collective excitation properties that have already led to fruitful results in the single specie case. Furthermore, the current control and the magnetic coils system that are necessary to tune the interactions among atoms by means of an external magnetic field has been entirely built-up, and is ready to work. This will allow to scan a wide range of magnetic field intensities (0-1000 G) and to perform a detailed Fano-Feshbach spectroscopy both on single specie and binary mixture, up to now never performed on ultracold  $^{39}\text{K}$ - $^{39}\text{K}$  and  $^{87}\text{Rb}$ - $^{39}\text{K}$  systems. Again, the very last

part of my Ph.D. work has been devoted to devise the optical system that is necessary to introduce a high power 3D optical lattice in the apparatus. This represents the next evolution of the set-up, since as we have seen before the investigation of ultracold mixtures loaded in a periodic potential opens a wealth of intriguing research perspectives, such as the determination of the superfluid-insulator phase diagram in the case of a heteronuclear mixture [49, 52, 53], peculiar of a purely bosonic ultracold system.

# Ringraziamenti

Questi tre anni di dottorato hanno rappresentato per me un'importante fase della vita. Per questo motivo desidero ringraziare *in primis* il prof. Massimo Inguscio per avermi dato l'opportunità, dopo il lavoro svolto nella tesi di Laurea, di partecipare alla costruzione di un nuovo apparato sperimentale, scommettendo ancora una volta sulla mia persona e sulla mia volontà, e infondendo di giorno in giorno entusiasmo e viva determinazione. Ancora di più desidero ringraziarlo, però, per avermi affiancato in quest'avventura al dott. Francesco Minardi, responsabile del nuovo esperimento. Durante questi tre lunghi ed intensi anni, Francesco, ho potuto apprezzare la tua persona, prima ancora della tua preziosa efficienza scientifica. Non è certo stato facile partire da zero, da una stanza vuota, per imboccare il sentiero impervio ed affascinante verso la realizzazione di questo progetto. Ma è stato bello. Ti ringrazio per avermi insegnato tutto ciò che mi hai insegnato, e non è stato poco. Per aver risposto alle mie domande, con pazienza, e per aver preso in considerazione ogni mia proposta o idea, discutendola, ma mai facendola apparire come inutile. Per aver saputo senza dubbio interpretare (e tollerare!) la mia esuberante personalità. Sono davvero orgoglioso di essere stato al tuo fianco in questi anni. Come collega, e come amico.

Un ringraziamento particolare va al dott. Luigi De Sarlo, per il notevole contributo apportato all'esperimento, ma ancor prima per essere stato un prezioso compagno di viaggio, anche quando il viaggio devia dalla rotta prevista...ma del resto è il nostro mestiere, no? Grazie per le discussioni, le battute, le risate, Guccini, e per la tua *expertise* informatica che sopperisce alle mie carenze mostruose in merito! Grazie inoltre al primo laureando dell'esperimento, adesso prode dottorando, ossia al dott. Giovanni Barontini: nonostante le tue spiccate capacità ed attitu-

dini teoriche (peraltro molto utili a questo lavoro di tesi), vedremo di volerti bene lo stesso! Grazie anche per il tuo spirito gioviale e umoristico, sollievo nei bui momenti dell'incomprensibilità degli eventi sperimentali! Un grazie ed un saluto al dott. Paolo Maioli, che dopo aver consistentemente contribuito alla costruzione dell'apparato si è ricongiunto in quel di Lione alla sua amata. Paolone, ci manchi!

Grazie poi al team BEC1, ossia ai dott. Chiara Fort, Jessica Lye, Vera Guarrera e Leonardo Fallani, ed al team BEC2, ovvero ai dott. Chiara D'Errico, Matteo Zaccanty, Francesca Ferlaino ed in particolare al dott. Giacomo Roati ed al prof. Giovanni Modugno le cui preziose conoscenze hanno costituito un saldo fondamento per il nuovo apparato. In particolare desidero ringraziare Leonardo in qualità di ricercatore di eccezionale valore, ottimo chitarrista e sincero amico: grazie per i suggerimenti scientifici, per quelli umani e, ovviamente, per gli struggenti assoli!

Grazie al dott. Michele Modugno e al dott. Francesco Riboli per le numerose discussioni, per il supporto teorico fornito nella stesura della tesi e per la prontezza di spirito che li contraddistingue.

Grazie al gruppo tecnico-elettronico del Lens, Mauro Giuntini, Marco De Pas e Alessio Montori per il supporto fornitomi in special modo durante la prima fase del dottorato.

Dal momento poi che l'unione fa la forza, un ringraziamento caloroso va ai dott. Andrea Bertoldi e Giacomo Lamporesi del gruppo MAGIA, sempre pronti a prodigarsi in nostro aiuto nei momenti di difficoltà. Ma a Giacomino va un grazie ciclopico anche per le sue qualità fuori dal laboratorio, come insostituibile vero amico, di quelli che comunque ti girino le cose intorno sono sempre lì. Grazie davvero, di persone come te il mondo è povero.

Grazie a tutti i miei amici ed ai componenti del mio gruppo musicale che hanno sopportato il mio ipercriticismo artistico durante la stesura della tesi!

Un grazie sincero ed un bacio a tutta la mia famiglia, ed in particolare a mia sorella Silvia e a mio cognato Alfredo per l'aiuto fornitomi in questi anni ma soprattutto per il piccolo (si fa per dire!) Gherardo, splendida luce apparsa nel buio. Grazie poi a mio padre Renzo, che ha saputo trovare nuova forza per spronarmi e consigliarmi quando tutto è parso crollare.

A te Chiara, amore, il bacio ed il grazie piu' dolce per avermi sopportato, consigliato e motivato durante i momenti duri e vacillanti della mia vita, e per avermi condotto verso quelli belli e solari. Senza di te mai avrei potuto ottenere ciò che ho ottenuto. Ti ringrazio per la tua sensibilità e per la tua forza di volontà, che sono state e saranno per me esempio e motivo di orgoglio.

## *Ringraziamenti*

---

Il mio ultimo ringraziamento, mamma, va a te, per l'entusiasmo con cui hai accolto l'inizio del mio dottorato e per i preziosi consigli che mi hai saputo dare fino al tramonto. Le mie mani, il mio cervello ed il mio cuore ti dedicano il loro lavoro di questi tre anni. Sono sicuro che da lassù apprezzerai le mie realizzazioni e continuerai a guidarmi in quelle a venire.

J.



# List of Figures

1.1	Schematic BEC phase diagram . . . . .	8
1.2	Variational analysis of the energy for an attractive condensate . . . . .	16
1.3	Normalization factors and centers positions (b) of a binary mixture . . . . .	22
1.4	Possible topologies for a binary mixture of two BECs. . . . .	24
1.5	Phase diagram of the normalization integrals . . . . .	26
1.6	Overlap diagrams for $N_1 = 100000, N_2 = 50000$ . . . . .	27
2.1	Optical dipole trap . . . . .	35
2.2	Energy bands, Bloch velocity and effective mass . . . . .	39
2.3	Plot of a Wannier function . . . . .	41
2.4	2D optical lattice . . . . .	44
2.5	3D optical lattice . . . . .	45
2.6	Mott phase momentum distribution after expansion . . . . .	50
2.7	Phase diagram of the Mott-Hubbard Hamiltonian . . . . .	53
3.1	Snapshot of the apparatus . . . . .	58
3.2	Atomic levels diagrams . . . . .	60
3.3	Snapshot of the laser sources breadboard . . . . .	61
3.4	Lasers frequency lock data scheme for potassium . . . . .	63
3.5	Snapshot of the AOM branches . . . . .	65
3.6	Schematics of the optical setup . . . . .	66
3.7	Magneto-optical trap . . . . .	67
3.8	Our 2D-MOT scheme . . . . .	70
3.9	The 2D-MOT chamber . . . . .	72

3.10	Top view of vacuum system . . . . .	74
3.11	Ioffe-Pritchard trap scheme . . . . .	78
3.12	Milli-trap scheme . . . . .	79
3.13	Milli-trap field simulations . . . . .	81
3.14	Milli-trap mean life and heating rate . . . . .	83
3.15	Parametric heating trap frequency measurement . . . . .	85
3.16	Dipolar oscillation trap frequency . . . . .	87
3.17	Quadrupole field controller circuit . . . . .	90
3.18	Milli-trap field controller circuit . . . . .	91
3.19	Magnetic coil support . . . . .	92
3.20	Transfer process simulation - (a) . . . . .	94
3.21	Transfer process simulation - (b) . . . . .	95
3.22	Selective removal of atoms through evaporation . . . . .	96
3.23	PSD and collision rate trend during an evaporation . . . . .	98
3.24	Evaporation frequency ramp (2 Gauss) . . . . .	100
3.25	Expansion of a Bose-Einstein Condensate . . . . .	104
3.26	Phase transition to a $^{87}\text{Rb}$ BEC . . . . .	106
4.1	2D-MOT schematic drawing (repeated) . . . . .	110
4.2	Time-of-flight fluorescence signal coming from atomic beam . . . . .	111
4.3	Plot of optimal 2D-MOT trapping beam parameters . . . . .	113
4.4	Pressure vs. dispensers current . . . . .	114
4.5	$^{39}\text{K}$ atomic flux and peak velocity from 2D-MOT . . . . .	115
4.6	$^{39}\text{K}$ flux intensity and velocity as a function of push beam power . . . . .	117
4.7	$^{39}\text{K}$ flux intensity and velocity as a function of push beam detuning . . . . .	118
4.8	Results of flux simulations for $^{39}\text{K}$ 2D-MOT . . . . .	122
5.1	Measured atom number of both species - Varying loading time . . . . .	130
5.2	Measured temperature of both species - Varying loading time . . . . .	131
5.3	Temperature of the mixture as a function of the atom number . . . . .	132
5.4	Runaway evaporation dynamics . . . . .	134
5.5	Experimental evidence for sympathetic cooling of $^{39}\text{K}$ . . . . .	135
5.6	Cross collisional relaxation for $^{39}\text{K}$ . . . . .	140
5.7	Experimental observation of the cross-thermalization . . . . .	141
5.8	Cross collisional relaxation for $^{39}\text{K}$ , three different atoms numbers . . . . .	142
5.9	Cross thermalization rates - experimental results . . . . .	145

# List of Tables

- 3.1 Table of experimental 3D-MOT parameters for  $^{87}\text{Rb}$ ,  $^{39}\text{K}$  and  $^{41}\text{K}$  . . . [75](#)
- 4.1 Table of experimental 2D-MOT parameters for  $^{87}\text{Rb}$ ,  $^{39}\text{K}$  and  $^{41}\text{K}$  . . . [119](#)



# Bibliography

- [1] M. H. Anderson, J. R. Ensher, M. R. Matthews, C. E. Wieman, E. A. Cornell, *Science*, **269**, 198 (1995); E. A. Cornell, C. E. Wieman, *Rev. Mod. Phys.*, **74**, 875 (2002).
- [2] K. B. Davis, M. O. Mewes, M. R. Andrews, N. J. Van Druten, D. S. Durfee, D. M. Kurn, W. Ketterle, *Phys. Rev. Lett.*, **75**, 3969 (1995); W. Ketterle, *Rev. Mod. Phys.*, **74**, 1131 (2002).
- [3] *Bose-Einstein condensation in atomic gases*, Proceedings of the International School of Physics "Enrico Fermi", course CXL, edited by M. Inguscio, S. Stringari, and C. E. Wieman, IOS Press, Amsterdam (1999).
- [4] M. Kozuma, L. Deng, E. W. Hagley, J. Wen, R. Lutwak, K. Helmerson, S. L. Rolston, and W. D. Phillips, *Phys. Rev. Lett.* **82**, 871 (1999).
- [5] Yu. B. Ovchinnikov, J. H. Müller, M. R. Doery, E. J. D. Vredenburg, K. Helmerson, S. L. Rolston, and W. D. Phillips, *Phys. Rev. Lett.* **83**, 284 (1999).
- [6] L. Fallani, F. S. Cataliotti, J. Catani, C. Fort, M. Modugno, M. Zawada, and M. Inguscio, *Phys. Rev. Lett.* **91**, 240405 (2003).
- [7] B. Eiermann, P. Treutlein, Th. Anker, M. Albiez, M. Taglieber, K.-P. Marzlin, and M.K. Oberthaler, *Phys. Rev. Lett.* **91**, 060402 (2003).
- [8] M. Greiner, O. Mandel, T. Esslinger, T.W. Hänsch, and I. Bloch, *Nature* **415**, 39 (2002).
- [9] L. Fallani, J. E. Lye, V. Guarrera, C. Fort and M. Inguscio, `cond-mat/0603655` (2006).
- [10] P. L. Gould, G. A. Ruff, and D. E. Pritchard, *Phys. Rev. Lett.* **56**, 827 (1986).
- [11] P. J. Martin, B. G. Oldaker, A. H. Miklich, and D. E. Pritchard, *Phys. Rev. Lett.* **60** 515, (1988).
- [12] P. Verkerk, B. Lounis, C. Salomon, C. Cohen-Tannoudji, J. Y. Courtois, and G. Grynberg, *Phys. Rev. Lett.* **68**, 3861 (1992).
- [13] O. S. Jessen, C. Gerz, P. D. Lett, W. D. Phillips, S. L. Rolston, R. J. C. Spreeuw, and C. I. Westbrook, *Phys. Rev. Lett.* **69**, 49 (1992).

- 
- [14] A. Hemmerich and T. W. Hänsch, *Phys. Rev. Lett.* **70**, 410 (1993).
- [15] G. Grynberg, B. Lounis, P. Verkerk, J. Y. Courtois, and C. Salomon, *Phys. Rev. Lett* **70**, 2249 (1993).
- [16] M. B. Dahan, E. Peik, J. Reichel, Y. Castin, and C. Salomon, *Phys. Rev. Lett.* **76**, 4508 (1996).
- [17] I. Carusotto, L. Pitaevskii, S. Stringari, G. Modugno, and M. Inguscio, *Phys. Rev. Lett.* **95**, 093202 (2005).
- [18] B.P. Anderson and M.A. Kasevich, *Science* **282**, 1686 (1998).
- [19] F. S. Cataliotti, S. Burger, C. Fort, P. Maddaloni, F. Minardi, A. Trombettoni, A. Smerzi, and M. Inguscio, *Science* **293**, 5531 (2001).
- [20] O.Morsch, J. H.Müller, M. Cristiani, D. Ciampini, and E. Arimondo, *Phys. Rev. Lett.* **87** 140402 (2001).
- [21] S. Burger, F.S. Cataliotti, C. Fort, F. Minardi, M. Inguscio, M.L. Chiofalo, and M.P. Tosi, *Phys. Rev. Lett.* **86**, 4447 (2001).
- [22] F. Ferlaino, P. Maddaloni, S. Burger, F. S. Cataliotti, C. Fort, M. Modugno, and M. Inguscio, *Phys. Rev. A* **66**, 011604 (2002).
- [23] A. Smerzi, A. Trombettoni, P. G. Kevrekidis, and A. R. Bishop *Phys. Rev. Lett.* **89**, 170402 (2002).
- [24] L. Fallani, L. De Sarlo, J. E. Lye, M. Modugno, R. Saers, C. Fort, and M. Inguscio, *Phys. Rev. Lett.* **93**, 140406 (2004).
- [25] L. De Sarlo, L. Fallani, J. E. Lye, M. Modugno, R. Saers, C. Fort, and M. Inguscio, *Phys. Rev. A* **72**, 013603 (2005).
- [26] C. J. Myatt, E. A. Burt, R. W. Ghrist, E. A. Cornell, and C. E. Wieman , *Phys. Rev. Lett.* **78**, 586 (1997).
- [27] F. Schreck, L. Khaykovich, K. L. Corwin, G. Ferrari, T. Bourdel, J. Cubizolles, and C. Salomon, *Phys. Rev. Lett.* **87**, 080403 (2001).
- [28] Z. Hadzibabic, C.A. Stan, K. Dieckmann, S. Gupta, M.W. Zwierlein, A. Görlitz, and W. Ketterle, *Phys. Rev. Lett.* **88**, 160401 (2002).
- [29] G. Roati, F. Riboli, G. Modugno, and M. Inguscio, *Phys. Rev. Lett.* **89**, 150403 (2002).
- [30] C. Silber, S. Günther, C. Marzok, B. Deh, Ph.W. Courteille, and C. Zimmermann, *Phys. Rev. Lett.* **95**, 170408 (2005).
- [31] T. Bourdel, L. Khaykovich, J. Cubizolles, J. Zhang, F. Chevy, M. Teichmann, L. Tarruell, S.J.J.M.F. Kokkelmans, and C. Salomon, *Phys. Rev. Lett.* **93**, 050401 (2004).
- [32] C. Chin, M. Bartenstein, A. Altmeyer, S. Riedl, S. Jochim, J. Hecker Denschlag, R. Grimm, *Science* **1128**, 305 (2004).
- [33] C. A. Regal, M. Greiner, D. S. Jin, *Phys. Rev. Lett.* **92**, 040403 (2004).

## BIBLIOGRAPHY

---

- [34] M. W. Zwierlein, J. R. Abo-Shaeer, A. Schirotzek, C. H. Schunck, and W. Ketterle, *Nature* **435**, 1047 (2005).
- [35] J. Kinast, S. L. Hemmer, M. E. Gehm, A. Turlapov, and J. E. Thomas, *Phys. Rev. Lett.* **92**, 150402 (2004).
- [36] G.B. Partridge, K.E. Strecker, R.I. Kamar, M.W. Jack, and R.G. Hulet, *Phys. Rev. Lett.* **95**, 020404 (2005).
- [37] G. Roati, E. de Mirandes, F. Ferlaino, H. Ott, G. Modugno, and M. Inguscio, *Phys. Rev. Lett.* **92**, 230402 (2004).
- [38] M. Köhl, H. Moritz, T. Stöferle, K. Günter, and T. Esslinger, *Phys. Rev. Lett.* **94**, 080403 (2005).
- [39] S. Inouye, J. Goldwin, M. L. Olsen, C. Ticknor, J. L. Bohn, and D. S. Jin, *Phys. Rev. Lett.* **93**, 183201 (2004).
- [40] C. A. Stan, M.W. Zwierlein, C. H. Schunck, S.M. F. Raupach, and W. Ketterle, *Phys. Rev. Lett.* **93**, 143001 (2004).
- [41] A. Simoni, F. Ferlaino, G. Roati, G. Modugno, and M. Inguscio, *Phys. Rev. Lett.* **90**, 163202 (2003).
- [42] G. Modugno, G. Roati, F. Riboli, F. Ferlaino, R. J. Brecha, and M. Inguscio, *Science* **297**, 2240 (2002).
- [43] C. Ospelkaus, S. Ospelkaus, K. Sengstock, and K. Bongs, *Phys. Rev. Lett.* **96**, 020401 (2006).
- [44] L. Viverit, C. J. Pethick, and H. Smith, *Phys. Rev. A* **61**, 053605 (2000).
- [45] M. Lewenstein, L. Santos, M. A. Baranov, and H. Fehrmann, *Phys. Rev. Lett.* **92**, 050401 (2004).
- [46] G. Modugno, M. Modugno, F. Riboli, G. Roati, and M. Inguscio, *Phys. Rev. Lett.* **89**, 190404 (2002).
- [47] Y. Takahashi, private communication.
- [48] F. Ferlaino, C. D'Errico, G. Roati, M. Zaccanti, M. Inguscio, G. Modugno, and A. Simoni, *Phys. Rev. A* **73**, 040702(R) (2006) and *Erratum, ibid.* **74**, 039903(E) (2006).
- [49] G.-P. Zheng, J.-Q. Liang, and W. M. Liu, *Phys. Rev. A* **71**, 053608 (2005).
- [50] E. Altman, W. Hofstetter, E. Demler and M. D. Lukin, *New J. Phys.* **5**, 113 (2003).
- [51] G.-H. Chen and Y.-S. Wu, *Phys. Rev. A* **67**, 013606 (2003).
- [52] T. Mishra, Ramesh V. Pai and B. P. Das, *cond-mat/0610121* (2006).
- [53] A. Isacsson, Min-Chu Cha, K. Sengupta, and S.M. Girvin, *Phys. Rev. B* **72**, 184507 (2005).
- [54] Rom, T., Best, T., Mandel, O., Widera, A., Greiner, M., Hänsch, T. W., and Bloch, I., *Phys. Rev. Lett.* **93**, 073002 (2004).

- [55] Ryu, C., Du, X., Yesilada, E., Dudarev, A. M., Wan, S., Niu, Q., and Heinzen, D. J., *cond-mat/0508201* (2005).
- [56] Moritz, H., Stöferle, T., Günter, K., Köhl, M., and Esslinger, T. *Phys. Rev. Lett.* **94**, 210401 (2005).
- [57] Winkler, K., Thalhammer, G., Lang, F., Grimm, R., Hecker-Denschlag, J., Daley, A. J., Kantian, A., Buechler, H. P., and Zoller, *cond-mat/0605196* (2006).
- [58] C. Ospelkaus, S. Ospelkaus, L. Humbert, P. Ernst, K. Sengstock, and K. Bongs, *Phys. Rev. Lett* **97**, 120402 (2006).
- [59] T. Volz, N. Syassen, D. M. Bauer, E. Hansis, S. Dürr, and G. Rempe, *Nature Physics Letters* **2**, 692 (2006).
- [60] H. Wang, A. N. Nikolov, J. R. Ensher, P. L. Gould, E. E. Eyler, W. C. Stwalley, J. P. Burke, Jr., J. L. Bohn, Chris. H. Greene, E. Tiesinga, C. J. Williams, and P. S. Julienne, *Phys. Rev. A* **62**, 052704 (2000).
- [61] S. N. Bose, *Z. Phys.* **26**, 178 (1924).
- [62] A. Einstein, *Sitzber. Kgl. Preuss. Akad. Wiss.*, **261** (1924); *ibidem*, **3** (1925).
- [63] F. Dalfovo, S. Giorgini, L. Pitaevskii, S. Stringari, *Rev. Mod. Phys.*, **71**, 453 (1999).
- [64] P.G. Drazin and R.S. Johnson, *Solitons: An Introduction*, Cambridge University Press, Cambridge, England (1988).
- [65] W.P. Reinhardt and C.W. Clark, *J. Phys. B* **30**, L785 (1997).
- [66] V.M. Perez-Garcia, H. Michinel, and H. Herrero, *Phys. Rev. A* **57**, 3837 (1998).
- [67] Th. Busch and J.R. Anglin, *Phys. Rev. Lett.* **87**, 010401 (2001). E.P. Gross, *Nuovo Cimento* **20**, 454 (1961).
- [68] L.P. Pitaevskii, *Zh. Éksp. Teor. Fiz.* **40**, 646 (1961) [*Sov. Phys. JETP* **13**, 451 (1961)].
- [69] L. Khaykovich, F. Schreck, G. Ferrari, T. Bourdel, J. Cubizolles, L. D. Carr, Y. Castin, and C. Salomon, *Science* **296**, 1290 (2002).
- [70] K. E. Strecker, G. B. Partridge, A. G. Truscott, and R. G. Hulet, *Nature* **417**, 150 (2002).
- [71] L. Deng, E. W. Hagley, J. Wen, M. Trippenbach, Y. Band, P. S. Julienne, J. E. Simsarian, K. Helmerson, S. L. Rolston, and W. D. Phillips, *Nature* **398**, 218 (1999).
- [72] K. Plättner, and P. Meystre, *Quant. Semiclas. Optics* **7**, 743 (1995).
- [73] M. Trippenbach, Y. Band, and P. Julienne, *Opt. Express* **3**, 530 (1998).
- [74] D. R. Murray and P. Öhberg, *J. Phys. B* **38**, (2005).
- [75] N. Bogoliubov, *J. Phys. USSR*, **11**, 23 (1947).
- [76] Y. Castin e R. Dum, *Phys. Rev. Lett.* **77**, 5315 (1996).

## BIBLIOGRAPHY

---

- [77] P. A. Ruprecht, M. J. Holland, K. Burnett, and M. Edwards, *Phys. Rev. A* **51**, 4704 (1995).
- [78] Yu. Kagan, G. V. Shlyapnikov, and J. T. M. Walraven, *Phys. Rev. Lett.* **76**, 2670 (1996).
- [79] F. Dalfovo and S. Stringari, *Phys. Rev. A* **53**, 2477 (1996).
- [80] H. Shi and W. M. Zheng, *Phys. Rev. A* **55**, 2930 (1997).
- [81] R. J. Dodd, M. Edwards, C. J. Williams, C. W. Clark, M. J. Holland, P. A. Ruprecht, and K. Burnett, *Phys. Rev. A* **54**, 66 (1996).
- [82] C. A. Sackett, H. T. C. Stoof, and R. G. Hulet, *Phys. Rev. Lett.* **80**, 2031 (1998)
- [83] J. L. Roberts, N. R. Claussen, S. L. Cornish, E. A. Donley, E. A. Cornell, and C. E. Wieman, *Phys. Rev. Lett.* **86**, 4211 (2001).
- [84] Yu. Kagan, A. E. Muryshev, and G. V. Shlyapnikov, *Phys. Rev. Lett.* **81**, 933 (1998).
- [85] L. Santos and G. V. Shlyapnikov, *Phys. Rev. A* **66**, 011602 (2002).
- [86] G. Baym and C. J. Pethick, *Phys. Rev. Lett.* **76**, 6 (1996).
- [87] G. Barontini, *Diploma Thesis*, Università di Firenze (2006).
- [88] G. Modugno, G. Ferrari, G. Roati, R. J. Brecha, A. Simoni, and M. Inguscio, *Science* **294**, 1320 (2001).
- [89] F. Riboli and M. Modugno, *Phys. Rev. A* **65**, 063614 (2002).
- [90] A. Sinatra, P. O. Fedichev, Y. Castin, J. Dalibard, and G. V. Shlyapnikov,
- [91] B.D. Esry, C. H. Greene, J.P. Burke and J. L. Bohn, *Phys. Rev. Lett.* **78**, 3594 (1997).
- [92] Tin-Lun Ho and V. B. Shenoy, *Phys. Rev. Lett.* **77**, 3276 (1996).
- [93] R. Grimm, M. Weidemüller, and Yu. B. Ovchinnikov, *Adv. At. Mol. Opt. Phys.* **42**, 95 (2000).
- [94] D. A. Steck, <sup>87</sup>Rb *D Line Data* (rev. 1.6), available online at <http://george.ph.utexas.edu/~dsteck/alkalidata/>, (2003).
- [95] S. Falke, E. Tiemann, C. Lisdat, H. Schnatz, and G. Grosche, *Phys. Rev. A* **74**, 032503 (2006).
- [96] L. Fallani, *PhD thesis*, Università delgi Studi di Firenze, Italia, (2005).
- [97] J. C. Slater, *Phys. Rev.* **87**, 807 (1976).
- [98] D. Jaksch, *PhD thesis*, Leopold- Franzens-Universität Innsbruck, Austria, (1999).
- [99] C. Zener, *Proc. R. Soc. London A* **145**, 523 (1934).
- [100] M. Greiner, *PhD thesis*, Ludwig-Maximilians-Universität München, Germany, (2003).
- [101] B. T. Seaman, L. D. Carr, and M. J. Holland, *Phys. Rev A* **72**, 033602 (2005).

- 
- [102] B. Wu and Q. Niu, *New Journ. Phys.* **5**, 104 (2003).
- [103] M. Machholm, C. J. Pethick, and H. Smith, *Phys. Rev. A* **67**, 053613 (2003).
- [104] M. P. A. Fisher, P. B. Weichman, G. Grinstein, and D. S. Fisher, *Phys. Rev. B* **40**, 546 (1989).
- [105] D. Jaksch, C. Bruder, J. I. Cirac, C. W. Gardiner, and P. Zoller, *Phys. Rev. Lett.* **81**, 3108 (1998).
- [106] M. W. Jack, and M. Yamashita, *Phys. Rev. A* **71**, 023610 (2005).
- [107] W. Zwerger, *J. Opt. B: Quantum Semiclass. Opt.* **5**, S9 (2003).
- [108] D. van Oosten, P. van der Straten, and H. T. C. Stoof, *Phys. Rev. A* **63**, 053601 (2001).
- [109] J. K. Freericks and H. Monien, *Europhys. Lett.* **26**, 545 (1994).
- [110] T. D. Kühner and H. Monien, *Phys. Rev. B* **58**, R14741 (1998).
- [111] F. Gerbier, A. Widera, S. Fölling, O. Mandel, T. Gericke, and I. Bloch, *Phys. Rev. A* **72**, 053606 (2005).
- [112] G. G. Batrouni, V. Rousseau, R. T. Scalettar, M. Rigol, A. Muramatsu, P. J. H. Denteneer, and M. Troyer *Phys. Rev. Lett.* **89**, 117203 (2002).
- [113] M.A. Ol'shanii, Y.B. Ovchinnikov, and V.S. Letokhov, *Opt. Commun.* **98**, 77 (1993).
- [114] E. L. Raab, M. Prentiss, A. Cable, S. Chu, D. E. Pritchard, *Phys. Rev. Lett.*, **59**, 26311 (1987).
- [115] C. Monroe, W. Swann, H. Robinson, C. Wieman, *Phys. Rev. Lett.*, **65**, 1571 (1990).
- [116] P. D. Lett, R. N. Watts, C. I. Westbrook, W. D. Phillips, *Phys. Rev. Lett.*, **61**, 169 (1988).
- [117] J. Dalibard, C. Cohen Tannoudji, *J. Opt. Soc. B*, **6**, 2023 (1989).
- [118] P. J. Hungar, D. S. Weiss, and S. Chu, *J. Opt. Soc. B*, **6**, 2058 (1989).
- [119] W. Ketterle, N. J. van Druten *Advances in atomic, molecular and optical physics*, B. Bederson H. Walther, **37**, 181 (1996).
- [120] C. Fort, A. Bambini, L. Cacciapuoti, F. S. Cataliotti, M. Prevedelli, G. M. L. Tino, and M. Inguscio, *Eur. Phys. J. D* **3**, 113 (1998).
- [121] K. Dieckmann, R. J. C. Spreeuw, M. Weidemüller, and J. T. M. Walraven, *Phys. Rev. A* **58**, 3891 (1998).
- [122] J. Schoser, A. Batär, R. Löw, V. Schweikhard, A. Grabowski, Yu. B. Ovchinnikov, and T. Pfau, *Phys. Rev. A* **66**, 023410 (2002).
- [123] C. J. Myatt, E. A. Burt, R. W. Ghrist, E. A. Cornell, and C. E. Wieman, *Phys. Rev. Lett.* **78**, 586 (1997).
- [124] G. Lamporesi, *Diploma Thesis*, Università di Firenze (2003).

## BIBLIOGRAPHY

---

- [125] A. L. Migdall, J. V. Prodan, W. D. Phillips, T. H. Bergeman, and H. J. Metcalf, *Phys. Rev. Lett.* **54**, 2596 (1985).
- [126] Y. Gott, M. Ioffe, and V. Tel'kovskii, *Nucl. Fusion. Suppl. Pt.* **3**, 1045 (1962).
- [127] D. E. Pritchard, *Phys. Rev. Lett.* **51**, 1336 (1983).
- [128] T. Esslinger, I. Bloch, and T.W. Hänsch, *Phys. Rev. A* **58**, R2664 (1998).
- [129] M.-O. Mewes, M. R. Andrews, N. J. van Druten, D. M. Kurn, D. S. Durfee, and W. Ketterle, *Phys. Rev. Lett.* **77**, 416 (1996).
- [130] A. G. Sveshnikov, V. I. Telegin, and N. N. Semashko, *Sov. Phys. Techn. Phys.* **18**, 836 (1973).
- [131] E. Majorana, *Nuovo Cimento*, **9**, 43 (1932).
- [132] R. Wang, M. Liu, F. Minardi, and M. Kasevich, `quant-ph/0605114` (2006).
- [133] T. Bergeman, G Erez, and M. J. Metcalf, *Phys. Rev. A* **35**, 1535 (1997).
- [134] R. Jáuregui, N. Poli, G. Roati, and G. Modugno, *Phys. Rev. A* **64**, 033403 (2001).
- [135] S. Stringari, *Phys. Rev. Lett.* **77**, 2360 (1996).
- [136] K. G. Singh, and D. S. Rokhsar, *Phys. Rev. Lett.* **77**, 1667 (1996).
- [137] M.-O. Mewes, M. R. Andrews, N. J. van Druten, D. M. Kurn, D. S. Durfee, C. G. Townsend, and W. Ketterle *Phys. Rev. Lett.* **77**, 988 (1996).
- [138] P. Maddaloni, M. Modugno, C. Fort, F. Minardi, and M. Inguscio, *Phys. Rev. Lett.* **85**, 2413 (2000).
- [139] M. Modugno, F. Dalfovo, C. Fort, P. Maddaloni, and F. Minardi, *Phys. Rev. A* **62**, 063607 (2000).
- [140] H. F. Hess, *Phys. Rev. B* **34**, 3476 (1986).
- [141] N. Masuhara, J. M. Doyle, J. C. Sandberg, D. Kleppner, T. J. Greytak, H. F. Hess, and G. P. Kochanski, *Phys. Rev. Lett.* **61**, 935 (1988).
- [142] K. B. Davis, M. O. Mewes, M. A. Joffe, M. R. Andrews, and W. Ketterle, *Phys. Rev. Lett.* **74**, 5202 (1995).
- [143] W. Petrich, M. H. Anderson, J. R. Ensher, and E. A. Cornell, *Phys. Rev. Lett.* **74**, 3352 (1995).
- [144] C. S. Adams, H. J. Lee, N. Davidson, M. Kasevich, and S. Chu, *Phys. Rev. Lett.* **74**, 3577 (1995).
- [145] B. M. Penetrante, J. N. Bardsley, M. A. Levine, D. A. Knapp, and R. E. Marrs, *Phys. Rev. A* **43**, 4873 (1991).
- [146] W. Ketterle, D.S. Durfee, D.M. Stamper-Kurn, `cond-mat/9904034` (1999).

- 
- [147] Z. T. Lu, K. L. Corwin, M. J. Renn, M. H. Anderson, E. A. Cornell, and C. E. Wieman, *Phys. Rev. Lett.* **77**, 3331 (1996).
- [148] M. Prevedelli, F. S. Cataliotti, E.A. Cornell, J.R. Ensher, C. Fort, L. Ricci, G. M. L. Tino, and M. Inguscio, *Phys. Rev. A* **59**, 886 (1999).
- [149] W. Wohlleben, F. Chevy, K. Madison, and J. Dalibard, *Eur. Phys. J. D* **15**, 237 (2001).
- [150] R. S. Williamson III, and T. Walker, *J. Opt. Soc. Am. B* **12**, 1393 (1995).
- [151] T. B. Swanson, D. Asgeirsson, J. A. Behr, A. Gorelov, and D. Melconian, *J. Opt. Soc. Am. B* **15**, 2641 (1998).
- [152] L. Spitzer, *Physics of Fully Ionized Gases*, Inter-science, New York (1962).
- [153] B. DeMarco and D.S. Jin, *Science* **285**, 1703 (1999).
- [154] F. Schreck, L. Khaykovich, K. L. Corwin, G. Ferrari, T. Bourdel, J. Cubizolles, and C. Salomon, *Phys. Rev. Lett.* **87**, 080403 (2001).
- [155] A. G. Truscott, K. E. Strecker, W. I. McAlexander, G. B. Partridge, and R. G. Hulet, *Science* **291**, 2570 (2001).
- [156] G. Ferrari, M. Inguscio, W. Jastrzebski, G. Modugno, G. Roati, and A. Simoni, *Phys. Rev. Lett.* **89**, 053202 (2002).
- [157] W. Ketterle and N. J. van Druten, *Adv. At. Mol. Opt. Phys.* **37**, 181 (1996).
- [158] O. J. Luiten, M. W. Reynolds, and J. T. M. Walraven *Phys. Rev. A* **53**, 381 (1996).
- [159] M. Anderlini, and D. Guéry-Odelin, *Phys. Rev. A* **73**, 032706 (2006).
- [160] L. De Sarlo, P. Maioli, G. Barontini, J. Catani, F. Minardi, and M. Inguscio, cond-mat/0701051 (2007), submitted to *Phys. Rev. A*.
- [161] B. DeMarco, J. L. Bohn, J.P. Burke Jr., M. Holland, and D.S. Jin, *Phys. Rev. Lett.* **82**, 4208 (1999).
- [162] M. Arndt, M. Ben Dahan, D. Guéry-Odelin, M. W. Reynolds, and J. Dalibard, *Phys. Rev. Lett.* **79**, 625 (1997).
- [163] C. R. Monroe, E. A. Cornell, C. A. Sackett, C. J. Myatt, and C. E. Wieman, *Phys. Rev. Lett.* **70**, 414 (1993).
- [164] V. V. Flambaum, G. F. Gribakin, and C. Harabati, *Phys. Rev. A* **63**, 1998 (1999).
- [165] A. Derevianko, J. F. Babb, and A. Dalgarno, *Phys. Rev. A* **63**, 052704 (2001); A. Derevianko, W. R. Johnson, M. S. Safronova, and J. F. Babb, *Phys. Rev. Lett.* **82**, 3589 (1999).
- [166] S. Brandt, *Data Analysis: Statistical and Computational Methods for Scientists and Engineers*, 3rd ed., Springer, 1998, ISBN 0387984984.